Turbulent flow past a circular cylinder-coherent structures and dissipation in the wake

by

Rory Hetherington

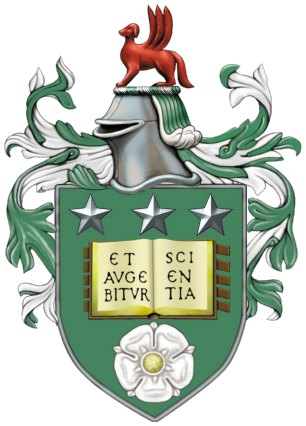

Centre for Doctoral Training in Fluid Dynamics

University of Leeds

A thesis submitted for the degree of

Doctor of Philosophy

November 2020

Declaration

The candidate confirms that the work submitted is their own. Appropriate credit has been given where reference has been made to the work of others. This copy has been supplied on the understanding that it is copyright material and that no quotation from this thesis may be published without proper acknowledgement.

Acknowledgements

Firstly, I would like to thank my team of supervisors, Nikolaos Nikitas, Robert Dorrell, Jeffrey Peakall, and Andrew Sleigh, for their continued support throughout this project. I would also like to thank those who helped in the setting up and running of experiments. This wouldn't have been possible without the guidance of Gareth Keevil and Helena Brown. Thanks also to Anthony Windross and Stephen Burgess from the workshop.

Next, I would like to thank all involved in the operational running of the Fluid Dynamics CDT here at Leeds, including the EPSRC for the funding opportunity. Many thanks to Claire Savy and Peter Jimack for all their help. It has also been a real pleasure to share an office space with such a fantastic group of fellow students and friends.

I would also like to thank my family and friends for their unconditional support throughout my time in Leeds. I cannot thank Robyn enough, you have been with me every step of the way.

Last but not least, I dedicate this work to my parents.

Abstract

The flow past a circular cylinder has been extensively investigated by researchers due to its widespread application to environmental and engineering flows. In most practical applications, the upstream flow is turbulent, yet this has received less attention in the literature. The influence of turbulence on the wake of a circular cylinder is investigated in this thesis through a combination of experiments and numerical simulations. Focus is placed on the generation of inflow turbulence, and the relationship between coherent structures and dissipation in the wake.

Free-stream turbulence is generated in simulations by projecting grid patterns onto the inlet patch. A new design is developed here which combines the best characteristics of both regular and fractal grid geometries. It has been shown that wakes created by each bar interact in an unpredictable manner, which can lead to vorticity clustering and poor turbulence homogeneity.

A circular cylinder is then placed in the wake of regular and fractal grids. A laminar inflow is also simulated for comparison. A surrogate of dissipation has been developed, which is tested on the circular cylinder wake, and only requires two components of velocity on a two-dimensional slice. In addition to this, a model is proposed which maps the distribution of dissipation and coherent structures. It has been suggested in the literature that dissipation is concentrated in the primary vortex rollers. However, here it is found to reside in between streamwise ribs.

Experiments on the circular cylinder wake are conducted using particle image velocity (PIV) to supplement numerical modelling. A turbulent inflow is generated from a biplane grid upstream of the cylinder. Structures in the wake are decomposed into coherent and stochastic components by a phase averaging procedure. Dissipation is evaluated in the two-dimensional PIV data by using the surrogate method developed in the numerical modelling work. It is concluded that stochastic turbulent fluctuations are more dissipative than coherent motions by an order of magnitude, but the two processes are locked for a short region in the circular cylinder wake. This has also been observed in the numerical simulations, and may indicate a non-classical form of turbulence decay.

Contents

List of Figures

List of Tables

Nomenclature

Abbreviations

ADV Acoustic Doppler velocimetry.

CFD Computational fluid dynamics.

CTA Constant temperature anemometry.

DFSEM Divergence-free synthetic-eddy method.

DNS Direct numerical simulation.

FVM Finite volume method.

HIT Homogeneous isotropic turbulence.

HWA Hot-wire anemometry.

LES Large-eddy simulation.

PIV Particle image velocimetry.

POD Proper orthogonal decomposition.

RANS Reynolds-averaged Navier-Stokes.

SEM Synthetic-eddy method.

SGS Subgrid-scale.

SST Shear-stress transport.

TGV Taylor-Green vortex.

TKE Turbulent kinetic energy.

UOD Universal outlier detection.

VGT Velocity gradient tensor.

VIV Vortex-induced vibration.

Greek

α Expansion coefficients.

$\boldsymbol{\phi}$ POD modes.

$\boldsymbol{\psi}$ POD Eigenvectors.

Δ Filter width.

η Kolmogorov lengthscale.

γ Specific gravity.

λ Taylor microscale.

μ Newtonian viscosity.

ν Kinematic viscosity.

ν_r Eddy viscosity.

Ω_{ij} Vorticity tensor.

ρ Density.

σ Porosity.

σ_{E} Eddy length scale.

τ Wave period.

τ_F Flow relaxation time.

τ_P Particle relaxation time.

τ_{ij} Stress tensor.

Θ Integral time scale.

θ_{s} Separation angle.

λ POD eigenvalues.

ε Dissipation rate.

φ Phase angle.

Lower-case Roman

$\boldsymbol{u''}$ Stochastic velocity.

$\boldsymbol{u'}$ Residual/SGS velocity.

$\boldsymbol{u}$ Fluctuating velocity.

f_a Acoustic frequency.

f_s Cylinder shedding frequency.

f_{pr} Pulse repetition frequency.

k Turbulent kinetic energy.

l Characteristic eddy size.

n Decay exponent.

p Modified pressure.

t_0 Largest grid bar width.

u x-component of fluctuating velocity.

$u(l)$ Characteristic velocity of an eddy of size l.

u_{rms} Root-mean-square (r.m.s) of streamwise velocity fluctuation.

v y-component of fluctuating velocity.

w z-component of fluctuating velocity.

x_0 Virtual origin.

x_* Wake interaction length.

Symbols

$\check{F}$ Normalised F.

$\hat{F}$ Fourier transform of variable F.

$\langle F \rangle$ Time-average of variable F.

$\overline{F}$ Filtering of variable F.

$\widetilde{F}$ Phase averaged F.

Upper-case Roman

$\boldsymbol{R}$ Covariance matrix.

$\boldsymbol{U}$ Eulerian velocity.

$\boldsymbol{U}_{\text{in}}$ Inlet velocity.

$\boldsymbol{U}_{\infty}$ Free-stream/bulk velocity.

$\boldsymbol{U}_m$ Centreline velocity deficit.

$\boldsymbol{U}_w$ Velocity deficit.

$\boldsymbol{X}$ POD data matrix.

$\mathcal{L}$ Characteristic length scale of the energy-containing turbulent eddies.

$\mathcal{U}$ Characteristic velocity scale of the energy-containing turbulent eddies.

$\mathscr{L}$ Characteristic length scale of the flow.

$\mathscr{U}$ Characteristic velocity scale of the flow.

$\overline{\boldsymbol{U}}$	Filtered/resolved velocity.
Re_0	Inlet Reynolds number.
Re_λ	Local Reynolds number based on the Taylor microscale.
Re_D	Reynolds number based on a cylinder diameter.
Re_I	Inlet/global Reynolds number.
Re_L	Local Reynolds number.
Re_M	Grid-inlet Reynolds number based on mesh spacing.
Re_T	Turbulent Reynolds number.
St	Strouhal number.
S_k	Stokes number.
A_{ij}	Velocity gradient tensor.
B	Number of fractal iterations.
C_ε	Kolmogorov equilibrium constant.
C_d	Drag coefficient.
C_l	Lift coefficient.
D	Cylinder diameter.
D_P	Seeding particle diameter.
I	Turbulence intensity.
L_{11}	Longitudinal integral lengthscale.
L_r	Recirculation length.
L_z	Cylinder length.
M	Grid mesh spacing.

P Pressure.

Q Second invariant of the velocity gradient tensor.

R Third invariant of the velocity gradient tensor.

$R(s)$ Autocovariance function.

S_{ij} Strain rate tensor.

T Taylor parameter.

U_{c} Centreline streamwise velocity.

Chapter 1

Introduction

Flow past a circular cylinder is a classical problem in fluid dynamics research, and has received considerable attention from theoreticians, experimentalists, and computational fluid dynamicists alike. Despite the relatively simple geometrical set-up, a complex wake is generated which may include: flow separation, shear layers, and recirculation. The most recognisable signature of the circular cylinder wake is the vortex street, where alternating concentrated regions of vorticity are generated periodically from the cylinder surface, and advect downstream by the mean flow. This can be seen across a wide range of applications: heat exchangers, telecommunication cables, chimney stacks, cylindrical buildings, aircraft landing gear, and bridge cables. It is therefore a problem which spans across a range of length scales, from small components in microfluidic devices, to massively separated flow in geophysical and astrophysical fluid dynamics. Controlling and predicting dynamics of the circular cylinder wake is important across a range of applications, such as: vortex-induced vibration (VIV) (Dalton et al., 2001), pedestrian comfort and pollutant dispersion (Franke and Frank, 2002), and bridge scour (Dargahi, 1990), to name a few.

In simple terms, the flow past a circular cylinder is an input-output system. Figure 1.1 presents a simplified picture of the flow past a circular cylinder. The base case for this type of flow is a smooth, infinitely long circular cylinder placed in a laminar free-stream. Although the base case has been thoroughly investigated in experiments and simulations, it is important for practical applications to consider departures from this base case. In reality, the cylinder may not be uniformly

circular in cross-section, will have some level of surface imperfections, and is of finite length, which may lead to end-effects. In addition to this, a cylinder is rarely placed in isolation and might be located in a boundary layer, or in the wake of another body.

With regards to inflow conditions, a circular cylinder can be placed in harsh environments, where turbulence levels are high, and the inflow is highly transient. In wind engineering for example, a laminar inflow is an exception rather than a rule (Ricci et al., 2017). In some applications such as tidal streams, turbulence intensity may exceed $I = 20\%$ (Bell, 1979). Despite the wealth of literature on the flow past a circular cylinder, relatively few studies consider the case of turbulent inflow. For example, the seminal work of Williamson (1996) provides a comprehensive review of the coherent structures formed in the wake of a circular cylinder, but only low-turbulence intensity levels ($I < 0.1\%$) were considered. However, interaction between free-stream turbulence and a circular cylinder has many interesting aspects, such as (Britter et al., 1979): distortion of turbulence by the mean flow, interaction between the turbulence and cylinder surface, effects of turbulence on the cylinder boundary layer and separation, interaction of turbulence with the wake flow.

In wind or water tunnel experiments, a laminar flow can be passed through a grid to generate a close approximation to homogeneous isotropic turbulence (HIT) (Batchelor, 1953). Almost all of the studies which consider a turbulent inflow are

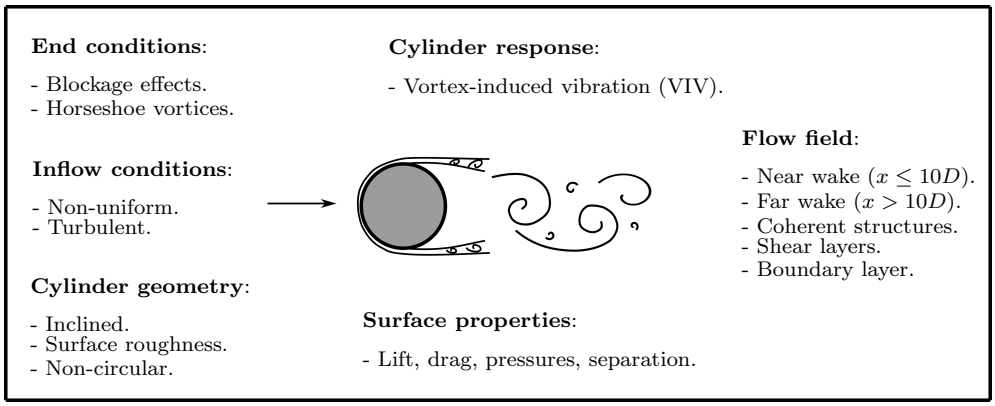

Figure 1.1: Input and output processes for the flow past a circular cylinder.

experimental and only evaluate fluid dynamic properties of the cylinder, such as: drag, lift, and pressure forces (Fage and Warsap, 1929; Bloor, 1964; Gerrard, 1965; Bearman and Morel, 1983). Theoretical models are limited to the special case of homogeneous and isotropic inflow (Eames et al., 2011). Similarly, computational modelling has also been restricted to HIT inflow (Aarnes et al., 2018). Although research of flow past a circular cylinder has been somewhat confined to HIT inflow, there has been recent interest in the bespoke generation of grid turbulence (Sakai and Vassilicos, 2016). This has been pioneered by experiments of multiscale and fractal grid-generated turbulence (Seoud and Vassilicos, 2007; Hurst and Vassilicos, 2007), which have shifted focus away from the fully developed HIT far wake and towards the turbulence production region. Multiscale and fractal grids have been found to generate elevated levels of turbulence, and an extended region in which the turbulence cascade is in non-equilibrium. Advances in custom grid-generated turbulence are yet to be applied to the study of bluff body flow, although Paul et al. (2018) simulated heat transfer of the circular cylinder in the wake of a single fractal grid element.

Despite the important role coherent structures play in heat, mass, and momentum transport, the identification of such structures has been a challenge in experiments due to the difficulty in measuring the velocity gradient tensor (Wallace, 2009). A current open question in the subject of bluff body wakes is the dissipative role of coherent structures. Goto and Vassilicos (2015) argued that a locking between the dissipation of coherent and stochastic motions may result in the non-equilibrium dissipation scaling. This argument was strengthened by Alves Portela et al. (2018), who detected a locking between coherent and stochastic dissipation components in the same downstream region of the square cylinder where non-equilibrium scaling was identified. Chen et al. (2018) investigated the relationship between coherent motions and dissipation, concluding that dissipation is concentrated in the primary rollers. This was in contrast to the model of Hussain and Hayakawa (1987), who conjectured that dissipation resides in regions of high mixing. However, the dynamics of streamwise ribs is absent from both models because measurements were taken at a single point in space, so it was not possible to separate ribs from rollers.

This thesis focuses on two aspects of the flow past a circular cylinder: inflow turbulence, and coherent structures in the wake. A method to generate free-stream turbulence in simulations is required. Ideally this method is capable of generating grid turbulence with the same characteristics observed from experiments, and can be tuned to produce different turbulence behaviour. Coherent structures in the circular cylinder wake are investigated numerically and experimentally. In addition to this, there is a lack of measurements in the literature for the dissipation field in the circular cylinder wake. A three-dimensional picture of the dissipation field and wake structures is required to understand how the two interact.

1.1 Research aims

The aim of this thesis is to improve understanding of the circular cylinder wake for a turbulent inflow. In particular, the relationship between coherent turbulent structures and dissipation will be investigated. To deliver this aim, the problem has been split into two distinct components: inflow turbulence generation, and cylinder wake dynamics. The objectives are as follows:

1 Develop a method to generate free-stream turbulence in simulations which can replicate bespoke grid turbulence from experiments.

   (a) Review the experimental literature of grid turbulence.

   (b) Simulate grid turbulence using different designs to compare turbulence produced by classical and novel grids.

   (c) Identify important parameters in grid construction which influence turbulence level, homogeneity, and length scales.

2 Explore the relationship between coherent structures and dissipation for simulations of laminar and turbulent flow past a circular cylinder.

   (a) Investigate the influence of free-stream turbulence on lift and drag of the circular cylinder.

   (b) Evaluate alternative methods of estimating the dissipation term which require fewer terms of the velocity gradient tensor.

(c) Construct a three-dimensional picture of the wake, including: rollers, ribs, and the dissipation field.

3 Investigate the circular cylinder wake experimentally using planar particle image velocimetry (PIV) for a turbulent free-stream, validating findings from the numerical modelling.

(a) Estimate dissipation along the centreline from a two-dimensional plane in the circular cylinder wake.

(b) Decompose the circular cylinder wake structures into coherent and stochastic motions, verifying the relationship between coherent and stochastic dissipation.

1.2 Thesis layout

This thesis consists of 8 chapters, including this introduction. A brief outline for each chapter is provided for the reader:

- Chapter 2 provides a review on the current understanding of free-stream turbulence generation, and its influence on the circular cylinder wake. Methods of generating turbulence in experiments are detailed, including the use of multiscale and fractal grids. Cylinder wake flow studies are reviewed, highlighting disparities in the control of inflow turbulence between experiments and simulations.

- Chapter 3 details methods of computational fluid dynamics, covering governing equations, boundary conditions, and large-eddy simulation (LES). Dissipation modelling in LES is reviewed, and turbulence models are validated on the Taylor-Green vortex problem.

- Chapter 4 is the first computational results chapter, concerning LES for a number of different grid geometries projected onto the inlet patch. A new fractal grid design is constructed which reduces vorticity clustering along the channel perimeter. Results from the projected inlet method are validated against wind tunnel experiments of grid turbulence.

- Chapter 5 provides a comparison between laminar and turbulent flow past a circular cylinder simulated with LES at a Reynolds number of 3900. Three cases are ran in total: (i) laminar inflow, (ii) regular grid turbulence inflow, (iii) fractal grid turbulence inflow. Turbulent inflow is generated from grid geometries introduced in Chapter 4. A new method of calculating dissipation in the circular cylinder wake is developed which only requires two components of velocity.

- Chapter 6 describes the experimental set-up employed in this study. A cylinder fitted with end plates is mounted downstream of a turbulence-generating grid within a recirculating water flume.

- Chapter 7 is the first experimental results chapter- particle image velocimetry of turbulent flow past a circular cylinder. Time-averaged wake dynamics are compared to literature results of experiments and numerical simulations from the low-turbulence free-stream case. Dissipation along the wake centreline is calculated by decomposing the velocity field into coherent and stochastic motions, from the method proposed in Chapter 5. Non-classical dissipation scaling is observed in the wake of the cylinder.

- Chapter 8 concludes the thesis, summarising the main findings and contributions. Further work to advance the present investigation is suggested.

Chapter 2

Free-stream turbulence and the circular cylinder wake

The present chapter is composed of two parts. Firstly, turbulence production and decay is discussed, with a focus on dissipation of freely-decaying turbulent flow. The energy cascade process is described, leading to a discussion on the mechanisms of dissipation. The preferred method of generating freely-decaying turbulence in experiments is to pass a uniform flow through a lattice of rods arranged into a grid, referred to as grid turbulence. Although square mesh grids have been used by experimentalists and theoreticians for over a century to generate and study turbulence, recent work on the subject of grid-generated turbulence has challenged the well established equilibrium dissipation scaling law. Secondly, an introduction and review of laminar flow past circular cylinders is presented. The base case for this flow configuration is that of an infinitely long circular cylinder placed in a laminar free-stream. Inconsistencies in simple measures of the wake across experiments and simulations are highlighted. Differences between reported values of the shedding frequency and recirculation length in the literature are compared, and possible sources of departure from the base case are discussed. The impact of free-stream turbulence on the circular cylinder wake is discussed, in particular how shedding is disrupted by inflow turbulence.

2.1 Freely decaying turbulence

A natural place to begin discussion of free-stream turbulence is the case of freely decaying turbulence. Turbulent flows consist of a wide range of scales, from the largest external scales which contain most of the energy, to the smallest scales where the majority of energy is dissipated. Energy at the large scales is injected from the mean flow and transferred into small scale fluctuations. This is the energy cascade description. Figure 2.1 presents a schematic of the energy cascade. Energy introduced at the large scales ℓ is transferred successively by inviscid processes to smaller scales, until viscous dissipation begins to dominate, and energy is dissipated into heat (Richardson, 1922).

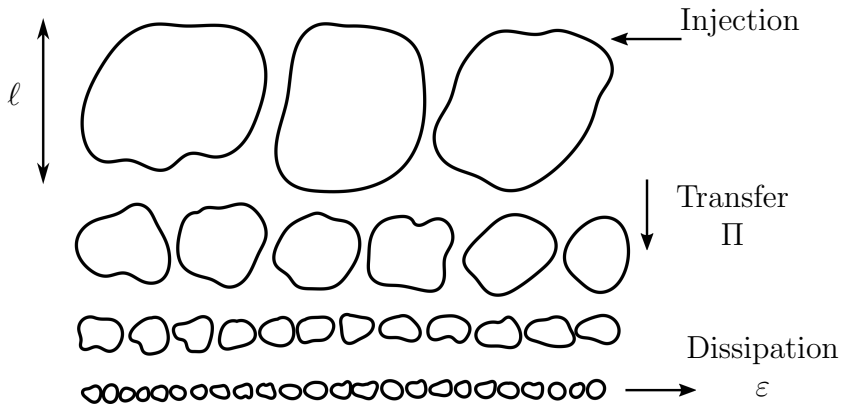

Figure 2.1: Energy cascade picture, adapted from Frisch et al. (1978).

An analytical description of the smallest scales of turbulence was introduced by Kolmogorov (1941), where turbulence at the smallest scales was described to be quasi-universal. This is often referred to as the K41 theory in the turbulence literature. From the largest scales to the smallest scales, the transfer of energy is governed by only two factors: kinematic viscosity ν, which is a physical property of the fluid; and the rate at which energy is destroyed, given by the dissipation ε. If the smallest motions have characteristic length and velocity scales denoted by η and $u(\eta)$ respectively, dissipation scales like (Pope, 2001)

$$\varepsilon \sim \nu \frac{u(\eta)^2}{\eta^2} \quad . \tag{2.1}$$

At the other end of the energy cascade, where the largest motions in a turbulent flow have typical length scale ℓ, and characteristic velocity $u(\ell)$, the rate at which energy is passed down the cascade from the largest motions is given by

$$\Pi \sim \frac{u(\ell)^3}{\ell} \quad . \tag{2.2}$$

If energy injected at the largest turbulent scales balances dissipation at the smallest scales then $\Pi \sim \varepsilon$. Along the cascade, viscosity begins to dominate flow dynamics when the turbulent scales yield a Reynolds number of unity, such that $Re_\eta \equiv \eta\, u(\eta)/\nu = 1$. The Reynolds number is a measure of inertial to viscous forces, and is defined by $Re = UL/\nu$, where U and L are characteristic velocity and length scales of the flow, respectively. Kolmogorov's first similarity hypothesis states that the smallest scales of motion in a turbulent flow have a universal form determined by the dissipation ε, and kinematic viscosity ν. Combining $Re_\eta = 1$ with (2.1) yields

$$\eta \equiv (\nu^3/\varepsilon)^{1/4} \quad , \tag{2.3}$$

$$u(\eta) \equiv (\nu\varepsilon)^{1/4} \quad . \tag{2.4}$$

Scales η and $u(\eta)$ are the Kolmogorov scales of turbulence, which characterise the smallest, dissipative eddies (Davidson, 2015).

2.1.1 Dissipation in turbulent flows

The mean turbulent kinetic energy dissipation rate, which is a fundamental quantity in turbulent flows (Sreenivasan and Antonia, 1997), plays a significant role in small-scale turbulence theory (Vassilicos, 2015). This has implications for many practical flow problems which may be characterised by enhanced turbulence production and mixing. Furthermore, the popular k-ε turbulence model of Jones and Launder (1972), requires both the kinetic energy k, and energy dissipation rate ε, as scale determining variables to close the system of equations. The dissipation

rate is given by (Hinze, 1975)

$$\varepsilon = \nu \left[\left\langle \frac{\partial u_i}{\partial x_j} \frac{\partial u_i}{\partial x_j} \right\rangle + \left\langle \frac{\partial u_i}{\partial x_j} \frac{\partial u_j}{\partial x_i} \right\rangle \right] \quad , \tag{2.5}$$

where Einstein summation convention is used over repeated indices, angled brackets indicate a time-averaged quantity, and u_i is the three-component fluctuating velocity vector for $i = 1, 2, 3$. Fluctuating velocity is obtained from the velocity field U_i by subtracting the time-average such that $u_i = U_i - \langle U_i \rangle$. A Cartesian coordinate system is adopted throughout this thesis. The three orthogonal components of direction x_1, x_2, x_3 are used interchangeably with the notation x, y, z. Similarly, the notation u_1, u_2, u_3 is used interchangeably with u, v, w. Given that ε is an averaged quantity, is may also be written as $\langle \varepsilon \rangle$. Several methods of arriving at (2.5) are presented in Section 2.1.4 of Davidson (2015).

From (2.5) it is seen that dissipation is more significant in regions where the velocity gradient tensor (VGT) $A_{ij} = \partial u_i / \partial x_j$ is large, i.e. large gradients of fluctuating velocity. Throughout the turbulence literature, ε takes different forms. For example, by introducing the strain rate tensor $S_{ij} = \frac{1}{2}(A_{ij} + A_{ji})$, dissipation can be written in a more compact form $\varepsilon = 2\nu \langle S_{ij} S_{ij} \rangle$. Dissipation appears as a sink in the energy equation, which is constructed from the governing equation of incompressible fluid flow- the Navier-Stokes momentum equation. The first term in (2.5) is the main contributor to ε in virtually all circumstances, which leads many researchers to drop the second term for convenience, and refer to the first term as the pseudo dissipation (Pope, 2001).

In total, (2.5) contains 12 terms, which are readily available in numerical simulations, but difficult to obtain experimentally, i.e. see the review of Wallace

(2009). For reference, the 12 individual terms of (2.5) are

$$\varepsilon = \nu \Bigg[2 \underbrace{\left\langle \left(\frac{\partial u}{\partial x}\right)^2 \right\rangle}_{1} + \underbrace{\left\langle \left(\frac{\partial v}{\partial x}\right)^2 \right\rangle}_{2} + \underbrace{\left\langle \left(\frac{\partial w}{\partial x}\right)^2 \right\rangle}_{3} + \underbrace{\left\langle \left(\frac{\partial u}{\partial y}\right)^2 \right\rangle}_{4} + 2 \underbrace{\left\langle \left(\frac{\partial v}{\partial y}\right)^2 \right\rangle}_{5} + \underbrace{\left\langle \left(\frac{\partial w}{\partial y}\right)^2 \right\rangle}_{6} + \underbrace{\left\langle \left(\frac{\partial u}{\partial z}\right)^2 \right\rangle}_{7} + \underbrace{\left\langle \left(\frac{\partial v}{\partial z}\right)^2 \right\rangle}_{8} + 2 \underbrace{\left\langle \left(\frac{\partial w}{\partial z}\right)^2 \right\rangle}_{9} + 2 \underbrace{\left\langle \frac{\partial u}{\partial y}\frac{\partial v}{\partial x} \right\rangle}_{10} + 2 \underbrace{\left\langle \frac{\partial u}{\partial z}\frac{\partial w}{\partial x} \right\rangle}_{11} + 2 \underbrace{\left\langle \frac{\partial v}{\partial z}\frac{\partial w}{\partial y} \right\rangle}_{12} \Bigg] \quad . \tag{2.6}$$

Due to the difficulty of measuring all 12 terms of the dissipation in experiments, assumptions on the flow field are often enforced. The simplest form of turbulent flow is homogeneous isotropic turbulence (HIT), which is invariant to rotation and translation. Isotropy requires that averaged functions of the velocity and its derivatives at a given point are invariant to rotation or reflection (Von Karman and Howarth, 1938). Homogeneity requires that averaged properties of the flow are invariant to translation, i.e. independent of position (Batchelor, 1953). If small scales are assumed to be locally isotropic, the following relations can be applied to the velocity gradients (Taylor, 1935; George and Hussein, 1991)

$$\left\langle \left(\frac{\partial u}{\partial x}\right)^2 \right\rangle = \left\langle \left(\frac{\partial v}{\partial y}\right)^2 \right\rangle = \left\langle \left(\frac{\partial w}{\partial z}\right)^2 \right\rangle \quad , \tag{2.7}$$

$$\left\langle \left(\frac{\partial u}{\partial y}\right)^2 \right\rangle = \left\langle \left(\frac{\partial u}{\partial z}\right)^2 \right\rangle = \left\langle \left(\frac{\partial v}{\partial x}\right)^2 \right\rangle = \left\langle \left(\frac{\partial v}{\partial z}\right)^2 \right\rangle = \left\langle \left(\frac{\partial w}{\partial x}\right)^2 \right\rangle = \left\langle \left(\frac{\partial w}{\partial y}\right)^2 \right\rangle \quad , \tag{2.8}$$

$$\left\langle \frac{\partial u}{\partial y}\frac{\partial v}{\partial x} \right\rangle = \left\langle \frac{\partial u}{\partial z}\frac{\partial w}{\partial x} \right\rangle = \left\langle \frac{\partial v}{\partial z}\frac{\partial w}{\partial y} \right\rangle = -\frac{1}{2}\left\langle \left(\frac{\partial u}{\partial x}\right)^2 \right\rangle \quad . \tag{2.9}$$

On substitution of (2.7), (2.8), (2.9) into (2.6), the pseudo dissipation commonly referred to as the X-wire form is obtained

$$\varepsilon_{\mathrm{xw}} = 3\nu \left[\left\langle \left(\frac{\partial u}{\partial x}\right)^2 \right\rangle + 2\left\langle \left(\frac{\partial v}{\partial x}\right)^2 \right\rangle \right] \quad . \tag{2.10}$$

Pseudo dissipation (2.10) can be utilised with constant temperature anemometry (CTA) probes. CTA is a preferred measurement technique in wind tunnel experiments. X-wire probes consist of two wires arranged in an X configuration and are capable of measuring two components of velocity. From $\varepsilon_{\mathrm{xw}}$ it is possible to retain the isotropic dissipation $\varepsilon_{\mathrm{iso}}$ by enforcing (2.8) and the isotropic condition $\langle(\partial v/\partial x)^2\rangle = 2\langle(\partial u/\partial x)^2\rangle$, to obtain

$$\varepsilon_{\mathrm{iso}} = 15\nu \left\langle \left(\frac{\partial u}{\partial x}\right)^2 \right\rangle \quad , \tag{2.11}$$

where Taylor's hypothesis $\partial/\partial x \equiv U^{-1}\partial/\partial t$ is commonly used to evaluate $\varepsilon_{\mathrm{iso}}$. Despite the widespread use of $\varepsilon_{\mathrm{iso}}$ due to its relative simplicity, it is only reliable when the turbulence is approximately isotropic, e.g. centrelines of jets/wakes, and far enough away from the wall of pipe/channel/boundary flow (Lefeuvre et al., 2014).

2.1.2 Grid turbulence

Grid turbulence is the preferred method of generating free-stream turbulence in the laboratory as the closest approximation to HIT available to the experimentalist. For grid-generated turbulence, in the Eulerian frame of reference, turbulence decays along the streamwise direction. In the Lagrangian frame moving downstream with a parcel of fluid, turbulence decays slowly over time. As a result, grid turbulence is not strictly homogeneous, but it decays at such a slow rate that homogeneity can be assumed, and it is very nearly isotropic (Batchelor, 1953). Historically, theoretical investigations of HIT have relied heavily on laboratory

experiments of grid turbulence, however, with the advent of direct numerical simulation, HIT can be generated numerically by simulating a box of periodic turbulence (Goto and Vassilicos, 2015).

Additionally, there are a number of reasons to generate grid turbulence in practical applications. Turbulent fluctuations can be combined with a bulk flow to study aerodynamic and hydrodynamic properties of objects placed in a turbulent free-stream. Grid turbulence can also be utilised in areas of engineering where enhanced mixing is desired. For example, if a grid is to be placed within a device to mix a combustible species, it is important to thoroughly distribute that species throughout the geometry, instead of producing regions of high concentration. In contrast, a wind tunnel experiment to investigate the aerodynamic properties of a solid body might only require a basic control of the turbulent inflow, such as setting an approximate turbulence intensity, which may be defined in the streamwise and crossflow directions by

$$I_1 = \frac{u_{\text{rms}}}{U_\infty} \ , \qquad I_2 = \frac{v_{\text{rms}}}{U_\infty} \ , \qquad I_3 = \frac{w_{\text{rms}}}{U_\infty} \ , \tag{2.12}$$

where $u_{\text{rms}} = \sqrt{\langle u^2 \rangle}$, $v_{\text{rms}} = \sqrt{\langle v^2 \rangle}$, $w_{\text{rms}} = \sqrt{\langle w^2 \rangle}$ are, respectively, the root-mean-square (r.m.s.) velocity fluctuations in the x, y, and z directions. Alternatively, turbulence intensity can also be defined using all 3 components of fluctuating velocity

$$I = \sqrt{\frac{1}{3}(I_1^2 + I_2^2 + I_3^2)} \ . \tag{2.13}$$

Numerous grid geometries have been designed and tested in numerical and experimental work. The grid can be active, i.e. moving in the laboratory frame and responding to the flow dynamics (Hideharu, 1991; Mydlarski and Warhaft, 1998; Cekli and van de Water, 2010), or passive and fixed in position. Only passive grids are considered in this thesis. The majority of studies have used a regular grid, constructed by forming a lattice of bars with constant diameter and equal spacing. When a uniform stream of fluid hits the grid, jets emerge through the gaps, instabilities in the shear layers grow, and turbulence is produced (see Figure 2.2).

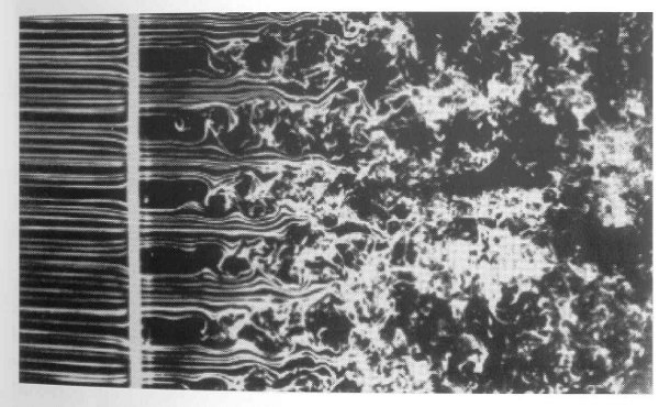

Figure 2.2: Visualisation of flow past an array of cylinders from Van Dyke (1982). Jets emerging through grid gaps interact and break down as they travel downstream. Flow is from left to right.

Regular grids have been extensively researched due to their simple construction, and advancements in turbulence theory have been developed alongside grid turbulence experiments. Early work sought to understand turbulent fluctuations (Taylor, 1922; Simmons and Salter, 1934), rigorously define isotropy (Taylor, 1935), and also describe homogeneity (Batchelor and Townsend, 1948; Batchelor, 1953). This led to further experiments focussed solely on grid turbulence. Mohamed and Larue (1990) split the flow field into three regions corresponding to the downstream position from the grid. Near grid there is a production of turbulent kinetic energy and the flow is grid geometry dependent, inhomogeneous, and anisotropic. The flow develops further downstream into Saffman turbulence (Saffman, 1967). Viscosity acts directly on the large-scale motions in the final decay region. Skrbek and Stalp (2000) developed a model to describe the final decay of turbulence, and influence of intermittency on the energy decay, applying findings to a number of grid turbulence experiments.

In defining the concept of isotropy from experiments of grid-generated turbulence, Taylor (1935) reasoned on ad-hoc grounding that dissipation scales by

$$\varepsilon = C_\varepsilon \frac{\mathcal{U}^3}{\mathcal{L}} \quad , \tag{2.14}$$

where C_ε is the Kolmogorov equilibrium constant, and $\mathcal{U}$, $\mathcal{L}$ are characteristic

turbulent velocity and length scales, respectively. The form of (2.14) is similar to (2.2), but with some change of notation. A characteristic time scale of the turbulence can be defined from $\mathcal{T} = \mathcal{L}/\mathcal{U}$, from which (2.14) can be interpreted as the rate of change of energy from the large scale turbulent motions. In the case of grid turbulence, large scale structures are generated near grid in the production region, which then break up into progressively smaller scales as they travel downstream. Choice of characteristic turbulent velocity and length scales vary between authors. Well established choices for $\mathcal{U}$ and $\mathcal{L}$ are generated from the streamwise component of velocity (Batchelor, 1953; Sreenivasan, 1984; Antonia and Pearson, 2000; Vassilicos, 2015)

$$\mathcal{U} = \sqrt{\frac{3}{2}}\, u_{\mathrm{rms}} \quad , \tag{2.15}$$

$$\mathcal{L} = L_{11} \quad , \tag{2.16}$$

where L_{11} is the longitudinal integral length scale, obtained by integrating the autocovariance function $R(s) = \langle u(x)u(x+s)\rangle$

$$L_{11}(x) = \frac{1}{\langle u^2(x)\rangle} \int_0^\infty R(s)\, \mathrm{d}s \quad , \tag{2.17}$$

where s is a separation distance in the streamwise direction x, and the integral (2.17) is usually taken up to the first zero crossing of the integrand.

Another important length scale in the study of grid turbulence is the Taylor microscale λ, which lies between the integral length scale and the Kolmogorov microscale. The Taylor microscale is defined by

$$\lambda^2 = \frac{\langle u^2\rangle}{\left\langle (\partial u/\partial x)^2 \right\rangle} \quad . \tag{2.18}$$

A local Reynolds number can be defined from the Taylor microscale by $Re_\lambda = u_{\mathrm{rms}}\lambda/\nu$. Taylor (1935) considered C_ε to be constant for geometrically similar boundaries, and far enough away from the grid where the mean velocity becomes uniform. Experimental evidence for constant C_ε in the initial period of decay followed in Batchelor (1953), who compiled data from numerous biplane grid

turbulence experiments. This was further strengthened by Sreenivasan (1984), who also collected biplane grid data and plotted the relationship between C_ε and Re_λ, here reproduced in Figure 2.3. It was concluded that C_ε becomes independent of Re_λ for $Re_\lambda \gtrsim 50$, and asymptotes towards a constant value which depends on the grid geometry. The assumption that C_ε is constant was referred to as "one of the cornerstone assumptions in turbulence theory" by Tennekes and Lumley (1972). The implications of constant C_ε are discussed in further detail in Section 2 of Vassilicos (2015)- "The Richardson-Kolmogorov Cascade".

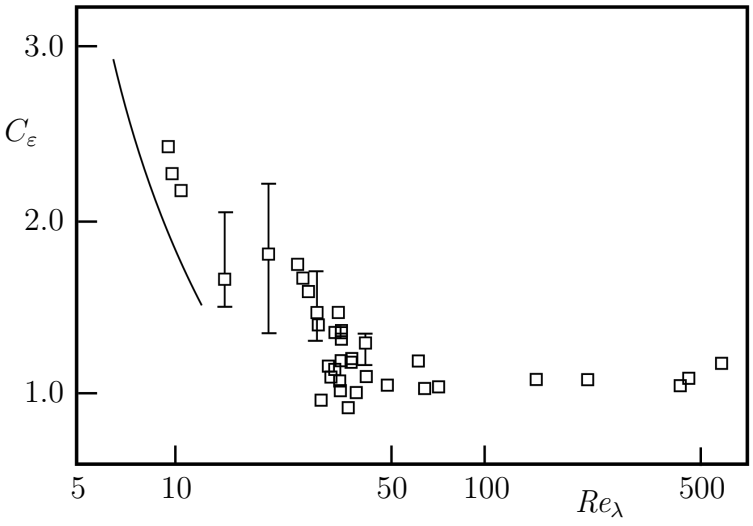

Figure 2.3: C_ε as a function of Re_λ from a range of biplane grid experiments. Plot reproduced from Table I of Sreenivasan (1984).

With a comprehensive understanding of regular grid turbulence, researchers turned to variations of the classic biplane grid by constructing grids with multiple bar diameters and mesh spacings. Such grids are referred to as multiscale, which is a general description encompassing a number of geometries. Grids can also be constructed from fractal patterns. Fractal grids are constructed by repeating a chosen shape on progressively smaller scales. Four multiscale grids from wind tunnel experiments are displayed in Figure 2.4. Fractal shapes are ubiquitous in nature, for example: tree canopies, coral reefs, coastal lines, and the respiratory system are all fractal geometries which have some interaction with fluid flow. Alongside a need to understand the flow past fractal shapes for environmental

fluid dynamics, Laizet and Vassilicos (2009) highlighted potential use throughout engineering, including: improved performance of inline mixers, heat exchangers, fluid injectors, pollutant dispersal/ventilation, and optimisation of combustion engines. Greater control of grid turbulence through multiscale/fractal geometries opens up the possibility of bespoke turbulence generation (Sakai and Vassilicos, 2016), which extends beyond grids, e.g. to combustions systems (Hampp and Lindstedt, 2016), and fractal orifices in pipes (Nicolleau, 2016). However, fractal grid-generated turbulence is yet to be adopted to the study of flow past a circular cylinder

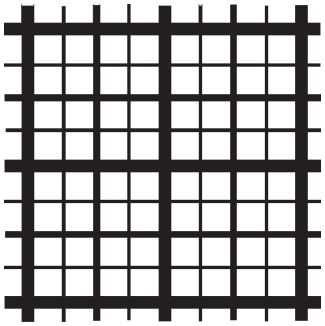

(a) Multiscale grid of Krogstad and Davidson (2011).

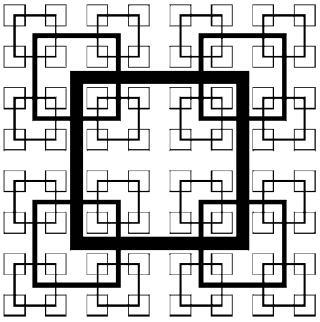

(b) Square-fractal grid of Hurst and Vassilicos (2007).

(c) Fractal grid of Hearst and Lavoie (2014).

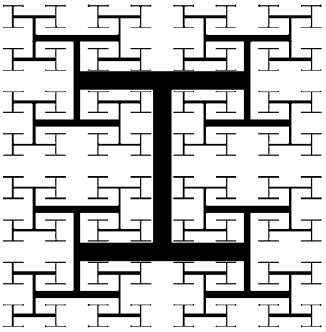

(d) I-fractal grid of Hurst and Vassilicos (2007).

Figure 2.4: Multiscale and fractal grid designs from wind tunnel experiments.

Alongside the motivation for generating fractal grid turbulence for environmental and engineering flows, fractal grid turbulence initially received considerable attention due to the non-classical turbulence decay behaviour observed in

wind tunnel experiments, pioneered by research conducted at Imperial College London, UK: Hurst and Vassilicos (2007); Seoud and Vassilicos (2007). Experimental findings confirmed the existence of a region close to the grid where the equilibrium scaling (2.14) is violated, such that C_ε varies like the inverse of a local Reynolds number

$$C_\varepsilon \propto \frac{\sqrt{Re_I}}{Re_\lambda} \ , \tag{2.19}$$

where Re_I is an inlet/global Reynolds number which may be defined using the mesh spacing, for example.

Subsequent experiments in wind tunnels and water flumes have confirmed the existence of non-constant C_ε in regions of well developed turbulence, conditions for which were set out in Laizet et al. (2013): Kolmogorov's $-5/3$ law is observed for at least one decade of wavenumbers, and the probability density function of streamwise velocity fluctuations is approximately Gaussian. Non-constant C_ε is not only confined to grid turbulence (Mazellier and Vassilicos, 2010; Valente and Vassilicos, 2011; Gomes-Fernandes et al., 2012; Valente and Vassilicos, 2012; Discetti et al., 2013; Nagata et al., 2013; Hearst and Lavoie, 2014; Isaza et al., 2014; Nagata et al., 2017), but also: boundary layers (Nedić et al., 2017); planar jets (Breda and Buxton, 2018); periodic box turbulence (Goto and Vassilicos, 2015); axisymmetric wakes (Dairay et al., 2015); and the square-cylinder wake (Alves Portela et al., 2018). To the author's knowledge, non-constant C_ε has not been detected or investigated in the wake of a circular cylinder.

Mazellier and Vassilicos (2010) describe non-constant C_ε as a result of "self-preserving single-length scale type of decaying homogeneous turbulence", where the ratio of the integral length scale L_{11} to the Taylor microscale λ remains constant in regions of decreasing Re_λ. In fact, this special case of decaying turbulence was predicted on entirely theoretical grounds by George (1992), who solved the energy spectra equation for a fixed length scale. However, the work of George (1992) was dismissed because there was no experimental evidence of non-classical decay behaviour at the time.

George and Wang (2009) provide explanation towards why multiscale and fractal grids produce different turbulence behaviour. For a given range of length scales, equilibrium requires a constant flux of turbulent kinetic energy across all

scales. If the net flux of energy is balanced, the energy spectra becomes steady. However, if this balance is disturbed, then non-equilibrium turbulence may be produced. Unlike the regular grid, which is constructed with only one bar diameter and equal spacing, multiscale and fractal grids add energy at multiple scales of motion. This alters the flux of energy from low to high wavenumbers, and the relative amount of energy at each wavenumber remains constant during decay. This is in contrast to the process depicted in Figure 2.1, because the Richardson-Kolmogorov cascade does not include details of hierarchical flow structures or cascade dynamics (Goto et al., 2017). Non-classical dissipation has since been observed in regular and multiscale grids (Valente and Vassilicos, 2012), however this behaviour was first detected in fractal grid experiments because fractal turbulence produces an elongated non-equilibrium range.

To understand how previous grid turbulence experiments failed to isolate the behaviour of C_ε, it is important to note the majority of experiments sought to study HIT, i.e. in the final period of decay where classical decay is found. The highly anisotropic and inhomogeneous flow near grid was of no interest to researchers. Additionally, the chosen measurement instrumentation also plays a role. A preferred method of experimentalists in the study of grid turbulence is hot-wire anemometry (HWA). A wire is placed in the flow field and temperature changes in time are related to flow speed. HWA is intrusive and unsuitable for the recirculating flow present near grid. Another drawback of HWA measurements is the difficulty found when probing regions of high turbulence. Since HWA measurements are fixed in space, researchers rely on Taylor's frozen turbulence hypothesis, which assumes that advection is dominated by the bulk flow and not turbulent motions. This is not possible for regions in the flow where turbulent intensity is large $I \gtrsim 15\%$ (Valente and Vassilicos, 2014), i.e. in the near grid region where the non-equilibrium range typically exists.

2.2 Flow past a circular cylinder

2.2.1 Vortex shedding

A region of disturbed flow is formed as a fluid moves relative to a bluff body, causing recirculation and formation of a wake. Bluff body flows are common in engineering and environmental applications. Simple structures such as circular cylinders, flat plates, and cubes, are basic components of larger structures in the fields of civil, hydraulic, mechanical, offshore, and wind engineering (Zdravkovich, 1997). Alongside the many applications of the flow past a circular cylinder, it is also an ideal test case for assessing the performance of experimental and numerical techniques due to the simple geometrical set-up and complexity of generated flow field. A number of reviews have documented this flow: Norberg (1987); Niemann and Hölscher (1990); Beaudan and Moin (1994); Williamson (1996). The coordinate system used throughout this thesis for the circular cylinder flow is defined in Figure 2.5.

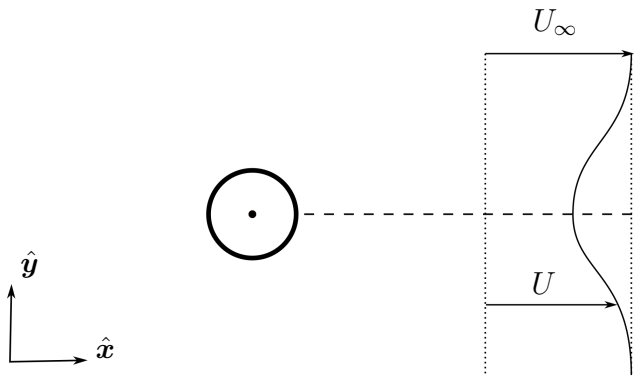

Figure 2.5: Schematic of the circular cylinder wake and coordinate axis. Streamwise ($\hat{\boldsymbol{x}}$) and normal direction ($\hat{\boldsymbol{y}}$) marked for reference, with axial direction ($\hat{\boldsymbol{z}}$) out of the page. A dot is placed at the coordinate system origin, which corresponds to the cylinder centre. Flow is from left to right.

The very first scientific investigation into vortex shedding is attributed to Vincenc Strouhal. In 1878, Strouhal conducted an experiment by moving wires through air using a hand-driven whirler. Strouhal observed that the frequency of

the Aeolian tone was proportional to U/D, where U was the relative air velocity, and D the wire diameter. This led to the introduction of an important nondimensional parameter in the study of circular cylinder flow- the Strouhal number $St = f_s \cdot D/U$, where f_s is the shedding frequency. The Strouhal number is a representation of the eddy shedding frequency. Theodore von Kármán carried out experiments to study the wake by towing a circular cylinder through a solution of sugar and water. Pioneering work from von Kármán contributed to understanding the formation and stability of the vortex street configuration. However, although often attributed to von Kármán, vortex streets were first sketched by Henri Bénard as he observed the formation of surface dimples as bluff bodies move through water (Bénard, 1908a,b).

Figure 2.6 presents an example of periodic shedding in a large scale environmental flow- a vortex street forming in the clouds above the Alejandro Selkirk Island, off the Chilean coast. This image was captured from the Landsat 7 satellite, on September 15, 1999. The island has a diameter of 1.5 km and the vortices advect hundreds of kilometres downstream.

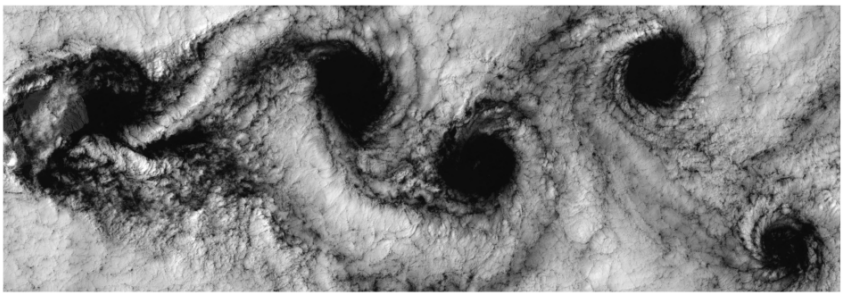

Figure 2.6: Satellite image of vortex shedding over the Alejandro Selkirk Island (Cahalan, 1999). To give an idea of scale- the island has a diameter of 1.5 km.

Another important nondimensional parameter, which is closely linked to the Strouhal number for the flow past a circular cylinder, is the Reynolds number Re. For the flow past a circular cylinder, the Reynolds number based on the cylinder diameter and inflow speed is given by $Re_D = U_\infty D/\nu$. The Strouhal number increases monotonically in the Reynolds number range $45 < Re_D < 1000$, after which it plateaus to $St \approx 0.21$ at approximately $Re_D = 10^3$ (Roshko, 1952).

Figure 2.7 displays an example of vortex shedding from a circular cylinder at $Re_D = 2000$. The cylinder surface can be defined using cylindrical coordinates (r, θ), where $r = D/2$ is the radial distance, and θ is the angle swept from the cylinder front ($\theta = 0°$) to a point on the surface. An angle of $\theta = 180°$ corresponds to the base. A stagnation point of zero flow velocity is found at the front and base of the cylinder. Flow separation occurs at an angle of θ_s, which is Reynolds number dependent, such that $\theta_s = 78.8 + 505 Re_D^{-1/2}$, for the range $270 \lesssim Re_D \lesssim 10^5$ (Jiang, 2020). For a Reynolds number of $Re_D = 2000$, this corresponds to $\theta_s = 90.1°$, which looks reasonable from Figure 2.7.

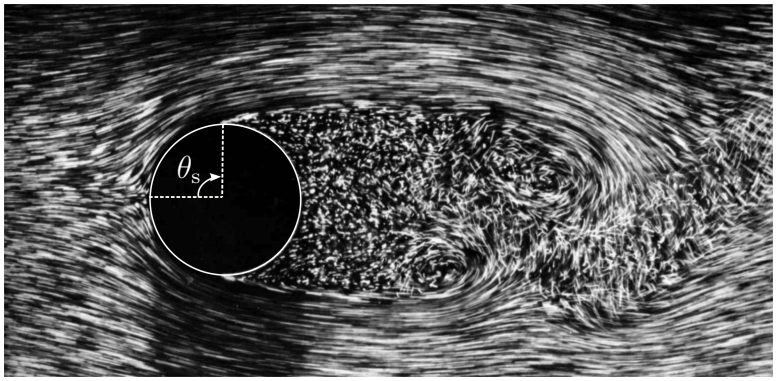

Figure 2.7: Visualisation of the circular cylinder wake flow at $Re_D = 2000$, including the definition of the separation point θ_s. Adapted from Van Dyke (1982). Flow is from left to right.

2.2.2 Wake structures and dissipation

Coherent structures play an important role in many turbulent flows such as bluff body wakes due to their influence on heat, mass, and momentum transport. Numerous definitions of a coherent structure exist, but here the definition of Hussain (1986) is used: "A coherent structure is a connected turbulent fluid mass with instantaneously phase-correlated vorticity over its spatial extent". This definition allows decomposition of turbulent fields into coherent and incoherent parts.

Despite the relative simplicity of the circular cylinder geometry, a complex wake is generated due to the interaction of three shear layer transitions in the same problem: the boundary layer, a separating free shear layer, and in the near

wake (Zdravkovich, 1990; Williamson, 1996). Here the convention of Ma et al. (2000) is used: $x/D < 3$ is the very near wake, where dynamics of the shear layer dominate, and $3 < x/D < 10$ is the near wake.

At low Reynolds numbers in the viscous limit $Re_D \ll 1$, the flow around a circular cylinder resembles potential flow (Zdravkovich, 1997). Separation occurs at approximately $Re_D = 5$, due to an increase in static pressure causing the boundary layer to slow, triggering separation (Taneda, 1956). At approximately $Re_D = 49$, the wake develops from a symmetrical fixed double separation bubble into an unsteady shedding regime. Increasing the Reynolds number further, the flow becomes asymmetric and unsteady. The flow remains laminar and von Kármán street vortices are created from shear layer instabilities, which are primarily two-dimensional (Singh and Mittal, 2005).

At $Re_D \approx 190$, the flow becomes three-dimensional, producing two discontinuities in the Strouhal-Reynolds number relation. From $Re_D = 190$ to 260, vortex loops and streamwise vortices are generated, identified by Williamson (1988) as mode A and B, respectively. Vortex loops with a wavelength of approximately $3D$ are formed as laminar primary vortices deform. Mode B fine-scale streamwise vortices have a wavelength of roughly $1D$. Streamwise vortices greatly alter the dynamics of the von Kármán vortices, but only on the upstream side (Bays-Muchmore and Ahmed, 1993). The primary von Kármán rollers are deformed, and there is a production of axial flow. Mode A and B structures were first identified numerically in the direct numerical simulation (DNS) of Thompson et al. (1994). Figure 2.8 is reproduced from the study of Williamson (1988), which forms some of the earliest work on the three-dimensionality of the wake. Two sets of structures are easily identified- mode A orientated vertically with wavelength $\sim \pi D$, and mode B orientated in the streamwise direction with wavelength $\sim 1D$. Figure 2.9 presents a schematic of the interaction between vortex loops and streamwise ribs, which are observed in the dye visualisation of Williamson (1988). Up until the review paper of Williamson (1996), the circular cylinder wake was mostly described as a two-dimensional process. Williamson (1996) detailed some of the complexities found in the wake, including: oblique, parallel, and cellular shedding; vortex dislocations; phase shocks and expansions; and vortex loops.

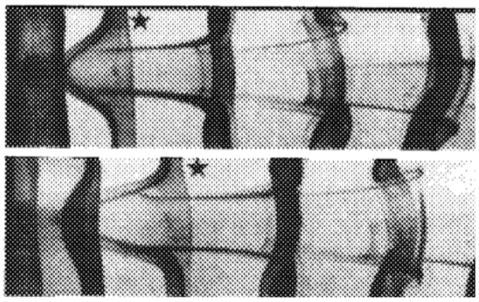

(a) Vortex loops ($Re_D \approx 180$).

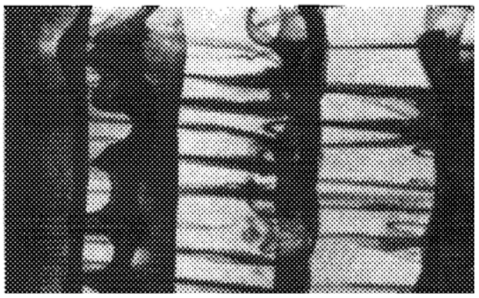

(b) Streamwise ribs ($Re_D \approx 285$).

Figure 2.8: Visualisation of vortex structures from dye washed off the circular cylinder surface. Flow is from left to right, and the cylinder is located along the left edge of each image. Adapted from Williamson (1988).

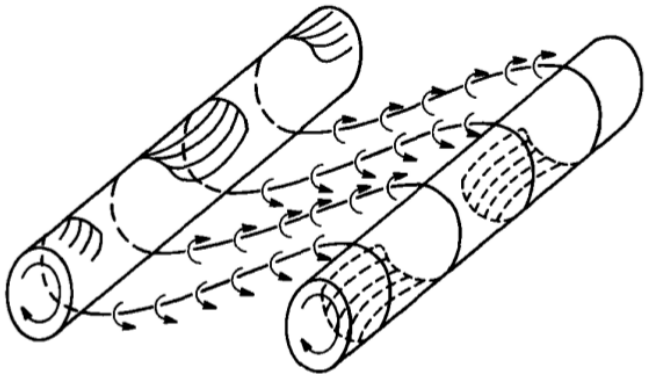

Figure 2.9: Interaction between vortex loops/rollers and streamwise vortices. Adapted from Hussain and Hayakawa (1987).

Beyond $Re \approx 250$, modelling the problem as two-dimensional leads to inaccurate calculated values of drag and lift coefficients. Two-dimensional simulations have been known to over-predict the fluid forces on the cylinder, e.g. see Beaudan and Moin (1994). A three-dimensional dependency on lift and drag were found in the earlier work of Braza et al. (1986). At $Re_D \approx 300$, the wake undergoes a fast transition from laminar to turbulent, and enters the subcritical regime (Norberg, 2003). Transition to turbulence occurs in the separated free shear layers, but flow in the direct vicinity of the cylinder remains laminar (Cardell, 1993). Norberg (2003) split the subcritical regime into lower and upper portions at a cut-off of $Re_D = 5000$. A notable difference between the lower and upper subcritical regimes

Re_D	Comment
~ 90	Eddies break off, form von Kármán street vortices (Zdravkovich, 1997).
140-500	Knots and fingers appear as footprints of secondary vortices (Gerrard, 1978).
185	Earliest 3D transition to mode A (Williamson and Roshko, 1988).
188.5	Floquet analysis predicts mode A structures (Barkley and Henderson, 1996).
260	Shedding enters mode B (Williamson, 1988).
300	Beginning of lower subcritical regime (Norberg, 2003).
1200	Shear layer becomes unstable (Prasad and Williamson, 1997a).
5000	Subcritical regime transitions to upper part (Prasad and Williamson, 1997b).
2×10^5	End of subcritical regime, boundary layer becomes turbulent (Norberg, 2003).
3.5×10^6	Boundary layer turbulent before separation (Kravchenko and Moin, 2000).

Table 2.1: Reynolds number regimes of laminar flow past a circular cylinder.

is the existence of vortex dislocations (Norberg, 1987; Prasad and Williamson, 1997a). The lower critical transition range ($Re_D = 2 \times 10^5$ to 5×10^5), is associated with a large drop in the drag coefficient from $C_d = 1.2$ to 0.3, known as the drag crisis (Roshko, 1952). In the upper critical transition range ($Re_D = 5 \times 10^5$ to 3.5×10^6), the drag coefficient increases from 0.3 to 0.7, and remains constant up to approximately $Re_D = 1 \times 10^7$ (Beaudan and Moin, 1994). The cylinder flow enters the post-critical regime at a Reynolds number of $Re_D = 3.5 \times 10^6$, at which point the boundary layer becomes turbulent before separation. A summary of flow regimes for a range of Reynolds numbers is presented in Table 2.1.

Figure 2.10 presents a topological model of the circular cylinder wake, proposed by Hussain and Hayakawa (1987) from their wind tunnel experiment. This model was constructed from vorticity data at a fixed Reynolds number of $Re_D = 13000$ by an array of 8 X-wire probes positioned at $x/D = 10, 20, 30, 40$. This picture presents a slice taken through 5 spanwise rollers of the vortex street. In line with the definition of Hussain (1986), rollers are coherent structures with phase-correlated vorticity over some spatial extent. The centre of each roller has been marked in Figure 2.10, and surrounded by a closed circle to mark its boundary. Successive vortices pull fluid into the wake and meet with engulfed free-stream flow at saddle points, creating regions of intense strain and turbulence production. The saddle points are dynamically the most significant point of the flow. Turbulence produced around the saddle points interacts with rollers, causing strong mixing. Although dissipation was not calculated in their study, Hussain and Hayakawa (1987) proposed that it is concentrated in these regions of strong turbulent mixing.

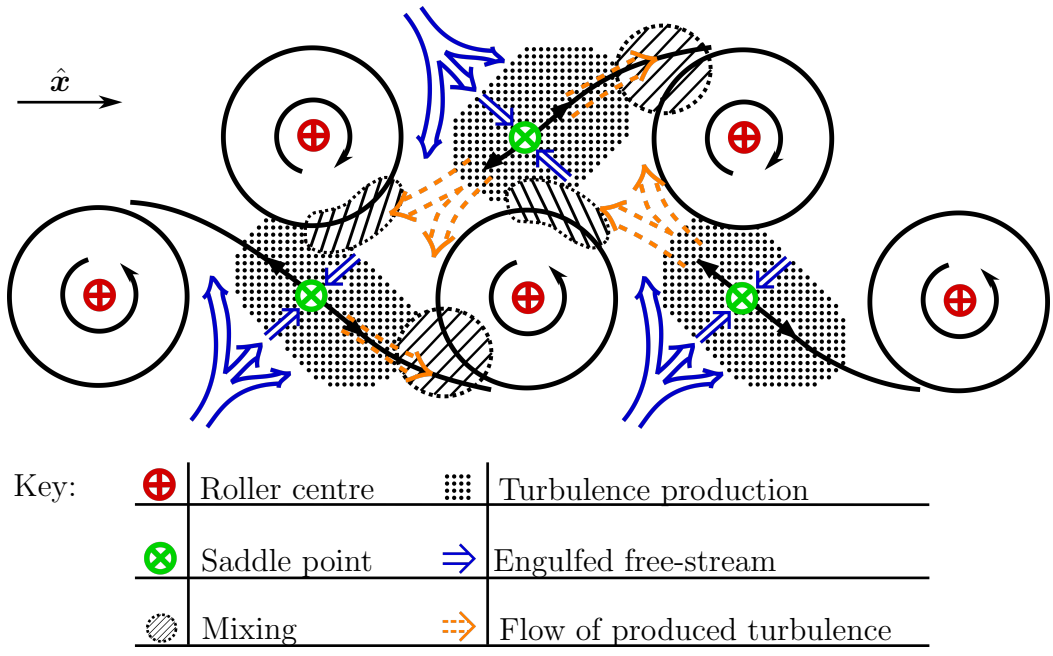

Figure 2.10: Topological features of the circular cylinder wake, adapted from the original model of Hussain and Hayakawa (1987) with the amendments of Chen et al. (2018).

Chen et al. (2018) sought to amend the model of Hussain and Hayakawa (1987) by including information on dissipation in the vortex street. Measurements were taken at a fixed Reynolds number of $Re_D = 2500$ at downstream positions $x/D = 10, 20, 40$. A surrogate of the dissipation rate, derived from an assumption of homogeneity (Lefeuvre et al., 2014), is calculated from 10 of the 12 terms of ε in (2.6). Phase averaged data suggested that energy dissipation is concentrated in the primary vortex rollers, and not in the regions of strong turbulent mixing as proposed by Hussain and Hayakawa (1987). To the author's knowledge, the experimental data of Chen et al. (2018), where 10 of the 12 dissipation terms were directly measured, is the most complete study of dissipation in the circular cylinder wake. However, a more complete picture of the interaction between coherent vortices in the near wake region and the dissipation rate is required to gain a better understanding of the circular cylinder wake.

2.2.3 Measurement challenges

To demonstrate the difficulty of controlling external variables in experiments and numerical simulations, two simple measures of the circular cylinder wake are considered: the recirculation length L_r, and the Strouhal number St. The recirculation length is taken to be the distance from the cylinder base to the sign change where $\langle U_1 \rangle$ first becomes positive. The Strouhal frequency can be deduced from pressure measurements on the cylinder surface, or from periodic velocity signals in the wake. Data is collected from across a range of experiments and simulations at a moderate Reynolds number of $Re_D = 3900$. This Reynolds number has been chosen because it is convenient- there are numerous studies carried out at this Reynolds number, and it is attainable in experiments and simulations. It is also of interest to the wider engineering community, for example, Demartino and Ricciardelli (2017) emphasised its relevance to the lower Reynolds number range experienced in the flow around cables, chimneys, and cooling towers. Finally, structures in the circular cylinder wake are unchanged for a Reynolds number below the critical value, i.e. for $Re_D < 2.5 \times 10^5$ (Zdravkovich, 1997), so findings at this Reynolds number can be extrapolated up to higher Reynolds numbers.

In Figure 2.11, shedding frequency is plotted against recirculation length for various experimental and numerical studies of the flow past a circular cylinder at $Re_D = 3900$. The data are also presented in Table 2.2, with supplementary information on methodology used for each study. The shape of each marker corresponds to the method used to collect each measurement, i.e. experiment, DNS, or LES. Data is further segregated by the aspect ratio of the cylinder. Solid markers correspond to aspect ratios exceeding $L_z/D = \pi$, where L_z is the cylinder length. This is an important distinction, because $L_z/D = \pi$ is commonly used in numerical simulations, yet might not appropriately represent an infinite circular cylinder (Ma et al., 2000). If the aspect ratio is $L_z/D \leq \pi$, the marker is left hollow. Mean values have been calculated for each method and are represented by grey markers. It can be seen that, despite scatter in the data, mean values obtained from each method are reasonably grouped about $L_r/D = 1.35$, and $St = 0.213$.

Figure 2.11 is inspected for trends in the data due to cylinder aspect ratio, level of turbulence modelling approximations, and free-stream flow conditions. Firstly,

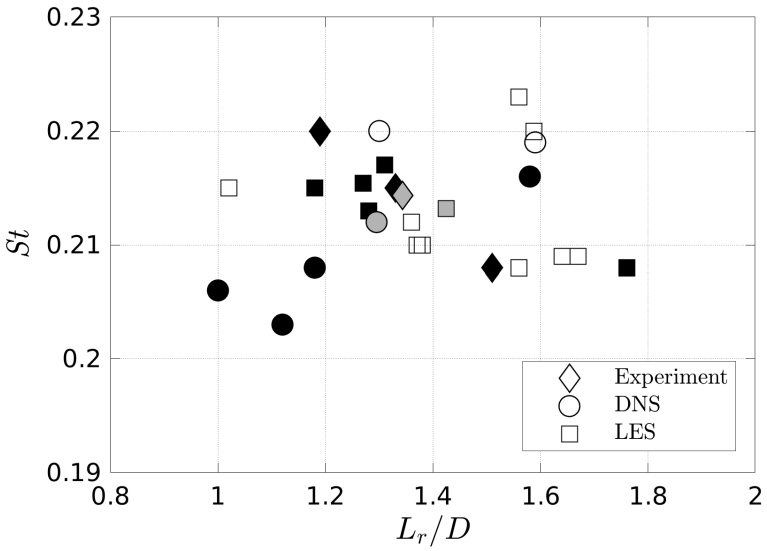

Figure 2.11: Shedding frequency versus recirculation length for experiments and simulations of the flow past a circular cylinder at Reynolds number 3900. Raw data is presented in Table 2.2. Hollow markers have been used where the nondimensional cylinder length is $L_z/D \leq \pi$, and solid markers otherwise. Grey markers denote mean values for each method.

there appears to be no link between aspect ratio and recirculation length, because there is no observable grouping between solid and hollow markers. Secondly, different turbulence models and mesh resolutions have been employed across the LES studies, therefore some scatter would be expected in those results. However, there is also considerable scatter in the DNS data, which is surprising because no modelling is employed, and all scales of turbulence are resolved down to the Kolmogorov scales (Pope, 2001). Correctly predicting L_r and St is not only important for model validation, but there are also physical consequences. For example, the Strouhal number is intimately linked to the vortex shedding frequency f_s, which plays an important role in vortex-induced vibration, mixing, lift and drag measurements, and acoustic noise (Williamson and Govardhan, 2004, 2008). This has led researchers to investigate methods to manipulate and control the circular cylinder wake, e.g. see Choi et al. (2008). The operation of energy harvesting devices also depends on the recirculation region, which is a factor in how quickly

the wake will recover from the velocity deficit (Akaydın et al., 2010).

One plausible explanation for the scatter in L_r is the inflow conditions. For example, in their PIV experiment at $Re_D = 3900$, Lourenco and Shih (1993) reported a recirculation length of $L_r/D = 1.18$, however, this was later documented in Kravchenko and Moin (2000) to be resulting from "inflow disturbances". Parnaudeau et al. (2008) reported a recirculation length of $L_r/D = 1.51$ from their PIV study, which closely agrees with the DNS (case II) of Ma et al. (2000) who found $L_r/D = 1.59$, and the PIV of Dong et al. (2006) where $L_r/D = 1.47$. Although it is possible to assess the accuracy of an experimental or numerical study on the flow past a circular cylinder by using all the compiled data to obtain a sensible range for St or L_r, it is more important to understand the causes of such a scatter in the data.

Reference	Type	St	L_r/D	L_z/D
Cardell (1993)	HWA	0.215	1.33	20
Lourenco and Shih (1993)	PIV	0.220	1.19	21
Mittal and Moin (1997)	LES	0.220	1.59	π
Kravchenko and Moin (2000)	LES	0.210	1.37	π
Ma et al. (2000)	DNS (Case I)	0.203	1.12	2π
	DNS (Case II)	0.219	1.59	π
	DNS (Case III)	0.206	1.00	1.5π
	LES (Case IV)	0.213	1.28	1.5π
	LES (Case V)	0.208	1.76	1.5π
Franke and Frank (2002)	LES (Nc=42)	0.209	1.64	π
Tremblay (2002)	DNS	0.220	1.30	π
	LES	0.215	1.02	π
Dong et al. (2006)	DNS	0.208	1.18	1.5π
Park et al. (2006)	LES (DVME)	0.212	1.36	π
Alkishriwi et al. (2006)	LES	0.217	1.31	1
Wissink and Rodi (2008)	DNS	0.216	1.58	8
Parnaudeau et al. (2008)	PIV	0.208	1.51	20
	LES	0.208	1.56	π
Ouvrard et al. (2010)	LES	0.223	1.56	π
Meyer et al. (2010)	LES (Cart. grid)	0.210	1.38	4
	LES (Curv. grid)	0.215	1.18	4
Lysenko et al. (2012)	LES (TKE)	0.209	1.67	π
Prsic et al. (2014)	LES	0.215	1.27	4

Table 2.2: Experiments and simulations on the flow past a circular cylinder at $Re_D = 3900$. Data is plotted in Figure 2.11. Inflow turbulence was deemed to be negligible in these studies.

2.2.4 The turbulent inflow case

So far only the ideal test case for the flow past a circular cylinder has been discussed- an infinitely long cylinder placed in a laminar free-stream flow. However, wake dynamics are also sensitive to: end conditions (Prasad and Williamson, 1997a); surface roughness (Shih et al., 1993); cross-sectional irregularities (Demartino and Ricciardelli, 2017); cylinder vibration (Chyu and Rockwell, 1996); aspect ratio (Norberg, 1994); and free-stream turbulence (Williamson, 1996). The two most common disturbances in practical applications are free-stream turbulence, and surface roughness (Zdravkovich, 1990). Although the circular cylinder wake is sensitive to inflow conditions, and free-stream turbulence is commonplace in practical applications, the laminar inflow condition is more widely investigated. For example: in the seminal vortex dynamics review paper of Williamson (1996), only low levels of inflow turbulence are analysed in depth. The cut-off for a smooth inflow was defined by a turbulence intensity of $I < 0.1\%$, and flow regimes were classified only by the Reynolds number. In laminar free-stream flow, the Reynolds number is the defining flow parameter. However, above a certain threshold, parameters based on free-stream turbulence become governing parameters of the flow field (Zdravkovich, 1990). These can be, but are not limited to: (i) turbulence intensity I; (ii) components of turbulence intensity in each direction I_1, I_2, I_3; (iii) longitudinal and lateral integral length scales L_{11}, L_{22}; (iv) the Taylor parameter $T = I_1(D/L_{11})^{0.2}$. Free-stream turbulence increases entrainment in the surface shear layers, which can influence vortex shedding, and aerodynamic properties such as drag (Bell, 1983).

Prior to Bloor (1964) and Gerrard (1965), little work had been carried out to characterise the inflow conditions. However, earlier work identified how even low-intensity free-stream turbulence alters the Reynolds number regimes, triggering the critical transition at Reynolds numbers below that for a laminar inflow (Fage and Warsap, 1929). This can be observed by a sharp decrease of the drag coefficient (Goldstein, 1965). In the subcritical Reynolds number range $Re_D = 300$ to 2×10^5, separation at the cylinder is laminar, and turbulent vortices are formed downstream in the wake (Bearman and Morel, 1983). Bloor (1964) studied the relationship between inflow turbulence and the Reynolds number at

which transition occurs in the boundary layer. Two turbulence intensities were tested: $I = 0.03\%$ and 1%. It was found that transition to a three-dimensional wake occurred at a lower Reynolds number for the higher turbulence intensity tested.

Gerrard (1965) found that in the sub-critical regime, inflow disturbances have a profound affect on fluid dynamical properties, such as: drag coefficient C_d, lift coefficient C_l, base pressure coefficient C_{pb}, and surface pressure. The sub-critical regime was subsequently referred to as the "disturbance-sensitive Reynolds number range". For a laminar inflow, a fall in the drag coefficient occurs at some critical Reynolds number. When a moderate level of turbulence is introduced into the free-stream ($I < 5\%$), a drag minimum is observed at a lower critical Reynolds number (Bell, 1979). Surry (1972) investigated the unsteady pressure distribution around the circular cylinder for a range of turbulence intensities $I_1 = 2.5\%$ to 14.7% in the subcritical regime for a Reynolds number range of $33800 \leq Re_D \leq 44200$. It was observed that the vortex shedding phenomenon is not disrupted by intense turbulence intensities, but there was a broadening of the Strouhal peak.

Batham (1973) took pressure measurements of the circular cylinder in a turbulent free-stream with Reynolds numbers 1.1×10^5 and 2.35×10^5. A complex pressure field was observed on the circular cylinder surface, independent of the Reynolds numbers tested. High free-stream turbulence intensities of $I > 10\%$ were found to suppress vortex shedding, attributed to the presence of turbulent bursts, causing small axial correlations and three-dimensionality at separation. In a similar experimental set-up to Batham (1973), Bruun and Davies (1975) also found a reduction in the spanwise correlation of pressure, indicating a breakdown of vortex shedding coherence. In their wind tunnel experiment, Symes and Fink (1978) found free-stream turbulence levels of 5% had a significant influence on the cylinder wake- increasing the rate of turbulent diffusion. Kiya et al. (1982) investigated the relationship between T, Re_D, and C_d for inflow with turbulence intensity I_1 ranging from 1.4% to 18.5%. The drag coefficient collapsed into a narrow region when plotted against the parameter $Re_D^{1.34}\,T$. However, the authors were sceptical on the relevance of parameter $Re_D^{1.34}\,T$ for the turbulent flow past a circular cylinder.

Cheung and Melbourne (1980) conducted wind tunnel tests of circular cylinders with two cylinder diameters under different turbulence intensities and obtained the variation curve of aerodynamic coefficients with Reynolds numbers $Re_D = 7\times10^4$ to 6×10^5, and turbulence intensities $I_1 = 0.4\%$ to 9.1%. They found that the critical Reynolds number at which transition occurs is less well defined when the free-stream flow is turbulent, compared to the laminar case. Blackburn and Melbourne (1996) investigated the time-varying lift coefficient of the circular cylinder for laminar and turbulent free-stream flow at Reynolds numbers in the range $Re_D = 1\times10^5$ to 5×10^5. The highest levels of turbulence, for $I_1 = 9.6\%$ to 18% and $L_{11}/D = 0.53$, provided the first evidence from wind tunnel experiments that high free-stream turbulence promotes early transition to supercritical flow. In the shear layers, free-stream turbulence lowers the Reynolds number at which instabilities arise to $Re_D = 1200$ (Prasad and Williamson, 1997a).

Most of the advances into understanding the wake of a circular cylinder in a free-stream turbulent flow have been developed through experiments, but some researchers have also investigated this flow by theoretical or computational approaches. Eames et al. (2011) developed a theoretical model to predict wake spreading in the presence of intense homogeneous and isotropic free-stream turbulence. Initially, a region of ballistic spreading is found, where the velocity deficit U_m/U_∞ decays like $1/x$. This is followed by diffusive spreading, where U_m/U_∞ decays like $1/\sqrt{x}$. Their model was complemented by experimental results from a recirculating water channel using acoustic Doppler velocimetry (ADV) measurements. Free-stream turbulence was measured at $L_{11}/D \approx 6.8$ and $I = 18\%$. Reasonable agreement was found between the model and experimental results, confirming a rapid spreading of the wake in intense free-stream turbulence.

Little attention has been placed on the simulation of turbulent flow past a circular cylinder. Instead, researchers use a coarse computational mesh at the inlet, which would dampen any turbulent fluctuations introduced into the free-stream (Breuer, 1998a; Lysenko et al., 2012). Aarnes et al. (2018) simulated turbulent flow past a circular cylinder by generating homogeneous isotropic turbulence in a box and advecting this past a circular cylinder. Transition to three-dimensionality was the focus, so the Reynolds number was kept relatively low in the range

$120 \leq Re_D \leq 350$. Free-stream turbulence generation was tuned to produce integral length scales of $L_{11}/D = 0.5, 0.75, 1.0$ and turbulence intensities in the range $I = 3.6\%$ to 13.5%. Free-stream turbulence increased instabilities in the mode A structures, which caused an enhanced interaction between mode A and B structures.

2.3 Concluding remarks

In this introductory chapter, two fundamental problems in the subject of fluid dynamics have been considered: grid-generated turbulence, and flow past a circular cylinder. These problems can be treated in isolation, and there is a wealth of information on each subject which is continuously growing. However, here they are studied in tandem to investigate the impact of turbulent flow past a circular cylinder, and its influence on coherent structures and dissipation in the wake.

It has been necessary to introduce methods of calculating the dissipation term, which takes different forms depending on the availability of the velocity gradient tensor. Measurement of the VGT is particularly challenging in experiments, which leads researchers to enforce isotropic assumptions, regardless of its suitability to the particular flow field. As a result, despite the important role dissipation plays in turbulent flow, its exact form is seldom reported.

Recent developments in the subject of multiscale/fractal grid-generated turbulence have been discussed, with particular focus on the dissipation of freely decaying turbulence. There are numerous motivations for studying grid-generated turbulence. Firstly, grid turbulence is the closest approximation to homogeneous isotropic turbulence (HIT) available to the experimentalist. It can therefore be generated to study the production and decay of turbulence, with fundamental consequences for turbulence theory and modelling. For example, by forcing turbulence at multiple scales, a non-classical form of dissipation has been produced in wind tunnel experiments. Additionally, there is vast potential in industrial fluid flow applications where it is desirable to fully control turbulence properties. Finally, fractal shapes are ubiquitous in nature, and therefore it is important to understand the turbulence produced by multiscale objects.

Despite advances in bespoke turbulence generation, the flow past a circular cylinder is most often studied for the case of smooth inflow where turbulence intensity is low ($I < 0.1\%$). A number of studies have been undertaken in the subcritical regime because it is an attainable Reynolds number in experiments and simulations. A Reynolds number of 3900 is especially well documented. However, simple measures of the circular cylinder wake, such as shedding frequency and recirculation length, have been shown to vary significantly between studies.

This was highlighted in the current chapter, and potential reasons for the scattering of data were considered. It was concluded that inflow conditions are a major factor to this, but a detailed assessment of the inflow turbulence is often overlooked. It is therefore desirable to fully control upstream turbulence conditions in order to study the influence of turbulence on the wake generated by a circular cylinder. Coherent structures in the wake are reasonably well understood for the case of a laminar inflow, and this has been reflected in a number of review papers. However, there is some uncertainty regarding the spatial organisation of dissipation in relation to the primary rollers. More research into the interaction between coherent structures and dissipation for the laminar inflow case is required, and a natural extension of this work is to consider how this changes under a turbulent inflow.

To summarise the current chapter and provide motivation for subsequent work- advances in free-stream turbulence theory have been developed alongside wind tunnel experiments of grid turbulence. In contrast, there is no consensus on the optimal method to customise turbulence in simulations. However, it was highlighted how the wake of a circular cylinder is sensitive to inflow conditions, especially turbulence characteristics. Coherent wake structures and turbulence dissipation are key to this. The vast majority of studies undertaken on the turbulent flow past a circular cylinder have been experiments focused on the aerodynamic properties, such as surface measurements of pressure, lift, and drag. More investigation is required to understand the role of coherent structures and dissipation in the wake of a circular cylinder placed in a turbulent flow.

Chapter 3

Dissipation modelling in LES

Having introduced the turbulent flows which are of interest in this study, attention turns to the modelling of such flows. Two major considerations of the modelling are: (i) estimating turbulence decay, (ii) representing regions of large separation. Large-eddy simulation (LES) is chosen as the best candidate for modelling free-stream turbulent flow past a circular cylinder, and this chapter begins with a description of the numerical procedure. Particular attention is placed on the subgrid-scale modelling, which acts to represent the dissipative nature of the smallest scales of motion. Model transport equations for subgrid-scale turbulent kinetic energy and turbulence dissipation rate are introduced and discussed in terms of freely decaying turbulence. In order to assess model performance, the Taylor-Green vortex (TGV) problem is chosen as a challenging test case. The TGV problem concerns the production and decay of vorticity in a triply-periodic box. The overly-dissipative nature of the popular Smagorinsky model is demonstrated and compared to a one-equation model. Implications of overly dissipative subgrid-scale models are discussed with respect to grid turbulence. Suggestions for a two-equation model which incorporates some of the recent findings from grid turbulence experiments are discussed.

3.1 Introduction

Advancements in computing and developments in turbulence modelling have led to a growing confidence in computational fluid dynamics (CFD). However, due to the wide range of length scales present in turbulent flows, a complete simulation resolving all scales is computationally expensive (Pope, 2001). To remedy this, computational fluid dynamicists utilise statistical properties of turbulence to introduce some form of modelling. Turbulence models generally fall into three categories, listed here in order of least computational to most computationally expensive: (i) Reynolds-averaged Navier-Stokes (RANS), (ii) large-eddy simulation (LES), (iii) direct numerical simulation (DNS). A trade-off exists between computational expense and numerical accuracy, therefore before running a simulation, a researcher must decide what level of modelling is to be introduced. For example, a DNS resolves all temporal and length scales down to the smallest dissipative motions. Due to the large range of resolved scales, DNS studies are generally more computationally expensive than RANS and LES, and the number of operations grows as $\sim Re^3$ (Pope, 2001). Since all scales of motion are explicitly resolved, no turbulence modelling is enforced. However, DNS is currently unrealistic for industrial flow problems due to the immense computational cost.

RANS modelling provides accessible results for industrial fluid flow problems thanks to reduced computing costs. However, it is well documented that some RANS turbulence models poorly represent flows with unsteady separation and vortex shedding (Pope, 2001). The Spalart–Allmaras model (Spalart and Allmaras, 1992) is a one-equation model which is cost effective, and relatively easy to implement. The SA model was developed for aerodynamic flows, and performs well for wall-bounded, adverse pressure gradients. The k-ε model of Jones and Launder (1972) and Launder and Sharma (1974) solves two transport equations- one for the turbulent kinetic energy k, and another for the turbulence dissipation ε. The k-ε model is widely adopted across engineering industry and is available in most commercial CFD codes thanks to its reasonable accuracy and computational cost. The major drawbacks of the k-ε model are the difficulty in integrating to the wall, and the tendency of the model to poorly represent areas of separation with large streamline curvature. The k-ε model performs best in flows with

low streamline curvature, and small mean pressure gradients. The k-ω model is often employed as an alternative to the k-ε model, due to the more accurate representation of the boundary layer (Menter, 2009). However, the k-ω model is sensitive to free-stream values of ω, which depend heavily on the arbitrarily defined values of ε and ω at the inlet. The shear-stress transport model (SST) combines the k-ω model near wall, and the k-ε model in the free-stream. The SST model has attracted considerable attention from the engineering industry. The model was originally developed by Menter (1993) as a method for simulating three-dimensional aerodynamic flows. Reynolds-stress models solve transport equations for components of the Reynolds-stress tensor, and an additional quantity, such as the dissipation ε. Therefore, no turbulence-viscosity assumption is employed. Reynolds-stress models perform well for flows with significant streamline curvature and secondary flow.

LES has been steadily growing in popularity across engineering applications, e.g. aerodynamics, noise prediction, and turbo-machinery (Sagaut, 2006). In a large-eddy simulation, the governing equations of fluid flow are spatially filtered by some cut-off length scale. Scales larger than the filter width Δ are resolved, providing an evolution of the large-scale eddies. Scales smaller than the filter width are mostly responsible for dissipation, and are parametrised using a subgrid-scale (SGS) model. According to Davidson (2015), the purpose of the SGS model is to "...mop up all the kinetic energy which cascades down from the large scales". The equations of LES were first formulated in the work of Smagorinsky (1963) as an approach to modelling atmospheric flows. The Smagorinsky model forms the basis of many subgrid-scale models to date, and was first used by Deardorff (1970) on a three-dimensional turbulent channel flow. Implementation of the Smagorinsky model requires a characteristic velocity scale of the subgrid motions, which can be calculated from the subgrid kinetic energy by assuming a balance between subgrid-scale dissipation and energy production.

Figure 3.1 presents a simplified picture of the difference between scale resolution of an LES and DNS. In the LES picture, scales smaller than Δ are accounted for by the SGS model. In a DNS, all scales of turbulence are resolved down to η, at which point energy is dissipated through heat. The purpose of LES is to obtain a flow field solution which converges towards a direct numerical simulation, but

without the required grid resolution. The mathematical operations responsible for filtering are introduced in Section 3.2.

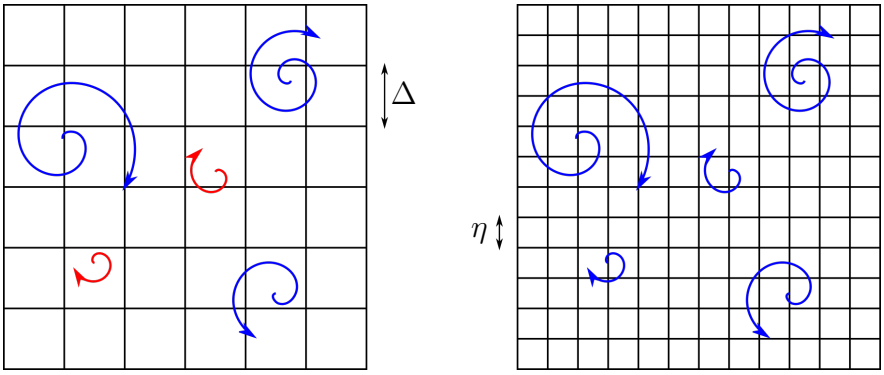

Figure 3.1: Schematic of scale resolution for LES (left) and DNS (right). Blue arrows represent resolved motions, red arrows represent modelled scales. An example of the grid filter width Δ, and Kolmogorov scale η is included.

3.1.1 Numerical implementation

Numerical simulations are carried out in OpenFOAM v4.1 (Open source Field Operation And Manipulation), an open-source software encompassing a range of solvers and pre/post-processing utilities for the solution of partial differential equations (Weller et al., 1998). A large collection of CFD solvers are available for incompressible, compressible, multiphase, combustion, and heat transfer flows. As a second-order finite volume method (FVM) code, OpenFOAM utilises the same methods and principles found in other CFD software codes, such as the commercial package Ansys Fluent. However, because OpenFOAM is open-source, the source code is available to the user, which makes it more flexible and easier to customise. This has led to increased interest from industry and academia. An informal introduction to the history and operation of OpenFOAM can be found in Chen et al. (2014), and a detailed description of the FVM is provided in Jasak (1996). For problems of incompressible bluff body flow, Robertson et al. (2015) found OpenFOAM and Fluent perform equally well, despite OpenFOAM being more sensitive to mesh quality. OpenFOAM was also found to be scalable up to 192 processors, therefore large problems can be decomposed and ran in parallel.

3.2 Filtering operation

The basis of LES is to filter governing equations of motion by some cut-off filter width Δ, which splits the flow into large and small scale motions. The velocity field $\boldsymbol{U}(\boldsymbol{x},t)$ is decomposed into a sum of two terms: a resolved component $\overline{\boldsymbol{U}}(\boldsymbol{x},t)$, and a subgrid-scale modelled component $\boldsymbol{u}'(\boldsymbol{x},t)$, such that

$$\boldsymbol{U}(\boldsymbol{x},t) = \overline{\boldsymbol{U}}(\boldsymbol{x},t) + \boldsymbol{u}'(\boldsymbol{x},t) \ . \tag{3.1}$$

As noted by Pope (2001), (3.1) has a similar form to the Reynolds decomposition, however $\overline{\boldsymbol{U}}$ is a random field, and the filtered residual is generally non-zero. Small scale structures are assumed to be universal, however the filtered velocity $\overline{\boldsymbol{U}}$ represents the larger scales which are geometry defined. The filtering operation is defined mathematically by a convolution (Leonard, 1975)

$$\overline{\boldsymbol{U}}(\boldsymbol{x},t) = \iiint_V G(\boldsymbol{r},\boldsymbol{x})\boldsymbol{U}(\boldsymbol{x}-\boldsymbol{r},t)\,\mathrm{d}\boldsymbol{r} \ , \tag{3.2}$$

where $G(\boldsymbol{r},\boldsymbol{x})$ is a chosen filter, and the integral is taken over the entire fluid domain. The following normalisation condition is imposed on the filter

$$\iiint_V G(\boldsymbol{r},\boldsymbol{x})\,\mathrm{d}\boldsymbol{r} = 1 \ . \tag{3.3}$$

Various choices for the filter function are available, the most common of which are: box or top-hat, Gaussian, and spectral or sharp cut-off filter. A comprehensive guide to filter functions is provided in Sagaut (2006). The top-hat filter is often implemented in finite volume discretisation codes (De Villiers, 2006), and is defined as follows

$$G(\boldsymbol{r},\boldsymbol{x}) = \begin{cases} 1/\Delta^3 & \text{for} \quad |\boldsymbol{x}-\boldsymbol{r}| \leq \Delta/2 \ , \\ 0 & \text{otherwise} \ . \end{cases} \tag{3.4}$$

A common choice for the filter width Δ is given by the geometric mean of the

computational cell sizes (Deardorff, 1970)

$$\Delta = (\Delta x \Delta y \Delta z)^{1/3} \ , \tag{3.5}$$

where Δx, Δy, Δz are the cell sizes in the x, y, z directions, respectively. This simple choice of filter width returns a filtered velocity field equal to the cell average of the velocity field. The filtering operation defined in (3.2) can be applied to the continuity equation, as follows

$$\overline{\frac{\partial U_i}{\partial x_i}} = \frac{\partial \overline{U}_i}{\partial x_i} - \int U_i(\boldsymbol{x} - \boldsymbol{r}, t) \frac{\partial G(\boldsymbol{r}, \boldsymbol{x})}{\partial x_i} \, \mathrm{d}\boldsymbol{r} \ , \tag{3.6}$$

$$= 0 \ , \tag{3.7}$$

which, for a homogeneous filter function $G(\boldsymbol{r}, \boldsymbol{x})$, simplifies to

$$\overline{\frac{\partial U_i}{\partial x_i}} = \frac{\partial \overline{U}_i}{\partial x_i} = 0 \ , \tag{3.8}$$

i.e. the filtered velocity field is divergence free. Another consequence of (3.8) is that filtering and spatial derivative operators commute. The same is also true for filtering and time derivatives. However, when a mesh is refined near a boundary, e.g. for a body-fitted grid, a filter width proportional to the grid spacing leads to an non-uniform filter. In this case, filtering and spatial derivatives no longer commute. For simulations ran on particularly distorted meshes, a significant error is introduced when the commutative assumption is enforced (Sagaut, 2006).

The filtering operation is also applied to the momentum equation

$$\frac{\partial \overline{U}_i}{\partial t} + \frac{\partial}{\partial x_j}(\overline{U_i U_j}) - \nu \frac{\partial^2 \overline{U}_i}{\partial x_j \partial x_j} = -\frac{1}{\rho} \frac{\partial \overline{p}}{\partial x_i} \ . \tag{3.9}$$

At this point, the non-linear convective term in (3.9) is recast by introducing the residual-stress tensor

$$\tau_{ij}^{\mathrm{r}} \equiv \overline{U_i U_j} - \overline{U}_i \overline{U}_j \ . \tag{3.10}$$

It is noted that as $\tau_{ij}^{\mathrm{r}} \to 0$, the model tends towards a DNS. The trace of

(3.10) is related to the kinetic energy of the residual motions by

$$k_{\mathrm{r}} \equiv \frac{1}{2}\tau^{\mathrm{r}}_{kk} \ , \tag{3.11}$$

$$= \frac{1}{2}\left(\overline{U_k U_k} - \overline{U}_k \overline{U}_k\right) \ , \tag{3.12}$$

from left to right, the two terms appearing on the RHS of (3.12) can be identified as the filtered kinetic energy field $\overline{E} = \frac{1}{2}\overline{U_k U_k}$, and the kinetic energy of the filtered field $E_{\mathrm{f}} = \frac{1}{2}\overline{U}_k \overline{U}_k$, respectively. Therefore, a decomposition of the filtered kinetic-energy is

$$\overline{E} = E_{\mathrm{f}} + k_{\mathrm{r}} \ . \tag{3.13}$$

The residual-stress tensor can be split into two parts

$$\tau^{\mathrm{r}}_{ij} = \frac{1}{3}\tau^{\mathrm{r}}_{kk}\delta_{ij} + \left(\tau^{\mathrm{r}}_{ij} - \frac{1}{3}\tau^{\mathrm{r}}_{kk}\delta_{ij}\right) \ , \tag{3.14}$$

where the first term on the RHS of (3.14) is the isotropic contribution, and the bracketed term is the anisotropic part, which is denoted by τ^{R}_{ij}. From this, (3.14) is re-written

$$\tau^{\mathrm{r}}_{ij} = \frac{2}{3}k_{\mathrm{r}}\delta_{ij} + \tau^{\mathrm{R}}_{ij} \ . \tag{3.15}$$

Inserting (3.10) and (3.15) into the filtered momentum equation (3.9) yields

$$\frac{\partial \overline{U}_i}{\partial t} + \frac{\partial}{\partial x_j}(\overline{U}_i \overline{U}_j) - \nu \frac{\partial^2 \overline{U}_i}{\partial x_j \partial x_j} = -\frac{1}{\rho}\frac{\partial \bar{p}}{\partial x_i} - \frac{\partial \tau^{\mathrm{R}}_{ij}}{\partial x_j} \ , \tag{3.16}$$

where the modified filtered pressure is denoted by a shorter overbar and defined by

$$\bar{p} \equiv \overline{p} + \frac{2}{3}k_{\mathrm{r}} \ . \tag{3.17}$$

The pressure equation is formed in the usual manner by taking the divergence of (3.16). Closure for (3.16) is achieved through modelling τ^{R}_{ij}.

3.3 Subgrid-scale modelling

The momentum equation (3.16) represents the evolution of filtered velocity field $\overline{U}$. Closure for the system is achieved through modelling the anisotropic residual-stress tensor τ_{ij}^{R} via some subgrid-scale model. The SGS model acts to represent scales smaller than the filter width, which are mostly responsible for dissipation.

Algebraic eddy viscosity models are considered first, where the residual stress tensor is assumed to be related to the strain rate tensor of the filtered velocity via an algebraic expression for the eddy viscosity

$$\tau_{ij}^{\mathrm{R}} = \tau_{ij}^{\mathrm{r}} - \frac{1}{3}\tau_{kk}^{\mathrm{r}}\delta_{ij} = -2\nu_{\mathrm{r}}\overline{S}_{ij} \ , \tag{3.18}$$

where ν_{r} is the eddy viscosity of the residual motions, and $\overline{S}_{ij}$ is the rate of strain of the filtered velocity field. The anisotropic form in (3.18) is rearranged to arrive at the commonly found form of the stress tensor

$$\tau_{ij}^{\mathrm{r}} = \frac{2}{3}k_{\mathrm{r}}\delta_{ij} - 2\nu_{\mathrm{r}}\overline{S}_{ij} \ . \tag{3.19}$$

Smagorinsky assumed the eddy viscosity of SGS motions is analogous to the eddy viscosity of RANS equations, described by Prandtl's mixing-length theory. From this comparison, the eddy viscosity is given by the product of characteristic SGS turbulence length and velocity scales

$$\nu_{\mathrm{r}} = l_{\mathrm{s}}^2\,\overline{\mathcal{S}} \ , \tag{3.20}$$

where l_{s} is the Smagorinsky lengthscale, and $\overline{\mathcal{S}} = (2\overline{S}_{ij}\overline{S}_{ij})^{1/2}$ is the characteristic filtered rate of strain. The Smagorinsky lengthscale is taken to be proportional to the filter width such that $l_{\mathrm{s}} = C_{\mathrm{s}}\Delta$, where C_{s} is the Smagorinsky coefficient. Combining (3.18) and (3.20) yields

$$\tau_{ij}^{\mathrm{r}} = \frac{2}{3}k_{\mathrm{r}}\delta_{ij} - 2C_{\mathrm{s}}^2\Delta^2\overline{\mathcal{S}}\,\overline{S}_{ij} \ . \tag{3.21}$$

In OpenFOAM, C_{s} is not explicitly defined (Castro et al., 2017), instead the

eddy viscosity of the residual motions is defined by

$$\nu_{\mathrm{r}} = C_{\mathrm{k}} \Delta \sqrt{k_{\mathrm{r}}} \ , \tag{3.22}$$

where $C_{\mathrm{k}} = 0.094$ is a model constant, and k_{r} represents the turbulent kinetic energy of the residual motions. Note from (3.22) that $\nu_{\mathrm{r}} \geq 0$, which determines that there is no energy backscatter- a process by which energy is transferred from small to large scales. Combining (3.18) and (3.22)

$$\tau_{ij}^{\mathrm{r}} = \frac{2}{3} k_{\mathrm{r}} \delta_{ij} - 2 C_{\mathrm{k}} \Delta \sqrt{k_{\mathrm{r}}} \, \overline{S}_{ij} \ . \tag{3.23}$$

There are different approaches to finding k_{r}. The Smagorinsky model assumption is considered here first because it is the simplest to implement and forms a basis for other models. An energy balance is enforced where the rate of transfer of energy to the residual motions

$$\mathcal{P}_{\mathrm{r}} = -\tau_{ij}^{\mathrm{r}} \overline{S}_{ij} \ , \tag{3.24}$$

is balanced by the subgrid-scale dissipation

$$\varepsilon_{\mathrm{r}} = C_{\epsilon} \frac{k_{\mathrm{r}}^{1.5}}{\Delta} \ , \tag{3.25}$$

that is

$$\tau_{ij}^{\mathrm{r}} \overline{S}_{ij} + C_{\epsilon} \frac{k_{\mathrm{r}}^{1.5}}{\Delta} = 0 \ . \tag{3.26}$$

Rearranging (3.23) and (3.26), by noting $\overline{S}_{ij} \delta_{ij} = 0$, gives

$$k_{\mathrm{r}} = 2 \frac{C_{\mathrm{k}}}{C_{\epsilon}} \Delta^2 (\overline{S}_{ij} \overline{S}_{ij}) \ . \tag{3.27}$$

The Smagorinsky constant can then be calculated from (3.20), (3.22), and (3.27)

$$C_{\mathrm{s}} = \left(\frac{C_{\mathrm{k}}^3}{C_{\epsilon}} \right)^{\frac{1}{4}} \ . \tag{3.28}$$

Using default values $C_{\mathrm{k}} = 0.094$ and $C_{\epsilon} = 1.048$ yields $C_{\mathrm{s}} = 0.168$. An alternative approach for determining Smagorinsky's constant is provided in Lesieur et al.

(2005), where it is stated "$C_\mathrm{s} \approx 0.18$ gives acceptable results for LES of isotropic turbulence". By assuming a balance between production and dissipation of SGS kinetic energy, the Smagorinsky model obtains an algebraic expression for k_r in terms of a scalar eddy viscosity, and resolved strain-rate tensor. The Smagorinsky model belongs to the general category of algebraic eddy viscosity models.

Yoshizawa (1986) derived a transport equation for the subgrid-scale kinetic energy k_r by subtracting the filtered equations of motion from the non-filtered equations, multiplying by the fluctuating velocity, and finally contracting with the assumption that SGS motions are isotropic. The resulting equation for k_r is

$$\frac{\partial k_\mathrm{r}}{\partial t} + \frac{\partial \overline{U}_j k_\mathrm{r}}{\partial x_j} - \frac{\partial}{\partial x_j}\left[\left(\nu + \frac{\nu_r}{\sigma_\mathrm{k}}\right)\frac{\partial k_\mathrm{r}}{\partial x_j}\right] = \mathcal{P}_\mathrm{r} - \varepsilon_\mathrm{r} \ , \tag{3.29}$$

where $\sigma_\mathrm{k} = 1$ is a model constant in OpenFOAM. The LHS of (3.29) represents transportation of k_r, i.e. terms are identified from left to right as: time derivative, advection, and diffusion of k_r. By neglecting the LHS, the Smagorinsky model is retained, i.e. local balance assumption reduces to $\mathcal{P}_\mathrm{r} = \varepsilon_\mathrm{r}$. With inclusion of the LHS of (3.29), no local balance is assumed.

To arrive at the form of $\mathcal{P}_\mathrm{r}$ found in the OpenFOAM code, the subgrid-scale stress tensor (3.19) is substituted into the production term (3.24)

$$\mathcal{P}_\mathrm{r} = -\tau^\mathrm{r}_{ij}\overline{S}_{ij} \ , \tag{3.30}$$

$$= -\left(\frac{2}{3}k_\mathrm{r}\delta_{ij} - 2\nu_\mathrm{r}\overline{S}_{ij}\right)\overline{S}_{ij} \ , \tag{3.31}$$

$$= 2\nu_\mathrm{r}\overline{S}_{ij}\overline{S}_{ij} \ , \tag{3.32}$$

$$= 2\nu_\mathrm{r}\overline{S}_{ij}\frac{\partial \overline{U}_i}{\partial x_j} \ . \tag{3.33}$$

Steps from (3.30) to (3.33) include: imposing incompressibility, and utilising symmetry properties of $\overline{S}_{ij}$. The form of the production term given in (3.33) is used in OpenFOAM.

3.3.1 Modelling dissipation

It is also possible to introduce a transport equation for ε_{r}. The exact form of the dissipation equation is often modelled in the high Reynolds number form (Speziale et al., 1991)

$$\frac{\partial \varepsilon_{\mathrm{r}}}{\partial t} + \frac{\partial \overline{U}_j \varepsilon_{\mathrm{r}}}{\partial x_j} - \frac{\partial}{\partial x_j}\left[\left(\nu + \frac{\nu_r}{\sigma_\varepsilon}\right)\frac{\partial \varepsilon_{\mathrm{r}}}{\partial x_j}\right] = C_{\varepsilon 1}\frac{\varepsilon_{\mathrm{r}}}{k_{\mathrm{r}}}\mathcal{P}_{\mathrm{r}} - C_{\varepsilon 2}\frac{\varepsilon_{\mathrm{r}}^2}{k_{\mathrm{r}}} \quad , \tag{3.34}$$

where $\sigma_\varepsilon = 1.3$, $C_{\varepsilon 1} = 1.44$, and $C_{\varepsilon 2} = 1.83$ are standard model coefficients which will be discussed later. From the computed fields of k_{r} and ε_{r}, the eddy viscosity is recovered from

$$\nu_t = C_\nu \frac{k_{\mathrm{r}}^2}{\varepsilon_{\mathrm{r}}} \quad , \tag{3.35}$$

for some modelling constant C_ν. If the turbulence is homogeneous, kinetic energy k_{r}, and dissipation ε_{r}, are spatially invariant, (3.29) and (3.34) reduce to

$$\dot{k_{\mathrm{r}}} = \mathcal{P}_{\mathrm{r}} - \varepsilon_{\mathrm{r}} \quad , \tag{3.36}$$

$$\dot{\varepsilon_{\mathrm{r}}} = C_{\varepsilon 1}\frac{\varepsilon_{\mathrm{r}}}{k_{\mathrm{r}}}\mathcal{P}_{\mathrm{r}} - C_{\varepsilon 2}\frac{\varepsilon_{\mathrm{r}}^2}{k_{\mathrm{r}}} \quad . \tag{3.37}$$

If the turbulence is freely decaying, for which grid turbulence is a prime example, there is no production mechanism, and the production term vanishes

$$\dot{k_{\mathrm{r}}} = -\varepsilon_{\mathrm{r}} \quad , \tag{3.38}$$

$$\dot{\varepsilon_{\mathrm{r}}} = -C_{\varepsilon 2}\frac{\varepsilon_{\mathrm{r}}^2}{k_{\mathrm{r}}} \quad . \tag{3.39}$$

Separation of variables k_{r} and ε_{r} can be achieved by manipulation of (3.38) and (3.39) to yield

$$\frac{\dot{\varepsilon_{\mathrm{r}}}}{\varepsilon_{\mathrm{r}}} = -C_{\varepsilon 2}\frac{\varepsilon_{\mathrm{r}}}{k_{\mathrm{r}}} = C_{\varepsilon 2}\frac{\dot{k_{\mathrm{r}}}}{k_{\mathrm{r}}} \quad , \tag{3.40}$$

from which a time integral can be constructed

$$\int \frac{\dot{\varepsilon_{\mathrm{r}}}}{\varepsilon_{\mathrm{r}}}\,\mathrm{d}t = \int C_{\varepsilon 2}\frac{\dot{k_{\mathrm{r}}}}{k_{\mathrm{r}}}\,\mathrm{d}t \quad . \tag{3.41}$$

At this point, it is common to assume that $C_{\varepsilon 2}$ is a fixed constant, and there-

fore does not vary in time. In which case the integral (3.41) has analytical solutions

$$k_{\mathrm{r}}(t) = k_0 \left(\frac{t}{t_0} \right)^{-n} \quad , \tag{3.42}$$

$$\varepsilon_{\mathrm{r}}(t) = \varepsilon_0 \left(\frac{t}{t_0} \right)^{-(n+1)} \quad , \tag{3.43}$$

where k_0 and ε_0 are reference values at time $t_0 = nk_0/\varepsilon_0$, and the decay exponent n is

$$n = \frac{1}{C_{\varepsilon 2} - 1} \quad , \tag{3.44}$$

which can be rearranged to find an expression for $C_{\varepsilon 2}$

$$C_{\varepsilon 2} = \frac{n+1}{n} \quad . \tag{3.45}$$

For the case of decaying homogeneous isotropic turbulence, experiments of the flow through a turbulence-generating grid find the exponent of decay from (3.42) to be in the range $n = 1.2$ to 1.4. Substituting $n = 1.3$ into (3.45) yields $C_{\varepsilon 2} \approx 1.77$. Additionally, experiments based on multiscale turbulence generation from fractal grids have found exponents of $n \approx 2$ (Valente and Vassilicos, 2011; Vassilicos, 2015), which leads to $C_{\varepsilon 2} = 1.5$. The generally accepted value of $C_{\varepsilon 2} = 1.92$ proposed by Launder and Sharma (1974) yields a decay exponent of $n = 1.09$. This choice of $C_{\varepsilon 2}$ is known to over predict the rate of spreading for the round jet (Pope, 2001). Table (3.1) presents common choices of model constants $C_{\varepsilon 1}$ and $C_{\varepsilon 2}$ throughout the literature.

A two-equation system based on a hybrid approach was proposed by Perot and Gadebusch (2007). In their model, the standard k-ε RANS turbulence model was modified to adapt to mesh resolution. In a coarse mesh limit, the Perot and Gadebusch model switches to a typical k-ε RANS. This is achieved by including an extra factor in the eddy viscosity equation which depends on the ratio of modelled to total turbulent kinetic energy $k_{\mathrm{r}}/(k_{\mathrm{r}} + k)$. The eddy viscosity is given by

$$\nu_{\mathrm{r}} = C_\mu \frac{k_{\mathrm{r}}^2}{\varepsilon_{\mathrm{r}}} \left(\frac{k_{\mathrm{r}}}{k_{\mathrm{r}} + k} \right) \quad , \tag{3.46}$$

where $C_\mu = 0.18$ is a model constant, and k is the resolved turbulent kinetic

Constant	Value	Comment
$C_{\varepsilon 1}$	1.55	Perot and Gadebusch (2007).
	1.44	Standard ε equation (Launder and Sharma, 1974).
	1.42	Pope (2001), originally Orszag et al. (1996).
$C_{\varepsilon 2}$	1.92	Standard ε equation (Launder and Sharma, 1974).
	1.83	Perot and Gadebusch (2007).
	1.77	Power law decay $n = 1.3$ from (3.45).
	1.71	Power law decay $n = 1.4$ from (3.45).

Table 3.1: Choice of model constants $C_{\varepsilon 1}$ and $C_{\varepsilon 2}$ from the literature.

energy. Perot and Gadebusch (2007) noted (3.46) returns to a typical RANS form $\nu_\mathrm{r} = C_\mu k_\mathrm{r}^2/\varepsilon_\mathrm{r}$ when all scales are modelled ($k = 0$). However, in the k-ε RANS model, $C_\mu = 0.09$, and in the RANS limit (3.46) returns an eddy viscosity which is a factor of 2 larger than the common RANS. No explanation for this difference in C_μ was offered by the authors. When all scales are resolved, i.e. $k_\mathrm{r} \to 0$ in the DNS limit, the model returns $\nu_\mathrm{r} \to 0$. Turbulent kinetic energy of the resolved field is calculated from the mean velocity field by $k = \frac{1}{2}|(\boldsymbol{U} - \langle \boldsymbol{U} \rangle)^2|$, where $\langle \boldsymbol{U} \rangle$ can be calculated from a spatial, temporal, or ensemble average.

Perot and Gadebusch (2007) proposed a form of $C_{\varepsilon 2}$ which "varies $C_{\varepsilon 2}$ from its theoretical limits of 11/6 at high Reynolds numbers to 3/2 at low Reynolds numbers", given by

$$C_{\varepsilon 2} = \frac{5}{3} + \frac{1}{180}\left(\sqrt{Re_\mathrm{T}^2 + 60 Re_\mathrm{T}} - Re_T\right) \quad , \tag{3.47}$$

on manipulation of (3.47), an alternative form is arrived at

$$C_{\varepsilon 2} = \frac{5}{3} + \frac{1}{3}\left(1 + \sqrt{1 + \frac{60}{Re_\mathrm{T}}}\right)^{-1} \quad . \tag{3.48}$$

Asymptotic behaviour of $C_{\varepsilon 2}$ is now considered. In the low turbulent Reynolds number limit of $Re_\mathrm{T} \to 0$, (3.47) returns $C_{\varepsilon 2} \to 5/3$. It is noted this contradicts the asymptotic value of $C_{\varepsilon 2} \to 3/2$ promised in Perot and Gadebusch (2007). In

the high turbulent Reynolds number limit as $Re_{\mathrm{T}} \to \infty$, the correct asymptotic behaviour is achieved from (3.48), that is $C_{\varepsilon 2} \to 11/6$. Figure 3.2 presents the variation of $C_{\varepsilon 2}$ with increasing Re_{T}.

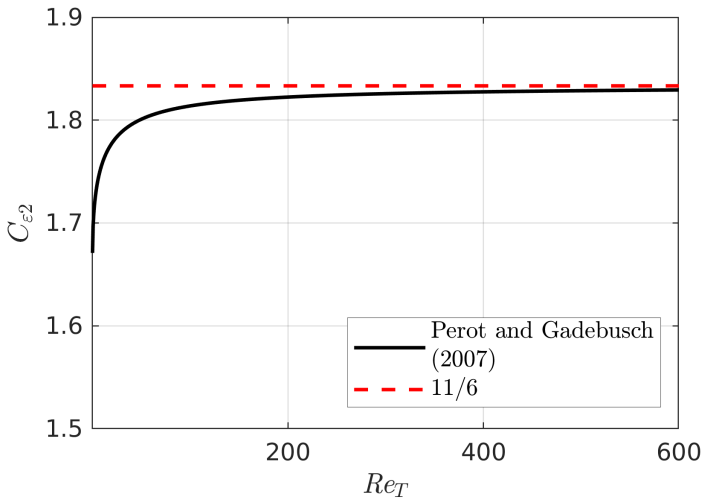

Figure 3.2: Asymptotic behaviour of $C_{\varepsilon 2}$ from the model of Perot and Gadebusch (2007).

Although the value of $C_{\varepsilon 2}$ is fixed at the limits $Re_{\mathrm{T}} \to 0$ and $Re_{\mathrm{T}} \to \infty$, there is no exact formulation for its behaviour between the limits. Presumably, this would require an adjustment based on the free-stream turbulence levels, $Re_{\mathrm{T}}|_{\infty}$. For example, a local measure of the flow turbulence Re_Q could be introduced which takes the form

$$Re_Q = \frac{Re_{\mathrm{T}} - Re_{\mathrm{T}}\big|_{\infty}}{\max(Re_{\mathrm{T}}) - Re_{\mathrm{T}}\big|_{\infty}} \ , \tag{3.49}$$

where $Re_{\mathrm{T}}\big|_{\infty}$ is recorded at a user-defined location in the domain which represents the bulk flow, i.e. in the undisturbed free-stream, and $\max(Re_{\mathrm{T}})$ is the maximum value found throughout the domain. The form of $C_{\varepsilon 2}$ can then be chosen

$$C_{\varepsilon 2} = \frac{3}{2} + \frac{1}{3}\left(1 - \max\{0, Re_Q\}\right) \ . \tag{3.50}$$

Figure 3.3 displays the behaviour of $C_{\varepsilon 2}$ for a range of Re_{T}. For low values of turbulent Reynolds number ($Re_{\mathrm{T}} < Re_{\mathrm{T}}\big|_{\infty}$), the model constant is inactive and

returns a value of $C_{\varepsilon 2} = 11/6$. Once the local turbulence level increases beyond the free-stream value of $Re_{\mathrm{T}}\big|_{\infty}$, $C_{\varepsilon 2}$ decreases linearly to a minimum value of $3/2$.

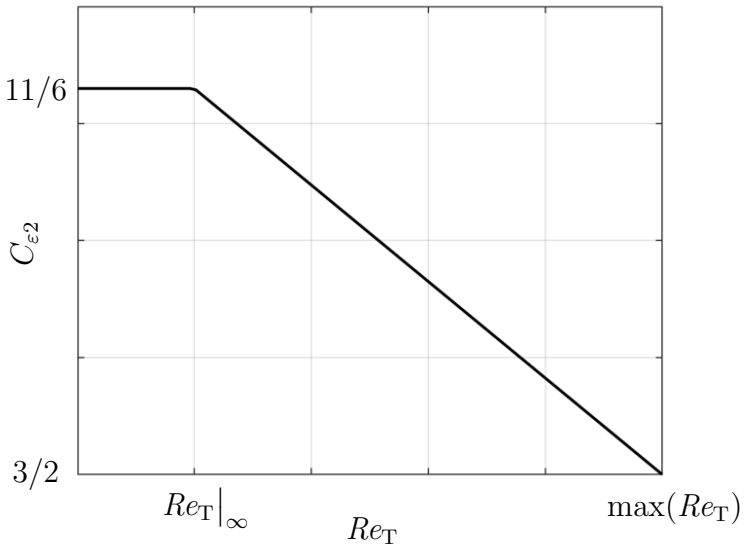

Figure 3.3: Variable $C_{\varepsilon 2}$ from (3.50).

3.4 Test case: the Taylor-Green vortex

A numerical benchmark case is considered to compare subgrid-scale models. To demonstrate the process of large eddies grinding down to progressively smaller sizes, Taylor and Green (1937) constructed a special case of flows with a known initial condition. The Taylor-Green vortex is a common benchmark for numerical codes to test vortex dynamics, transition to turbulence, turbulence decay, and energy dissipation. The TGV problem was set as a challenging case in the 1st and 2nd International Workshop on High-Order CFD Methods (Wang et al., 2013), and as a result, its solution is well documented, for example see: DeBonis (2013), Aubard et al. (2013), Bull and Jameson (2014).

3.4.1 Initialisation and case set-up

The TGV problem consists of a triply periodic box initialised with blobs of vorticity. The domain has dimensions $-\pi L \leq (x, y, z) \leq \pi L$, where L is a reference length scale. The flow field is initialised at $t = t_0$ on a Cartesian mesh with velocity field

$$U(\boldsymbol{x}, t_0) = A\cos(ax)\sin(by)\sin(cz) \ , \tag{3.51}$$

$$V(\boldsymbol{x}, t_0) = B\sin(ax)\cos(by)\sin(cz) \ , \tag{3.52}$$

$$W(\boldsymbol{x}, t_0) = C\sin(ax)\sin(by)\cos(cz) \ , \tag{3.53}$$

where a, b, c, A, B, C are constants. If incompressibility is enforced, (3.51)-(3.53) leads to the following condition

$$Aa + Bb + Cc = 0 \ , \tag{3.54}$$

which can be satisfied by

$$a = b = c = 1/L \ , \tag{3.55}$$

$$A = -B = V_0 \ , \tag{3.56}$$

$$C = 0 \ , \tag{3.57}$$

where V_0 is a reference velocity scale. Substitution of (3.55)-(3.57) into the generalised initial velocity field (3.51)-(3.53), yields

$$U(\boldsymbol{x}, t_0) = V_0 \sin\left(\frac{x}{L}\right) \cos\left(\frac{y}{L}\right) \cos\left(\frac{z}{L}\right) \quad , \tag{3.58}$$

$$V(\boldsymbol{x}, t_0) = -V_0 \cos\left(\frac{x}{L}\right) \sin\left(\frac{y}{L}\right) \cos\left(\frac{z}{L}\right) \quad , \tag{3.59}$$

$$W(\boldsymbol{x}, t_0) = 0 \quad , \tag{3.60}$$

$$p(\boldsymbol{x}, t_0) = p_0 + \frac{\rho_0 V_0^2}{16}\left[\cos\left(\frac{2x}{L}\right) + \cos\left(\frac{2y}{L}\right)\right]\left[\cos\left(\frac{2z}{L}\right) + 2\right] \quad , \tag{3.61}$$

where the pressure field is obtained in the usual manner by forming a Poisson equation from the velocity field, and p_0 and ρ_0 are reference values of pressure and density respectively.

From reference length and velocity scales L and V_0, a Reynolds number is defined by $Re = V_0 L/\nu$. A nondimensional time can also be defined by $t^* = t/(L/V_0)$. Reference length and velocity scales of $L = 1$ and $V_0 = 1$ have been chosen here, from which a Reynolds number of 1600 is set by adjusting the kinematic viscosity. A Reynolds number of 1600 was stipulated for submission to the 1st and 2nd International Workshop on High-Order CFD Methods (Wang et al., 2013), therefore a wealth of fully resolved numerical simulations have been ran at this Reynolds number.

For a compressible flow, the dissipation rate is given by the sum of three components: strain-based, pressure dilation-based, and viscosity-based (Bull and Jameson, 2014). Theoretically, only the strain-based term is non-zero for the incompressible limit. Compressible simulations have shown that the strain-based term dominates, and therefore incompressibility can be assumed at this Reynolds number (DeBonis, 2013; Bull and Jameson, 2014). If the flow is incompressible, density is constant $\rho = \rho_0$. Based on the chosen reference scales and the incom-

pressibility assumption, the initial flow field is governed by

$$U(\boldsymbol{x}, t_0) = \sin(x)\cos(y)\cos(z) \quad , \tag{3.62}$$

$$V(\boldsymbol{x}, t_0) = -\cos(x)\sin(y)\cos(z) \quad , \tag{3.63}$$

$$W(\boldsymbol{x}, t_0) = 0 \quad , \tag{3.64}$$

$$p(\boldsymbol{x}, t_0) = \frac{\rho_0}{16}\Big[\cos(2x) + \cos(2y)\Big]\Big[\cos(2z) + 2\Big] \quad . \tag{3.65}$$

The initial flow field described by (3.62)-(3.65) is generated in Matlab for a number of grid densities. To visualise the initial flow field, the curl of (3.62)-(3.64) is taken to obtain the vorticity field

$$\omega_x(\boldsymbol{x}, t_0) = -\cos(x)\sin(y)\sin(z) \quad , \tag{3.66}$$

$$\omega_y(\boldsymbol{x}, t_0) = -\sin(x)\cos(y)\sin(z) \quad , \tag{3.67}$$

$$\omega_z(\boldsymbol{x}, t_0) = 2\sin(x)\sin(y)\cos(z) \quad , \tag{3.68}$$

from which the z-component of vorticity is displayed in Figure 3.4. As time evolves, vortices in Figure 3.4 roll up, stretch, and interact. This develops into turbulence, with scales developing in a very precise manner, not simply just by period doubling (Berselli, 2005).

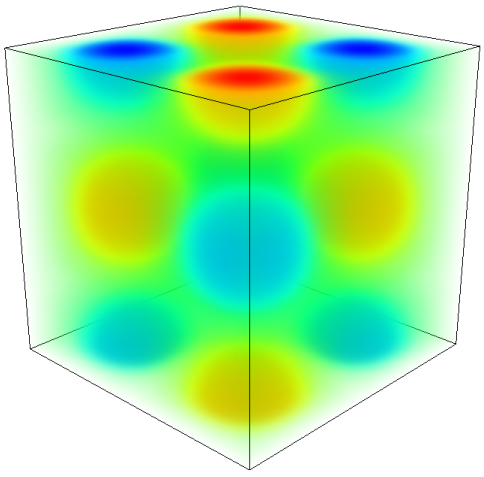

Figure 3.4: Volume rendering of ω_z at $t = t_0$ from (3.68). Negative to positive z-vorticity is represented by colours blue to red, respectively.

From initialisation to decay, DeBonis (2013) identify 4 regions of flow behaviour:

I. Inviscid flow. Vortices evolve and break up ($0 \leq t^* < 7$).

II. Smooth vortical structures undergo changes in their structure ($t^* = 7$).

III. Dissipation peaks, coherent structures break down ($t^* = 9$).

IV. Decay to turbulence ($t^* > 9$).

Two approaches will be taken in this study. The first is to simulate the TGV problem with direct numerical simulation, i.e. no turbulence modelling. From this reference data, the Smagorinsky and k-equation SGS models will be compared. By running a DNS alongside the LES, it is possible to isolate the behaviour of the subgrid-scale model. The purpose of running an LES is to fully capture large structures, and successfully model smaller structures. A DNS resolves all scales, right down to the Kolmogorov scales where dissipation dominates. The TGV problem is designed to produce progressively smaller scales, therefore it is possible to track the evolution of small scales and assess the suitability of an SGS model.

A coarse, medium, and fine grid have been created in the `blockMesh` application of OpenFOAM. A fixed time step of $\Delta t^* = 1 \times 10^{-3}$ has been set for the coarse 64^3 grid. The time step is halved every time the mesh is refined, as in Bull and Jameson (2014). Simulations are ran for 20 dimensionless time units to record the full production and decay of vortical structures. Coarse grid simulations can be ran locally on a desktop PC with 4 cores. Medium and fine grid simulations are ran on the Leeds HPC ARC3, with 24 and 96 cores, respectively. See Table 3.2 for a summary of the numerical parameters used in the current study.

A minimum of 512 degrees of freedom was required for submission to the 1st and 2nd workshop on high-order CFD methods. However, the goal in this current study is to assess the modelling capabilities of subgrid-scale models on relatively coarse (64, 128 DOF) meshes. Numerical dissipation is expected to contribute to inaccuracies on coarse meshes, therefore reference data from high-order methods in the literature is supplemented with DNS simulations in the current study.

Case	Mesh	Δt^*	Machine	Cores
Coarse	64^3	1×10^{-3}	Desktop	4
Medium	128^3	5×10^{-4}	ARC3 Leeds	24
Fine	256^3	2.5×10^{-4}	ARC3 Leeds	96

Table 3.2: Cell density and time stepping for the coarse, medium, and fine meshes.

Case	Mesh	Model
Smag64	64^3	LES Smagorinsky (Smagorinsky, 1963).
kEqn64	64^3	LES k-equation (Yoshizawa, 1986).
DNS64	64^3	DNS.
DRP-512	512^3	High-resolution explicit finite difference method of DeBonis (2013).

Table 3.3: Case set-up and models for the TGV problem.

Combining high-resolution literature results and coarse DNS simulations allows for a full assessment of the LES subgrid-scale model in isolation. Turbulence models, mesh densities, and abbreviations of each case can be found in Table 3.3.

3.4.2 Impact of subgrid-scale model

Following the guidelines for submission to the International Workshop on High-Order CFD Methods (Wang et al., 2013), evolution of the flow is assessed by various diagnostic quantities. The volume-averaged integrated kinetic energy is given by

$$E_k = \frac{1}{\rho_0 V} \int_V \rho \frac{u_i u_i}{2} \, \mathrm{d}V \quad , \tag{3.69}$$

where V is the domain volume. For constant density $\rho = \rho_0$, (3.69) transforms to

$$E_k = \frac{1}{(2\pi)^3} \int_V \frac{u_i u_i}{2} \, \mathrm{d}V \quad . \tag{3.70}$$

Kinetic energy dissipation rate (KEDR) can be obtained directly from the

kinetic energy E_k by taking the time derivative

$$\varepsilon(E_k) = -\frac{\mathrm{d}E_k}{\mathrm{d}t} \quad . \tag{3.71}$$

Integrated enstrophy is defined by

$$\zeta = \frac{1}{\rho_0 V} \int_V \rho \frac{\omega_i \omega_i}{2} \, \mathrm{d}V \quad , \tag{3.72}$$

which is analogous to the dissipation produced through vorticity, or turbulence. For an incompressible flow it can be shown that

$$\varepsilon(\zeta) = 2\nu\zeta \quad . \tag{3.73}$$

DeBonis (2013) compared the two forms of dissipation given in (3.71) and (3.73) for a range of grid densities. If the computational grid is too coarse, vortical structures are poorly resolved, and dissipation through turbulence is underpredicted. This manifests in a discrepancy between profiles of $\varepsilon(E_k)$ and $\varepsilon(\zeta)$. From this it could be seen that their 64^3 grid was not able to fully capture all vortical structures. However, dissipation computed directly from the kinetic energy $\varepsilon(E_k)$ matched closely to the reference data. Therefore, although the coarse 64^3 grid was unable to produce enough dissipation through resolved turbulence, numerical dissipation ε_{num} accounted for the rest, where

$$\varepsilon_{\text{num}} = \varepsilon(E_k) - \varepsilon(\zeta) \quad . \tag{3.74}$$

There are two approaches for producing the correct level of dissipation. The first is to reduce numerical dissipation as much as possible. Another approach is that of implicit LES, where no subgrid-scale model is used, but the grid density is chosen such that ε_{num} provides a suitable amount of dissipation.

Before running LES simulations on coarse meshes of 64^3, a DNS on a mesh of 128^3 is ran to highlight the difficulty in modelling the TGV problem. To visualise vortex development, isosurfaces of z-vorticity are presented in Figure 3.5. At $t^* = 0$, the initial field compromises periodically stacked regions of high vorticity

(Figure 3.5a). As the flow develops, vortices stretch, roll up, and interact. At $t^* = 20$ it can be seen that large structures have broken down (Figure 3.5b).

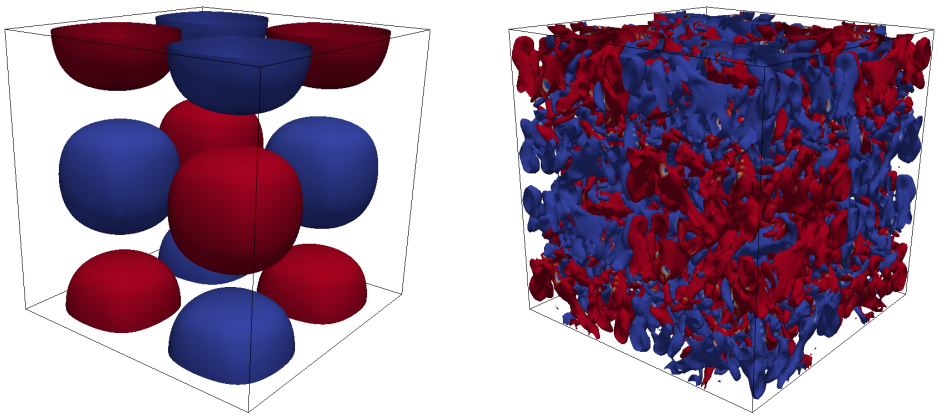

(a) $t^* = 0$ (b) $t^* = 20$

Figure 3.5: DNS of the Taylor-Green vortex on a 128^3 mesh. Isosurfaces of $|\omega_z| = 0.7$ (red and blue represent negative and positive values respectively).

To further illustrate the importance of small-scale structures in the TGV problem, isovolumes of Q at different stages of flow development are produced for the current DNS and compared to the high-order flux reconstruction scheme of Bull and Jameson (2014). Isovolumes of $Q = -\frac{1}{2}A_{ij}A_{ji}$, where A_{ij} is the velocity gradient tensor, are commonly visualised to identify turbulent structures (Hunt et al., 1988). In Figure 3.6a, good agreement can be seen between the coarse DNS and high-order method in the initial stage at $t^* = 2.5$. From $t^* = 2.5$ to $t^* = 5$ there is an emergence of fine, feather-like structures. The very smallest feather structures are not captured with the DNS. At $t^* = 8$ and $t^* = 10.75$ it becomes apparent that a mesh density of 128^3 is unable to fully resolve the smallest scales, however the large-scale dynamics are reasonably well captured.

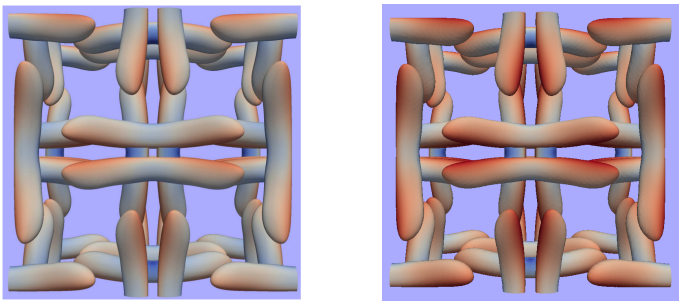

(a) $t^* = 2.5$, $Q = 0.5$.

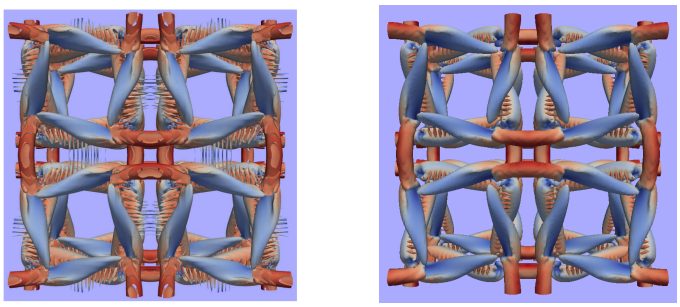

(b) $t^* = 5$, $Q = 1.5$.

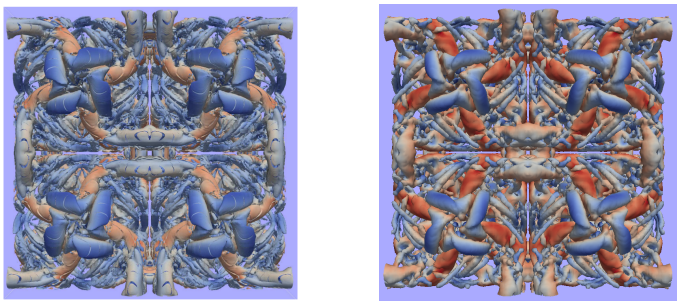

(c) $t^* = 8$, $Q = 1.5$.

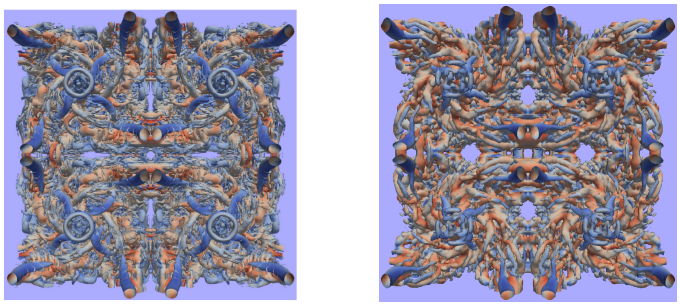

(d) $t^* = 10.75$, $Q = 1.5$.

Figure 3.6: Q isovolumes coloured by velocity magnitude. Left column: high-order flux reconstruction (FR) DNS of Bull and Jameson (2014) with cell density 64^3. Right column: current DNS with cell density 128^3.

Attention now turns to the predicted energy decay from the Smagorinsky and k-equation SGS models. SGS models are evaluated on their accuracy to correctly dissipate energy. Volume-averaged energy is recorded at time intervals of $t^* = 0.25$ for the full duration. Figure 3.7 presents the time-evolution of energy decay. Included is the high-resolution results of DeBonis (2013). The k-equation performs reasonably well for $t^* < 4$, and is in close agreement to the DNS and high-resolution results. However, the Smagorinsky model immediately begins to dissipate energy, even in the inviscid period. Ideally the SGS model is inactive in the inviscid period and returns a small turbulent viscosity ν_T. Once the smooth vortical structures evolve and break down into turbulence ($t^* > 9$), the LES and DNS tested on the 64^3 grid all begin to collapse onto one another. This suggests that turbulence modelling becomes less of a factor towards the end of the simulation, perhaps because the turbulent structures are under-resolved with the coarse grid.

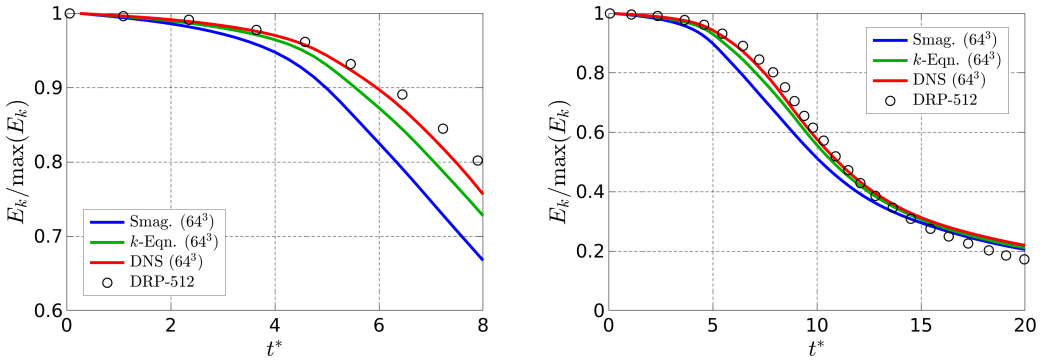

(a) Inviscid period of decay.

(b) Full simulation duration.

Figure 3.7: Volume-integrated energy decay in time, normalised by its maximum value. DRP-512: high-resolution explicit finite difference method of DeBonis (2013).

Time-evolution of dissipation is calculated two ways. First, it is calculated from the enstrophy, which represents dissipation due to turbulence (Figure 3.8a). Secondly, it is derived straight from the rate of change of kinetic energy (Figure 3.8b). Dissipation is a small scale phenomenon, therefore using a coarse mesh, or an overly-dissipative SGS model will cause an under-prediction in ε. It is clear

from Figure 3.8a that the grid of 64^3 is incapable of capturing the vortex dynamics, even with DNS.

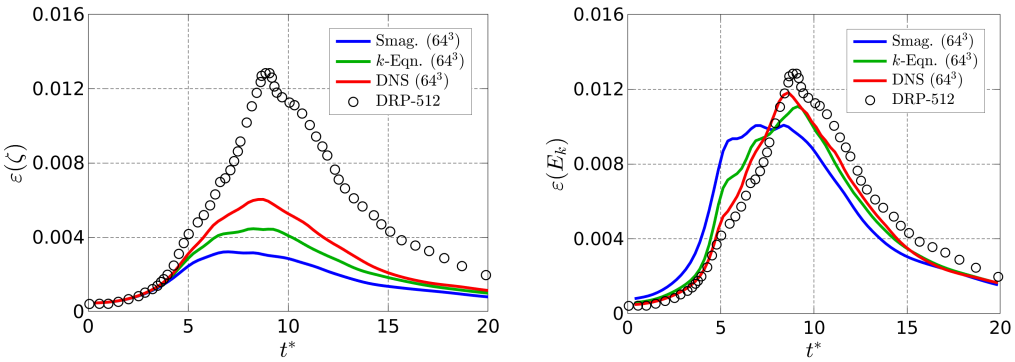

(a) KEDR computed from enstrophy ζ. (b) KEDR computed from energy E_k.

Figure 3.8: Time-evolution of the kinetic energy dissipation rate (KEDR). DRP-512: high-resolution explicit finite difference method of DeBonis (2013).

Although the same mesh density has been used between the DNS and LES, a different level of $\varepsilon(\zeta)$ has been observed between each simulation. To further inspect this, the following ratios are calculated

$$\varepsilon_{f1} = \frac{\varepsilon(\zeta)|_{\text{Smag}}}{\varepsilon(\zeta)|_{\text{DNS}}} \quad , \qquad \varepsilon_{f2} = \frac{\varepsilon(\zeta)|_{k\text{-Eqn}}}{\varepsilon(\zeta)|_{\text{DNS}}} \quad , \tag{3.75}$$

where $\varepsilon(\zeta)|_{\text{Smag}}$, $\varepsilon(\zeta)|_{\text{DNS}}$, and $\varepsilon(\zeta)|_{k\text{-Eqn}}$ are the dissipation terms evaluated by each modelling approach. Figure 3.9 displays the results calculated by the dissipation fractions defined in (3.75). At peak dissipation ($t^* = 8.75$), both SGS models return minimums in ε_{f1}, and ε_{f2}. At $t^* = 8.75$, the k-equation model underestimates dissipation by $\approx 27\%$, while the Smagorinsky model under estimates dissipation by $\approx 49\%$.

Figure 3.10 highlights the role of turbulent viscosity. Isocontours of Q are presented for simulations of the TGV problem at dimensionless time $t^* = 5$. Fine structures circled in green are visible in the DNS and k-equation simulations which are not present with the Smagorinsky model. In Figure 3.10d, isovolumes of high turbulent viscosity are overlaid with isocontours of $Q = 1.5$, as predicted by the

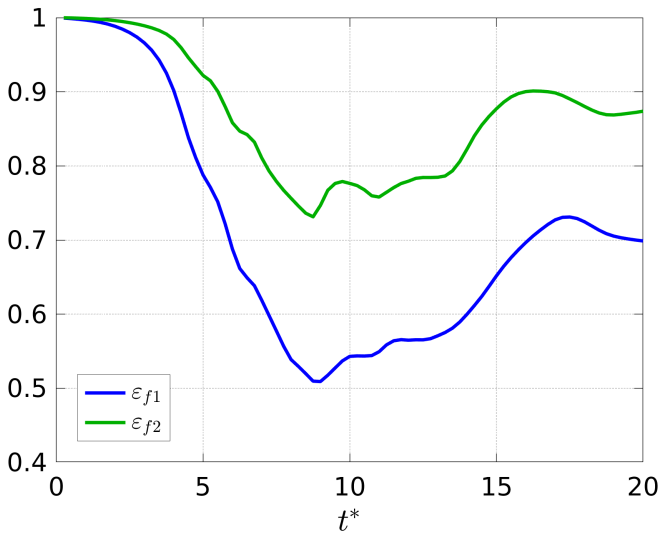

Figure 3.9: Kinetic energy dissipation rate (KEDR) computed from enstrophy ζ.

Smagorinsky model. Regions in which the Smagorinsky model is unable to predict finer structures corresponds directly to higher values of turbulent viscosity.

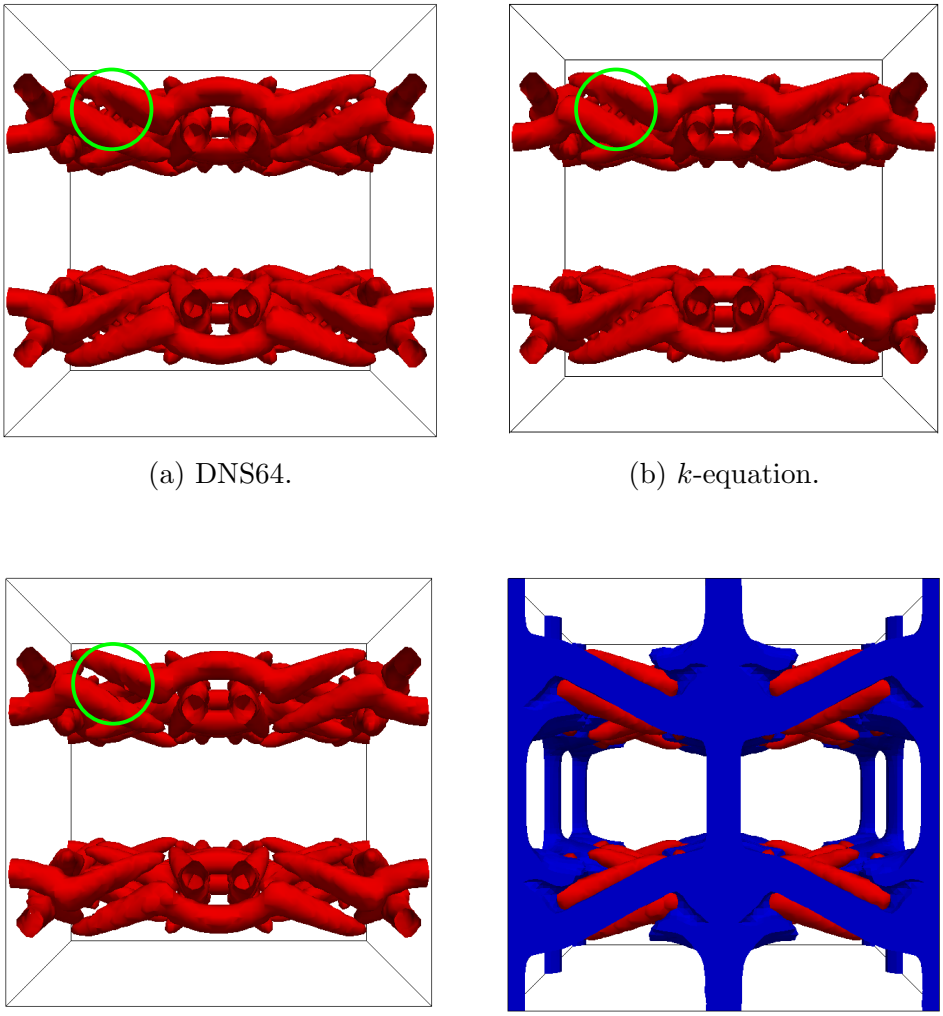

(a) DNS64.

(b) k-equation.

(c) Smagorinsky.

(d) Fig. 3.10c with isovolumes of ν_T.

Figure 3.10: Isocontours of $Q = 1.5$ at $t^* = 5$ for each turbulence model on a 64^3 mesh resolution. Fine connecting structures have been circled in the DNS and k-equation model, which are not present in the Smagorinsky model. To understand this, isovolumes of $\nu_T/\max(\nu_T)$ are plotted in the range $[0.3, 1]$ over the Smagorinsky solution.

3.5 Chapter conclusions

Turbulence modelling approaches have been discussed in the current chapter. When simulating free-stream turbulence, it is imperative to choose a subgrid-scale (SGS) model which controls the level of dissipation. Two stock SGS models have been introduced: the Smagorinsky algebraic model of Smagorinsky (1963), and the one-equation k-equation model of Yoshizawa (1986). The extension to a two-equation model has been discussed, which has the potential to incorporate some of the recent findings from wind-tunnel experiments, where a different behaviour in the turbulence dissipation has been observed (Hurst and Vassilicos, 2007; Seoud and Vassilicos, 2007; Vassilicos, 2015).

Models are tested on the three-dimensional Taylor-Green vortex (TGV) problem as a challenging test case which incorporates inviscid processes, turbulence production, and dissipation. The Smagorinsky model was found to dissipate energy indiscriminately, without the presence of a physical mechanism. This has been observed in the initial period of inviscid development with the TGV problem. However, the one-equation model of Yoshizawa (1986) performs better, and is a closer match to a DNS ran on the same mesh. Volume-averaged integrated kinetic energy is evaluated during the TGV development. Towards the end of the simulation, once structures have been given enough time to break down, the DNS and LES ran on the 64^3 grid contain the same amount of energy. This demonstrates that regardless of the turbulence modelling employed, dissipation due to a coarse mesh can be a dominate factor in overall dissipation.

To summarise, the method of LES has been set out in the present chapter. Dissipation is of interest to the study of free-stream turbulence and wake dynamics, therefore dissipation modelling has been the focus of this current chapter. The k-equation SGS model has performed reasonably well on a challenging vortex test case, and is therefore chosen to model grid turbulence using LES.

Chapter 4

Simulating grid turbulence

Numerical simulations of grid turbulence are investigated in the current chapter. A total of 4 grids are considered: regular, multiscale, and two fractal designs. A new grid design is constructed to address problems of flow homogeneity and vorticity clustering. Typically, a turbulence-generating grid is constructed by tiling a single element until the entire experimental cross-section is covered. With the two fractal-type grids studied here, only one grid element is considered. By only considering a single grid element instead of tiling multiple elements into a sheet, the interaction between jets and wakes can be observed, driving discussion on flow homogeneity and grid design. Measurements of the velocity gradient tensor are taken directly behind each grid, which is not possible when taking intrusive measurements in a wind tunnel. The first key outcome of this chapter is to inspect the wake generated behind each grid element by sampling data across a plane normal to the streamwise direction. This provides new information on the cross-sectional distribution of turbulence from such grids. The second key outcome of this chapter is to evaluate velocity gradients in the near grid region to better understand the production and decay of turbulence, in addition to the dissipation rate.

4.1 Introduction

Methods to generate free-stream turbulence in experiments and simulations have been introduced in Section 2.1. It was seen that complex grid geometries are used in experiments to customise grid turbulence (Hurst and Vassilicos, 2007; Vassilicos, 2015; Nagata et al., 2017). However, no consensus exists on an optimal method to generate turbulence in simulations, and the solution of an LES is known to be sensitive to inlet conditions, as highlighted in the review papers of Tabor and Baba-Ahmadi (2010) and Wu (2017). Conditions required for an LES inlet condition were set out by Tabor and Baba-Ahmadi (2010): stochastically varying, represent scales down to the filter, compatible with the Navier-Stokes equation, and easy to specify turbulent properties. Tabor and Baba-Ahmadi (2010) split inlet conditions into two categories: precursor, and synthetic.

Precursor methods utilise pre-existing results, which could be obtained by experimental data or CFD. For example, Wu et al. (2006) passed data from a channel flow simulation into an inlet section of a diffuser, therefore shortening the streamwise inlet development length. However, extracting the solution of a precursor simulation for use in a separate simulation requires added computational memory, which may not be available. To address this, synthetic methods have been developed which create a turbulent inlet condition in situ, requiring less computational memory.

Synthetic methods combine generated turbulence with a mean flow to produce an inlet condition. For industrial engineering flow applications, the development of a synthetic turbulence generator has two major advantages: (i) reduced development length for wall bounded flows such as the channel and diffuser sections of an aeroengine combustor (Zhou et al., 2017); (ii) representation of a turbulent inlet, which is important in wind engineering where a laminar inflow is an exception rather than a rule (Ricci et al., 2017). Care must be taken to generate appropriate fluctuations which are correlated in time and space. In a study of the backward-facing step by Aider et al. (2007), random white noise, which holds no temporal or spatial correlation, was combined with a bulk flow to yield an inlet condition. The resulting flow field revealed an overestimation of the recirculation length, and a reduction in the shedding frequency. Turbulent content in

the free-stream served to amplify shear layer instabilities. The energy spectra of generated white noise does not correctly represent turbulence because energy is distributed across all wavenumbers, which is unrealistic for a turbulent flow, and as a result the fluctuations die out (Jarrin et al., 2006).

To generate turbulent inflow, Jarrin et al. (2009) split their computational domain into two regions, implementing LES where high accuracy is necessary, and RANS elsewhere. Information is passed from the RANS region into the LES domain via a synthetic-eddy method (SEM). Their study compromised 3 test geometries: channel, duct, and aerofoil. Using the SEM, the upstream RANS solution can be used to generate an unsteady turbulent inflow condition for the LES region. Comparisons were made between: SEM, the random method, and the method of Batten et al. (2004). The Fourier decomposition type approach of Batten et al. (2004) was deemed inappropriate when specifying an inhomogeneous length scale in the channel flow, or predicting the separation on the aerofoil. The random method could not replicate coherence at the inlet which led to laminarisation downstream. SEM outperformed both methods in every aspect studied, and is a promising method for the generation of synthetic turbulence as it is can be applied to complex geometries and is independent of the spatial discretisation (Dhamankar et al., 2017).

A modification to the SEM was developed by Poletto et al. (2013) which guarantees that the fluctuating velocity field is divergence-free. The SEM method detailed in Jarrin et al. (2009) was applied to the fluctuating vorticity field to create the divergence-free synthetic-eddy method (DFSEM). Eddies randomly created within an eddy bounding box are advected through the inlet patch (see Figure 4.1). The shape function was also reworked to create anisotropic length scales, leading to a divergence-free restriction on the shape function. A turbulent channel flow test case was performed to compare the DFSEM to the original SEM, the VORTEX method of Sergent (2002), and the sythesized turbulence approach of Davidson and Billson (2006). A periodic LES channel flow was chosen as the validation data set. The DFSEM produced more accurate representation of turbulent structures downstream from the inlet. When comparing the development of Reynold stress components and skin friction, the closest agreement to

the periodic LES was found with the DFSEM. A number of channel flow studies have validated the DFSEM condition. Poletto et al. (2013) and Skillen et al. (2016) both found the condition to trigger turbulence at the walls, and reduce the development length. The DFSEM has also been implemented in the study of Dean vortices in pipe flow (Tunstall et al., 2016; Hufnagel et al., 2018). Hufnagel et al. (2018) implemented a pseudo-spectral method DNS, and visualised wave-like structures using proper orthogonal decomposition (POD). Tunstall et al. (2016) simulated the flow through a T-junction pipe elbow using OpenFOAM.

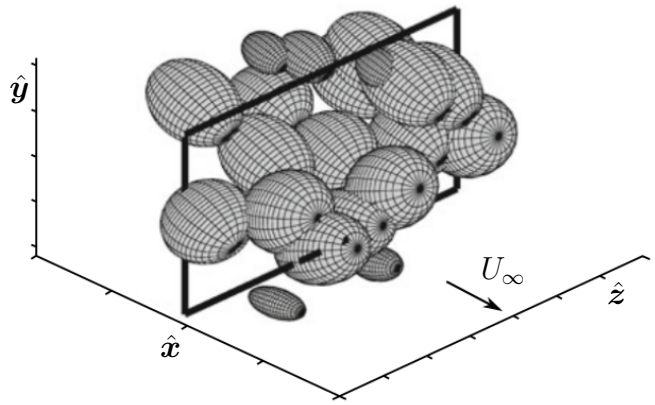

Figure 4.1: Schematic of the eddy generation process in the DFSEM, adapted from Poletto et al. (2013). Eddies are randomly generated within an eddy bounding box, and subsequently advected through the inlet plane by a bulk flow along the streamwise direction.

The aforementioned studies have all used the DFSEM condition on wall-bounded flows. However, the procedure for generating an inflow condition upstream of a bluff body geometry is not known. The advection of eddies generated in the DFSEM bounding box into a free-stream has yet to receive any attention. All previous studies have instead focused on the production of structures once the DFSEM eddies have interacted with wall boundaries.

Direct numerical simulation of grid turbulence has been made possible through the implementation of immersed boundary method (IBM) and terascale parallel high performance computing capabilities (Laizet and Vassilicos, 2009). There exists a wealth of literature detailing DNS on the flow past thin sheets with fractal

geometry cut outs, for example Nagata et al. (2008), Suzuki et al. (2010), Suzuki et al. (2013), Zhou et al. (2014). However, high resolution simulations of fractal grid turbulence are currently restricted to academic research, due to immense computational cost. Blackmore et al. (2013) took a simplified approach to generating grid turbulence. Instead of simulating flow past an array of cylinders or a thin sheet, parts of the inlet were blocked with solid patches representing a biplane grid. A major advantage of this technique is there is no requirement for a body fitted mesh with refinement around walls. They performed a parametric study, varying bar width, grid spacing, computational cell density, and domain size. Turbulence downstream of each permutation was analysed by computing energy spectra, integral length scales, and turbulence intensities. A triple inlet was deemed more suitable than the single and double inlet, because it did not restrict the growth of turbulent structures. Blackmore et al. (2013) only studied a regular grid, but they showed that the projected inlet technique produces turbulence comparable to grid-generated turbulence. With the recent interest in multiscale and fractal grid turbulence, a natural extension of the projected inlet method is to test a range of grid designs.

The first objective of this chapter is to focus on grid design. Important parameters of grid turbulence are reviewed in order to better understand how the design of each grid influences the characteristics of turbulence. This includes turbulence decay and length scales generated from each grid. This motivates the design of a new type of grid, which combines benefits of the regular grid design with benefits from fractal-type grids. The second objective of this chapter is to compare the turbulence generated by each grid design. Data is sampled along the centreline to assess streamwise development, and on a plane normal to the streamwise direction to compare turbulence characteristics of each grid element.

4.2 Parameters of grid turbulence

Following a parcel of fluid in the Lagrangian frame of reference, turbulence decay can be described by a power-law fitting to the velocity variance (Von Karman

and Howarth, 1938; Saffman, 1967)

$$\langle u_1^2 \rangle = a(t - t_0)^{-n} \quad , \tag{4.1}$$

where u_1 is the velocity fluctuation in the streamwise direction, a is a coefficient which depends on the initial conditions, t_0 is the virtual origin where the turbulence becomes fully developed (Krogstad and Davidson, 2010), and n is the decay exponent. A Cartesian coordinate system (x, y, z) is used interchangeably with (x_1, x_2, x_3). Similarly, the notation u_1, u_2, u_3 is used interchangeably with u, v, w. The streamwise direction is aligned along x, and crossflow directions are denoted by y and z. Mohamed and Larue (1990) proposed an alternative form of (4.1) by using Taylor's hypothesis to convert from time to downstream position, and dividing throughout by the square of the mean velocity, such that

$$\frac{\langle u_1^2 \rangle}{U^2} = A \left(\frac{x_1 - x_0}{M} \right)^{-n} \quad , \tag{4.2}$$

where A is the decay coefficient, x_0 is the virtual origin, and M is the regular grid spacing. If a regular grid is not used, M in (4.2) becomes some relevant length scale of the grid, for example Krogstad and Davidson (2011) used the integral length scale at a fixed downstream position. Unlike t_0 in (4.1), x_0 in (4.2) is not the point where turbulence becomes fully developed, but rather some distance upstream of that point (Krogstad and Davidson, 2010). It is often convenient to take natural logarithms of (4.2) to yield

$$\ln \left[\frac{\langle u_1^2 \rangle}{U^2} \right] = \ln A - n \ln \left[\frac{x_1 - x_0}{M} \right] \quad , \tag{4.3}$$

from which a linear fit can be made to find a suitable A, x_0, and n. Alternatively, A can be eliminated by taking a two-point differencing scheme (Krogstad and Davidson, 2011)

$$n = - \frac{\ln \left[\frac{\langle u_1^2 \rangle (x + \Delta x - x_0)}{\langle u_1^2 \rangle (x - \Delta x - x_0)} \right]}{\ln \left[\frac{x + \Delta x - x_0}{x - \Delta x - x_0} \right]} \quad , \tag{4.4}$$

where the virtual origin x_0 can be estimated by a least-squares approach. Estimating n from (4.4) is susceptible to noise, however this is only a concern in experiments when taking measurements in the far wake.

The classical range of decay exponents is $6/5 \leq n \leq 10/7$, where the lower bound $n = 6/5$ is the classical prediction of Saffman (1967), and the upper bound $n = 10/7$ is described by Batchelor and Townsend (1948) and Ossia and Lesieur (2000). Substantial evidence for the classical decay range has been provided over decades of grid turbulence research: Comte-Bellot and Corrsin (1966); Mohamed and Larue (1990); Krogstad and Davidson (2010). However, large decay exponents where $n > 10/7$ has been observed for fractal grid-generated turbulence: Hurst and Vassilicos (2007); Seoud and Vassilicos (2007); Mazellier and Vassilicos (2010); Valente and Vassilicos (2011); Nagata et al. (2013).

For isotropy, turbulent fluctuations in the streamwise direction should be approximately equal to crossflow fluctuations. To test this, a measure of isotropy is calculated by the ratio

$$\frac{\langle q^2 \rangle}{3\langle u_1^2 \rangle} \equiv \frac{\langle u_1^2 + u_2^2 + u_3^2 \rangle}{3\langle u_1^2 \rangle} \quad , \tag{4.5}$$

where it is noted that a value of unity corresponds to a flow where streamwise fluctuations are balanced by cross-stream contributions.

To further test for homogeneity and isotropy along the centreline, skewness S_u and flatness F_u are obtained from moments of velocity fluctuation (Pope, 2001)

$$\hat{\mu}_n = \frac{\langle u^n \rangle}{\sigma_u^n} \quad , \tag{4.6}$$

where σ is the variance, and setting $n = 3, 4$ corresponds to skewness and flatness, respectively. Skewness is a measure of high speed events, and for HIT it is expected to find $S_u \approx 0$. Spikes in F_u represent high flow intermittency, as would be expected in the production area. In the ideal case of HIT, a PDF of turbulent velocities follow a Gaussian distribution with $F_u = 3$. Measures of skewness and flatness can be used to determine the approximate downstream position at which the flow recovers homogeneity. Krogstad and Davidson (2012) investigated homogeneity behind a regular grid (cg), and two multiscale grids ($msg1$, $msg2$). Cross-stream variations of velocity skewness near grid were largest behind cg.

However, at approximately 50 integral length scales, profiles of streamwise velocity skewness S_u recover a homogeneous value of 0 for cg and $msg1$, but $S_u \approx -0.15$ for $msg2$. For their conventional grid design, 50 integral length scales corresponds to approximately 30 mesh spacings, where the mesh spacing M is the separation distance between the centres of neighbouring bars. It was concluded that $msg2$ needs more time to become homogeneous because of lower solidarity, and larger length scales generated near grid.

The Taylor microscale is often referred to as the diameter of the smallest eddies responsible for energy dissipation. Although this is not strictly true, it is a well defined and useful length scale for the study of grid turbulence (Pope, 2001). The Taylor microscale λ is defined by

$$\lambda^2 = \frac{\langle u_1^2 \rangle}{\left\langle (\partial u_1/\partial x_1)^2 \right\rangle} \quad . \tag{4.7}$$

In previous experiments, the general trend of λ in the decay region has been well documented. In regular grid experiments, it has been shown to increase monotonically. If the turbulence decays as a power law, then $\lambda \propto x_1^{0.5}$ (Batchelor, 1953). However, for multiscale and fractal grids, evidence suggests λ becomes constant (Seoud and Vassilicos, 2007). Constant λ was attributed to the smallest fractal iterations in the wind tunnel experiment of Nagata et al. (2017).

A constant Taylor microscale has implications for the decay characteristics. To demonstrate this, (4.7) is considered without averaging, and for a constant Taylor microscale, $\lambda = \lambda_0$

$$\lambda_0^2 = \frac{u_1^2}{(\partial u_1/\partial x_1)^2} \quad , \tag{4.8}$$

which reduces to a 1st order homogeneous ODE

$$\frac{\mathrm{d}u_1}{\mathrm{d}x_1} \pm \frac{1}{\lambda_0} u_1 = 0 \quad , \tag{4.9}$$

which has analytical solutions

$$u_1^2 \propto \exp\left(\pm \frac{x_1}{2\lambda_0} \right) \quad . \tag{4.10}$$

Turbulence intensity must remain finite for $x_1 \to \infty$, hence the positive solution in (4.10) is unphysical and discarded. The negative solution corresponds to exponential decay of turbulence intensity. Therefore, exponential decay present in the decay region of grid turbulence directly corresponds to constant Taylor microscale.

The integral length scale is obtained from integration of the autocovariance function $R(s) = \langle u_1(x_1)u_1(x_1+s)\rangle$. In experimental measurements and numerical simulations, $R(s)$ decreases monotonically towards zero, then oscillates around zero. As in Krogstad and Davidson (2011), $R(s)$ is only considered up to its first zero crossing r_0. Taylor's frozen turbulence hypothesis has been used to evaluate $R(s)$. The longitudinal integral length scale is given by

$$L_{11}(x_1) = \frac{1}{\langle u_1^2(x_1)\rangle} \int_0^{r_0} R(s)\,\mathrm{d}s \quad . \tag{4.11}$$

4.3 Developing a new grid design

4.3.1 Projected inlet method

Figure 4.2 presents a simple example of the projected inlet method. The same inflow velocity and domain bounding box is used across simulations for a fairer comparative study. The bounding box of the computational domain is fixed by a width of $W = 120\,\text{mm}$ in crossflow directions, and a streamwise length of $4W$. The inlet of each grid has been split into two patches: (i) zero velocity at solid patches, where grid bars are projected; (ii) non-zero velocity $\boldsymbol{U}_{\text{in}} = (U_{\text{in}}, 0, 0)$ in the gaps between grid bars. Velocity at the outlet boundary is prescribed using the mixed OpenFOAM boundary condition `inletOutlet`, which switches from zero gradient to a fixed value if back flow occurs. Zero gradient for pressure is prescribed across the full inlet patch. Pressure is fixed at the outlet boundary, with value 0. All other boundary patches are periodic- see Table 4.1 for further information. An adjustable time-step is enforced, guaranteeing a Courant-Friedrichs-Lewy (CFL) of less than 0.75. Data is sampled for at least 125 000 iterations of the flow to obtain converged statistics, as per Laizet et al. (2013). LES simulations are ran in OpenFOAM v4.1 using the k-equation SGS model of Yoshizawa (1986), which was described in Chapter 3. A description of the numerical settings selected throughout this study are detailed in Appendix A.

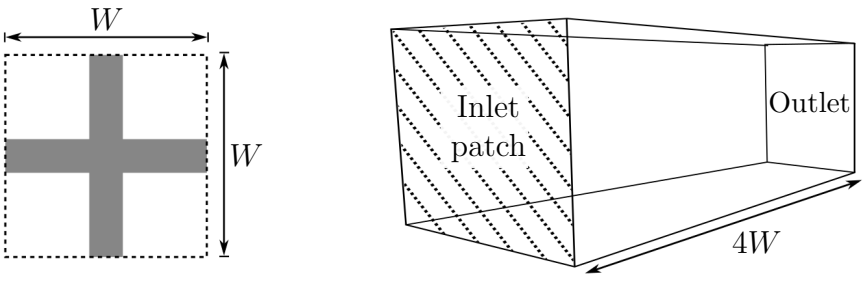

Figure 4.2: Example of the projected inlet method. Left: a cross is projected onto the inlet plane. All cells marked in grey are set to zero velocity. Right: computational domain, including inlet patch onto which each grid design is projected.

4.3.2 Grid construction

Naming conventions differ slightly throughout the literature and between grid designs. Figure 4.3 displays the notation used in this study. Regular and multiscale grids are constructed with bars of varying thickness t_i, and mesh spacing M_i, where subscripts $i = 0, \ldots, (N-1)$ indicate the iteration level. A regular grid has only one mesh spacing, whereas a multiscale grid has multiple mesh spacings. By definition: $M_{\max} \equiv M_0$, and $t_{\max} \equiv t_0$. For fractal-type grids, a comparable measure of mesh spacing is the bar length L_i. Length and thickness of bars is scaled between iterations through scaling parameters R_L and R_t, such that $L_i = (R_L)^i\, L_0$, and $t_i = (R_t)^i\, t_0$. Similarly, by definition: $L_{\max} \equiv L_0$.

A grid-based Reynolds number is defined from the inflow velocity U_{in}, and a choice of length scale. For regular and multiscale grids, it is common to use the largest mesh spacing M_0, and bar width t_0. The mesh Reynolds number is denoted by Re_M when a mesh spacing is used, and Re_0 when bar width t_0 is used. For a fractal grid, the length of the largest bar L_0 can be used, however Hurst and Vassilicos (2007) introduced a length scale which takes solidarity σ into account. Solidarity is defined by the ratio of solid blockage to cross-sectional area when the grid is projected onto a two-dimensional plane. The effective mesh length is defined by

$$M_{\text{eff}} = \frac{4T^2}{P}\sqrt{1-\sigma}\ , \tag{4.12}$$

where T^2 is the cross-sectional area, and P is the fractal perimeter of the grid. In this study the fractal perimeter has been taken as the sum of all jet perimeters,

Patch	$\boldsymbol{U}$ [m/s]	p [m^2/s^2]	k [m^2/s^2]
Inflow	$(U_{\text{in}}, 0, 0)$	`zeroGradient`	1×10^{-4}
Inlet grid	$(0, 0, 0)$	`zeroGradient`	0
Outlet	`inletOutlet`	0	`inletOutlet`
Side patches	`cyclic`	`cyclic`	`cyclic`

Table 4.1: Boundary patch prescriptions in OpenFOAM for the grid turbulence channel.

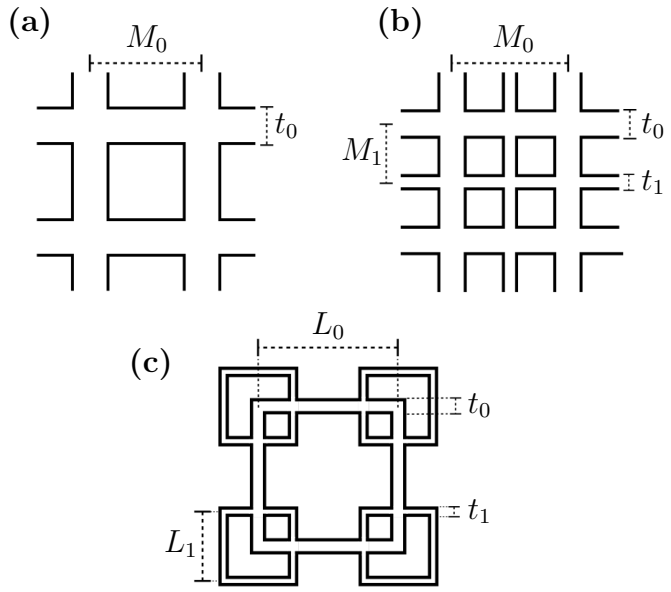

Figure 4.3: Dimensions and naming conventions of common turbulence-generating grids: (a) regular, (b) multiscale, (c) square-fractal.

without including edges which coincide with cyclic boundary conditions.

By approximating the position along the domain centreline at which the wake of the largest bars first meet, Mazellier and Vassilicos (2010) obtained a streamwise length scale onto which centreline mean velocity and turbulence intensity profiles collapse- the wake interaction length scale x_*

$$x_* = \frac{L_0^2}{t_0} \quad . \tag{4.13}$$

Figure 4.4 presents a schematic of the wake interaction length scale x_*, adapted from Mazellier and Vassilicos (2010). It can be seen that x_* corresponds to the downstream position at which the wake from the largest bars meets. Although x_* is defined by crude geometrical arguments, it has been successfully adopted throughout experiments (Gomes-Fernandes et al., 2012), and numerical simulations (Nagata et al., 2008). Valente and Vassilicos (2011) noted that x_* is also applicable to regular grids.

An important parameter to consider when designing a fractal grid geometry

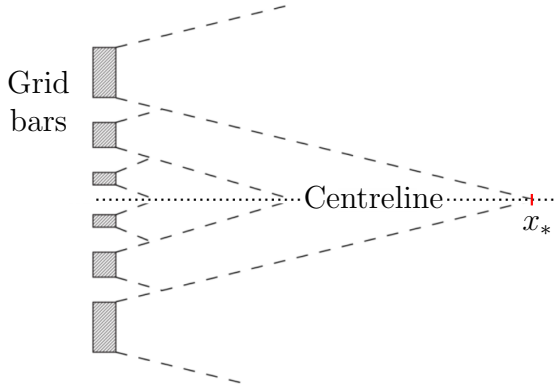

Figure 4.4: Schematic of wake interaction on the centreline, adapted from Mazellier and Vassilicos (2010).

is the fractal dimension D_f, defined by (Hurst and Vassilicos, 2007)

$$D_f = -\frac{\log(B)}{\log(R_L)} \in [1, 2] \ , \tag{4.14}$$

where B is the number of patterns at each iteration, which is 4 in the case of a square-fractal grid constructed by squares (e.g. see Figure 4.3). The influence of D_f on flow homogeneity has been studied. Hurst and Vassilicos (2007) tested a number of fractal grids with various space-filling parameters $D_f \leq 2$, finding greatest homogeneity when $D_f = 2$. To ensure $D_f = 2$ with $B = 4$, (4.14) requires that $R_L = 0.5$.

Hearst and Lavoie (2014) reported inhomogeneities in their cross-fractal grid experiment in the near field. The authors noted that this result contradicted previous fractal grid turbulence experimental results. The cause of poor transverse homogeneity was not addressed, however a bar length scaling of $R_L = 0.44$ was used in their design, resulting in a space-filling parameter of $D_f = 1.71$.

In a preliminary numerical study, two square-fractal grids with identical design were tested, but with different space-filling parameters: $D_f = 1.8$, and $D_f = 2$. Contours of velocity magnitude for both grids is presented in Figure 4.5. High velocity streaks along the domain perimeter are present when $D_f = 1.8$, resulting in transverse inhomogeneities- a conclusion which aligns with the problems encountered in Hearst and Lavoie (2014). As hoped, these streaks are not present in

the space-filling grid where $D_f = 2$. It is clear that even though solidarity might be fixed between two grid designs, how this solidarity is spread across the inlet patch is free to vary. If the majority of inlet blockage is located in the centre of the inlet patch, this could lead to inhomogeneities, resulting from persistent jets around the perimeter.

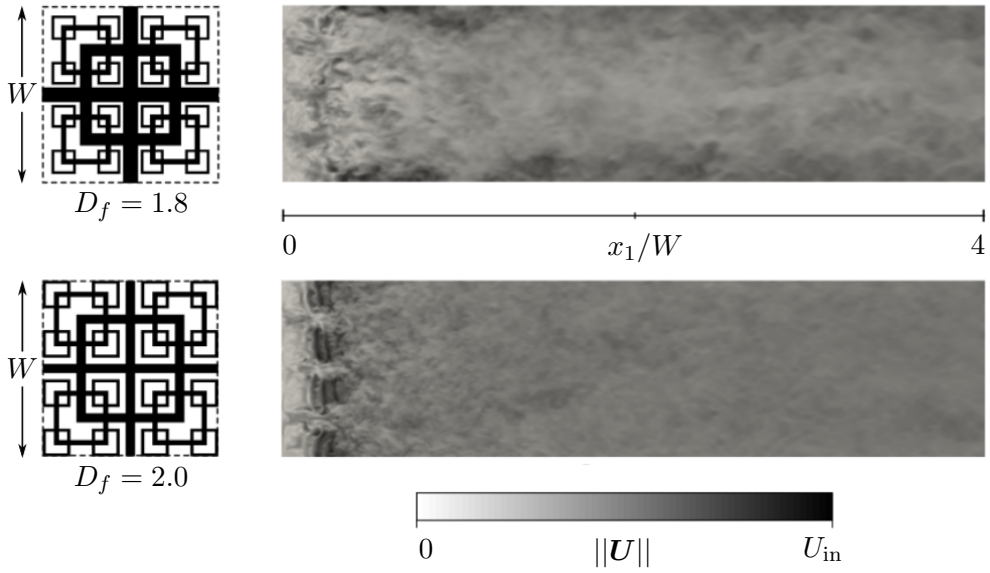

Figure 4.5: Contours of velocity magnitude for two square-fractal grids with different space-filling parameter D_f.

4.3.3 Selected grid designs

To address the problems of homogeneity reported throughout the literature, a new type of grid geometry is designed which combines separate strengths from regular and fractal designs. Compared to square-fractal grids, a regular grid uniformly spreads solidarity across the channel. However, alongside a need for better homogeneity, it may also be desirable to force near grid turbulence across a number of length scales, as with a fractal grid geometry.

A combined-fractal design has been created by layering square-fractal and cross-fractal elements, with the addition of one large cross (Figure 4.6). There are

a number of advantages to the cross-fractal grid. With an additional iteration, this introduces an extra length scale. Furthermore, small elements along the perimeter in the cross-fractal design help to break up large jets produced by the square-fractal grid. The new combined-fractal design has a perimeter increase of $\sim 12\%$ over the square-fractal grid.

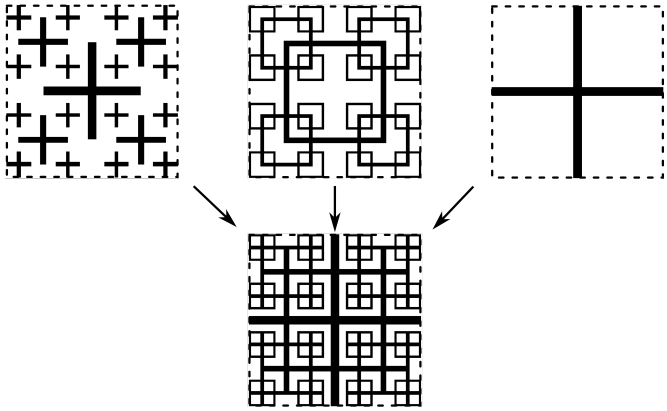

Figure 4.6: Layering cross-fractal and square-fractal elements to generate the combined-fractal grid, with the addition of one large cross to block the wake centreline.

Four grid geometries have been generated and superimposed onto the inlet patch as a blockage (Figure 4.7). Each grid has been designed to obstruct the centreline, allowing a comparative study to be made on centreline statistics. The regular grid is conventional in design, constructed by taking a lattice of bars with constant thickness and spacing. The multiscale grid is constructed from bars of two separate diameters and spacings. The fractal design in this study combines a square-fractal grid of 3 iterations, with two central bars arranged in a cross, similar to the design of Hearst and Lavoie (2014). It is ensured that the fractal design has $D_f = 2.0$. All four grids have solidarity of $\sigma = 44\%$, matching the grid inlet study of Blackmore et al. (2013), and experimental study of Krogstad and Davidson (2012). A summary of grid-based length scales are presented in Table 4.2. In Figure 4.9, contours of velocity and the mesh structure at the inlet patch are displayed for each grid design. A mesh independence study is conducted on the combined-fractal grid to ensure the chosen computational mesh sufficiently

resolves the flow field. The combined-fractal grid has been used because it is expected to generate the smallest scales of turbulence, and will therefore require the most mesh refinement. Details of the mesh independence study are provided in Appendix B.

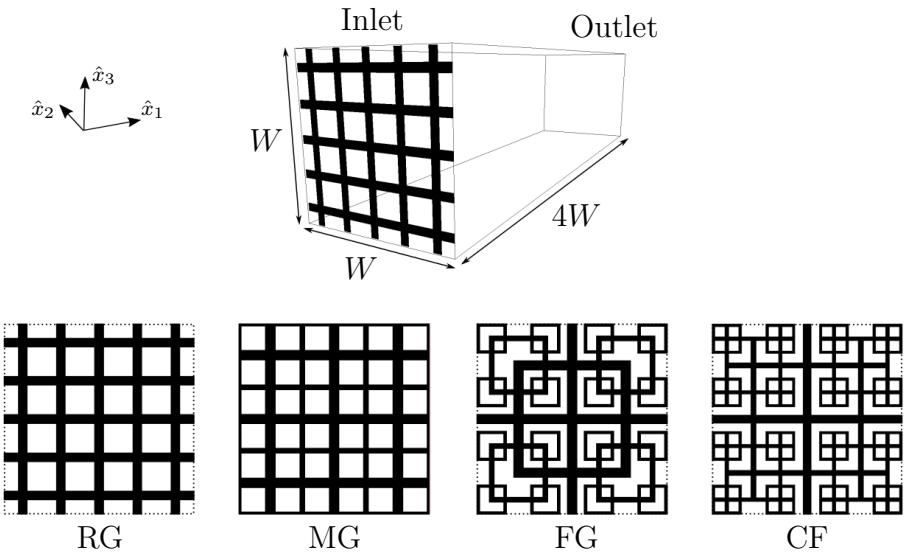

Figure 4.7: Top: domain size and Cartesian coordinate system orientation. Bottom: grid inlet configurations of present study for the regular (RG), multiscale (MG), square-fractal (FG), and combined-fractal (CF) grids.

Homogeneity for each grid design is considered by analysing the solidarity distribution across the inlet patch. To describe this graphically, a square with side lengths L_B is centred in the middle of the inlet patch and superimposed over the grid geometry. The area of the square is increased, and solidarity is recorded at each increment. Solidarity distributions found in Figure 4.8 highlight two key points. There are two fixed points which are constant across the grids. One at $L_\mathrm{B}/W = 0$, because the centreline of each grid is blocked, and another at $L_\mathrm{B}/W = 1$ where $\sigma = 44\%$ is recovered. However, there is freedom between these two fixed points, and it can be seen that the combined-fractal grid quickly approaches $\sigma = 44\%$ and remains relatively constant. The combined-fractal design differs from the typical fractal design because it moves blockages towards the

	Regular (RG)	Multiscale (MG)	Square-fractal (FG)	Combined-fractal (CF)
L_i (mm)	-	-	67.5, 33.8, 16.9	67.5, 33.8, 16.9
t_i (mm)	6.0	6.5, 3.5	6.1, 3.3, 1.8	5.6, 3.9, 2.6, 1.8
M_i (mm)	24.0	40.0, 20.0	-	-
P (m)	1.80	2.16	3.52	3.98
M_{eff} (mm)	23.9	20.0	12.2	10.8
x_* (m)	0.10	0.25	0.75	0.81
Re_0	5000	5437	5116	4684

Table 4.2: Grid-based length scales. All grids have fixed inflow velocity $U_{\text{in}} = 1\,\text{m/s}$ and solidarity $\sigma = 44\%$.

perimeter. This is expected to result in better homogeneity across the x_2-x_3 plane.

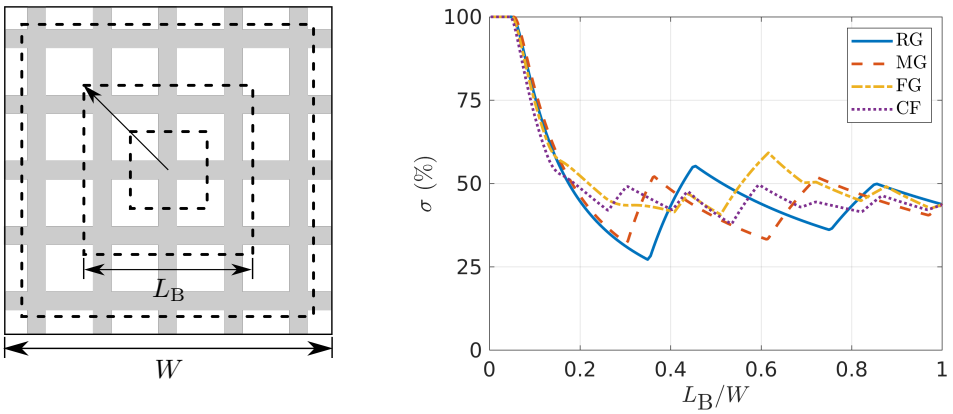

Figure 4.8: Solidarity distribution across the inlet plane. For a given grid, an imaginary box with side length L_B is drawn in the centre (left). As the box expands outwards, solidarity is recorded at each L_B (right).

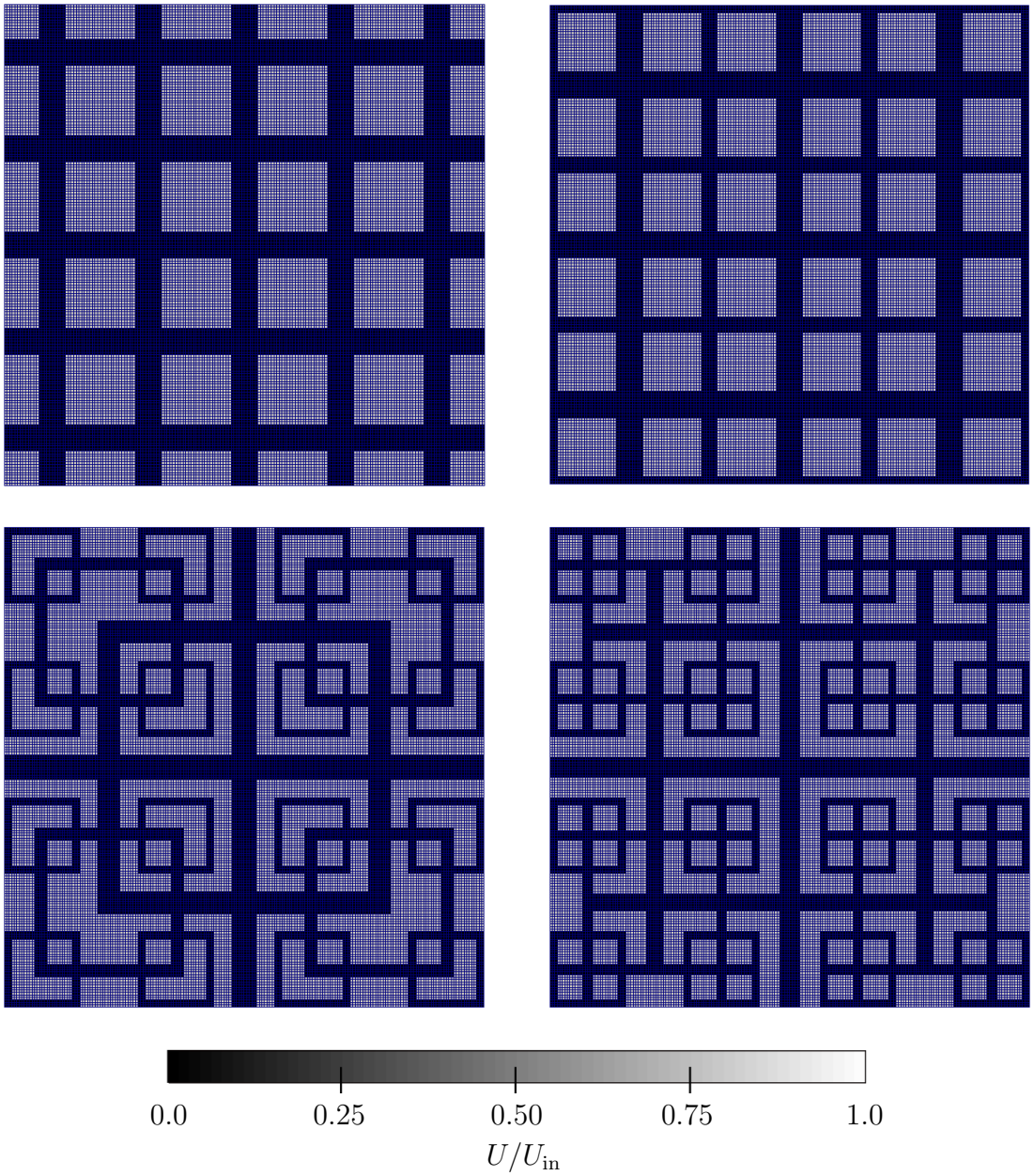

Figure 4.9: Mesh distribution and velocity at the inlet patch of each grid design.

4.4 Flow homogeneity

Figure 4.10 displays position of sample lines in the domain. Velocity is sampled along the domain centreline and at fixed downstream positions spanning across the channel. The majority of grid turbulence studies only report centreline development of turbulence. However, in order to assess flow homogeneity, it is also required to sample across the channel. A total of 4 downstream positions are recorded at $x_1/W = 1, 2, 3, 4$.

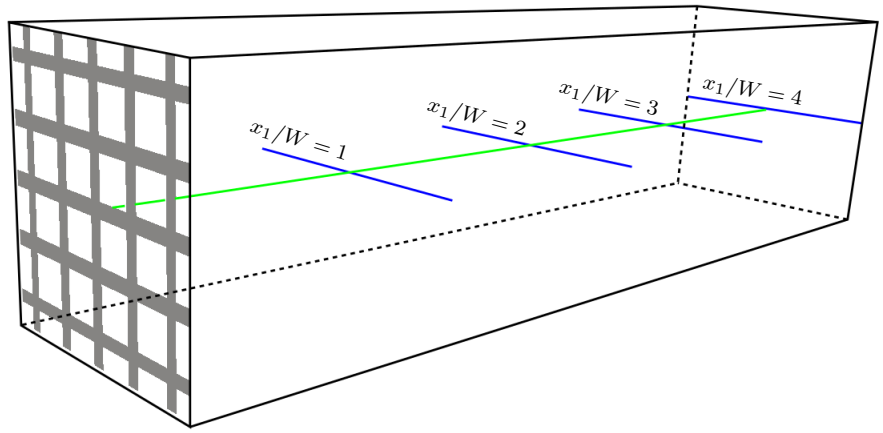

Figure 4.10: Location of probes across the channel at 4 separate downstream locations from which velocity is sampled.

4.4.1 Streamwise turbulence development

Figure 4.11 displays instantaneous contours of velocity magnitude, normalised by the inlet velocity, on the two-dimensional slice defined by $x_2 = 0$. A vertical slice at $x_2 = 0$ is taken to assess the impact of the centre cross, which is common to all 4 grids. Although the centre plane of $x_2 = 0$ sits behind a vertical bar for all grid designs, a different flow field is generated due to the neighbouring jet and bar wakes. A characteristic of the regular grid is that each bar wake is identical and equally spaced. Therefore, the turbulence produced is more predictable. However, with the multiscale and fractal grids, it is not immediately obvious at which

downstream position bar wakes will interact, if at all. For example, it can be seen in Figure 4.11 that, although both fractal grids have a similar construction along the line $x_1 = x_2 = 0$, the middle cross is more dominate in the combined-fractal grid case.

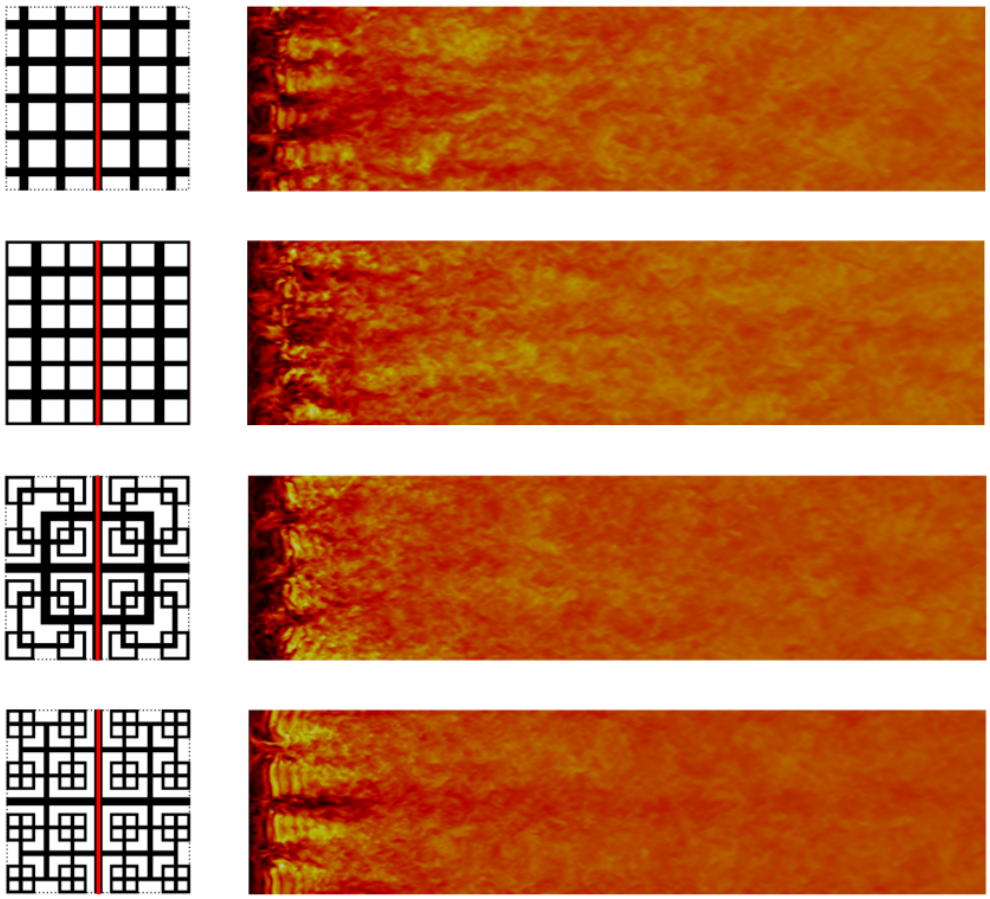

Figure 4.11: Contours of instantaneous velocity magnitude $|\boldsymbol{U}|/U_{\text{in}}$ along the plane $x_2 = 0$ (red line). Flow is from left to right.

Figure 4.12 displays instantaneous contours of velocity magnitude, normalised by the inlet velocity, on the two-dimensional slice defined by $x_2 = -33.75\,\text{mm}$. A slice at $x_2 = -33.75\,\text{mm}$ is sampled because this runs through the largest fractal iteration, common to the fractal-type grids, and also provides information on the development of the bar wakes in the regular and multiscale cases. Figure 4.12 indicates that the regular grid produces orderly bar wakes that break up as they

travel downstream. This is not seen in the fractal grid- the second square-fractal iteration creates a persistent jet.

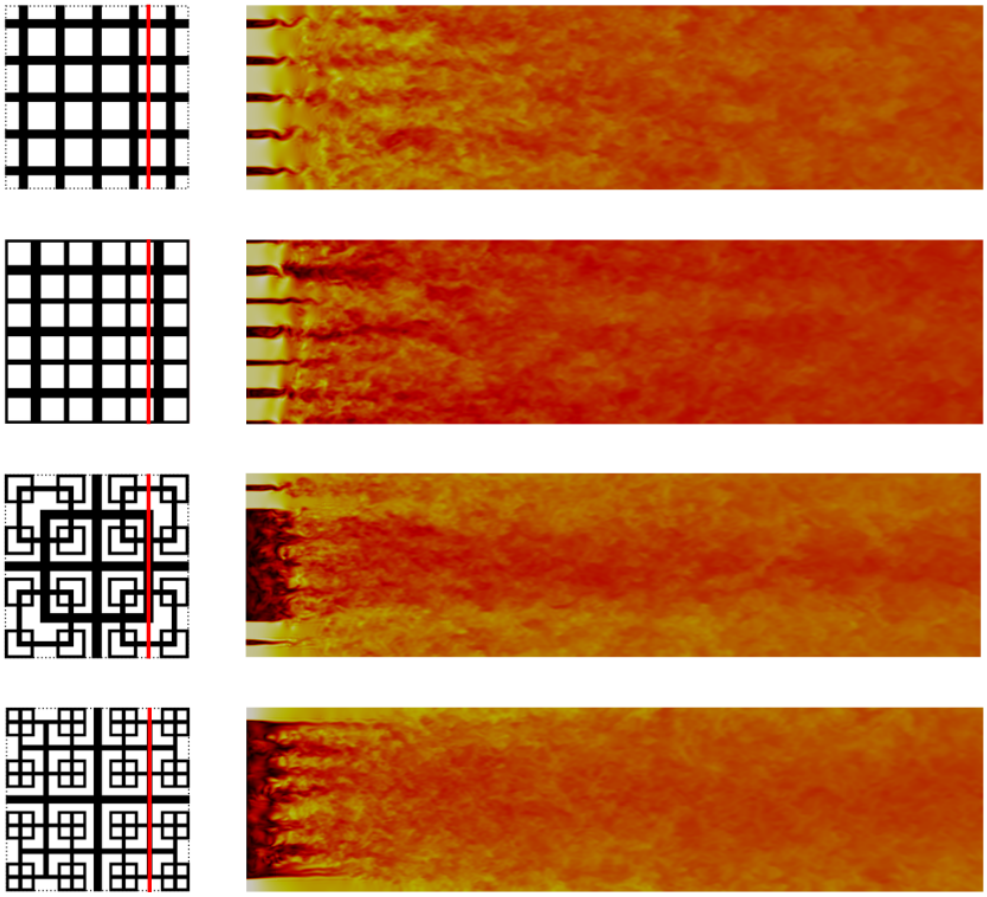

Figure 4.12: Contours of instantaneous velocity magnitude $|\boldsymbol{U}|/U_{\text{in}}$ along the plane $x_2 = -33.75\,\text{mm}$ (red line). Flow is from left to right.

Figure 4.13 provides information on the wake created in the corners and along the perimeter. A diagonal slice $x_2 = x_3$ is taken to give a better understanding of flow around the perimeter, which is an important design factor in the combined-fractal grid. Behind the fractal grid FG, a total of 15 wakes can be counted in the diagonal plane. As they travel downstream, some of the wakes join together, and 5 distinct wakes are then observed. These have been marked on Figure 4.13 for clarity. A green dot is placed at a point on the diagonal where a jet emerges from a gap in the second fractal iteration, which can be seen to travel downstream without breaking up from interaction with neighbouring wakes. Such high speed

streaks are not observed in the combined-fractal case, although it can be seen once again that the centre cross produces a wake which persists into the domain.

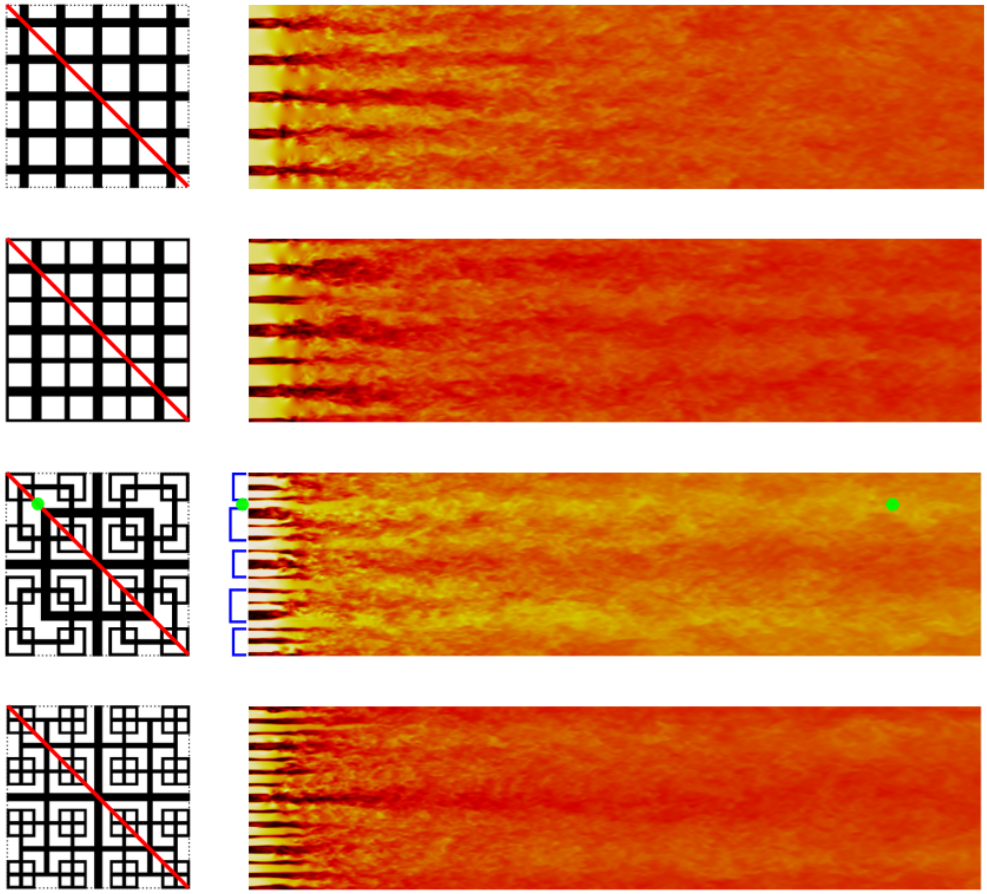

Figure 4.13: Contours of instantaneous velocity magnitude $|\boldsymbol{U}|/U_{\text{in}}$ along the diagonal slice defined by $x_2 = x_3$ (red line). Points of interest have been marked on the fractal case using green dots and blue braces. Flow is from left to right.

Figure 4.14 presents time-averaged velocity along the centreline for each grid design. The centreline behind each grid is blocked by a central bar, therefore a recirculation region is observed near grid. The cross-fractal grid produces the smallest recirculation region, and recovers towards its asymptotic value quicker. When the streamwise coordinate is nondimensionalized by the width of the largest bar t_0, profiles collapse slightly better. This is reasonable, because the middle cross which blocks the centreline of each grid is constructed by bars of width t_0. However, there are more factors to the centreline velocity deficit than t_0, because wakes created from neighbouring bars interact at different downstream positions, which was demonstrated in Figure 4.11. Figure 4.14 indicates how jets created around the middle cross interact and feed into the centreline. This has implications for flow homogeneity, because it is sub-optimal to create large wakes behind bars which are not broken down by perimeter jets and wakes.

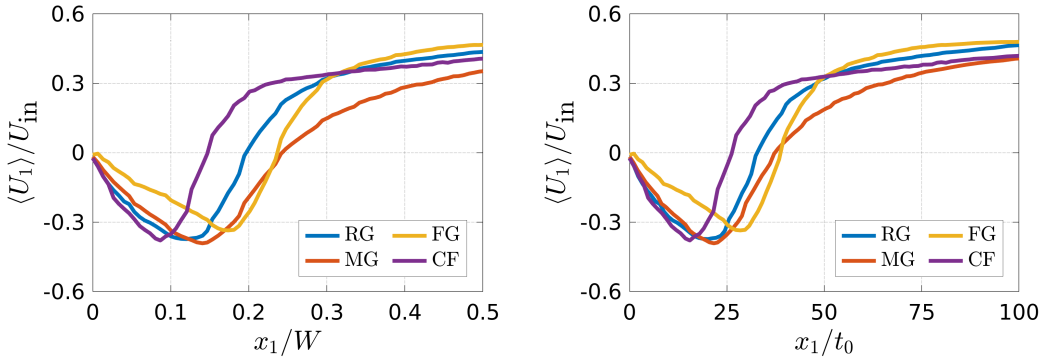

Figure 4.14: Time-averaged streamwise velocity along the domain centreline with different normalisation of downstream coordinate x_1.

Figure 4.15 displays centreline development of the root-mean-square (r.m.s) streamwise velocity fluctuations $u_{\text{rms}} = \sqrt{\langle u_1^2 \rangle}$, normalised by U_∞. Included are the wind tunnel data of Nagata et al. (2017) from their *RG3* grid at $Re_0 = 5900$, which bears closest resemblance to the regular grid design of the current study. A reasonable agreement is found between the regular grid RG and the experimental results of Nagata et al. (2017), strengthening the validity of the projected inlet method for creating realistic grid turbulence. However, decay of u_{rms} is considerably different for the other grids. Behind the MG, FG, and CF grids at downstream position $x_1/(L_0/2) \approx 1$, u_{rms} begins to decay quickly. This

is in contrast to the profile of RG, where the decay at $x_1/(L_0/2) \approx 1$ is more gradual.

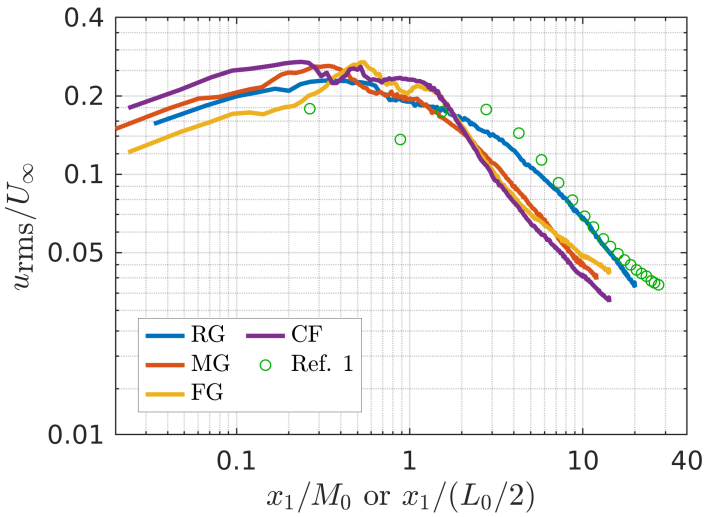

Figure 4.15: Development of streamwise r.m.s velocity along the centreline. Ref. 1: *RG3* of Nagata et al. (2017).

Figure 4.16 presents the results of fitting the power law of (4.4) to the decay of $\langle u_1^2 \rangle$. A marked difference in the shape of n is observed behind the two fractal grids. Similar to the behaviour seen in Figure 4.15, the decay exponent recorded behind the RG and MG grids steadily increases to $n \approx 2$ and $n \approx 1.6$, respectively. Behind the FG grid, the decay exponent steadily increases to $n \approx 1.8$, after which it then drops to $n \approx 1$ and flattens out. A prolonged period of $n \approx 1.8$ is observed behind the CF grid. Higher decay exponents have been the focus of multiple studies e.g. Hurst and Vassilicos (2007); Seoud and Vassilicos (2007); Krogstad and Davidson (2012); Hearst and Lavoie (2014), and the current results reinforce some of those findings- multiscale-generated turbulence displays non-classical decay behaviour.

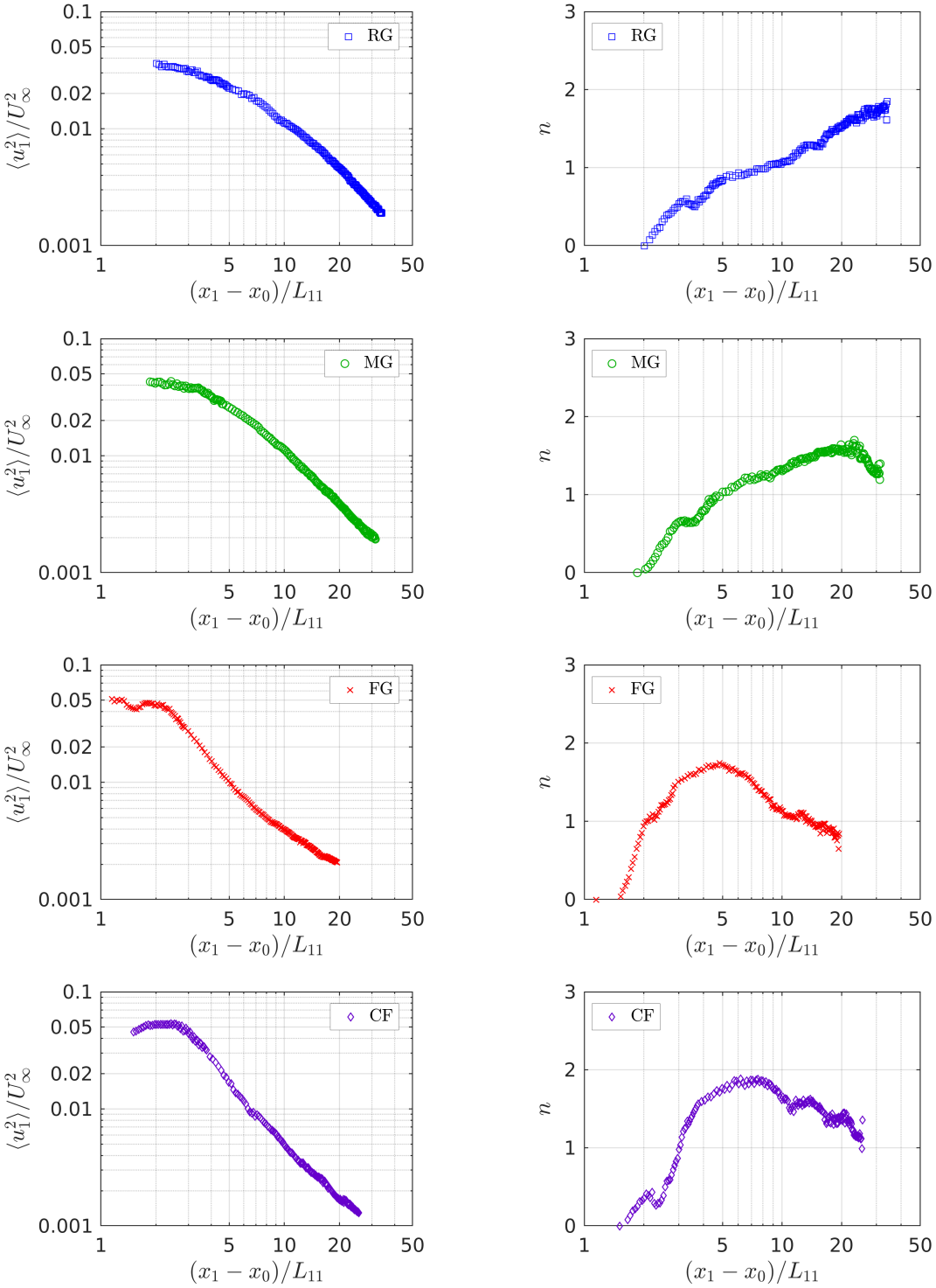

Figure 4.16: Decay characteristics along the centreline of each grid. Decay exponent n is calculated using (4.4).

Figure 4.17 displays the downstream development of $\langle q^2 \rangle / 3 \langle u_1^2 \rangle$ from (4.5). Immediately behind each grid for $x_1/W < 1$, the flow is highly anisotropic. This is the turbulence production region. The flow then recovers further downstream. An asymptotic value of 0.9 is achieved for the regular, multiscale, and combined-fractal grids. However, the fractal grid produces an asymptotic value of 0.8, suggesting the turbulence generated behind the fractal grid is more anisotropic than the other grids.

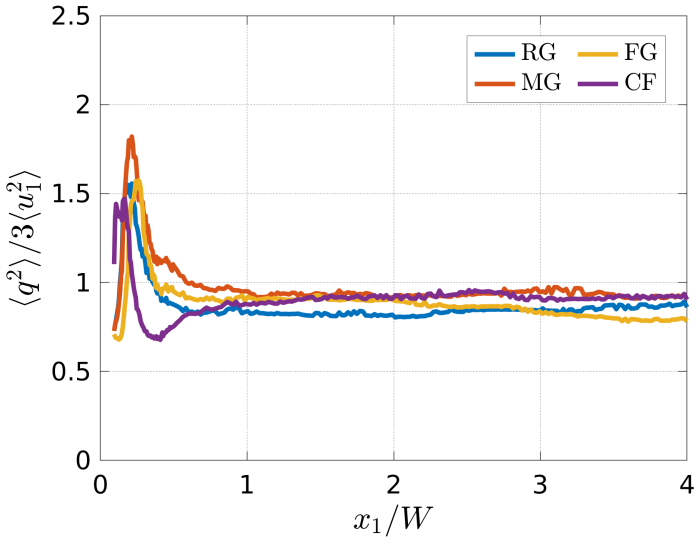

Figure 4.17: Streamwise development of $\langle q^2 \rangle / 3 \langle u_1^2 \rangle$ along the domain centreline.

Centreline skewness and flatness are plotted in Figure 4.18. The regular, multiscale, and combined-fractal grids approach the expected values of $S_u = 0$ and $F_u = 3$ for HIT. Slightly elevated S_u and F_u are reported from the fractal grid.

Figure 4.19 displays the Taylor microscale (4.7). Nagata et al. (2017) found profiles of λ/L_0 to collapse when plotted against x_1/x_*. However, in the current study, profiles of λ collapse when nondimensionalized by t_0 and plotted against x_1/M_0 or $x_1/(L_0/2)$. Also plotted is the fit of $\lambda \propto x_1^{0.5}$ (Valente and Vassilicos, 2011; Hearst and Lavoie, 2014; Nagata et al., 2017). The Taylor microscale is some intermediate length scale which lies between the integral length scale L_{11}, and the Kolmogorov microscale η (Pope, 2001). However, it is not immediately obvious how λ is set. The results displayed in Figure 4.19 suggest that the middle cross

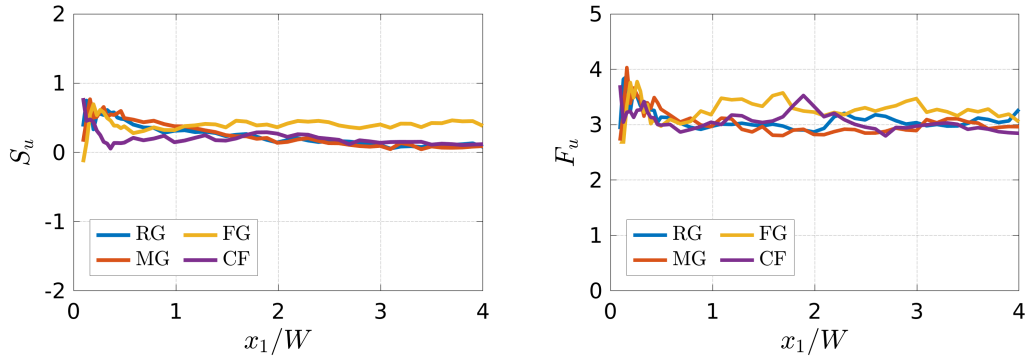

Figure 4.18: Skewness and flatness profiles along the domain centreline.

has a profound affect on the generation of λ, because the profiles are collapsed when nondimensionalized by t_0.

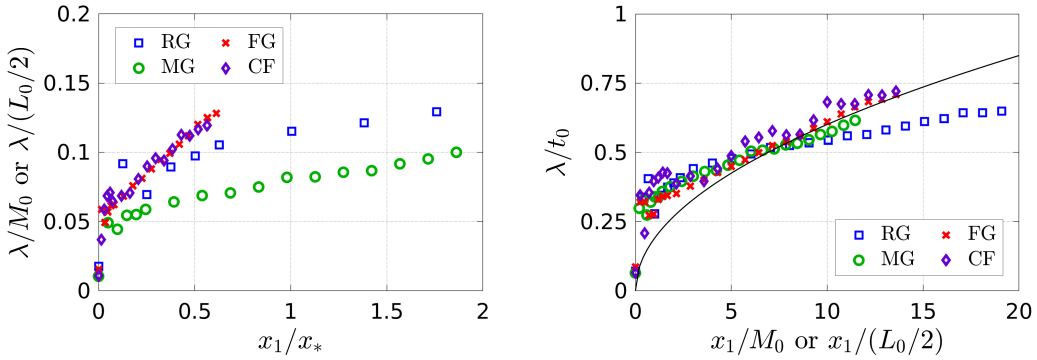

Figure 4.19: Centreline profiles of the Taylor microscale λ.

The local Reynolds number $Re_\lambda = u_{\text{rms}}\lambda/\nu$, defined using the streamwise Taylor microscale λ is displayed in Figure 4.20. Each grid produces a similar level of turbulence near grid. This is evidence that fractal-type grids produce elevated levels of turbulence (Hurst and Vassilicos, 2007), because in the current study, Re_0 is considerably lower for the combined-fractal case. However, the streamwise development of Re_λ behind the fractal-type grids is different to that of the regular and multiscale grids. Behind the fractal grids, decay of Re_λ is abrupt, as observed in previous investigations e.g. Hurst and Vassilicos (2007); Mazellier and Vassilicos (2010); Gomes-Fernandes et al. (2012); Nagata et al. (2013); Vassilicos (2015);

Nagata et al. (2017). Further downstream and it can be seen that the fractal grid asymptotes to a similar Re_λ as in the regular and multiscale grid cases. This is not seen for CF, which instead continues to decay further, reaching a lower asymptotic value of Re_λ compared to other grids.

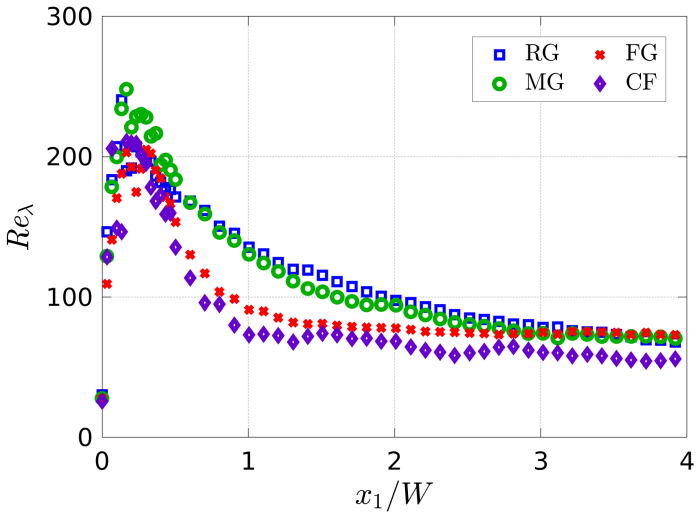

Figure 4.20: Streamwise development of local turbulent Reynolds number Re_λ.

Figure 4.21 displays the centreline development of the integral length scale L_{11}. Included are the data of Nagata et al. (2017) from their regular grid named *RG3*, ran at Reynolds number $Re_0 = 5900$ and with solidarity $\sigma = 25\%$. Also plotted are the data from the projected inlet study of Blackmore et al. (2013) where $Re_0 = 36000$ and $\sigma = 44\%$. Profiles of L_{11} are seen to collapse better when nondimensionalized against t_0. Although the studies have different Re_0 and σ, a close agreement on how the integral length scale grows as a function of downstream position can be seen.

A line of best fit is added to the data to find the growth rate of integral length scale

$$L_{11} = A\left(\frac{x_1 - x_0}{M}\right)^m \quad , \tag{4.15}$$

where A is a constant, x_0 is the virtual origin, and m is the length scale growth rate. For the regular grid tested in the current LES, the growth rate estimated from (4.15) is $m = 0.39$. This compares well to experimental results: $m = 0.38$

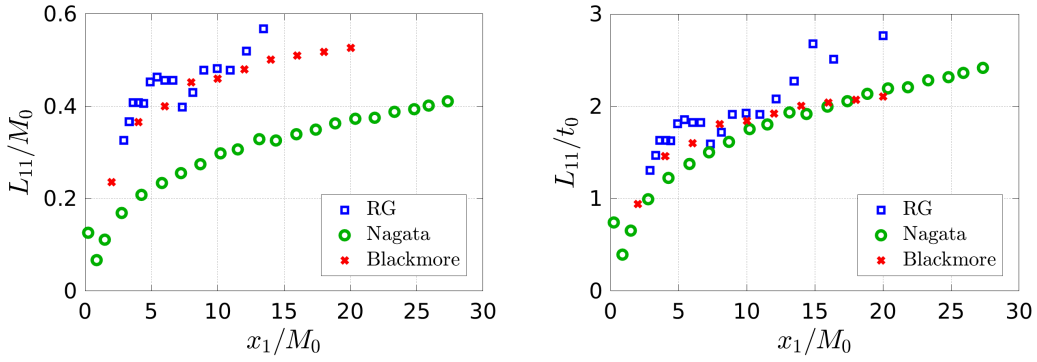

Figure 4.21: Growth of the longitudinal integral length scale behind regular grids. RG is the regular grid in the current LES. Reference data of Nagata et al. (2017) at $Re_0 = 5900$ and $\sigma = 0.25$. Triple inlet of Blackmore et al. (2013) at $Re_0 = 9000$ with $\sigma = 0.44$.

(Nagata et al., 2017), $m = 0.40$ (Krogstad and Davidson, 2011). However, fitting (4.15) to the data of Blackmore et al. (2013) yields $m = 0.29$. These results are in close agreement to the power-law energy decay prediction of Saffman turbulence which yields $L_{11} \propto (x_1 - x_0)^{0.4}$, for a virtual origin $x_0 = 0$.

Figure 4.22 displays the growth of the integral length scale along the centreline for each grid. A reference line of $L_{11} \propto x_1^{0.4}$ has been superimposed onto the plot. The fractal grid FG produces the largest L_{11} along the centreline. A likely cause of such a large L_{11} along the centreline of the FG case is the dominant flow dynamics generated by the middle cross. In the CF case, structures from the central cross are less dominant. Different length scales have been used to nondimensionalise the integral length scale for each grid, but no grid length scale appears to collapse the profiles of L_{11}. It is concluded that it is not possible to predict the integral length scale produced from a grid by just considering certain grid based length scales, such as width of largest bar t_0. This may be true close to the grid, where the wake from each bar is pronounced, but the streamwise development of L_{11} depends on the interaction of surrounding jets and wakes. For example, directly behind each grid it can seen that $L_{11}/t_0 \approx 1$, so the integral length scale in the near wake is heavily influenced by t_0. However, despite the predictability of L_{11}/t_0 directly behind the grid, growth of the integral length scale depends on the structures

generated by neighbouring wakes.

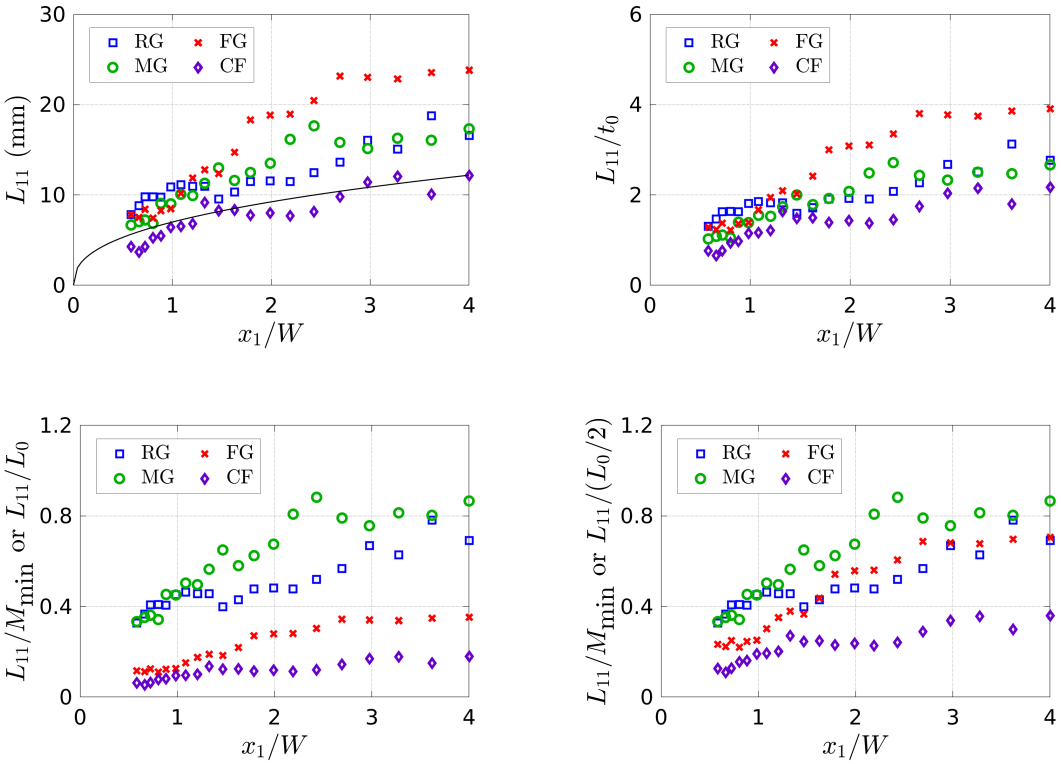

Figure 4.22: Centreline development of the longitudinal integral length scale. A solid line of $L_{11} \propto x_1^{0.4}$ corresponding to Saffman turbulence is included on the first plot.

4.4.2 Cross-channel homogeneity

Skewness and flatness across the channel at downstream position $x_1/W = 2$ are plotted in Figure 4.23. Similar to profiles along the centreline, i.e. Figure 4.18, skewness and flatness across the channel approach their HIT expected values of $S_u = 0$ and $F_u = 3$.

Figure 4.24 presents time-averaged profiles of velocity magnitude $\langle |\boldsymbol{U}| \rangle = \langle U_i U_i \rangle^{1/2}$, nondimensionalized by the inlet velocity, across the channel at 4 streamwise positions. At $x_1/W = 1$, the grid shadow is present across each grid. A wake is visible behind each of the 5 bars in the RG case. However in the MG case, only the largest bars leave a noticeable wake shadow. Profiles behind FG are

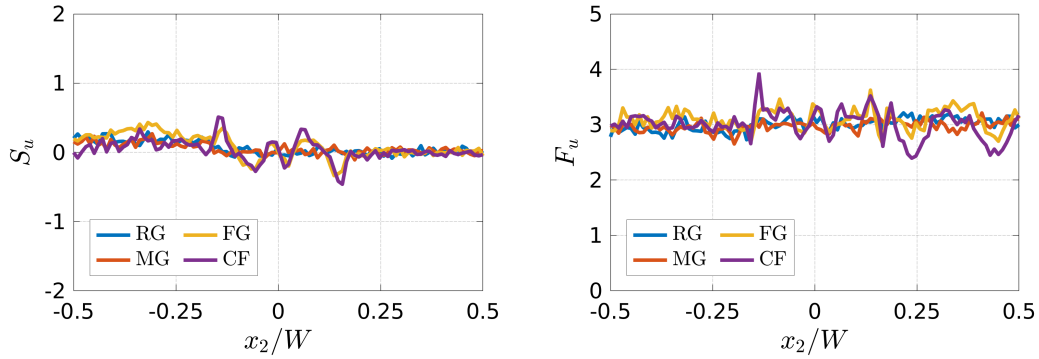

Figure 4.23: Skewness and flatness profiles in the crossflow direction x_2, at $x_1/W = 2$.

reasonably flat when compared to the CF grid. At $x_1/W = 4$, all 4 profiles have flattened, but velocity behind the regular grid is considerably higher than the other grids. This is despite all grids sharing the same solidarity $\sigma = 44\%$, and inflow velocity $U_{\text{in}} = 1\,\text{m/s}$.

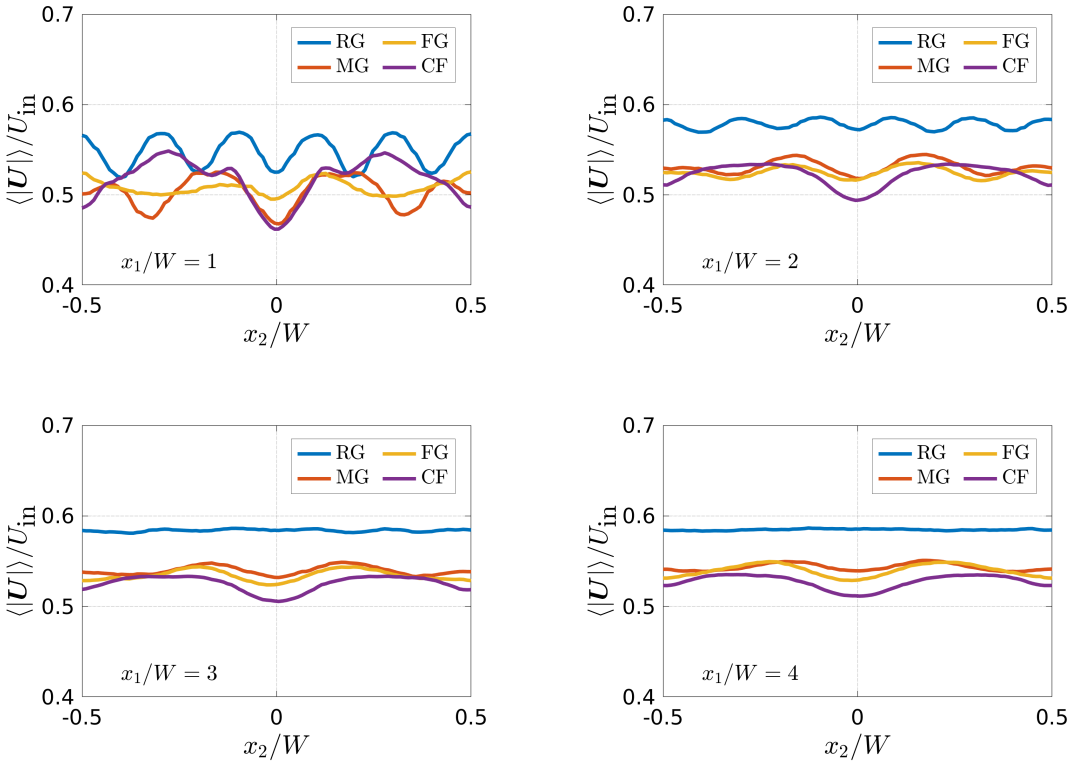

Figure 4.24: Profiles of time-averaged nondimensional velocity magnitude $|\boldsymbol{U}|$ across the channel at streamwise locations $x_1/W = 1, 2, 3, 4$.

Figure 4.25 presents time-averaged velocity magnitude $U = \langle U_i U_i \rangle^{1/2}$ for a slice at downstream position $x_1/W = 2$, nondimensionalized by the centreline value. It is immediately clear that jets generated from the regular grid are broken up, and the ratio U/U_c is reasonably constant across the slice. Jets have been generated by the largest iteration of the multiscale grid, and not completely broken up by the second iteration of smaller bars. In the fractal grid case, the middle cross has had a profound affect on the velocity field, dominating the smaller iterations placed around the perimeter. This is directly compared to the combined-fractal grid, where it can be seen that the wind shadow of the middle cross has spread more. This is encouraging for the combined-fractal grid design- jet break up at the perimeter can be controlled by spreading solidarity away from the centre.

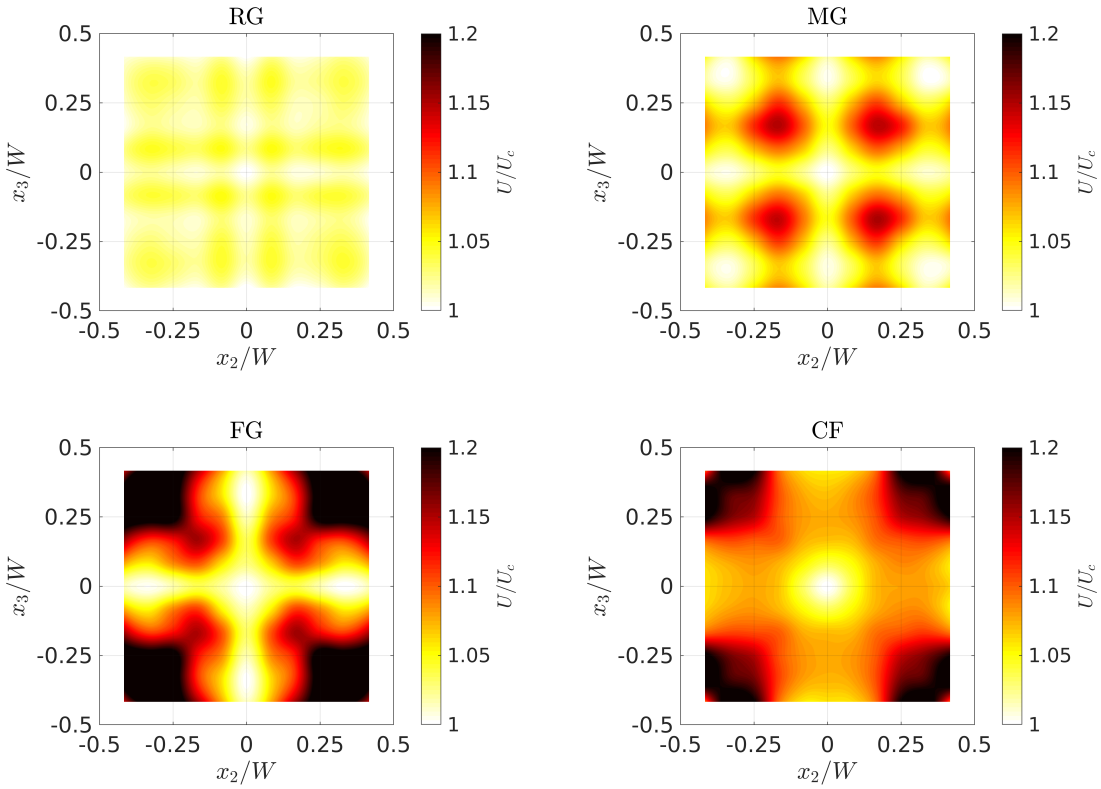

Figure 4.25: Time-averaged streamwise velocity for a two-dimensional slice at $x_1/W = 2$.

Figure 4.26 presents time-averaged turbulence intensity $\langle u_i u_i \rangle/2$, recorded on the x_2-x_3 plane at downstream position $x_1/W = 2$. Contours have been nondi-

mensionalized by the centreline value. There is little indication of the wind shadow in profiles of turbulence intensity for the regular grid. In the multiscale wake, turbulence intensity is lowest in the gaps between the largest iteration, i.e. the locations where the smallest bars cross. For the fractal grid FG, turbulence intensity is highest behind the 4 corners of the largest fractal square. This may be a result of vorticity clustering, therefore indicating poor homogeneity. Behind the combined-fractal grid, turbulence intensity is reasonably uniform, apart from at the very perimeter of each corner.

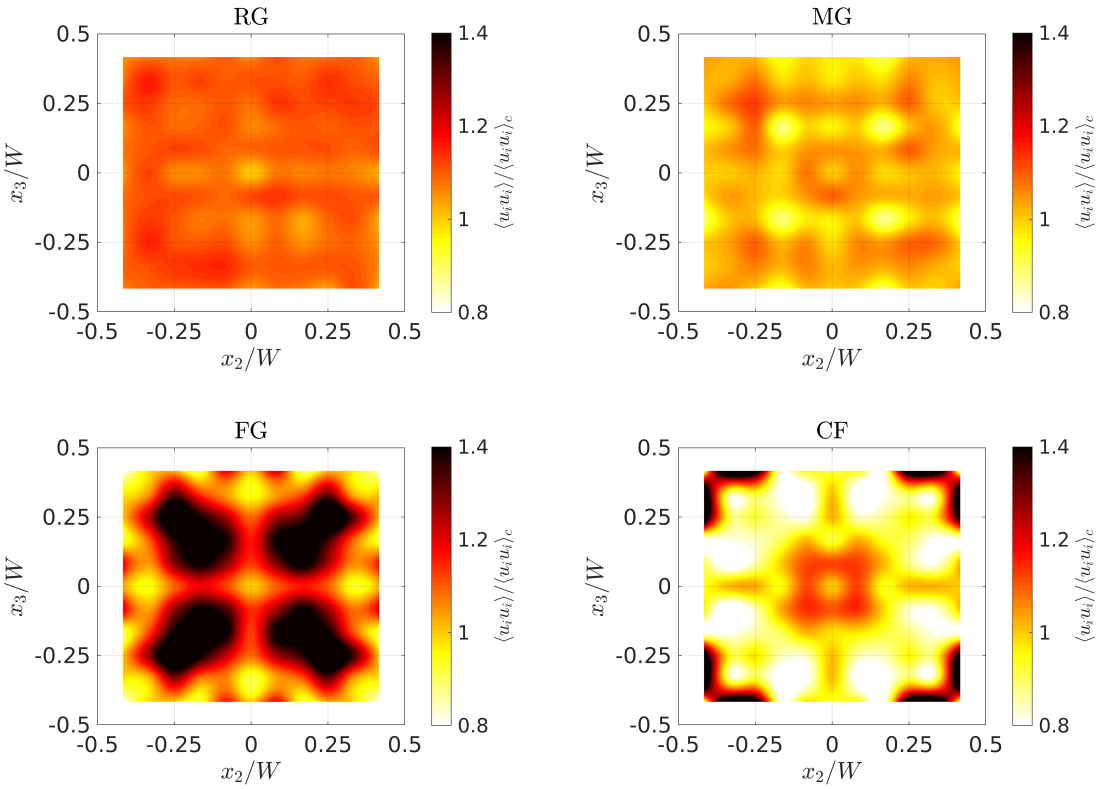

Figure 4.26: Time-averaged turbulence intensity for a two-dimensional slice at $x_1/W = 2$.

Figure 4.27 presents the integral length scale L_{11} at a number of points on the x_2-x_3 plane, located at downstream position $x_1/W = 2$. Unlike previous wind tunnel experiments where L_{11} is sampled along the centreline, Figure 4.27 provides more information on the turbulent scales generated by each grid bar. Length scales produced by the regular and multiscale grid are more uniform on

the slice, which is to be expected, because the solidarity is sufficiently spread across the inlet patch. Clearly a major factor to the turbulence produced behind the fractal-type grids is the middle cross, which dominates the integral length scales produced.

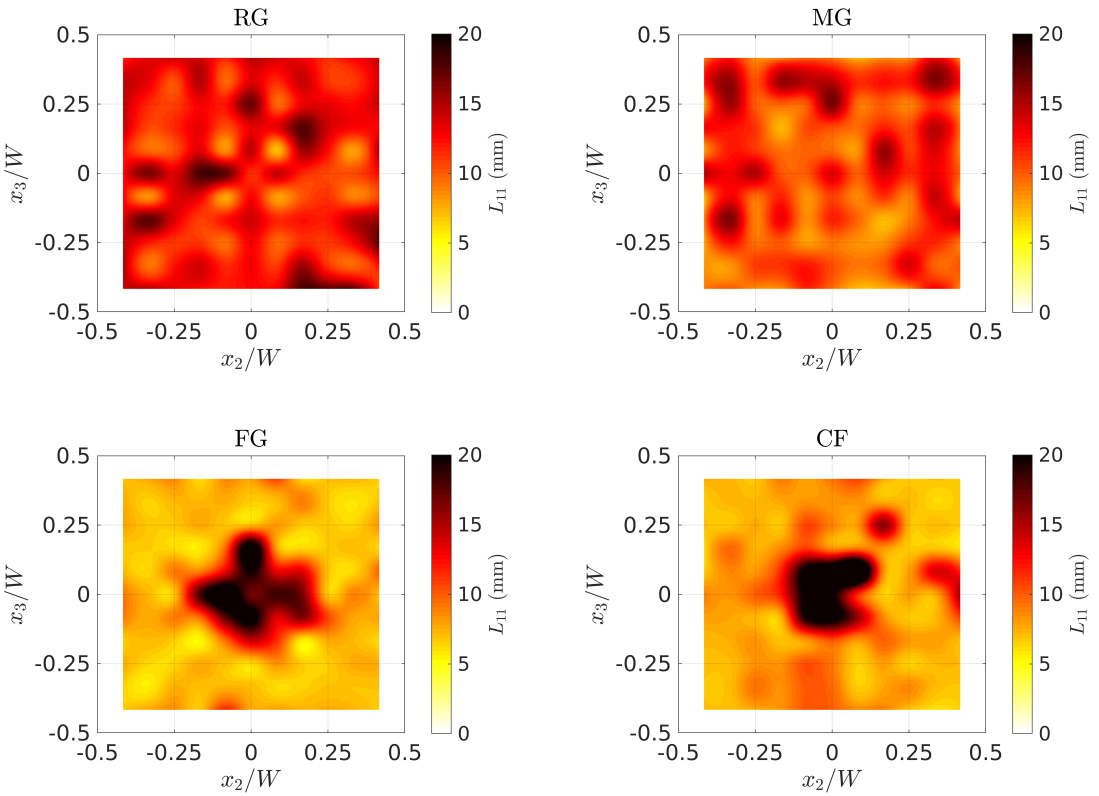

Figure 4.27: Integral length scale L_{11} for a two-dimensional slice at $x_1/W = 2$.

Figure 4.28 displays the relationship between the integral length scale and Taylor microscale. Data is sampled on the x_2-x_3 plane, located at downstream position $x_1/W = 2$. Figure 4.28 presents additional information on the length scales generated by each grid, namely how the relationship between L_{11} and λ varies across the full grid element. The fractal grid FG has produced turbulence where the ratio of integral length scale to Taylor microscale is approximately constant, and there appears to be a lower bound at $L_{11}/\lambda = 2$. There is some deviation away from $L_{11}/\lambda = 2$ where the central cross produces large integral length scales of turbulence. This is especially true for the fractal cases FG and CF. Non-equilibrium turbulence has been attributed to regions where the ratio

L_{11}/λ is constant (Vassilicos, 2015). This has only been studied previously as a function of streamwise position, i.e. following a parcel of decaying turbulence. But here data is collected from a fixed streamwise position, so the turbulence isn't decaying with respect to position. Figure 4.28 highlights that only collecting data along the centreline can be misleading, because statistics vary greatly in the x_2-x_3 plane, especially for fractal grid designs.

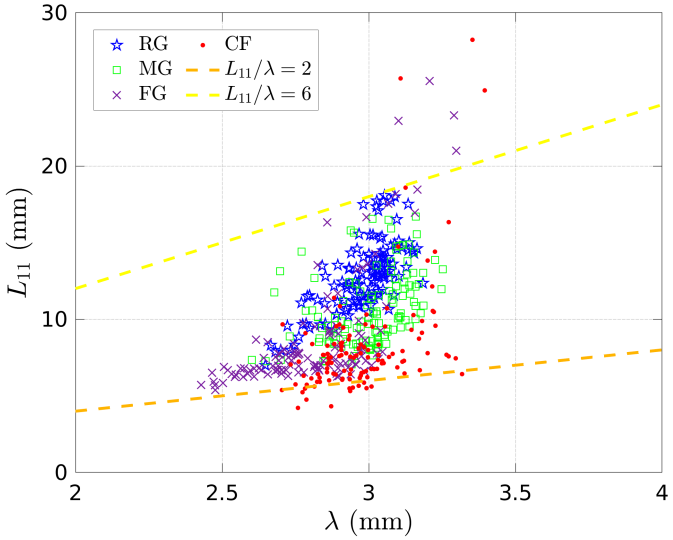

Figure 4.28: Scatter plot of integral length scale L_{11} versus Taylor microscale λ for each grid inlet design. Included are lines of $L_{11}/\lambda = 2, 6$.

4.4.3 Vorticity clustering

To identify structures and turbulence clustering behind each grid design, vorticity magnitude $\omega \equiv ||\boldsymbol{\omega}|| = \sqrt{\omega_i \omega_i}$ is normalised at each downstream position $x_1 = x'$ by its maximum value at that downstream position in the x_2-x_3 plane, such that

$$\breve{\omega}(x_1 = x') = \frac{\omega(x_1 = x')}{\max\{\omega(x_1 = x')\}} \quad . \tag{4.16}$$

By the same method, the normalised streamwise component of vorticity $\breve{\omega}_x$ is computed. It is necessary to normalise vorticity for each downstream position in order to remove the effects of decay (Laizet and Vassilicos, 2011). Without

normalisation, only structures directly behind the grid where vorticity is highest would be visible.

Figure 4.29 presents isosurfaces of instantaneous vorticity magnitude generated by the regular, multiscale, and fractal-type grids. Directly behind each grid, vorticity structures are elongated in the streamwise direction. Larger streaks are present behind the regular and multiscale grid, with the combined-fractal grid producing the smallest streaks. Clumping in the square-fractal and combined-fractal grids is observed, consistent with the findings of Laizet and Vassilicos (2011), who found fractal grids produce clustering in the vorticity field. Clustering is believed to originate from the varied development lengths of wakes behind fractal iterations. Larger structures are shed from the middle cross and take longer to interact with perimeter fractal iterations. In contrast to multiple wake development lengths, a regular grid produces jets which interact at a fixed downstream position.

Figure 4.30 presents a side view of the square-fractal and combined-fractal generated turbulence. Streamwise regions of interest have been labelled 1-4 to compare the turbulence development of each grid wake. In the near grid (region 1), the fractal grid FG produces streamwise elongated structures. In region 2, both grids produce a concentration of vorticity behind the large cross. Development of this centreline vorticity clustering is significantly different between the two grids. In region 3, vorticity along the centreline of the combined-fractal grid begins to equalise with vorticity around the perimeter. However, in the FG fractal case, a centreline streak of low vorticity is observed, which persists downstream.

Figures 4.29 and 4.30 highlight an important difference between the turbulence generated by regular, multiscale, square-fractal, and combined-fractal grids. Jets emerging from the regular and multiscale geometries are uniform across the inlet patch, which leads to a well defined transition between the production and decay regions. In the square-fractal and combined-fractal cases, jets are spread non-uniformly across the inlet patch, and therefore interaction occurs at a range of downstream positions. Figure 4.30 also highlights the importance of smaller fractal iterations surrounding the large centreline cross. In the square-fractal case, structures shed from the centre cross dominate smaller perimeter structures in

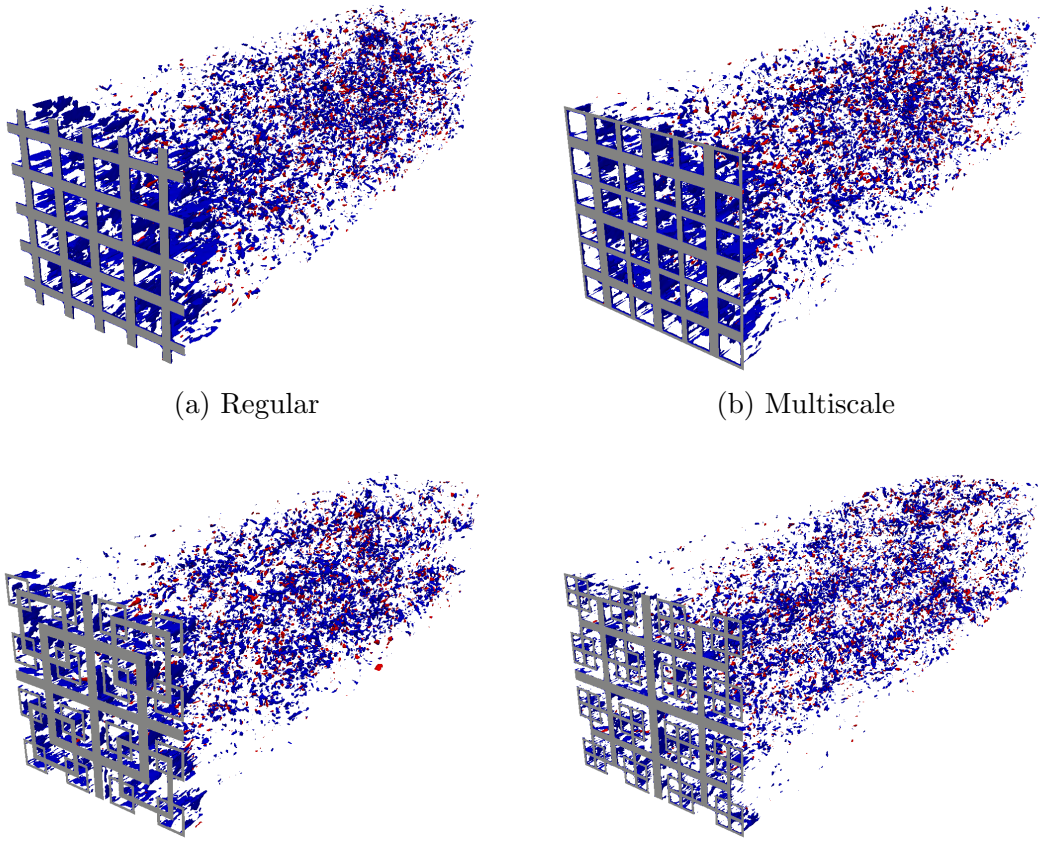

(a) Regular

(b) Multiscale

(c) Square-fractal.

(d) Combined-fractal.

Figure 4.29: Instantaneous vorticity isosurfaces in the wake of each grid. Blue: vorticity magnitude normalised by its maximum value at each streamwise position. Red: x-component of vorticity normalised by its maximum value at each streamwise position.

the near grid. At some point downstream, perimeter structures begin to dominate. In the combined-fractal case, centreline and perimeter structures are well balanced far downstream.

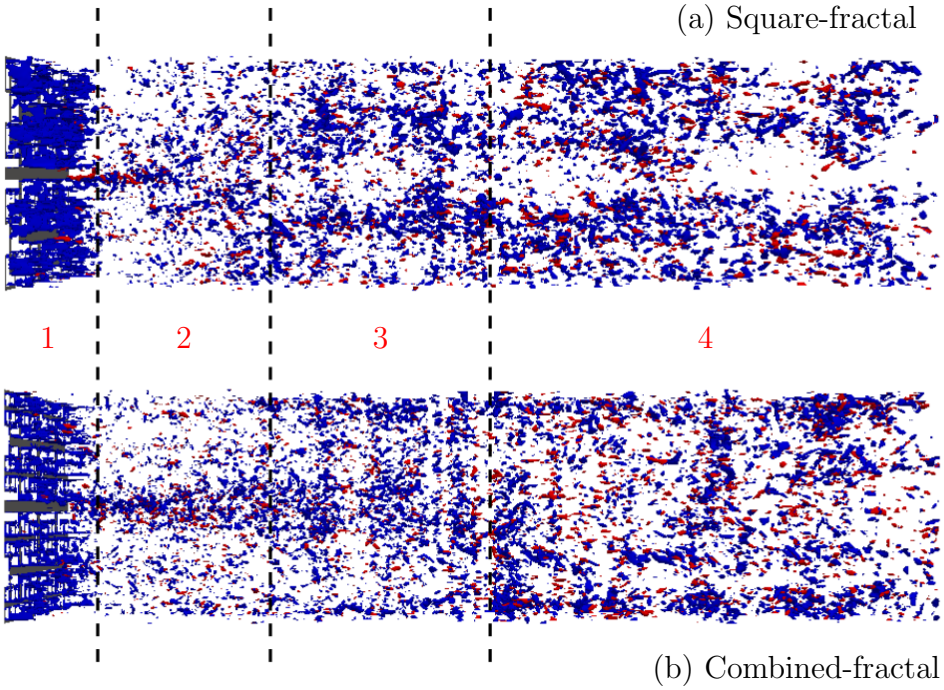

Figure 4.30: Side view of Figure 4.29 for the fractal-type grids. Regions of interest are labelled 1-4.

4.5 Non-equilibrium dissipation

4.5.1 Estimating dissipation

Calculation of the dissipation rate requires evaluation of spatial velocity gradients, which are difficult to obtain experimentally. A discussion on methods to calculate dissipation was provided in Chapter 2.1.1, but some of the points will be revisited here. The dissipation rate is given by (Hinze, 1975)

$$\varepsilon = \nu \Bigg[2\underbrace{\left\langle \left(\frac{\partial u}{\partial x}\right)^2 \right\rangle}_{1} + \underbrace{\left\langle \left(\frac{\partial v}{\partial x}\right)^2 \right\rangle}_{2} + \underbrace{\left\langle \left(\frac{\partial w}{\partial x}\right)^2 \right\rangle}_{3} + \underbrace{\left\langle \left(\frac{\partial u}{\partial y}\right)^2 \right\rangle}_{4} + 2\underbrace{\left\langle \left(\frac{\partial v}{\partial y}\right)^2 \right\rangle}_{5} + \underbrace{\left\langle \left(\frac{\partial w}{\partial y}\right)^2 \right\rangle}_{6} + \underbrace{\left\langle \left(\frac{\partial u}{\partial z}\right)^2 \right\rangle}_{7} + \underbrace{\left\langle \left(\frac{\partial v}{\partial z}\right)^2 \right\rangle}_{8} + 2\underbrace{\left\langle \left(\frac{\partial w}{\partial z}\right)^2 \right\rangle}_{9} + 2\underbrace{\left\langle \frac{\partial u}{\partial y}\frac{\partial v}{\partial x} \right\rangle}_{10} + 2\underbrace{\left\langle \frac{\partial u}{\partial z}\frac{\partial w}{\partial x} \right\rangle}_{11} + 2\underbrace{\left\langle \frac{\partial v}{\partial z}\frac{\partial w}{\partial y} \right\rangle}_{12} \Bigg] \quad . \tag{4.17}$$

Evaluating all 12 terms of (4.17) is possible in simulations, and therefore data is available right up to the grid. In the current simulations, the velocity gradient tensor is evaluated along the centreline during run time. For comparison, ε_{iso}, and ε_{xw} are also calculated by

$$\varepsilon_{\text{iso}} = 15\nu \left\langle \left(\frac{\partial u}{\partial x}\right)^2 \right\rangle \quad , \tag{4.18}$$

$$\varepsilon_{\text{xw}} = 3\nu \left[\left\langle \left(\frac{\partial u}{\partial x}\right)^2 \right\rangle + 2\left\langle \left(\frac{\partial v}{\partial x}\right)^2 \right\rangle \right] \quad . \tag{4.19}$$

Figure 4.31 presents the centreline development of ε_{iso} and ε_{xw}, nondimensionalized by the full dissipation ε. It is immediately apparent that ε_{xw} underestimates ε, and this is evident behind all 4 grids. Valente and Vassilicos (2012) reported a similar result, however the full dissipation was not available for comparison, and

measurements were only taken at a single point in the far field. Profiles of $\varepsilon_{\text{iso}}/\varepsilon$ approach a fixed value of approximately 0.89 for all cases. Neither ε_{iso} or ε_{xw} have been found to be a suitable candidate to estimate ε.

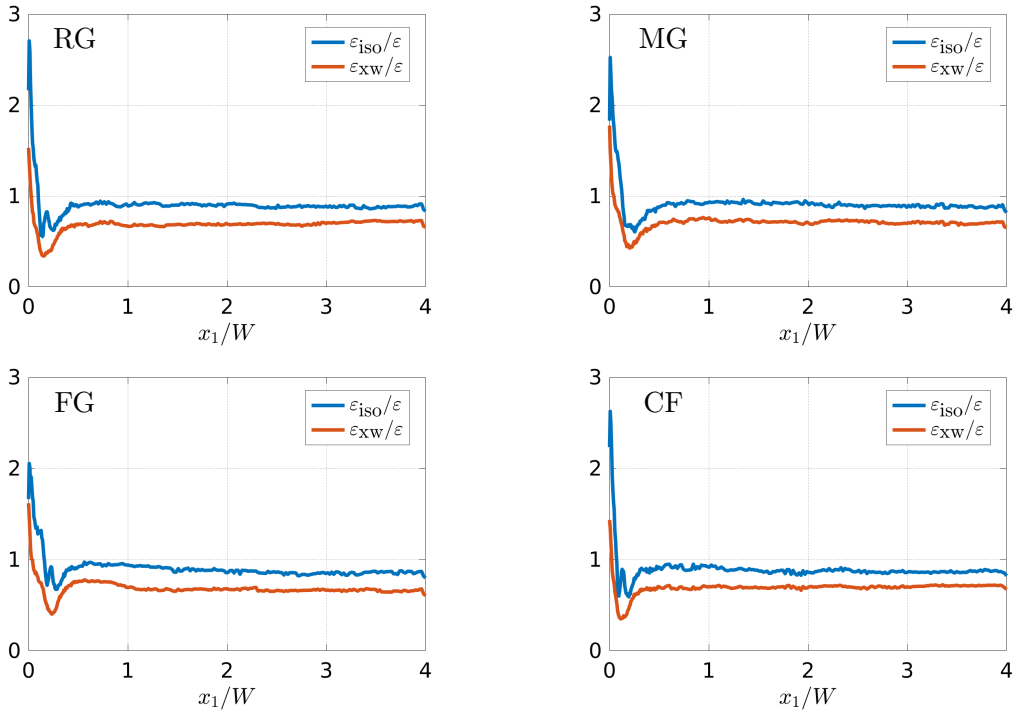

Figure 4.31: Centreline development of ratios $\varepsilon_{\text{iso}}/\varepsilon$ and $\varepsilon_{\text{xw}}/\varepsilon$.

To assess at which downstream position each grid injects dissipation, (4.17) is evaluated along the centreline and displayed in Figure 4.32. Dissipation behind the regular (RG) and multiscale (MG) grids display similar behaviour. A maximum is reached near grid at $x_1/W \approx 0.2$, at which point the profiles decrease monotonically. Dissipation behind the fractal grid (FG) is characterised by a slow build-up towards a peak at $x_1/W \approx 0.2$, but is significantly reduced for the region $x_1/W < 0.1$. The opposite is true in the combined-fractal CF wake, where dissipation is large in the initial build-up, and displays a peak closer to the grid.

To further understand the contrasting dissipation behaviour observed between the regular/multiscale grids and the fractal-type grids, each individual term in (4.17) is calculated and plotted in Figure 4.33. The last 3 terms in (4.17) are found to be negative, therefore their sign is swapped in the plot to aid readability. In

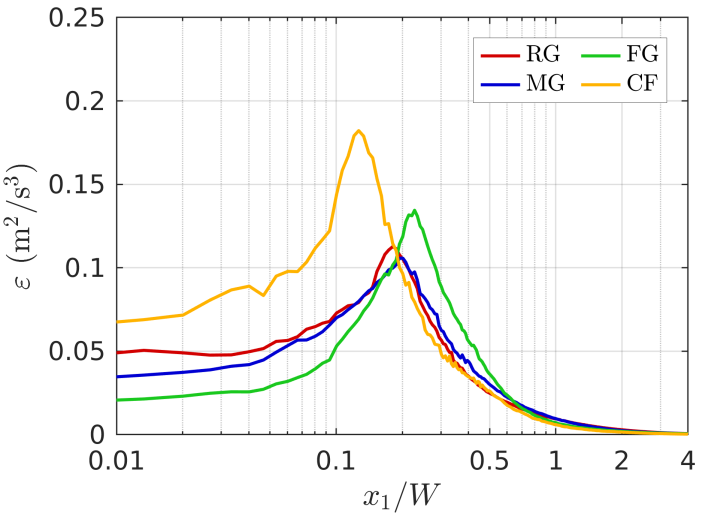

Figure 4.32: Streamwise development of dissipation along the centreline for each grid.

the cases of the regular and combined-fractal grids, a significant proportion of the dissipation near grid ($x_1/W < 0.1$) is found to be generated by the 3 terms $\langle(\partial u/\partial x_i)^2\rangle$. Due to isotropy in the y and z directions, there are 5 pairs of terms which are approximately equal. For example, $\langle(\partial v/\partial x)^2\rangle \approx \langle(\partial w/\partial x)^2\rangle$ is one such pair. Terms 1 and 12 of the dissipation ε in (4.17) are distinct. Behind the CF grid, $\langle(\partial u/\partial x)^2\rangle$ is particularly active in the region $x_1/W < 0.2$. However, elevated levels of dissipation in the CF grid case are not solely attributed to just one term of ε, as all terms make a contribution.

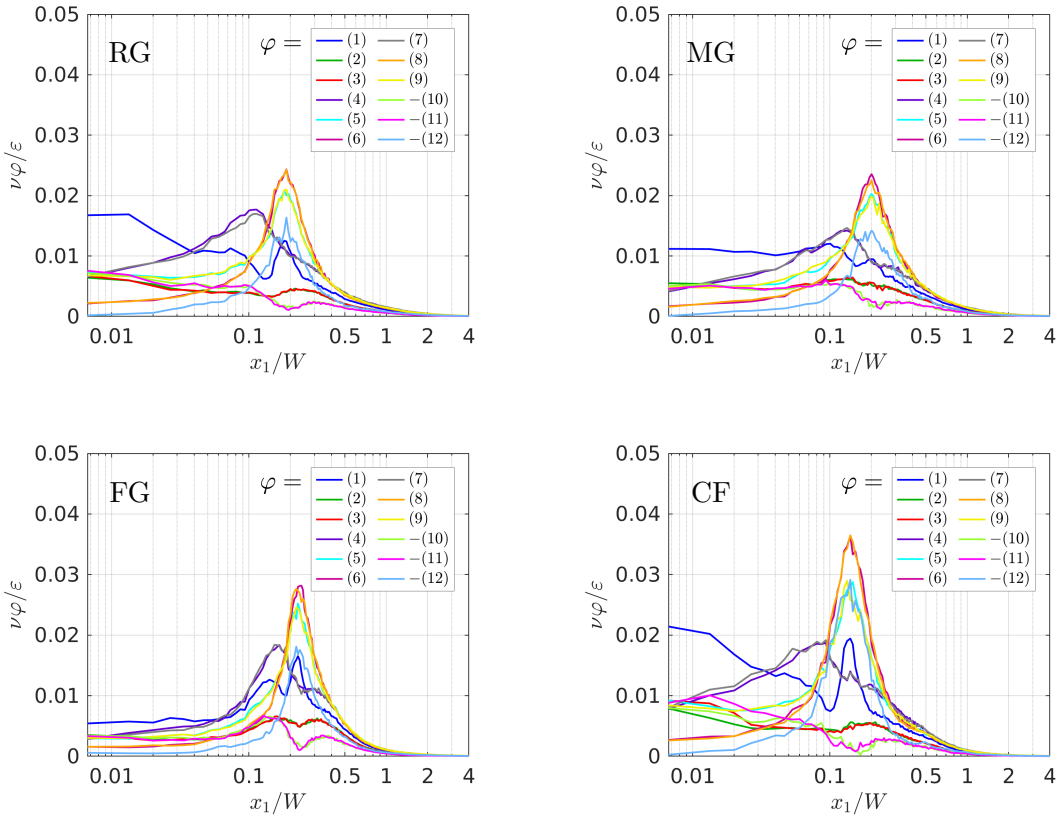

Figure 4.33: Streamwise development of each term belonging to ε from (4.17).

4.5.2 Non-equilibrium effects

Combining the equilibrium dissipation scaling law $\varepsilon = C_\varepsilon \mathcal{U}^3/\mathcal{L}$ with the Taylor microscale $\lambda^2 \equiv \nu \mathcal{U}^2/\varepsilon$ implies

$$C_\varepsilon Re_\lambda \propto \frac{\mathcal{L}}{\lambda} \ . \tag{4.20}$$

An implication of (4.20) is that as the Reynolds number is increased, a greater range of turbulent length scales are produced. If it is assumed that $C_\varepsilon = \text{const}$, and the decay region of grid turbulence where Re_λ is a decreasing function with downstream position is considered, (4.20) suggests the ratio L_{11}/λ should decrease like Re_λ. However, constant L_{11}/λ has been observed in experiments (Vassilicos, 2015), and therefore $C_\varepsilon \propto 1/Re_\lambda$.

Figure 4.34 displays the relationship between L_{11}/λ and Re_λ. Profiles of constant C_ε are included in each plot, which indicates dissipation in equilibrium. Behind the regular, multiscale, and combined-fractal grids, L_{11}/λ is approximately constant, which indicates a region of non-equilibrium. This was observed in the wake of regular, multiscale, and fractal grids in the wind tunnel experiment of Nagata et al. (2017). Behind the fractal grid however, the profile of L_{11}/λ is decreasing slightly with increasing Re_λ. This suggests a wider region of non-equilibrium in the FG wake.

Finally, the development of C_ε along the centreline is presented in Figure 4.35. Included are the data of Valente and Vassilicos (2011) for a square-fractal grid at different inlet speeds. A remarkable agreement is observed between experimental results and the regular and combined fractal cases. A greater increase in C_ε is observed for the FG wake, once again indicating elevated levels of non-equilibrium.

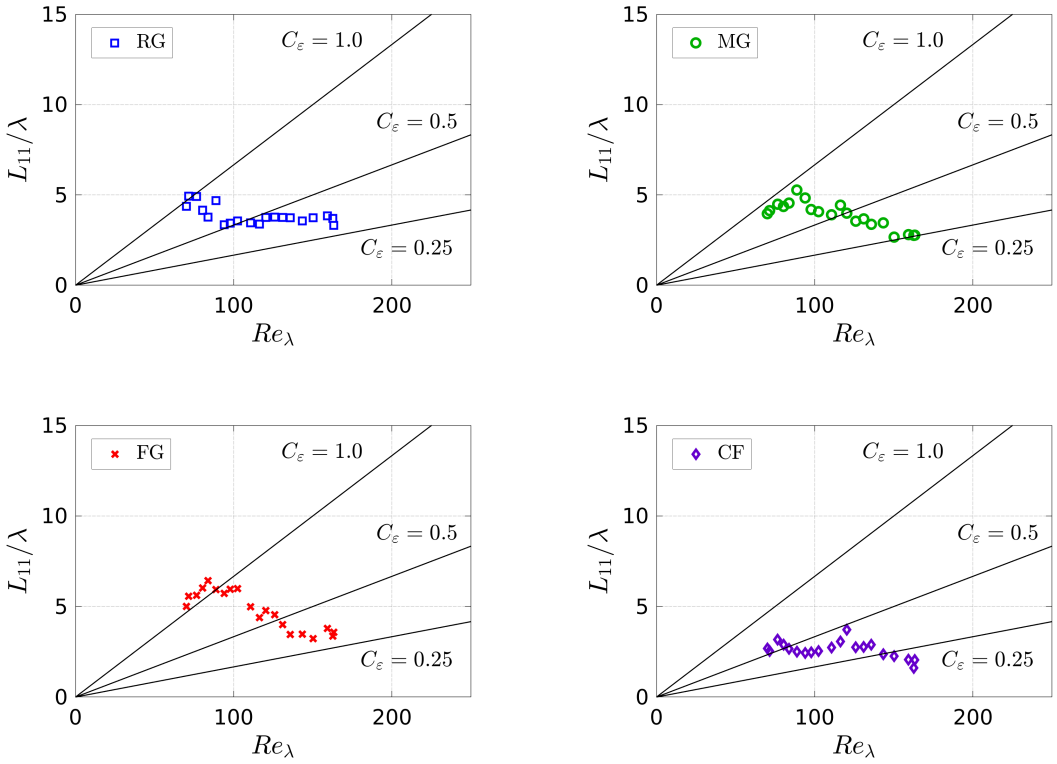

Figure 4.34: Ratio of longitudinal integral length scale L_{11} to Taylor microscale λ.

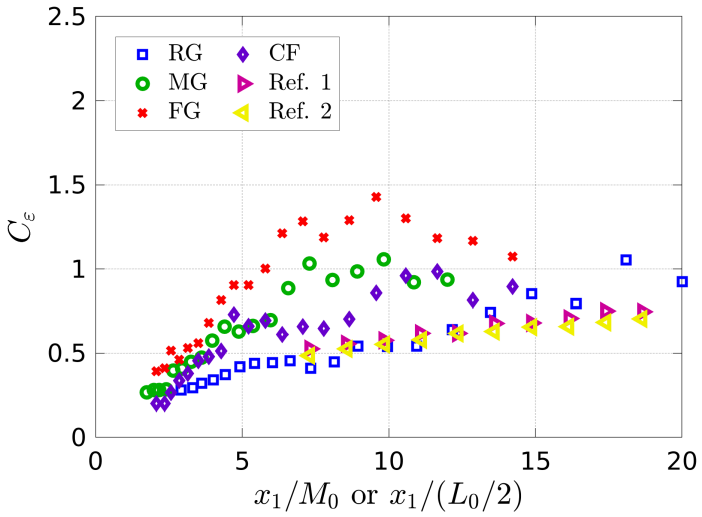

Figure 4.35: Streamwise development of the dissipation constant. Included are experimental data of Valente and Vassilicos (2011) from a square-fractal grid tested at: $U_\infty = 10\,\mathrm{m/s}$ (Ref. 1), $U_\infty = 15\,\mathrm{m/s}$ (Ref. 2).

4.6 Chapter conclusions

Simulations of grid turbulence have been carried out using the projected inlet method of Blackmore et al. (2013). A regular, multiscale, and two fractal grids have been tested. To allow a fair comparison between grids, solidarity, domain size, and inflow velocity, have been kept the same across all simulations. A solidarity of $\sigma = 44\%$ is chosen to match previous investigations of Blackmore et al. (2013) and Krogstad and Davidson (2012). Power-law decay and generated length scales are in close agreement with experimental results, suggesting some universality between investigations, and therefore the projected inlet method has successfully generated grid turbulence. This method can be utilised by experimentalists to test grid designs before they are deployed in wind and water tunnel tests.

A new fractal-type grid, referred to as the combined-fractal grid, has been designed with the aim of improving homogeneity across the grid element. The new design is constructed from a combination of I-fractal and square-fractal grids. The smallest I-fractal iterations were added to improve flow homogeneity by pushing more solidarity towards the grid element perimeter. This has been confirmed in visualisation of the vorticity field. Less clustering is produced along the grid elements perimeter. Homogeneity was also affected by the relative size of the middle cross compared to neighbouring grid bars. If the middle cross is too large, the flow might initially look to be developing towards HIT, but after an initial period of decay, the mean flow begins to dominate the decaying turbulent field. This was confirmed by sampling data from a cross-sectional plane, whose normal is orientated in the streamwise direction. It was seen how both fractal-type grids produce large turbulent length scales along the centreline. Poor homogeneity was reported in the wind tunnel experiment of Hearst and Lavoie (2014), which contradicted previous fractal grid experiments. Two explanations are offered here. Firstly, their grid was constructed with a length scaling parameter of $R_{\mathrm{L}} = 0.44$, resulting in a space-filling parameter of $D_f = 1.71$. This is known to be too low (Hurst and Vassilicos, 2007), and almost certainly contributed to inhomogeneity. A parameter study has been conducted on D_f, and high velocity streaks were observed at the channel perimeters when $D_f < 2.0$. Secondly, it is suspected that their central cross was too big, i.e. t_0 was too large, introducing even more flow

inhomogeneity. Although only one element was considered in the two fractal grids tested here, and therefore homogeneity would improve if more elements were tiled, it is still important to understand the wake generated by a single element. For example, it was observed that neighbouring wakes generated by grid bars behind the fractal grid do not always interact, which can generate high speed velocity streaks.

Despite having the lowest grid Reynolds number Re_0, the combined-fractal design produces a local Reynolds number Re_λ which was comparable to other grids tested in this study. Elevated turbulence levels are often desirable in experiments, and the combined-fractal grid shows promise of this. Decay of Re_λ was also found to be abrupt. In addition to this, large decay exponents of $n \approx 2$ were observed behind the combined-fractal grid. This finding supports the claim from experimentalist that turbulence decay is altered by the fractal grid geometries.

To understand how the fractal and combined-fractal grids produce different decay characteristics, the full form of the dissipation term is evaluated along the centreline. This includes measurements directly behind the grid, which are not possible to collect in HWA wind tunnel experiments due to the high level of turbulence intensity and anisotropy in the production region. Surrogates of the exact dissipation were also calculated to compare their accuracy. Results suggest that the common X-wire approximation to the dissipation ε_{xw} significantly under predicts the true value. However, the isotropic form ε_{iso} was found to be a reasonable estimate in the far field. Elevated levels of dissipation were observed in the production region of the combined-fractal grid. This was investigated further by considering each term of the full dissipation. It was found that, whilst all 12 terms play a role in generating high levels of ε, the terms $\langle(\partial u/\partial x_i)^2\rangle$ are significant contributors. Non-equilibrium turbulence decay is assessed in the wake of each grid. Usual markers of non-equilibrium are calculated, i.e. constant L_{11}/λ, and increasing C_ε. Although some non-equilibrium effects are detected behind the regular, multiscale, and combined-fractal grids, the fractal grid produces a longer region of non-equilibrium dissipation.

To conclude, numerical simulations of grid turbulence can be used to guide experimentalists on grid design. Care must be taken when designing such grids,

because flow homogeneity can be difficult to guarantee. A key finding of this chapter is that fractal grids can be constructed which spread solidarity away from the centre, much like a regular grid. However, it is difficult to predict how the wakes created from each bar will interact with jets from the grid gaps. The projected inlet technique is a suitable method to generate free-stream turbulence, and this has been confirmed with regular, multiscale, and fractal-type grids. Different turbulent characteristics, such as non-equilibrium decay, have been observed behind each grid. There is potential for researchers to customise grid turbulence towards their application, for example, grid elements of the inlet can be arranged to produce a non-uniform profile of turbulence. It is also possible to assign some time-varying profile at the inlet to model gusts of turbulence, which is a key property in wind engineering. In the following chapter, the projected inlet method will be used to generate custom free-stream turbulence past a circular cylinder.

Chapter 5

Simulating turbulent flow past a circular cylinder

Turbulent flow past a circular cylinder is investigated numerically for a circular cylinder Reynolds number of 3900. Three types of inflow are generated at the inlet. The first case is laminar inflow, which is the most common configuration found in the literature on flow past a circular cylinder. The second and third inflow conditions are of non-negligible turbulence, generated by projecting grid blockages onto the inlet patch. The simplest grid geometry to use on the inlet patch is the biplane grid, constructed from a lattice of vertical and horizontal bars. The second type of grid used is the combined-fractal, which produces a range of length scales due to the multiscale nature of the grid design. The influence of inflow turbulence on the circular cylinder wake is analysed for each inlet grid geometry. Time-averaged velocity profiles reveal how upstream turbulence produces a narrowed wake. Dissipation is split into coherent and stochastic components, and a new surrogate of dissipation is developed which outperforms other methods, and can be evaluated with fewer terms of the velocity gradient tensor. The velocity gradient tensor is analysed for snapshots in time, making it possible to compare the topology of turbulence in the wake for each inlet case. Turbulence dissipation is found to be concentrated in between streamwise ribs, which is in contrast to the model of Chen et al. (*J. Fluid Mech.*, vol. 835, 2018, pp. 271–300), where it resides in the primary rollers.

5.1 Introduction

The flow past a circular cylinder at Reynolds number $Re_D = 3900$, where D is the cylinder diameter, has been investigated extensively in both experiments and numerical simulations. Some of the main findings were discussed in Chapter 2, so only a brief review is covered here. The first point to note is that inflow turbulence plays a different role between experiments and simulations. In experiments it can be difficult to produce a smooth flow upstream of the circular cylinder. This was observed in the experiment of Lourenco and Shih (1993), where turbulence of an unspecified level was introduced into the inflow, causing early separation in the shear layers and a reduced recirculation length. However, in numerical simulations, turbulence is difficult to produce at the inlet. Instead researchers opt to prescribe a laminar inflow, because mesh grading at the inlet would dissipate any turbulence regardless (Breuer, 1998b; Lysenko et al., 2012). This is reflected in the vast amount of numerical studies carried out on laminar flow past a circular cylinder (Beaudan and Moin, 1994; Mittal and Moin, 1997; Kravchenko and Moin, 2000; Franke and Frank, 2002; Dong et al., 2006; Meyer et al., 2010; Prsic et al., 2014).

To the author's knowledge, the most relevant study concerning the simulation of turbulent flow past a circular cylinder is Aarnes et al. (2018). However, this study was undertaken at a lower Reynolds number range $180 < Re_D < 250$ to investigate the transition to three-dimensionality, and turbulence was artificially generated prior to seeding through the inlet. Here a different approach is taken. With the increased interest in customising grid turbulence (Sakai and Vassilicos, 2016), the next step in the study of turbulent flow past a circular cylinder is better control of the inflow turbulence. Simulation of grid turbulence was considered in Chapter 4 by projecting grid designs onto the inlet patch. A circular cylinder can now be placed in the wake of a regular and combined-fractal grid. A schematic of the flow field and computation set-up, including coordinate system used, is presented in Figure 5.1.

Despite the lack of simulations concerning a turbulent flow past a circular cylinder, there are numerous motivations for simulating this flow. One key advantage of simulations over experiments is the ease at which the whole flow field

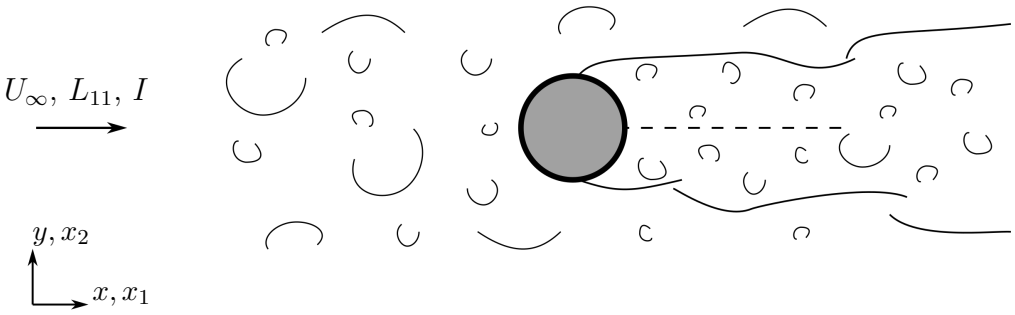

Figure 5.1: Schematic of turbulent flow past a circular cylinder. Inflow is characterised by bulk velocity U_∞, integral length scale L_{11}, and turbulence intensity I. Axial direction (z, x_3) out the page.

can be sampled, including the recirculation region. This is especially true for the velocity gradient tensor VGT, which is difficult to measure in experiments (Wallace, 2009). However, the VGT is required to identify coherent structures, which are important to understand in terms of interactions between primary vortex rollers and smaller three-dimensional structures in the wake.

The VGT is also required when measuring the dissipation rate ε. In the low-turbulence wind tunnel experiment of Browne et al. (1987), single hot wires and single X-wires were placed in the far field ($x/D = 420$) for a cylinder wake flow at Reynolds number $Re_D = 1170$. Taylor's frozen turbulence hypothesis was enforced to calculate velocity derivatives. They reported the isotropic form of dissipation ε_{iso} to be approximately 45% smaller than ε. Hao et al. (2008) also found ε_{iso} to be smaller than ε, but only by 10% in their circular cylinder wind tunnel experiment conducted at downstream position $x/D = 240$, and Reynolds number $Re_D = 2000$. Chen et al. (2018) enforced homogeneity in the transverse plane (y-z) to calculate a surrogate of dissipation ε_{yz}, which served as a reference value for the true mean energy dissipation for their study of the circular cylinder wake. Measurements were recorded at downstream positions $x/D = 10, 20$, and 40 for a Reynolds number of $Re_D = 2500$. Dissipation was found to be concentrated in the coherent spanwise vortex rollers, in contrast with the model of Hussain (1986) and Hussain and Hayakawa (1987) where it resides in regions of high mixing.

It is noted here that Browne et al. (1987) and Chen et al. (2018) sampled the wake flow at considerably different streamwise locations, i.e. $x/D = 420$ and $x/D = 10$ to 40, respectively. Therefore it is possible that dissipation resides in the primary rollers close to the circular cylinder, but once primary rollers are broken down, it moves into areas of high mixing. However, Browne et al. (1987) and Chen et al. (2018) both collected measurements at a single point in space, which makes it difficult to build a three-dimensional picture of the interaction between dissipation and coherent structures.

This chapter aims to improve understanding of the dissipation in the wake of a circular cylinder for laminar and turbulent inflow. It is important to establish the projected inlet method for the simulation of free-stream turbulence flow past a circular cylinder. The affect of inflow turbulence on the wake structures will be studied. In addition to this, a three-dimensional picture of the turbulence dissipation will be developed, which is absent from the literature. The present chapter is structured as follows. First, the numerical procedure is outlined and the smooth inflow case is simulated for validation against experimental data. The next step is to project a grid onto the inlet patch and simulate free-stream turbulent flow past a circular cylinder. Wake dynamics are compared between simulations to capture the effects of free-stream turbulence. This comparison includes a look into the turbulence topology through analysis of the velocity gradient tensor. Finally, a model of the interaction between coherent structures and the dissipation is developed.

5.2 Laminar inflow case

5.2.1 Numerical procedure

Flow past a circular cylinder at Reynolds number $Re_D = 3900$ is modelled numerically using large-eddy simulation. A Cartesian coordinate system is used to define the computation domain, i.e. orthogonal basis of x, y, z (or equivalently x_1, x_2, x_3) which are referred to here as, respectively: streamwise, normal, and axial directions. Index notation x_i $(i = 1, 2, 3)$ is only used briefly when it is convenient to introduce Einstein summation convention. The 3 components of veloc-

Patch	$\boldsymbol{U}$ (m/s)	p (m^2/s^2)	k (m^2/s^2)
Inflow	$(U_{\text{in}}, 0, 0)$	`zeroGradient`	1×10^{-4}
Outlet	`inletOutlet`	0	`inletOutlet`
Cylinder wall	$(0, 0, 0)$	`zeroGradient`	0
Side patches	`symmetry`	`symmetry`	`symmetry`
Top/bottom	`cyclic`	`cyclic`	`cyclic`

Table 5.1: Boundary patch prescriptions in OpenFOAM for the simulations of flow past a circular cylinder.

ity are given by U, V, W. Similarly, velocity fluctuations are denoted by u, v, w. A circular cylinder of diameter 6 mm is placed at the origin of the computational domain. Coordinates of the circular cylinder axis are given by: $x = y = 0$, and $z \in [0, 40\,\text{mm}]$. This yields an axial length of $L_z = 6.\dot{6}D$, which complies with the recommended $L_z \geq \pi D$ found to be sufficient in previous studies at the same Reynolds number- Ma et al. (2000), Kravchenko and Moin (2000), and Parnaudeau et al. (2008). The domain extends $\pm 10D$ in the crossflow direction, and $15D$ in the downstream direction, similar to the domain of Ma et al. (2000). The inlet plane is positioned $30D$ upstream of the cylinder because additional simulations with a turbulent inflow require an extended development length.

For the laminar inflow case, a fixed velocity of $\boldsymbol{U} = (U_{\text{in}}, 0, 0)$ is prescribed across the full inlet patch to yield a circular cylinder Reynolds number of $Re_D = 3900$. Velocity at the outlet boundary is prescribed using the OpenFOAM boundary condition `inletOutlet`, which switches from `zeroGradient` to `fixedValue` if back flow occurs. This boundary condition is suitable for the advection of vortical structures through the outlet. Zero gradient for pressure is prescribed across the full inlet patch. Pressure is fixed at the outlet boundary, with value 0. A symmetry boundary condition is prescribed at the side patches for all fields. Periodic boundary conditions are specified at the cylinder ends, replicating an infinite aspect ratio. Table 5.1 presents a summary of the boundary conditions used for velocity and pressure.

As in Parnaudeau et al. (2008), the turbulent wake is assumed to be fully

developed after $T = 150D/U_\infty$. With the flow parameters considered in this study, $D = 6\,\text{mm}$ and $U_\infty = 0.78\,\text{m/s}$, this corresponds to 1.15 s. Additionally, a minimum of 52 shedding periods will be collected to ensure statistical convergence (Parnaudeau et al., 2008). An estimation of the time taken to capture 52 shedding periods is calculated by setting a Strouhal frequency of $St = 0.215$, which is in agreement with results from literature. From $St = 0.215$ it is estimated that 52 sheds corresponds to 1.86 s of flow time. Therefore, each simulation is ran till 3 seconds is acquired, from which the first 1.15 s is discarded.

Figure 5.2 displays the meshing strategy employed. A region of close refinement near the cylinder is controlled by the number of radial elements N_r. A minimum of 48 computational cells are required over a spanwise length of $L_z = \pi D$ (Franke and Frank, 2002; Parnaudeau et al., 2008; D'Allessandro et al., 2016). Therefore, for a cylinder length of $L_z = 6.6\dot{6}$, $N_z = 100$ is sufficient. Figure 5.3 presents a slice through the mid-plane of a computational mesh with approximately 20 million cells, demonstrating the mesh distribution of the O-type grid employed in this study. Refinement is concentrated around the cylinder surface in body fitted layers, which increase in thickness away from the surface in the radial direction.

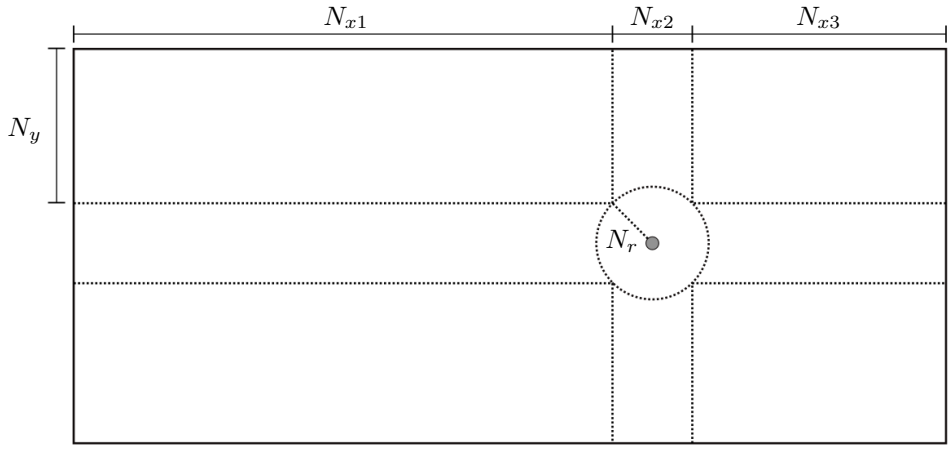

Figure 5.2: Blocking and meshing strategy for the circular cylinder simulations.

LES simulations were ran in OpenFOAM v4.1. A description of the numerical settings selected throughout this study are detailed in Appendix A. Additionally,

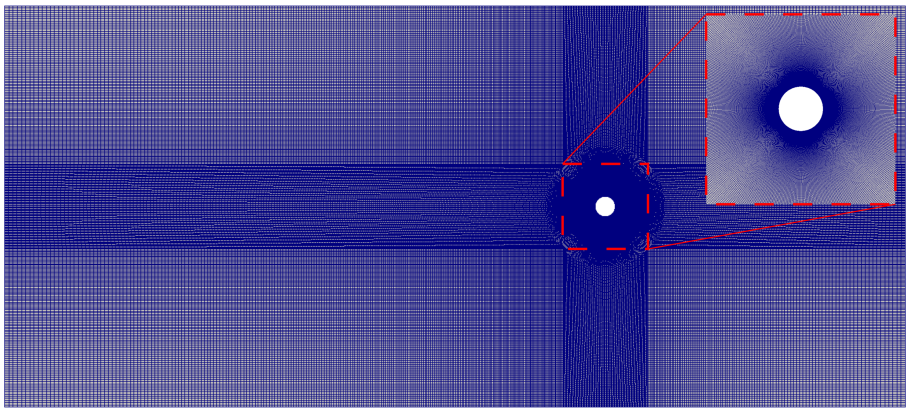

Figure 5.3: A slice through the O-grid mesh and close up of cyinder surface mesh layers.

the k-equation SGS model of Yoshizawa (1986) was detailed in Chapter 3. It is necessary to conduct a mesh independence study on the laminar inflow case to ensure the chosen computational mesh sufficiently resolves the flow field in the wake. Table 5.2 presents the details of 4 structured grids used to determine the minimum resolution required for the number of radial elements N_r (see meshing strategy Figure 5.2). The recirculation length is reported for each simulation, which is taken to be the distance from the cylinder base to the sign change where $\langle U \rangle$ first becomes positive. Included are the PIV results of Parnaudeau et al. (2008), where it was found that $L_r/D = 1.51$.

Case	Re_D	N_r	N_z	N $(\times 10^6)$	L_r/D
LI1	3900	50	100	8.8	0.82
LI2	3900	100	100	10.4	1.39
LI3	3900	200	100	16.4	1.49
LI4	3900	300	100	25.2	1.49
Exp.	3900	-	-	-	1.51

Table 5.2: Mesh independence grids for the laminar inflow (LI) case. Experimental results of Parnaudeau et al. (2008).

Figure 5.4 presents the development of time-averaged streamwise velocity $\langle U \rangle / U_\infty$, and variance $\langle u^2 \rangle / U_\infty^2$ along the wake centreline. Included are the PIV experimental results of Parnaudeau et al. (2008). Zero velocity is observed at the cylinder wall due to the no-slip condition, followed by a region of recirculation in the near wake of each grid. Profiles of $\langle U \rangle$ then recover further downstream to an asymptotic value. Two peaks are visible in the profiles of variance $\langle u^2 \rangle$, which is in agreement with Parnaudeau et al. (2008). The coarsest mesh resolution LI1 has generated a considerably shorter recirculation region $L_r/D = 0.82$, it is therefore unable to sufficiently capture the shedding phenomena. The meshes of LI3 and LI4 both predict a recirculation length of $L_r/D = 1.49$, which is in close agreement to the PIV results from literature: $L_r/D = 1.51$.

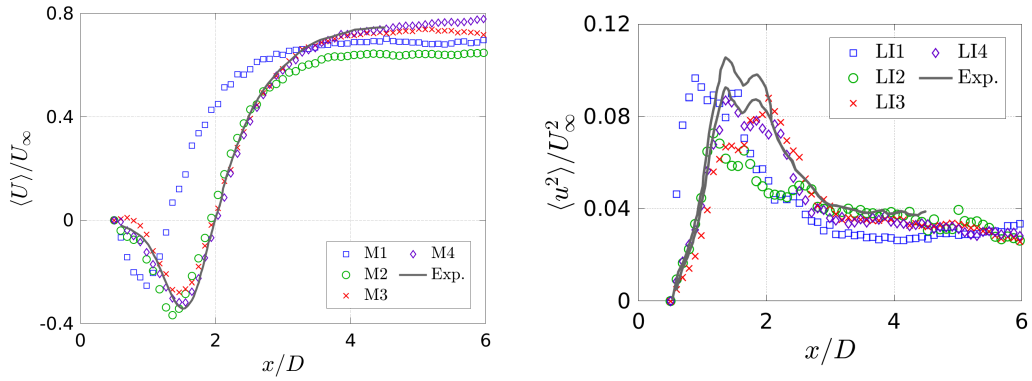

Figure 5.4: Centreline development of time-averaged streamwise velocity and velocity variance. PIV data are from the experiment of Parnaudeau et al. (2008).

Figure 5.5 presents profiles of velocity at 3 downstream locations in the wake: $x/D = 1.06, 1.54, 2.02$. A velocity deficit is observed behind the cylinder in profiles of time-averaged streamwise velocity $\langle U \rangle$. Profiles of $\langle U \rangle$ close to the cylinder ($x/D = 1.06$) are characterised by a U-shape, which evolves into a sharper V-shape further downstream. Typically, experiments and numerical simulations have reported two distinct mean streamwise velocity profiles at $x/D = 1.06$, those being U-type and V-type solution.

The presence of a U-shape has been confirmed across previous numerical and experimental studies (Ma et al., 2000; Parnaudeau et al., 2008), therefore it is

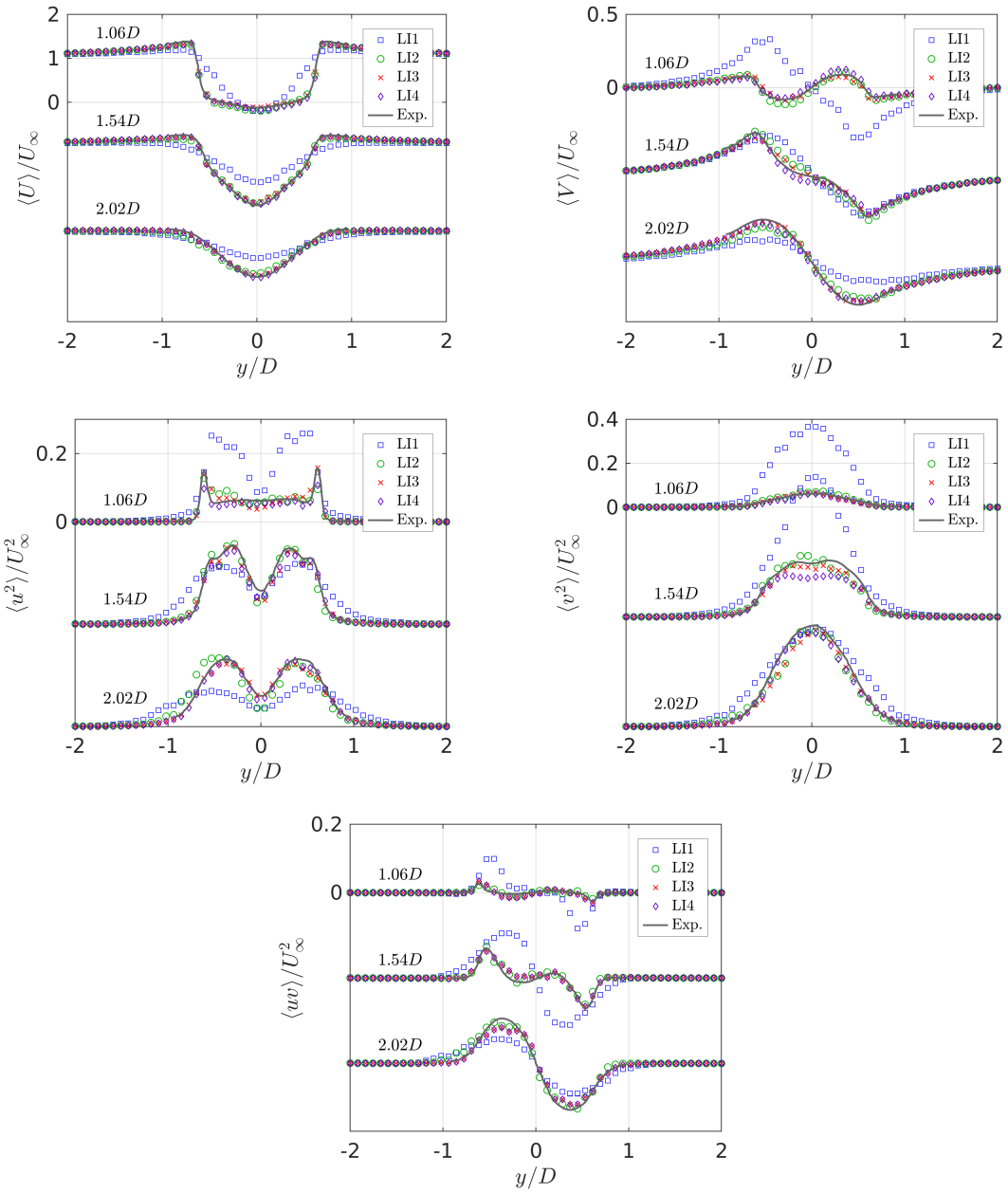

Figure 5.5: Mesh independence test. Time-averaged velocities in the near wake, for 3 streamwise locations: $x/D = 1.06, 1.54, 2.02$. Profiles at $x/D = 1.54$ and $x/D = 2.02$ have been shifted to fit onto the same figure as $x/D = 1.06$. PIV experimental results of Parnaudeau et al. (2008).

encouraging to find it here for the mesh resolutions of LI2, LI3, and LI4. However, the coarsest mesh resolution LI1 predicts a V-shape, which was reported in the experimental data of Lourenco and Shih (1993), and is most likely a result of inflow turbulence. Antisymmetry about $y = 0$ is observed in profiles of $\langle V \rangle$ for all mesh resolutions. Apart from LI1, all other mesh resolutions are in close agreement to the experimental data. This has been seen across the profiles of velocity variance: $\langle u^2 \rangle$, $\langle v^2 \rangle$, and $\langle uv \rangle$.

To summarise this mesh independence study, a coarse grid is unable to predict the correct recirculation length, and the velocity deficit recovers too quickly as a result. A similar effect was observed in the experiment of Lourenco and Shih (1993), where inflow turbulence caused an early separation in the shear layers and a reduced recirculation length. The mesh resolution of LI2 showed some improvement to LI1, but still predicted a slightly reduced recirculation length of $L_r/D = 1.39$, and a lower asymptotic value of $\langle U \rangle$ (Figure 5.4). Acceptable agreement has been observed between the PIV results of Parnaudeau et al. (2008) and the mesh resolutions LI3, LI4. Therefore it is concluded that $N_r = 200$ is sufficient to capture the wake dynamics.

5.3 Grid turbulence inflow

A regular and combined-fractal grid are projected onto the inlet patch for the turbulent inflow simulations. These two cases were chosen from the findings of Chapter 4. A regular grid is chosen because it is the most common grid design used throughout experiments, and is the closest approximation to homogeneous isotropic turbulence. This is contrasted to the new combined-fractal design, which is constructed from a fractal pattern of varying bar widths and lengths. The inlet is split into two patches: (i) zero velocity at solid patches, where grid bars are projected; (ii) non-zero velocity $\boldsymbol{U}_{\text{in}} = (U_{\text{in}}, 0, 0)$ in the gaps between grid bars. This configuration is displayed in Figure 5.6.

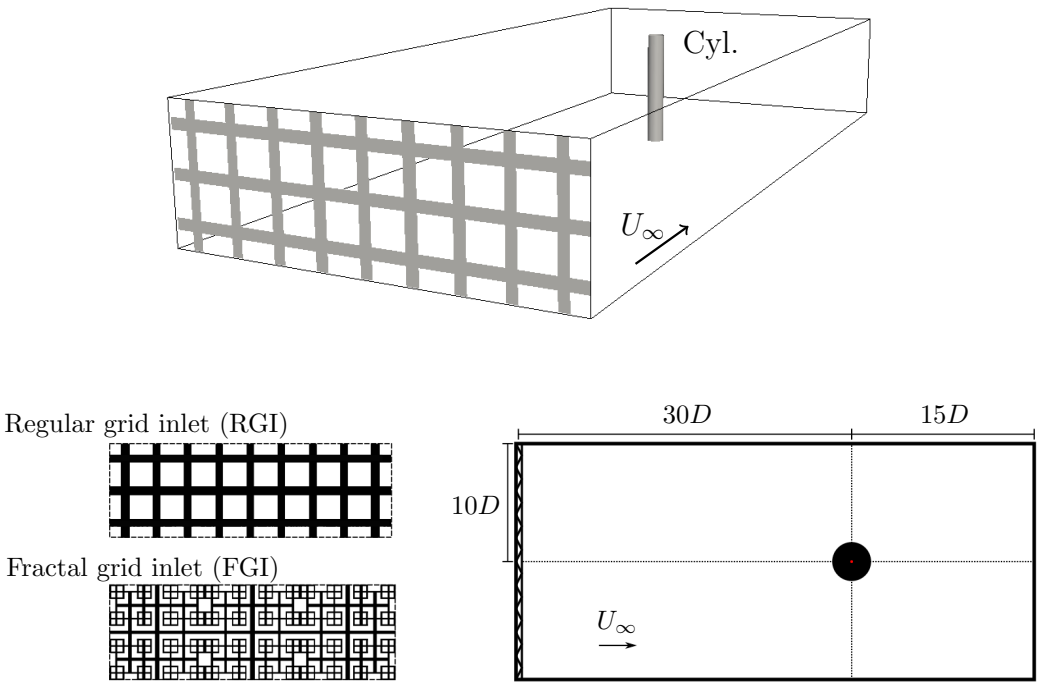

Figure 5.6: Top: regular grid with cylinder placed in the free-stream. Screen shot from Paraview geometry creation. Bottom: regular and fractal grid designs projected onto the inlet patch, and two-dimensional slice of the computational domain (not to scale).

To yield a cylinder Reynolds number of $Re_D = 3900$, the inflow velocity

U_{in} is adjusted by trial and error until a free-stream velocity of $U_\infty \approx 0.78$ is achieved. To monitor this, a number of probes are placed between the grid and cylinder, along the domain centreline. Velocity is recorded at each location and time-averaged to obtain U_∞. Figure 5.7 displays the Reynolds number Re_D for each grid, upstream of the cylinder. It is trivial to control the laminar inflow Reynolds number, but it can be seen how the grid turbulence cases display a velocity deficit, before building towards a free-stream velocity U_∞. It has been ensured that the turbulence behind each grid has enough time to develop before passing the cylinder. A reasonable match in Re_D for each simulation has been achieved. It is noted that profiles of Re_D begin to feel influence from the cylinder at approximately $x/D = -5$. In the short region $-5 < x/D < -0.5$, velocity decreases from a free-stream value of U_∞, to zero velocity at the circular cylinder.

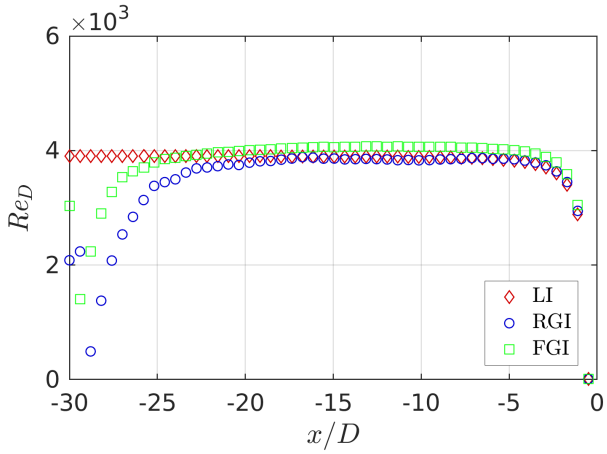

Figure 5.7: Reynolds number along the domain centreline, from the inlet ($x/D = -30$), to the cylinder front ($x/D = -0.5$).

To obtain lift and drag forces on the circular cylinder, the OpenFOAM forces library is specified in the `controlDict` file. A time-series of pressure and viscous forces are generated in each direction (x, y, z). The total force on the cylinder is obtained by taking the sum of the pressure and viscous forces. Time series of drag and lift are extracted from the streamwise (x) and normal (y) components of force, respectively. Coefficients of lift and drag forces can then be calculated

by

$$C_l = \frac{F_l}{\frac{1}{2}\rho U_\infty^2 A_{\text{ref}}} \ , \tag{5.1}$$

$$C_d = \frac{F_d}{\frac{1}{2}\rho U_\infty^2 A_{\text{ref}}} \ , \tag{5.2}$$

where F_l and F_d are the lift and drag forces experienced on the cylinder surface, respectively, and A_{ref} is a reference area taken to be the total surface area of the cylinder. A Discrete Fourier Transform (DFT) of the lift coefficient is computed in Matlab to extract the shedding frequency f_s, which can then be used to calculate the Strouhal frequency $St = f_s D/U_\infty$.

In addition to the upstream Reynolds number, turbulence levels are also recorded. The turbulence intensity in each direction is given by

$$I_1 = \frac{u_{\text{rms}}}{U_\infty} \ , \qquad I_2 = \frac{v_{\text{rms}}}{U_\infty} \ , \qquad I_3 = \frac{w_{\text{rms}}}{U_\infty} \ , \tag{5.3}$$

where $u_{\text{rms}} = \sqrt{\langle u^2 \rangle}$, $v_{\text{rms}} = \sqrt{\langle v^2 \rangle}$, $w_{\text{rms}} = \sqrt{\langle w^2 \rangle}$ are, respectively, the root-mean-square (r.m.s.) velocity fluctuations in the x, y, and z directions. Turbulence intensity percentage is given by

$$I = \sqrt{\frac{1}{3}\left(I_1^2 + I_2^2 + I_3^2\right)} \ . \tag{5.4}$$

A distinction is made here between I and I_1, although it is not always clear in the literature which turbulence intensity has been used. It is common to only use I_1 and refer to this as the turbulence intensity. Another important parameter in the characterisation of inflow turbulence is the approximate size of large-scale eddies, given by the longitudinal integral length scale L_{11}

$$L_{11}(x) = \frac{1}{\langle u^2(x) \rangle} \int_0^\infty \langle u(x) u(x+s) \rangle \, \mathrm{d}s \ . \tag{5.5}$$

Figure 5.8 presents $I\,(\%)$ and L_{11}/D recorded upstream of the circular cylinder. Although the turbulence intensity $I\,(\%)$ grows initially near grid in the turbulence production region, it begins to decay towards the cylinder. The integral

length scale close to the inlet is scattered due to the presence of unbroken jets emerging from the turbulence-generating grid. At $x/D = -20$, it begins to settle, and then steadily grow towards the cylinder. The regular grid has produced a higher level of turbulence intensity $I\,(\%)$, and a larger integral length scale L_{11}. The most likely reason for this, which was observed in Chapter 4, is the width of the central bar. Figure 5.8 highlights the importance of monitoring the inflow conditions between the inflow and circular cylinder, because turbulence levels and length scales develop along the streamwise direction, and cannot simply be taken at a single point. The region $-10 < x/D < -5$ is considered to be far enough away from the inlet, such that turbulence has time to develop, but is also unaffected by the cylinder. Therefore, measures of free-stream velocity, integral length scale, and turbulence intensity have been calculated by taking averages in this region. Table 5.3 presents chosen simulation parameters and free-stream flow conditions for each run.

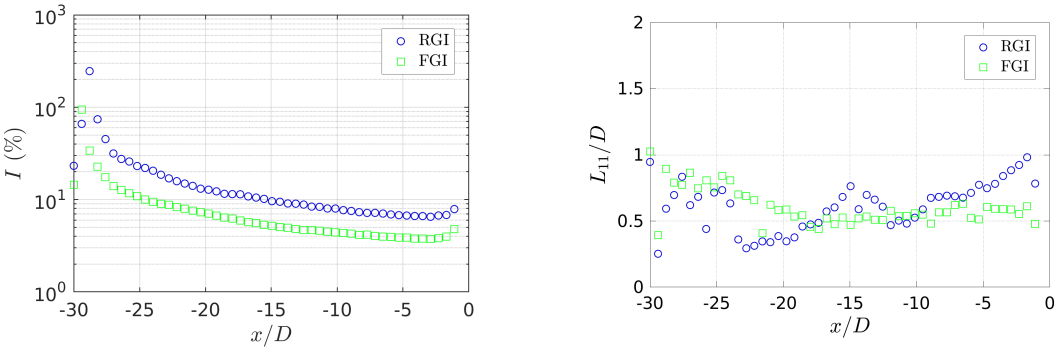

Figure 5.8: Turbulence intensity I and integral length scale L_{11}/D between the grid inlet and circular cylinder.

Figure 5.9 plots the mean drag coefficient $\langle C_d \rangle$ against the turbulence parameter $Re_D^{1.34}T$, where $T = I_1(D/L_{11})^{0.2}$ is the Taylor parameter. This plot has been reproduced from Kiya et al. (1982), with addition of results from the current simulations. The wind tunnel experiments of Fage and Warsap (1929); Surry (1972); Bruun and Davies (1975); Kiya et al. (1982) were ran at a higher Reynolds number range ($10^4 < Re_D < 10^6$), and the turbulence is assumed to be fully developed. It is clear from Figure 5.9 why this Reynolds number range is chosen, because it covers the sharp decrease in the drag coefficient. Profiles

	Inflow conditions				*Averaged properties*		
	Re_D	L_{11}/D	I_1, I_2, I_3 (%)	I (%)	St	$\langle C_d \rangle$	L_r/D
LI	3900	0.00	0.0, 0.0, 0.0	0.0	0.218	1.03	1.49
RGI	3850	0.67	7.1, 7.1, 7.1	7.3	0.207	1.18	0.88
FGI	4050	0.56	3.9, 6.7, 4.4	4.1	0.224	1.35	0.96

Table 5.3: Inflow conditions and averaged properties for the laminar/turbulent flow past a circular cylinder.

of $\langle C_d \rangle$ are reasonably well collapsed by $Re_D^{1.34}$ across the experiments, which is encouraging because $Re_D^{1.34}$ contains defining parameters of turbulent flow past a circular cylinder, i.e. Reynolds number, turbulence intensity, and integral length scale.

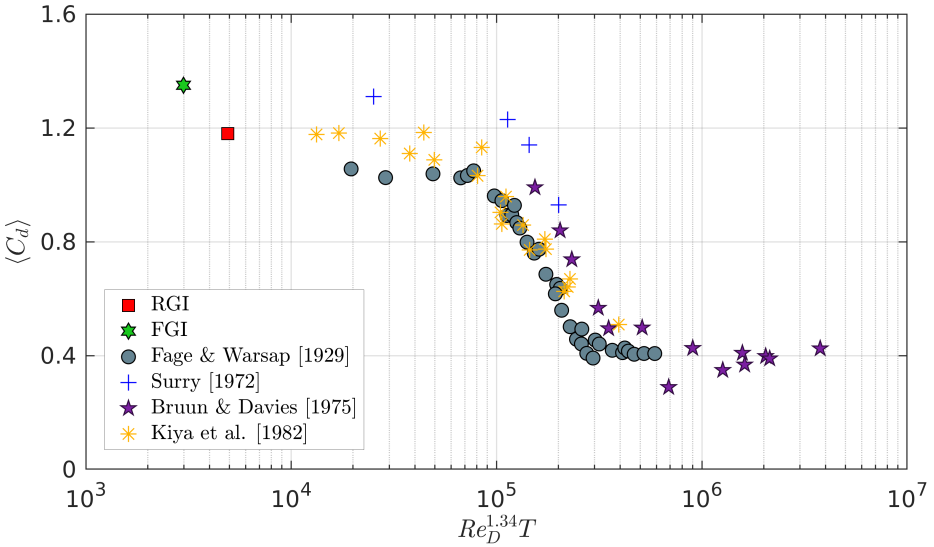

Figure 5.9: Mean drag coefficient $\langle C_d \rangle$ plotted against the parameter $Re_D^{1.34}T$ for the current simulations and previous experiments.

In the range reported here, increasing $Re_D^{1.34}T$ leads to asymptotic behaviour towards $\langle C_d \rangle = 0.4$. However, profiles of $\langle C_d \rangle$ for the lower limits ($Re_D^{1.34}T < 10^5$), asymptote towards different values. The experimental data of Kiya et al. (1982) match with the RGI case, while the data of Surry (1972) are closer to FGI. Kiya

et al. (1982) were aware of the limitations, concluding: "It is doubtful, however, whether the parameter $Re_D^{1.34}T$ uniquely controls all the aspects of the flow past a circular cylinder immersed in turbulent streams".

5.4 Cylinder shedding response

5.4.1 Mean wake profiles

Figure 5.10 plots the mean streamwise velocity and velocity variance along the wake centreline. Included is the PIV experiment of Parnaudeau et al. (2008). At the cylinder base ($\theta = 180°$), the velocity is zero due to the no-slip condition. A region of recirculating flow is found in the very near wake ($x/D < 2$), where the velocity reaches a minimum of $U_{\min}$. Profiles of $\langle U \rangle$ then recover and asymptote towards the free-stream value U_∞. The laminar inflow matches closely to the experimental results- correctly predicting the position of a velocity minimum $U_{\min}$, and producing a similar recirculation length. Free-stream turbulence has reduced the recirculation length, and produced different behaviour for $x/D > 4$. An increase in $\langle u^2 \rangle$ is observed directly behind the cylinder as the turbulence develops spatially. A maximum is then reached at an approximate position of $x/D = 1.5$. Two peaks in the very near wake $x/D < 2$ are present in the PIV data of Parnaudeau et al. (2008). Norberg (1998) also reported two peaks in their study and attributed one of the two peaks to the cross over of mode B streamwise ribs.

Figure 5.11 presents profiles of velocity at 3 downstream locations in the wake: $x/D = 1.06, 1.54, 2.02$. Profiles of $\langle U \rangle$ at $x/D = 1.06$ reveal how inflow turbulence causes an early separation in the shear layers and therefore a small recirculation region. A U-shape is predicted in the laminar inflow case (LI), and with the PIV of Parnaudeau et al. (2008). A V-shape is predicted for the turbulent inflow cases (RGI, FGI), and the PIV of Lourenco and Shih (1993).

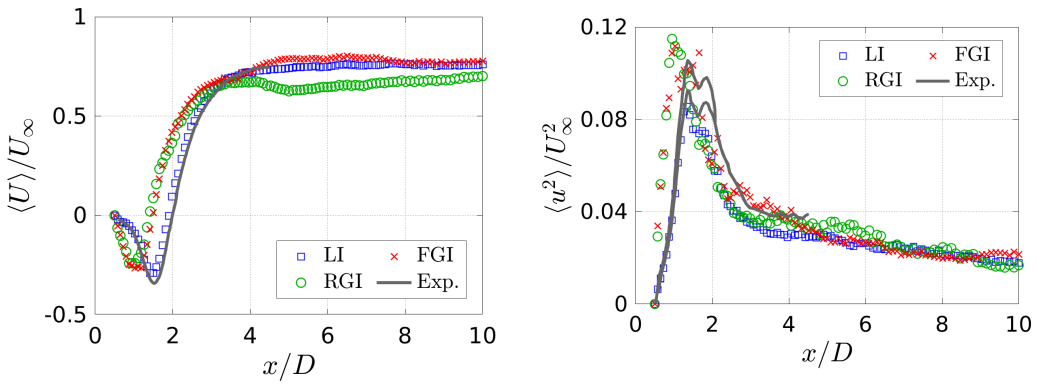

Figure 5.10: Mean streamwise velocity and velocity variance along the wake centreline for the circular cylinder at $Re_D = 3900$. PIV experimental results of Parnaudeau et al. (2008).

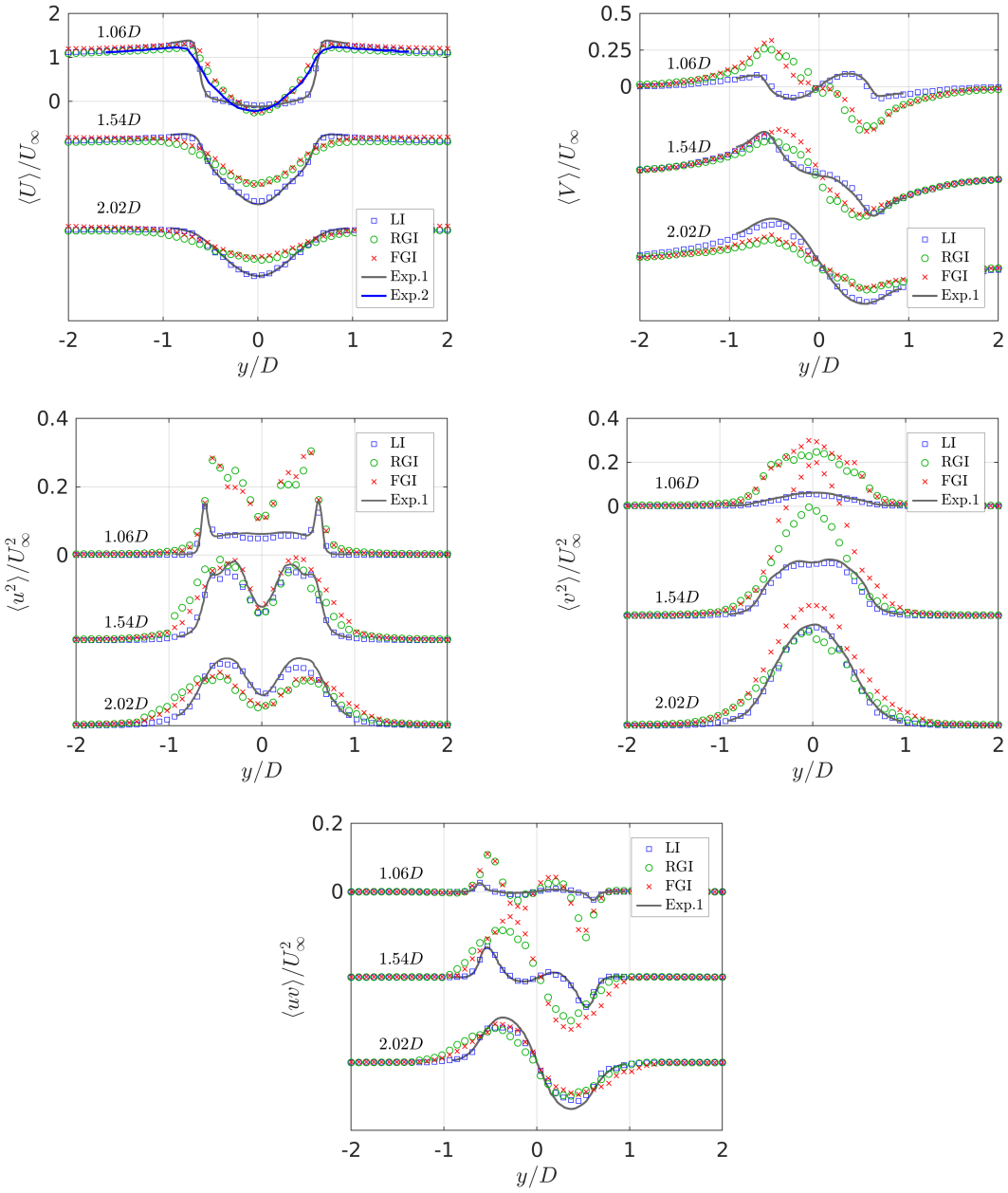

Figure 5.11: Time-averaged velocities in the near wake for 3 streamwise locations: $x/D = 1.06, 1.54, 2.02$. Profiles at $x/D = 1.54$ and $x/D = 2.02$ have been shifted to fit onto the same figure as $x/D = 1.06$. Exp. 1: PIV experimental results of Parnaudeau et al. (2008). Exp. 2: PIV experimental results of Lourenco and Shih (1993).

5.4.2 Phase averaging procedure

Turbulent signals downstream of a wake generator, such as a cylinder, can be decomposed into time-averaged, phase averaged, and stochastic components. Periodic shedding from the cylinder contributes to the phase averaged component of the turbulent signal. For an arbitrary turbulent time series signal $f(t)$, a decomposition is defined by (Hussain and Reynolds, 1970)

$$f = \langle f \rangle + \widetilde{f} + f'' \ , \tag{5.6}$$

where $\langle f \rangle$ is the time-average, $\widetilde{f}$ is the phase averaged component, and f'' is the stochastic component. The phase averaging procedure is defined by

$$\widetilde{f} = \lim_{N \to \infty} \frac{1}{N} \sum_{n=0}^{N} f(t + n\tau) - \langle f \rangle \ , \tag{5.7}$$

for some wave period τ, corresponding to the periodic vortex shedding of the circular cylinder.

To perform phase averaging, a trigger signal is required to determine the wave phase at each time step. Hussain and Reynolds (1970) developed the theory of phase averaging by conducting experiments of flow past ribbons with controlled oscillation. A reference signal can be extracted directly or indirectly from the velocity field by conditional averaging, e.g. Sung and Yoo (2001), Lourenco et al. (1997), Kim et al. (2002). However, a time series of lift on the geometry surface has been generated in the current study, which can be processed to deduce phase information (Braza et al., 2006).

Shedding from the circular cylinder is periodic, which results in a sinusoidal profile of the lift coefficient C_l. Each instance in time corresponds to a phase angle $\varphi \in [-\pi, \pi]$ of shedding. A Hilbert transform of the lift coefficient C_l is taken to yield the phase angle φ for each time step. Time-series of the phase angle is then discretised into 32 bins, such that $\varphi = -\pi + 2\pi(n/32)$, for $n = 0, 1, \ldots, 31$. Figure 5.12 presents the resulting phase averaged lift coefficients $\widetilde{C}_l$ for each simulation. Each profile is symmetrical about $\varphi/\pi = 0$, where a maximum in $\widetilde{C}_l$ is found. This phase corresponds to a vortex shed from the bottom surface of the

circular cylinder. A phase angle of $\varphi/\pi = -1$ corresponds to shedding of a vortex from the top of the circular cylinder, and a minimum in C_l is experienced. The coefficient of lift increases drastically with a turbulent inflow, which has been seen in experiments, albeit for larger Reynolds numbers $Re_D > 1 \times 10^5$ (Blackburn and Melbourne, 1996).

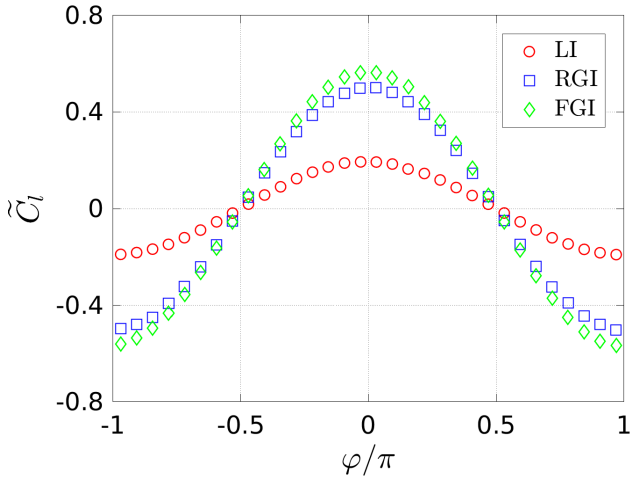

Figure 5.12: Phase averaged coefficient of lift $\widetilde{C}_l$ as a function of phase angle φ/π.

5.4.3 Wake structures

Figure 5.13 display contours of velocity magnitude sampled on a 2D slice along the mid-plane. The plane extends 6 diameters upstream, 14 diameters downstream, and 4 diameters either side. Snapshots have been taken at a phase of $\varphi/\pi = -1$ to allow for a fairer comparison between simulations. This particular phase angle is characterised by the shedding of a vortex from the top of the cylinder. In the laminar inflow case (LI), a well defined von Kármán street is visible. This can also be seen in the turbulent inflow cases, however, there appears to be a breakdown of the primary vortex shedding further downstream.

Although contours of vorticity are commonly used to visualise the flow field and structures, this method is unsuitable for identifying vortices because there is no distinction between shearing, and the swirling motion of a vortex. The

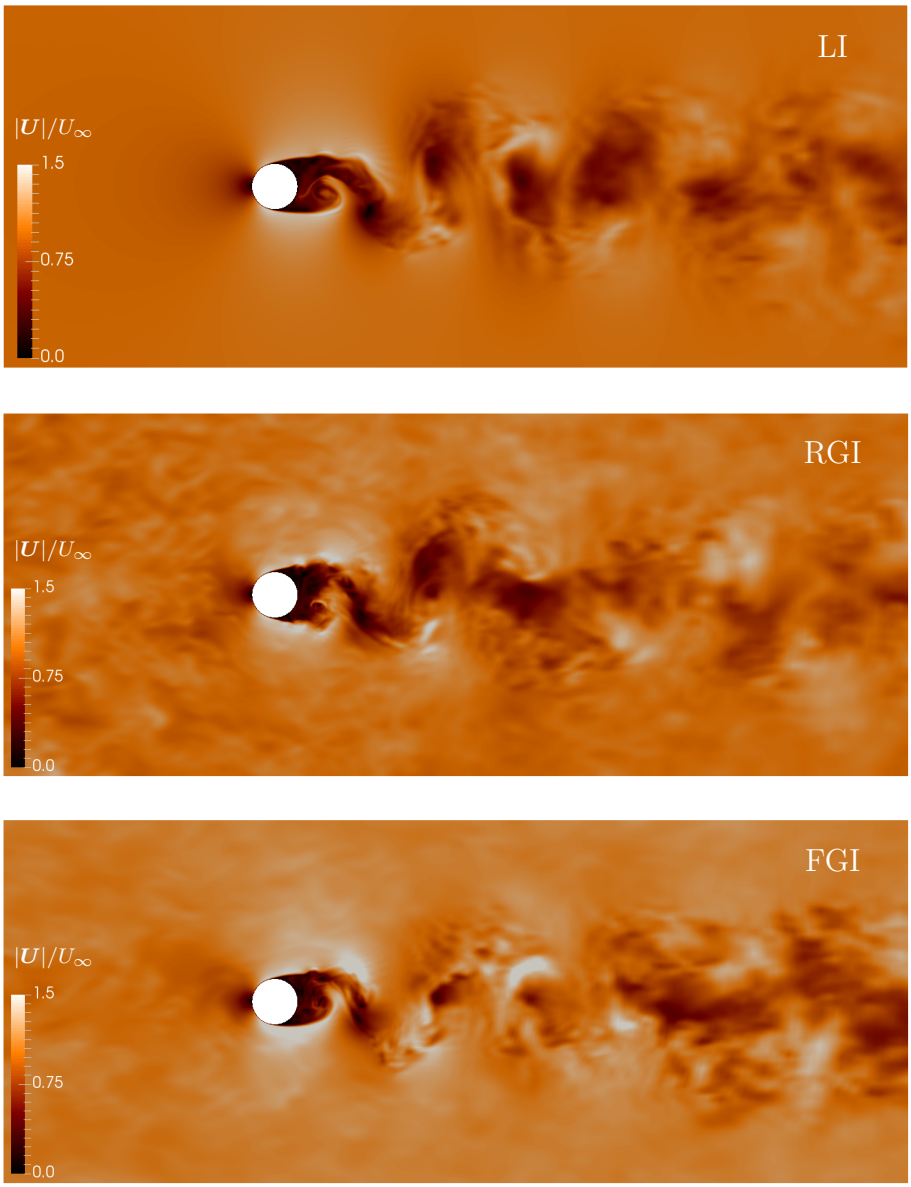

Figure 5.13: Contours of velocity magnitude along the axial mid-plane $z = L_z/2$. Each snapshot is taken at phase angle $\varphi/\pi = -1$.

velocity gradient tensor serves as the starting point for many theories of vortex identification, and there are typically two approaches. The first approach is to

decompose the VGT into strain and rotation rate tensors, $A_{ij} = S_{ij} + \Omega_{ij}$, where

$$S_{ij} = \frac{1}{2}(A_{ij} + A_{ji}) \ , \tag{5.8}$$

$$\Omega_{ij} = \frac{1}{2}(A_{ij} - A_{ji}) \ . \tag{5.9}$$

A second approach is through the characteristic equation. Let λ_i denote the eigenvalues of the VGT, the characteristic equation for A_{ij} is (Hunt et al., 1988)

$$\lambda_i^3 + P\lambda_i^2 + Q\lambda_i + R = 0 \ , \tag{5.10}$$

where P, Q, R are the first, second, and third invariants of the velocity gradient tensor, respectively. The invariants of a second order tensor can be related to its eigenvalues by here utilising properties of the roots of a cubic equation, along with eigenvalue theory (Davidson, 2015)

$$P = (\lambda_1 + \lambda_2 + \lambda_3) = -\text{tr}(A_{ij}) \ , \tag{5.11}$$

$$Q = (\lambda_1\lambda_2 + \lambda_2\lambda_3 + \lambda_3\lambda_1) = -\frac{1}{2}\text{tr}(A_{ij}^2) \ , \tag{5.12}$$

$$R = (\lambda_1\lambda_2\lambda_3) = -\det(A_{ij}) \ . \tag{5.13}$$

The first invariant is zero due to incompressibility, i.e. $P = (\lambda_1 + \lambda_2 + \lambda_3) = 0$. The second invariant is re-written here to highlight its physical importance.

$$Q = -\frac{1}{2}A_{ij}A_{ji} \ , \tag{5.14}$$

$$= -\frac{1}{2}(S_{ij} + \Omega_{ij})(S_{ij} - \Omega_{ij}) \ , \tag{5.15}$$

$$= \frac{1}{2}(\Omega_{ij}\Omega_{ij} - S_{ij}S_{ij}) \ , \tag{5.16}$$

from which it can be seen that the sign of Q is an indicator of the balance between rotation and strain. It is possible to rewrite (5.16) in terms of the vorticity vector

by noting $\Omega_{ij}\Omega_{ij} = \omega_i\omega_i/2$, from which

$$Q = \frac{1}{4}(\omega_i\omega_i - 2S_{ij}S_{ij}) \ , \tag{5.17}$$

$$= Q_\omega + Q_S \ . \tag{5.18}$$

It can also be shown that $Q = \mathrm{tr}(\boldsymbol{H})/2$, where $\boldsymbol{H}$ is the pressure Hessian- see Lesieur et al. (2005) for discussion. The Q-criterion (Hunt et al., 1988), is a vortex identification method which exploits two properties of vortices: (i) vorticity dominates strain such that $Q > 0$, (ii) a local pressure minimum is observed in vortex cores. However, requiring that there is a pressure minimum is a weak argument, as highlighted by Jeong and Hussain (1995)- "Thus, the existence of a local pressure minimum is neither a sufficient nor a necessary condition for the presence of a vortex core in general". Jeong and Hussain (1995) proposed a definition of a vortex from considering the eigenvalues of the symmetric tensor $\boldsymbol{S}^2 + \boldsymbol{\Omega}^2$. If the eigenvalues are ordered such that $\lambda_1 \geq \lambda_2 \geq \lambda_3$, a sufficient condition for a vortex is that $\lambda_2 < 0$.

The third invariant R provides a measure of compression and stretching (Davidson, 2015), therefore Q and R can be used in tandem to classify different regions of turbulence. Every realisation of A_{ij} in a turbulent flow corresponds to a point on the Q-R diagram and can be classified according to the quadrant it lies within. Additional classifications of the Q-R diagram are found by considering the discriminant function for incompressible flow

$$\Lambda_L = Q^3 + \frac{27}{4}R^2 \ . \tag{5.19}$$

Eigenvalues of A_{ij} form a complex conjugate pair when $\Lambda_L > 0$, and this corresponds to closed streamlines (when moving in the Lagrangian reference frame). When $\Lambda_L < 0$, the eigenvalues are real. Table 5.4 provides a classification of vortex behaviour based on the sign of Λ_L and R. Zeros of the discriminant function (5.19) are given by

$$Q^* = -3\left(\frac{R^2}{4}\right)^{1/3} \ . \tag{5.20}$$

	$R > 0$	$R < 0$
$\Lambda_L > 0$	Vortex compression	Vortex stretching
$\Lambda_L < 0$	Bi-axial strain	Axial strain

Table 5.4: Turbulent structure identification from Perry and Chong (1987).

As a reference, a R-Q diagram is constructed from DNS data of forced isotropic turbulence (Li et al., 2008), accessed from the Johns Hopkins turbulence database (Wan et al., 2016). The full data set compromises velocity and pressure fields on a 1024^3 grid for 5028 time samples. Temporal and spatial derivatives are also available. Data in Figure 5.14 has been generated from the velocity gradient tensor at a snapshot in time ($t = 1$). A total of 16^3 uniformly distributed positions are sampled from. Behaviour of the flow at each sample point is classified by its position on the R-Q diagram, which is divided into 6 separate regions ($I - VI$) by the lines $Q = 0$, $R = 0$, and $\Lambda_L = 0$. As hoped, common features of the Q-R diagram for homogeneous isotropic turbulence can be observed. These are: (i) clustering around $R = Q = 0$, (ii) a tear-drop shape with a Vieillefosse tail (Vieillefosse, 1984).

Figure 5.15 presents a view from above the von Kármán vortex street. In the laminar inflow case, the primary rollers are easily identified, and there are no structures in the neighbourhood. This is in contrast to the turbulent inflow simulations, where the vortex sheet is less well defined, and structures from the free-stream turbulent flow are engulfed into the wake. Figure 5.16 presents the same field of Q isocontours from a side view. Each wake looks similar- the primary shedding structures are identified, and there are streamwise ribs running between the rollers.

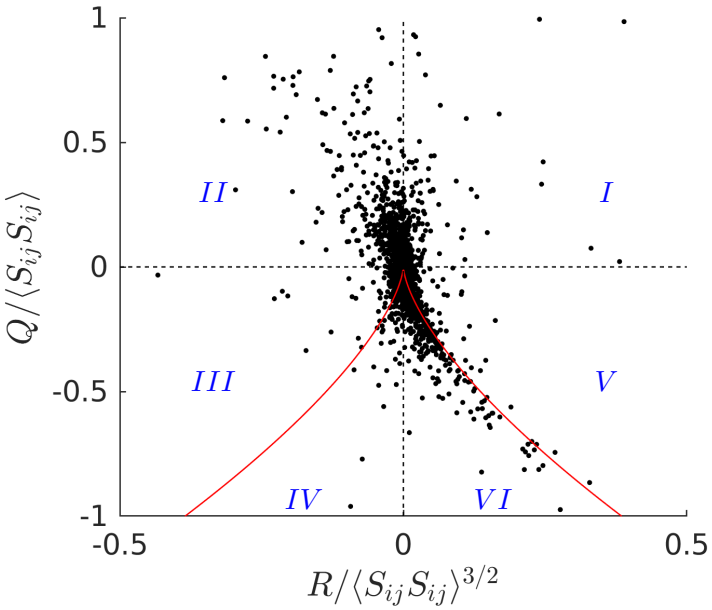

Figure 5.14: *R-Q* diagram constructed from results of triply periodic, forced isotropic turbulence DNS of Li et al. (2008). The discriminant function $\Delta_L = 0$ has been represented as a solid red line.

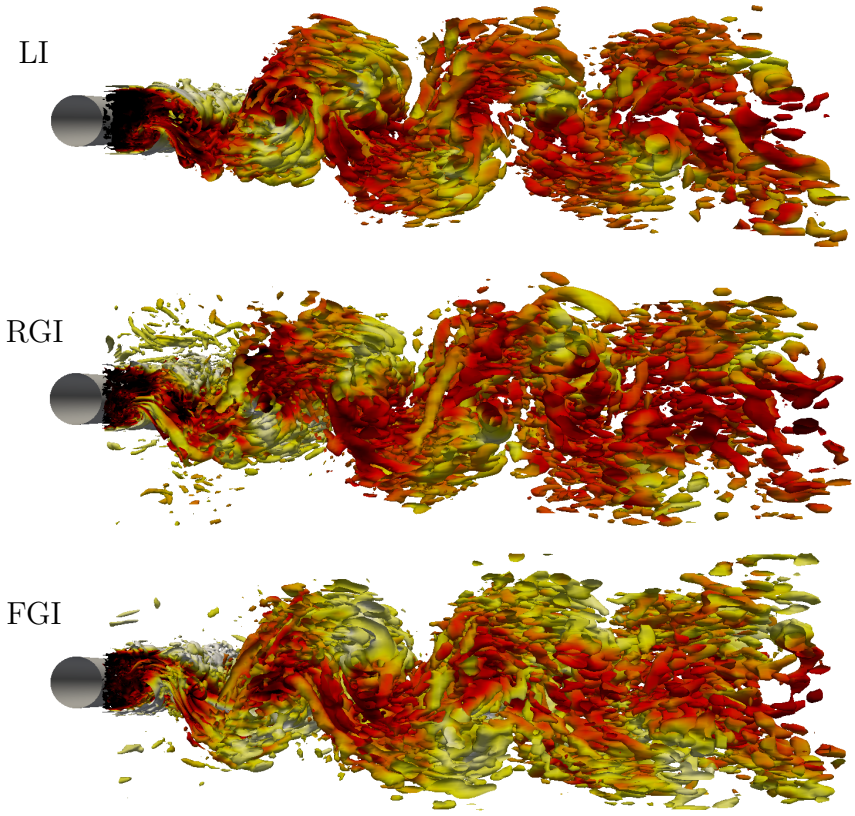

Figure 5.15: Snapshot of the circular cylinder wake for each inflow case. Coherent structures are visualised by isovolumes of $Q = 10000$, and coloured by normal velocity V to highlight the different sides of the primary vortex rollers. Each snapshot is taken at phase angle $\varphi/\pi = -1$.

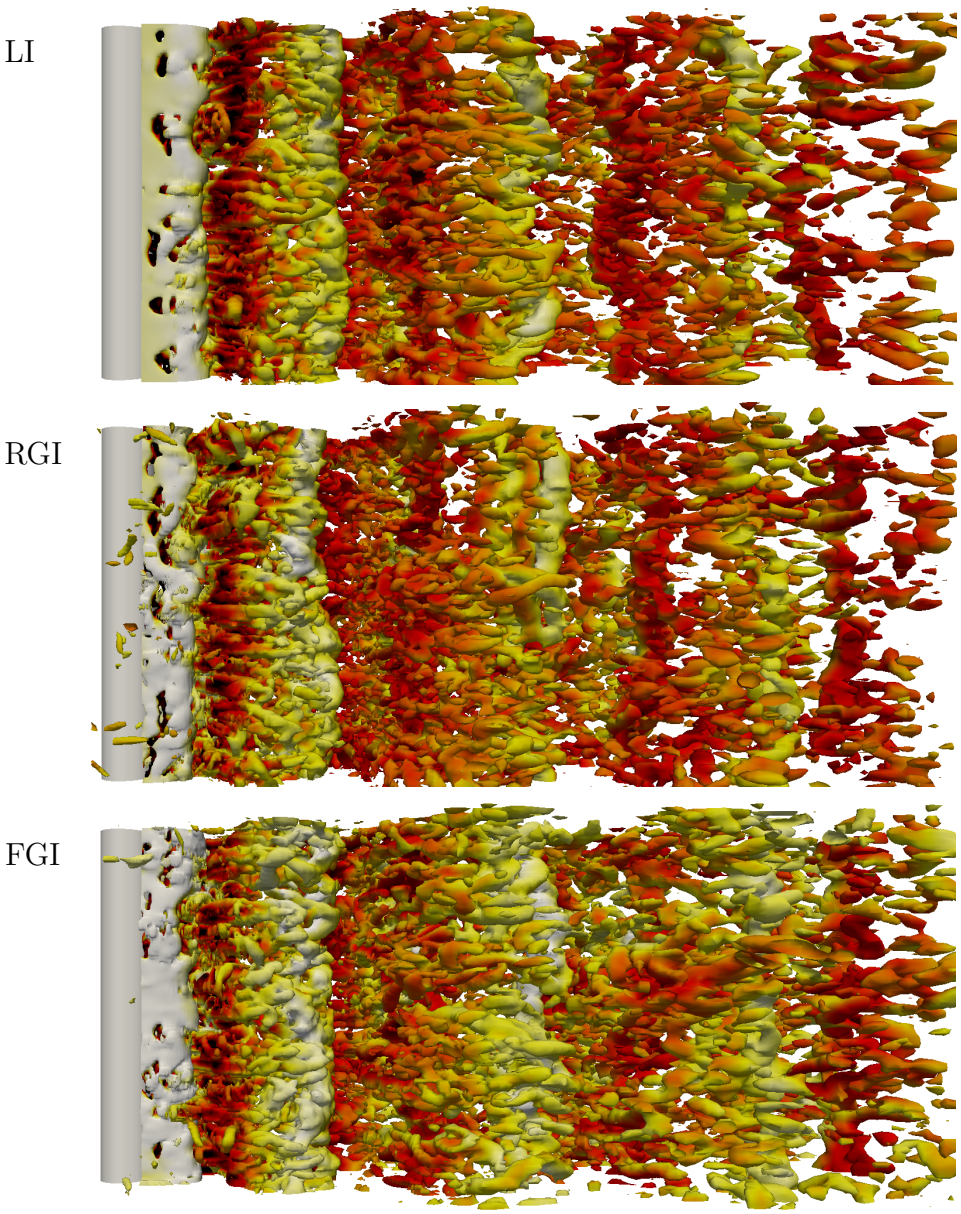

Figure 5.16: Snapshot of coherent structures in the circular cylinder wake for each inflow case. See Figure 5.15 for further description.

5.4.4 Role of non-normality

In Figure 5.17, contours of $Q = 5000$ coloured by V are presented for the case of the laminar inflow at $Re_D = 3900$. To compare the cylinder wakes produced by each inlet grid, only a small portion of the computational domain is considered. A sampling box is centred at $(x, y, z) = (5D, 0, 0)$ and extends $10D$ in the streamwise direction, and $4D$ in both the normal and axial direction. As can be seen in Figure 5.17, the chosen location of the box covers a number of primary and secondary shedding structures (Williamson, 1996).

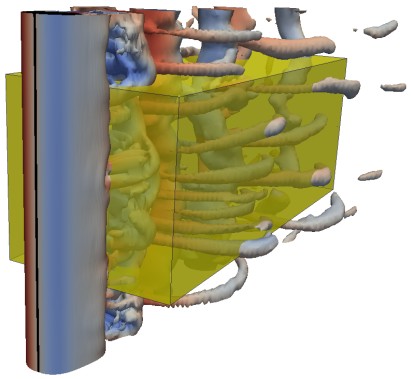

Figure 5.17: Snapshot of the cylinder wake for the laminar inflow case (LI). Coherent structures are visualised by isovolumes of $Q = 5000$, and coloured by normal velocity V to highlight the different sides of the primary vortex rollers. The region of interest for the present study is highlighted by a faint yellow box in the cylinder wake.

Figure 5.18 displays the Q-R diagram for each inflow condition. The percentage of points which lie in each region is marked in square brackets. Each Q-R diagram takes on a classical tear-drop shape, and there is significant clustering around the Vieillefosse tail. Interestingly, despite the changes in wake dynamics between a laminar and turbulent inflow, each region contains approximately the same percentage of points across each inlet condition.

Keylock (2018) introduced an alternative approach to analysing the VGT by first taking a Schur decomposition. The VGT is decomposed by $\boldsymbol{A} = \boldsymbol{B} + \boldsymbol{C}$, where $\boldsymbol{B}$ contains dynamics driven by the eigenvalues, and $\boldsymbol{C}$ contains non-normal

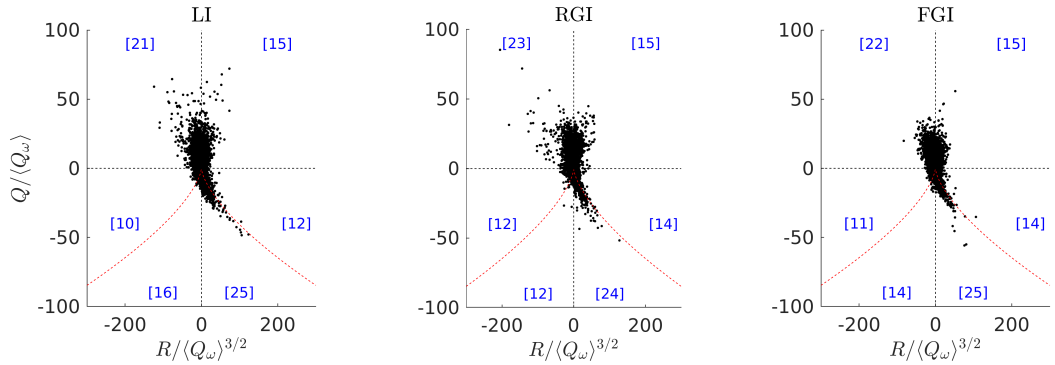

Figure 5.18: Q-R diagram for each inflow case. Each region is marked by the percentage of points occupied within that region.

effects of the VGT. A measure of normal versus non-normal dynamics is therefore

$$\kappa_{\mathrm{B,C}} = \frac{\|\boldsymbol{B}\| - \|\boldsymbol{C}\|}{\|\boldsymbol{B}\| + \|\boldsymbol{C}\|} \quad . \tag{5.21}$$

Figure 5.19 displays the joint probability distribution for marker $\kappa_{\mathrm{B,C}}$, conditioned on each region of the Q-R diagram. Also plotted are profiles of $p(\kappa_{\mathrm{B,C}})$ from Keylock (2018), produced from the HIT data of Li et al. (2008). The greatest departure from HIT comes in regions 4 and 6 for the laminar inflow case, where profiles of $p(\kappa_{\mathrm{B,C}})$ are skewed towards unity. This corresponds to clustering around the Vieillefosse tail. By definition, as $\kappa_{\mathrm{B,C}} \rightarrow 1$, normal effects dominate non-normal effects. As turbulence is introduced into the free-stream flow, the profile $p(\kappa_{\mathrm{B,C}})$ moves towards the results obtained from HIT.

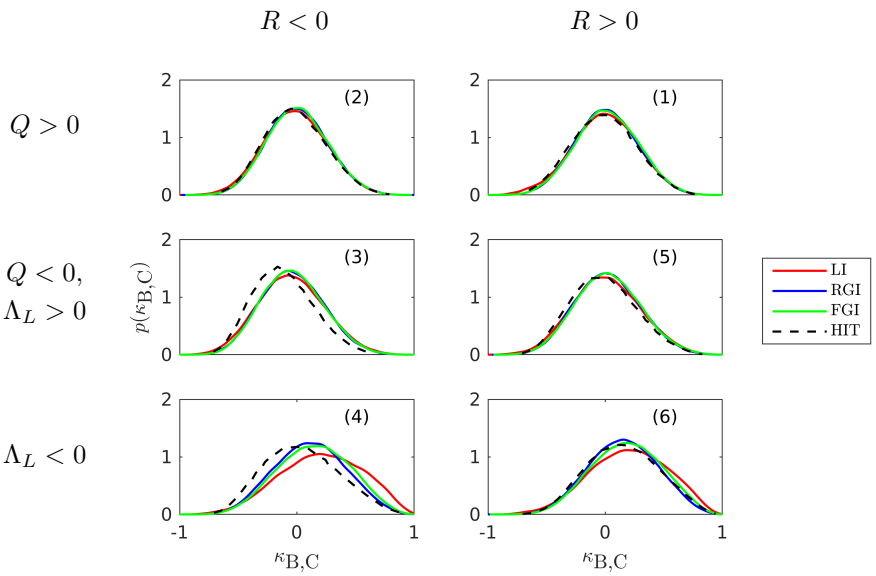

Figure 5.19: Probability distribution function of $\kappa_{\mathrm{B,C}}$ for each region in the Q-R space. HIT results reproduced from Keylock (2018).

5.5 Dissipation in the wake

5.5.1 Surrogates of dissipation

An introduction to the dissipation rate ε was provided in Chapter 2. To summarise here: the dissipation rate is a key feature of any turbulent flow (Sreenivasan and Antonia, 1997; Vassilicos, 2015), but is difficult to accurately obtain experimentally (Wallace, 2009). As a result, researchers enforce approximations and take surrogates of ε. The full dissipation rate is given by (Hinze, 1975)

$$\varepsilon = \nu \left[\left\langle \frac{\partial u_i}{\partial x_j} \frac{\partial u_i}{\partial x_j} \right\rangle + \left\langle \frac{\partial u_i}{\partial x_j} \frac{\partial u_j}{\partial x_i} \right\rangle \right] \quad , \tag{5.22}$$

where Einstein summation convention is used over repeated indices. The 12 terms contained in (5.22) are

$$\begin{aligned} \varepsilon = \nu \Bigg[& 2 \underbrace{\left\langle \left(\frac{\partial u}{\partial x} \right)^2 \right\rangle}_{1} + \underbrace{\left\langle \left(\frac{\partial v}{\partial x} \right)^2 \right\rangle}_{2} + \underbrace{\left\langle \left(\frac{\partial w}{\partial x} \right)^2 \right\rangle}_{3} + \underbrace{\left\langle \left(\frac{\partial u}{\partial y} \right)^2 \right\rangle}_{4} \\ & + 2 \underbrace{\left\langle \left(\frac{\partial v}{\partial y} \right)^2 \right\rangle}_{5} + \underbrace{\left\langle \left(\frac{\partial w}{\partial y} \right)^2 \right\rangle}_{6} + \underbrace{\left\langle \left(\frac{\partial u}{\partial z} \right)^2 \right\rangle}_{7} + \underbrace{\left\langle \left(\frac{\partial v}{\partial z} \right)^2 \right\rangle}_{8} \\ & + 2 \underbrace{\left\langle \left(\frac{\partial w}{\partial z} \right)^2 \right\rangle}_{9} + 2 \underbrace{\left\langle \frac{\partial u}{\partial y} \frac{\partial v}{\partial x} \right\rangle}_{10} + 2 \underbrace{\left\langle \frac{\partial u}{\partial z} \frac{\partial w}{\partial x} \right\rangle}_{11} + 2 \underbrace{\left\langle \frac{\partial v}{\partial z} \frac{\partial w}{\partial y} \right\rangle}_{12} \Bigg] \quad . \end{aligned} \tag{5.23}$$

In Chapter 4, individual terms of (5.23) were calculated for simulations of grid turbulence. Each grid geometry produced unique initial conditions of turbulence and dissipation. Differences in the dissipation between each grid design can be explained by the contribution of each term in (5.23). It was shown that in the wake of turbulence-generating grids, large-scale anisotropy is present near grid,

therefore the isotropic form of dissipation

$$\varepsilon_{\text{iso}} = 15\nu \left\langle \left(\frac{\partial u}{\partial x} \right)^2 \right\rangle \quad , \tag{5.24}$$

is unsuitable near grid. Even in the far field (20 mesh spacings or 40 integral length scales for the regular grid), ε_{iso} underestimated ε by approximately 5-10%. If two components of velocity are measured, perhaps from an X-wire probe, dissipation can be calculated from

$$\varepsilon_{\text{xw}} = 3\nu \left[\left\langle \left(\frac{\partial u}{\partial x} \right)^2 \right\rangle + 2 \left\langle \left(\frac{\partial v}{\partial x} \right)^2 \right\rangle \right] \quad . \tag{5.25}$$

If homogeneity is assumed in the transverse plane (y-z plane of Figure 5.1), such as in the wake of a square cylinder, it can be shown that $\langle (\partial v/\partial y)(\partial w/\partial z) \rangle \approx \langle (\partial v/\partial z)(\partial w/\partial y) \rangle$ (Lefeuvre et al., 2014). This is combined with the continuity equation and (5.23) to yield

$$\begin{aligned} \varepsilon_{yz} = \nu \Bigg[& 4 \left\langle \left(\frac{\partial u}{\partial x} \right)^2 \right\rangle + \left\langle \left(\frac{\partial v}{\partial x} \right)^2 \right\rangle + \left\langle \left(\frac{\partial w}{\partial x} \right)^2 \right\rangle + \left\langle \left(\frac{\partial u}{\partial y} \right)^2 \right\rangle \\ & + \left\langle \left(\frac{\partial w}{\partial y} \right)^2 \right\rangle + \left\langle \left(\frac{\partial u}{\partial z} \right)^2 \right\rangle + \left\langle \left(\frac{\partial v}{\partial z} \right)^2 \right\rangle \\ & + 2 \left\langle \frac{\partial u}{\partial y} \frac{\partial v}{\partial x} \right\rangle + 2 \left\langle \frac{\partial u}{\partial z} \frac{\partial w}{\partial x} \right\rangle - 2 \left\langle \frac{\partial v}{\partial z} \frac{\partial w}{\partial y} \right\rangle \Bigg] \quad . \end{aligned} \tag{5.26}$$

Figure 5.20 displays the centreline development of ε for the laminar inflow case ran at $Re_D = 3900$. Also plotted are the surrogates ε_{iso}, ε_{xw}, and ε_{yz}. In the most complete study of dissipation in the wake of a circular cylinder, Chen et al. (2018) used ε_{yz} as a reference value for ε. However, without direct measurements of ε, it is unknown how closely ε_{yz} represents the true dissipation. In the current study it can be seen that ε_{yz} is indeed the closest approximation to ε. Surprisingly, ε_{iso} performs better than ε_{xw}, despite containing less terms of the VGT.

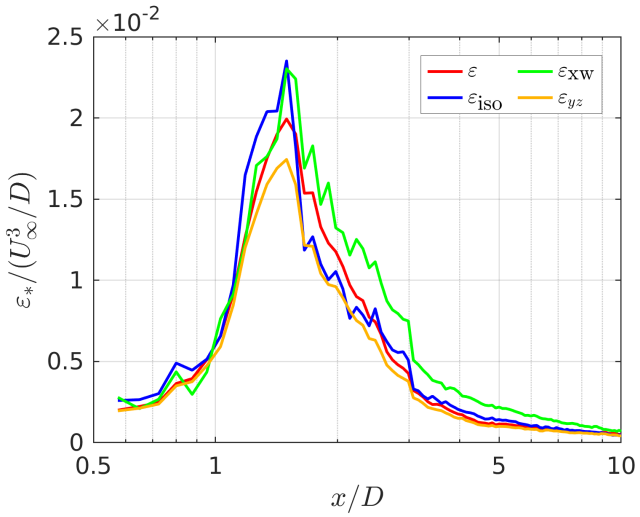

Figure 5.20: Wake centreline profiles of dissipation ε and surrogates for the laminar inflow case (LI) ran at $Re_D = 3900$.

5.5.2 Phase averaged dissipation

A property of the phase averaging procedure is that dissipation $\varepsilon = 2\nu\langle S_{ij}S_{ij}\rangle$ can be decomposed into phase averaged and stochastic components (Hussain and Reynolds, 1970; Alves Portela et al., 2018), such that

$$\varepsilon = 2\nu\langle \widetilde{S}_{ij}\widetilde{S}_{ij}\rangle + 2\nu\langle S''_{ij}S''_{ij}\rangle \ , \tag{5.27}$$

where $\widetilde{S}_{ij}$ and S''_{ij} are the strain rate of phase averaged and stochastic velocity components, respectively.

Surrogates of ε have been introduced, which enforce certain assumptions on the local turbulence. The level of accuracy for these surrogates was demonstrated for the circular cylinder wake in Figure 5.20. However, here a different approach will be taken. The first step is to take the form given in the decomposition (5.27), and reduce both the coherent and stochastic terms to a simpler form. In the analysis that follows, stochastic motions are assumed to be isotropic, while phase averaging requires separate treatment.

The stochastic component is considered first, and written out in full form

$$\varepsilon'' = 2\nu\langle S''_{ij}S''_{ij}\rangle \ , \tag{5.28}$$

$$= 2\nu\left\langle (S''_{11})^2 + (S''_{22})^2 + (S''_{33})^2 + 2(S''_{12})^2 + 2(S''_{13})^2 + 2(S''_{23})^2 \right\rangle \ , \tag{5.29}$$

where the symmetry property of the rate of strain tensor ($S_{ij} = S_{ji}$) has been used. The small scales are not strongly affected by the type of wake generator, and isotropy is a reasonable assumption for the small scales for both the square and circular cylinder (Thiesset et al., 2013). By assuming local isotropy, an estimation of ε for 2D planar PIV was provided by Tanaka and Eaton (2007). The same treatment is applied here for stochastic motions, from which the following conditions are enforced

$$2\langle (S''_{33})^2\rangle = \langle (S''_{11})^2\rangle + \langle (S''_{22})^2\rangle \ , \tag{5.30}$$

$$\langle (S''_{12})^2\rangle = \langle (S''_{23})^2\rangle = \langle (S''_{13})^2\rangle \ , \tag{5.31}$$

to yield, on substitution into (5.29), an estimation for the stochastic dissipation on the x-y plane is given by

$$\varepsilon''_{xy} = 3\nu\left[\langle (S''_{11})^2\rangle + \langle (S''_{22})^2\rangle + 4\langle (S''_{12})^2\rangle\right] \ . \tag{5.32}$$

The rate of strain for the phase averaged velocity field is now considered. Large scale motions in the cylinder wake are anisotropic (Thiesset et al., 2013), therefore the same treatment used to arrive at (5.32) cannot be followed for the phase averaged component. Chen et al. (2018) measured velocity derivatives in the wake of a circular cylinder and found $\widetilde{(\partial u/\partial y)^2}$ and $\widetilde{(\partial v/\partial x)^2}$ to be at least an order of magnitude larger than the remaining phase averaged velocity derivatives. This is because the coherent shedding vortices are associated with the coherent spanwise vorticity $\widetilde{\omega}_z (= \widetilde{\partial v/\partial x} - \widetilde{\partial u/\partial y})$. If the coherent shedding vortices are associated with ω_z, this process is largely two-dimensional, and the phase averaged component of axial velocity is therefore negligible, such that it can be assumed $\widetilde{w} = 0$, and $S^2_{33} = 0$. It is also assumed that phase averaged velocities do not vary in the z-direction, such that $\partial\widetilde{u}_i/\partial z = 0$. A similar method was followed by Alves Portela et al. (2018) for the square-cylinder, who collapsed their DNS

data onto one plane by averaging in the spanwise direction to improve statistical convergence. The form of (5.29) for a phase averaged field is therefore

$$\widetilde{\varepsilon}_{xy} = 2\nu \left[\langle (\widetilde{S}_{11})^2 \rangle + \langle (\widetilde{S}_{22})^2 \rangle + 2\langle (\widetilde{S}_{12})^2 \rangle \right] \quad . \tag{5.33}$$

It is encouraging to see the $\widetilde{S}_{12}^2$ term is retained in (5.33), because this is the major contributor to $\widetilde{\varepsilon}$ (Chen et al., 2018). The dissipation term has been split into phase averaged and stochastic components, from which it is assumed that stochastic motions are isotropic, and phase averaged fields do not vary along the axial direction. This results in stochastic and phase averaged terms (5.32) and (5.33), which can be combined to obtain the full form of dissipation

$$\varepsilon_{xy} = \widetilde{\varepsilon}_{xy} + \varepsilon''_{xy} \quad . \tag{5.34}$$

Figure 5.21 presents centreline dissipation ε for the circular cylinder laminar inflow case. Also included are the reference value ε_{yz} used in Chen et al. (2018), and ε_{xy} developed in this chapter. A close agreement between ε and ε_{xy} can be observed, even at the peak level of dissipation.

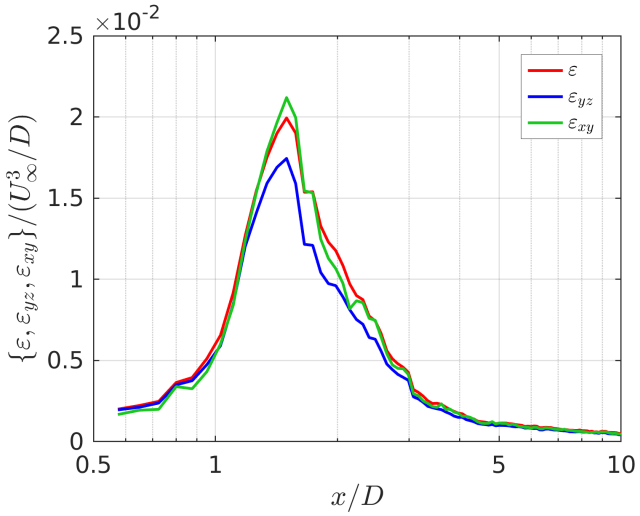

Figure 5.21: A comparison between surrogates of dissipation along the wake centreline for the laminar inflow case.

To understand how coherent and stochastic motions contribute to the velocity

gradient tensor, individual terms are introduced

$$C_{ij} = \frac{\langle(\widetilde{A}_{ij})^2\rangle}{\left(\frac{U_\infty}{D}\right)^2} \quad , \quad F_{ij} = \frac{\langle(A''_{ij})^2\rangle}{\left(\frac{U_\infty}{D}\right)^2} \quad , \tag{5.35}$$

where $\widetilde{A}_{ij} = \partial\widetilde{u}_i/\partial x_j$ and $A''_{ij} = \partial u''_i/\partial x_j$ are the velocity gradient tensors of the coherent and stochastic motions, respectively. Figure 5.22 plots each term of C_{ij} and F_{ij} for the laminar inflow case. It is immediately clear that C_{12} and C_{21} are major contributors to dissipation of coherent motions. This result supports the findings of Chen et al. (2018), i.e. terms associated with coherent spanwise vorticity $\widetilde{\omega}_z(= \widetilde{\partial v/\partial x} - \widetilde{\partial u/\partial y})$ are approximately one order of magnitude larger than other terms.

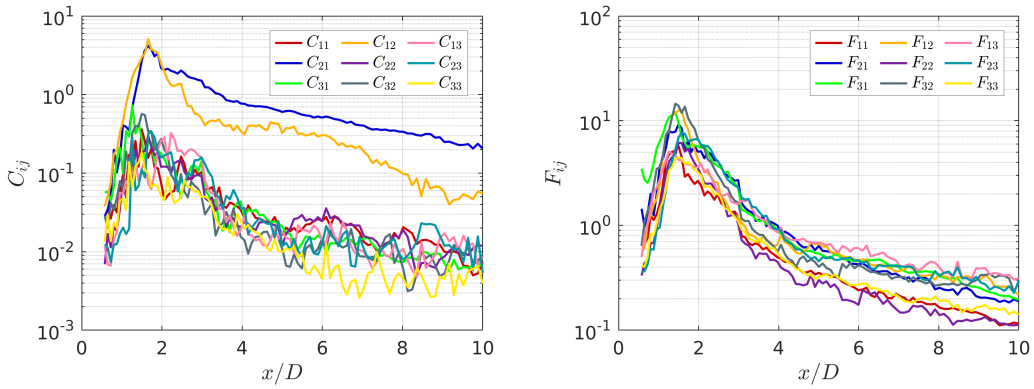

Figure 5.22: Comparison between terms C_{ij} and F_{ij} along the wake centreline for the laminar inflow case.

In addition to this, isotropy conditions (5.30), (5.31) have been enforced on the stochastic motions. To test the validity of these assumptions, the following are calculated

$$K_1 = \frac{\langle(S''_{11})^2\rangle + \langle(S''_{22})^2\rangle}{2\langle(S''_{33})^2\rangle} \quad , \quad K_2 = \frac{\langle(S''_{23})^2\rangle}{\langle(S''_{12})^2\rangle} \quad , \quad K_3 = \frac{\langle(S''_{13})^2\rangle}{\langle(S''_{12})^2\rangle} \quad , \tag{5.36}$$

where for isotropy it would be expected to find $K_1 = K_2 = K_3 = 1$. Figure 5.23 plots each isotropy condition, and K_1, K_2, K_3 are all reasonably close to their isotropic value. This strengthens the approach taken in this chapter to arrive at ε_{xy}.

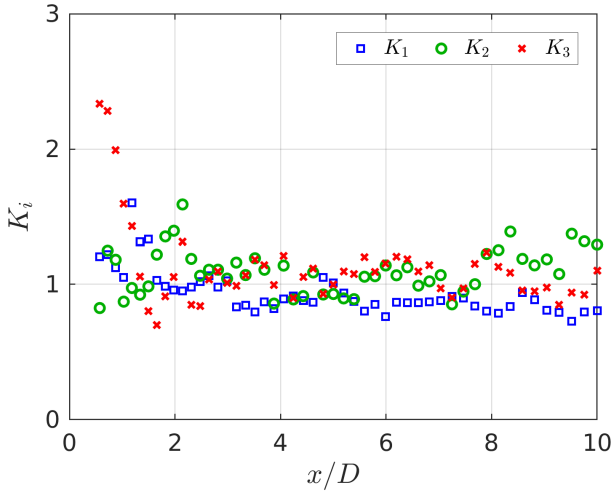

Figure 5.23: Measure of isotropy K for the laminar inflow circular cylinder wake. Every second data point is plotted for image clarity.

The ratio of stochastic to phase averaged components is shown in Figure 5.24. Although dissipation through stochastic motions is significantly larger than dissipation through coherent motions, the ratio between the two is reasonably constant for all inflow cases. This constancy in the ratio $\varepsilon''/\widetilde{\varepsilon}$ has been argued to arise from a locking between stochastic and coherent motions, and has been identified in the wake of a square cylinder (Alves Portela et al., 2018). Additionally, it is suggested that a locking between the two may be a cause of non-equilibrium turbulence (Goto and Vassilicos, 2015; Alves Portela et al., 2018).

5.5.3 Circular cylinder wake model

This chapter concludes with a look into the relationship between coherent structures in the circular cylinder wake and the dissipation field ε. In the current simulations, snapshots of the dissipation field have been collected. Each snapshot is taken at the same phase angle ($\varphi/\pi = -1$), and the wake is cropped to isolate 5 streamwise rollers. Contours of $Q = 15000$ are generated to visualise coherent structures, and isovolumes of $\exp(-\varepsilon) \in [0, 0.75]$ highlight regions of intense dissipation. Thresholds of Q and $\exp(-\varepsilon)$ were varied and chosen by trial and error to isolate primary rollers and streamwise ribs. Figures 5.25 and 5.26 display

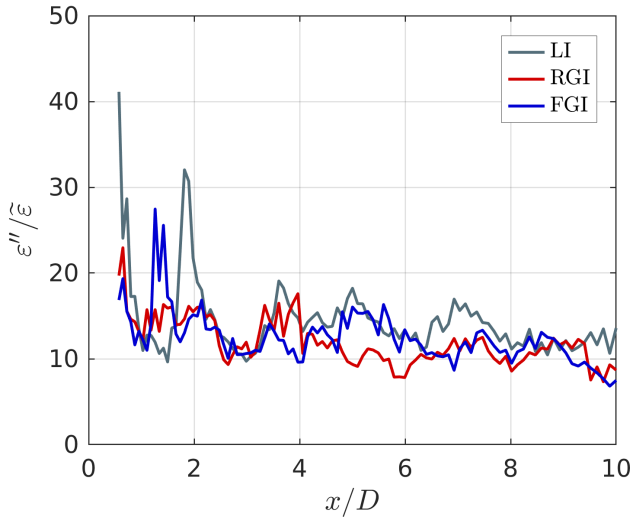

Figure 5.24: Ratio of stochastic to phase averaged dissipation along the centreline for the laminar inflow case.

structures in the wake for each inflow condition. When the turbulence dissipation field is viewed in isolation, it takes the same shape as the von Kármán vortex street. This is to be expected, but it is not immediately clear if the dissipation field is linked to the primary rollers. However, when the Q field is included, it becomes apparent that dissipation resides in between the streamwise ribs. This is confirmed in Figure 5.27 which provides a closer look at the wake structures and dissipation field for the laminar inflow case.

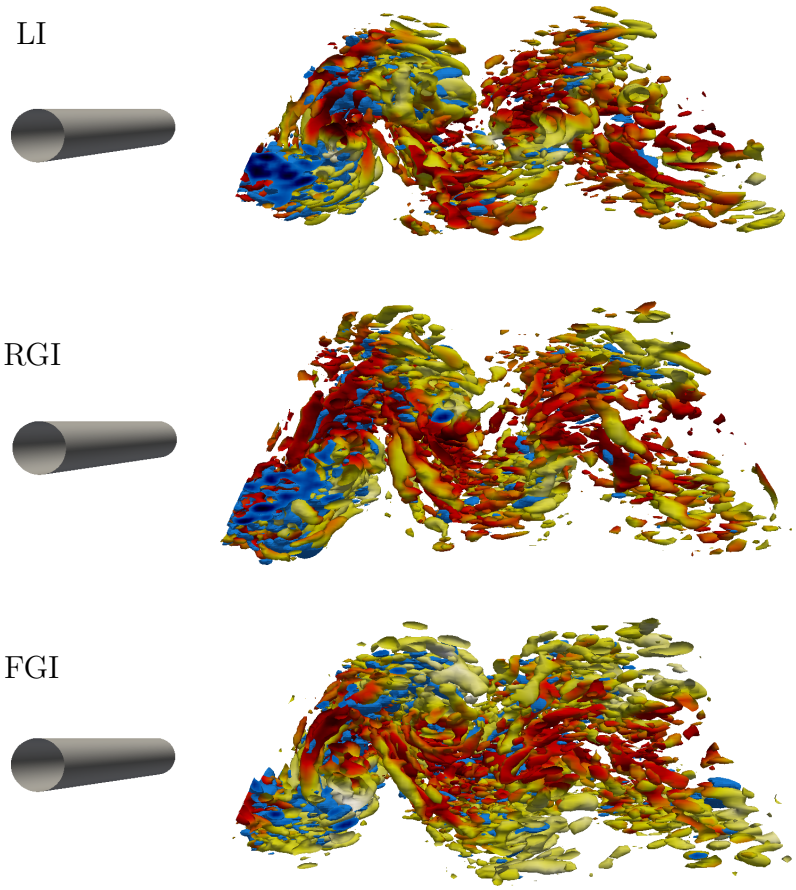

Figure 5.25: Top view of coherent structures and dissipation in the circular cylinder wake. Isocontours of $Q = 15000$ are coloured (dark red to yellow) by velocity magnitude $|\boldsymbol{U}|$. Dissipation is visualised by isovolumes of $\exp(-\varepsilon) \in [0, 0.75]$. Only a portion of the wake has been visualised to isolate 5 primary rollers.

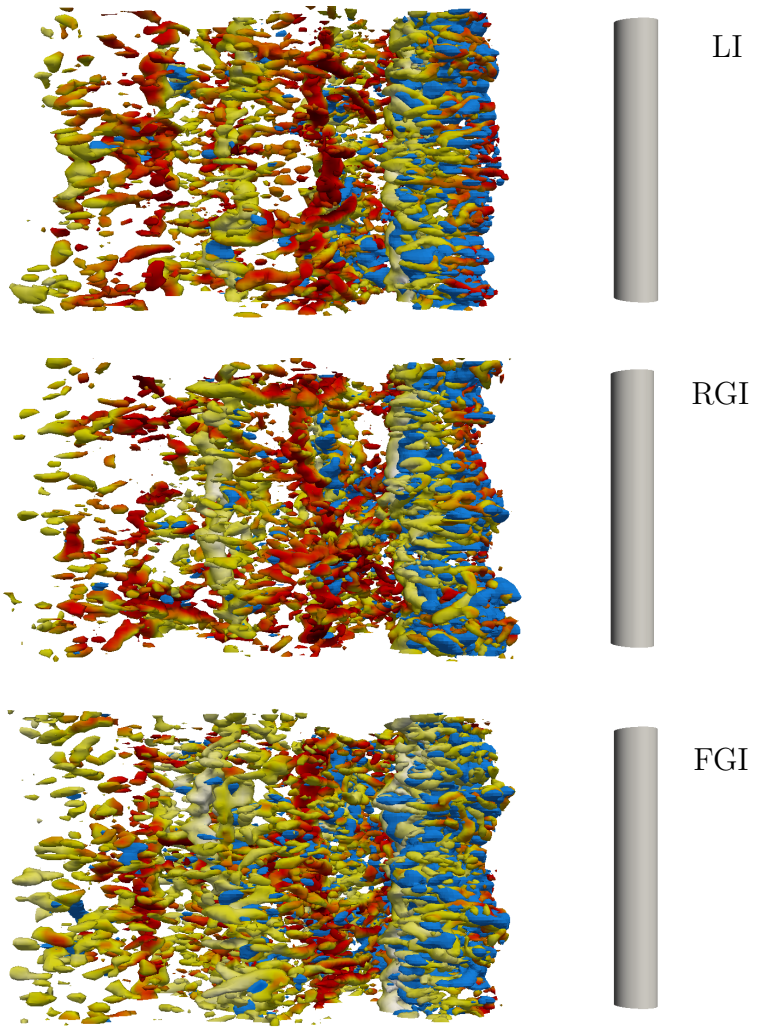

Figure 5.26: Side view of coherent structures in the wake. See Figure 5.25 for further description.

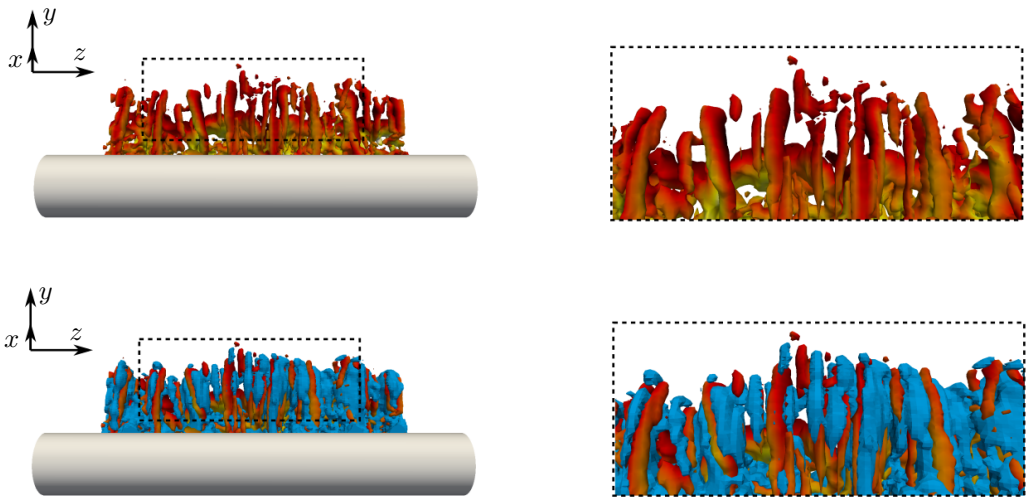

Figure 5.27: A closer look at the structures and dissipation field in the cylinder wake for the laminar inflow case.

With the findings from the current chapter, the model of Chen et al. (2018) is returned to. Hussain and Hayakawa (1987) concluded that dissipation is concentrated in regions of high mixing, however, Chen et al. (2018) proposed that it resides in the primary rollers. Neither study allowed for the presence of streamwise ribs, because the X-wire probes used in their wind tunnel experiments only detected periodic shedding, which is attributed to the primary rollers. An alternative model is proposed here in Figure 5.28, which incorporates findings from the current chapter. Dissipation resides in between streamwise ribs, which has been identified in both the laminar and turbulent inflow cases.

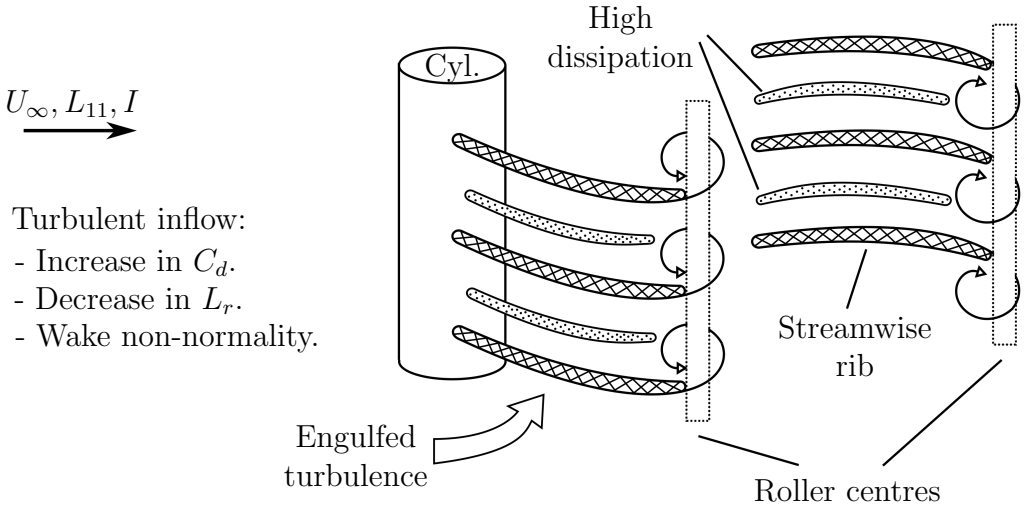

Figure 5.28: Topological features of the circular cylinder wake, adapted from the model of Chen et al. (2018), and extended into the third dimension $\hat{z}$. Strands of concentrated dissipation are present in between streamwise ribs.

5.6 Chapter conclusions

The influence of free-stream turbulence on the flow past a cylinder at Reynolds number $Re_D = 3900$ has been investigated through large-eddy simulation. Turbulence has been generated in the free-stream by projecting regular (RGI) and fractal (FGI) grids onto the inlet patch. A laminar inflow (LI) has also been simulated as the base case for this flow, which allows for validation of the numerical method. The RGI case produces a turbulent inflow with integral length scale $L_{11} = 0.67D$ and turbulence intensity $I = 7.3\%$, compared to the FGI case where $L_{11} = 0.56D$ and $I = 4.1\%$.

Time-averaged profiles of velocity in the wake for the turbulent inflow cases reveal a shortened development. This results in a shorter recirculation length, and a reduced velocity deficit. This effect has been observed in previous experiments. The PIV of Lourenco and Shih (1993) has been used as a benchmark for validation of numerical models in the past. However, inflow conditions were undocumented, and an unspecified level of turbulence was introduced into the free-stream. In contrast, the PIV of Parnaudeau et al. (2008) had low levels of free-stream turbulence ($I < 0.1\%$), and their results match with the current laminar inflow (LI) case. Aerodynamic properties of the circular cylinder have also been altered. Inflow turbulence has been shown to significantly increase the coefficient of drag, from $\langle C_d \rangle = 1.03$ in the laminar case, to 1.18 and 1.37 in the regular and fractal grid cases, respectively. It is surprising to see such a drastic increase between the regular and fractal grid cases, because free-stream turbulence intensity and integral length scales are comparable between the two simulations.

Primary vortex rollers and streamwise ribs are identified in both the laminar and turbulent inflow cases. However, free-stream turbulence has contributed to a break down of these coherent structures. The Q-R diagram is constructed from a snapshot of each wake. There is little difference between each case, which is most likely due to the universality of turbulence. However, inflow turbulence has been seen to drastically alter the parameter $\kappa_{\mathrm{B,C}}$, which is a measure of normal to non-normal dynamics. The laminar inflow case produces a wake which skews the probability distribution function of $\kappa_{\mathrm{B,C}}$ towards unity, indicating that normal contributions in the shedding modes are dominant. When the inflow is turbulent,

profiles of $p(\kappa_{\mathrm{B,C}})$ shift towards a mean value of zero, approaching results obtained from HIT. Therefore, non-normality plays a greater role in the wake dynamics of the cylinder when free-stream conditions are turbulent.

Commonly used surrogates for the dissipation field have been compared for the circular cylinder wake. A reasonable agreement was achieved with ε_{yz}, which is derived on an assumption of homogeneity in the transverse plane. The isotropic and X-wire forms of dissipation were less successful. The velocity gradient tensor has been decomposed into coherent and stochastic components. The coherent portion accounts for periodic shedding from the circular cylinder wake, and is associated with the primary rollers. The stochastic component is a measure of the background turbulence level. From this decomposition it is possible to calculate the dissipation field for the coherent $\widetilde{\varepsilon}$ and stochastic ε'' motions. The ratio $\varepsilon''/\widetilde{\varepsilon}$ has been computed for each simulation, and it is found to be constant in the region $x/D < 10$. This has been attributed in the literature to a locking effect between coherent and stochastic cascades, and may indicate non-equilibrium behaviour.

It has been demonstrated that $\widetilde{\varepsilon}$ is dominated by the two-dimensional primary rollers, and that ε'' arises from approximately isotropic motions. From this it is possible to reduce the amount of terms required to estimate $\widetilde{\varepsilon}$ and ε'', and their sum returns a surrogate of ε which only requires measurements of the VGT on the x-y plane, denoted here by ε_{xy}. Calculation of ε_{xy} only requires two-components of velocity, it is therefore suitable when only a two-dimensional plane of the flow field is sampled, such as with planar PIV. This will be explored further in Chapter 7, when measurements of the circular cylinder wake are collected experimentally using planar PIV.

A model has been proposed which describes the interaction of coherent motions and dissipation in the circular cylinder wake. This has built upon the previous work of Chen et al. (2018), who suggested that dissipation is concentrated in the primary rollers. Results from the current chapter are in disagreement with this conclusion. It is found that dissipation resides between streamwise ribs. More work is required to understand the interaction between dissipation and coherent structures.

Chapter 6

Experimental set-up

Experiments in the present study were performed in the Sorby Environmental Fluid Dynamics Laboratory, University of Leeds. The experimental set-up is described in this chapter, including the recirculating water flume, biplane turbulence generating grid, and circular cylinder design. Free-stream flow conditions are profiled using acoustic Doppler velocimetry probes. The technique of particle image velocimetry is then detailed for the current experiments.

6.1 Flume components

Tests were carried out in the open surface hydraulic recirculating flume in the Sorby Environmental Fluid Dynamics Laboratory, University of Leeds. A schematic of the test section is displayed in Figure 6.1. Optical access is provided through the floor and side walls by panels of Perspex. The remaining flume walls are made from black opaque fibreglass. The working section of the water flume has dimensions of 12 m × 1 m, and can be filled to a height of 0.7 m. At the far end of the flume is a reservoir with two Fybroc 1500 series pumps, capable of high shear and low turbulence. Fluid is pumped back from the reservoir to the entrance by a large diameter pipe which sits under the flume floor. The pump speed can be controlled via a variable frequency inverter. Figure 6.2 presents the bulk flow speed for a range of pump frequency settings. At the flume entrance, the flow is passed through a honeycomb mesh which has elements of diameter 6 mm.

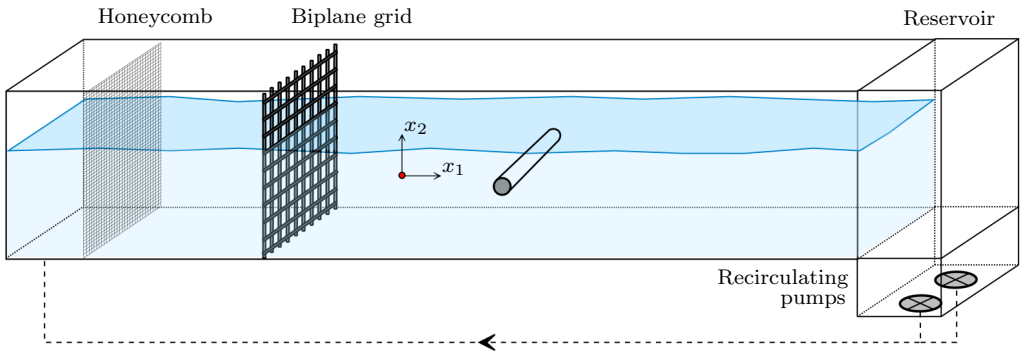

Figure 6.1: Schematic of the recirculating flume in the Sorby lab, University of Leeds.

The cylinder is a rigid hollow aluminium tube with outer diameter 25 mm and length 1 m, giving an aspect ratio of approximately 40. A black anodised finish is applied to the cylinder to reduce reflection from the laser light sheet. Circular end-plates with diameter $3D$ are fitted to suppress the production of structures at either end of the cylinder. Between the flume wall and end-plate, there is a gap of approximately $1.5D$. For each run, the cylinder Reynolds number is calculated by considering the temperature-dependent kinematic viscosity, and free-stream flume

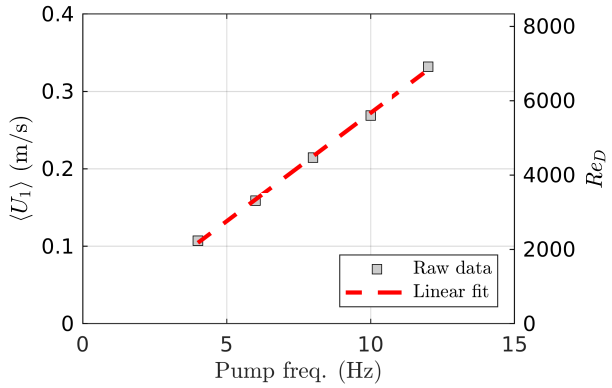

Figure 6.2: Relationship between flume pump frequency and flow velocity.

Pump freq. (Hz)	U_∞ (m/s)
4	0.1072
6	0.1588
8	0.2146
10	0.2689
12	0.3318

Table 6.1: Raw data for Figure 6.2.

speed. Water temperature is monitored throughout the experiments and found to have an average value of 12°C. This corresponds to a kinematic viscosity of $\nu = 1.2 \times 10^{-6}$ m^2/s. Circular end plates with diameter $3D$ are fitted to suppress the production of structures at either end of the cylinder (Figure 6.3a). Between the flume wall and end plate, there is a gap of approximately $1.5D$ (see Figure 6.3b). Temperature of flume water is monitored to ensure the correct Reynolds number $Re_D = U_\infty D/\nu$ is recorded. For each run, the corresponding Reynolds number is calculated by considering the temperature-dependent kinematic viscosity, and free-stream flume speed.

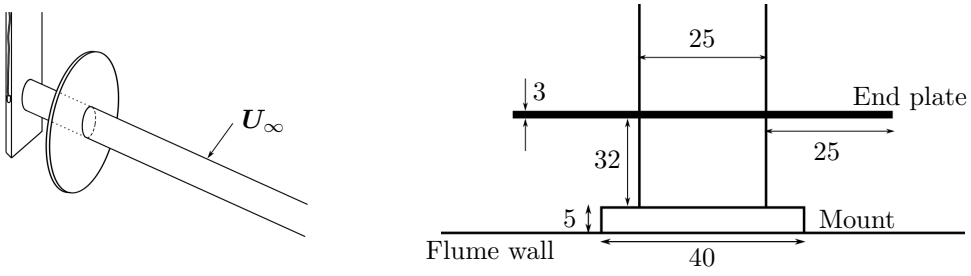

(a) Mount and dye injector.

(b) End plate (units in millimetres).

Figure 6.3: Cylinder mount and end plate design.

To produce a turbulent inflow, a biplane grid is placed 2 m upstream of the cylinder. The biplane grid has a mesh spacing of $M = 96$ mm, and grid bar

diameters of 25 mm. The grid sits flush in the flume and spans 10 rods horizontally and 10 rods vertically. A schematic of the biplane grid design and placement in the flume is displayed in Figure 6.4.

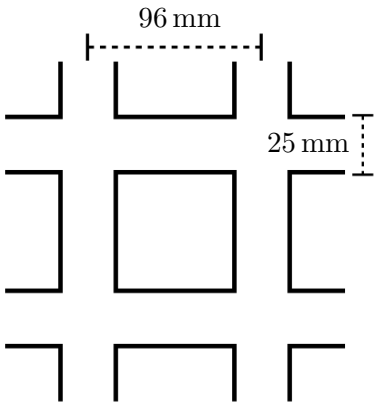

(a) Mesh spacing and bar thickness of the biplane grid.

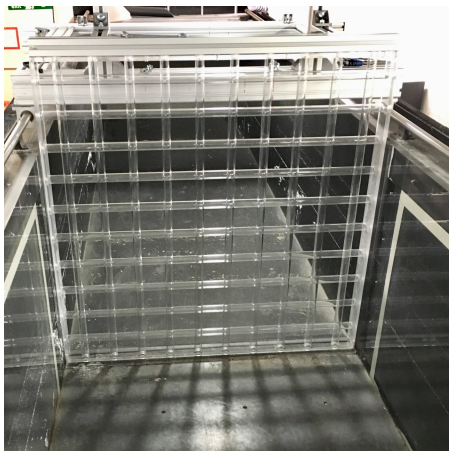

(b) Biplane grid positioned in the flume.

Figure 6.4: Biplane turbulence-generating grid construction.

6.2 Acoustic Doppler velocimetry description

6.2.1 Instrumentation

Acoustic Doppler velocimetry probes are experimental instruments to measure flow velocity in a remote sampling volume. Measured phase shift between transmitted and received signals is related to flow velocity by Doppler shift theory. ADV is capable of recording instantaneous velocities at high sampling rates. The sensors can be easily deployed and provide accurate mean velocity, variance, and covariance of the flow field (Voulgaris and Trowbridge, 1998).

Acoustic signals are emitted from a central transmitter at a pulse repetition frequency f_{pr}. A fraction of the acoustic energy is scattered back from Talisman 30 polymer seeding particles to receivers arranged around the transmitter. A total of 4 receivers are placed equidistant around the transmitter. Each receiver

is angled towards the central beam at 30°, focusing onto an intersection point. A Nortek Vectrino II profiler ADV probe (see Thomas et al. (2017) for details on technical characteristics and operation), is used in the current investigation is shown in Figure 6.5a. The Vectrino II probe is capable of recording at a number of positions simultaneously in order to calculate spatial profiles with a 30 mm range, however, in this investigation the ADV is set-up to record at a single point in space. The receiver marked with red paint is aligned such that it points in the same direction as the bulk flow, i.e. along the streamwise direction. In addition to velocity data, the ADV also records the signal-to-noise ratio (SNR), and the correlation (COR). The signal-to-noise-ratio provides a measure of the recorded acoustic signal received. Velocities are recorded along the angle bisector of the line from the transmitter to the sampling volume, and the line from the sampling volume to the receiver. In Figure 6.5b this corresponds to the angle bisector between blue and red lines. Although the ADV is an intrusive device, the clearance between the transmitter and sampling volume is large enough to have minimal effect on the flow measurement (Cea et al., 2007).

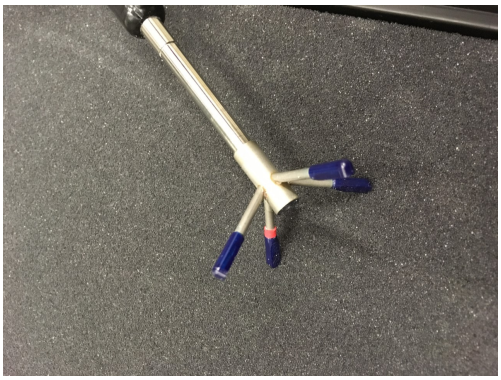

(a) Nortek Vectrino II ADV sensor used in the experiments.

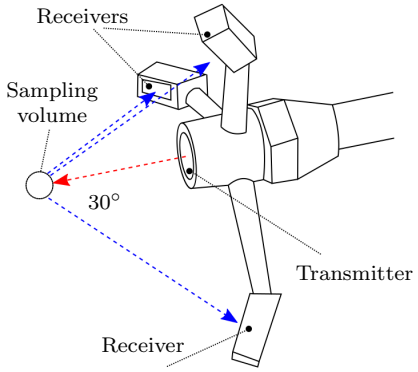

(b) ADV configuration with 3 receivers, adapted from Chanson (2008).

Figure 6.5: Acoustic Doppler velocimeter (ADV) probe head.

Three-component velocity is recorded 50 mm from the transmitter bottom in the sweet spot where the signal-to-noise ratio is maximum (Thomas et al., 2017). Data were sampled for a period of 300 seconds at a frequency of 100 Hz. The rate

of change of phase shift $\Delta\phi$ is given by

$$\frac{\mathrm{d}\phi}{\mathrm{d}t} = \frac{1}{\tau}\arctan\left[\frac{\sin(\phi(t))\cos(\phi(t+\tau)) - \sin(\phi(t+\tau))\cos(\phi(t))}{\cos(\phi(t))\cos(\phi(t+\tau)) + \sin(\phi(t+\tau))\sin(\phi(t))}\right] \quad , \tag{6.1}$$

where τ is the time between transmissions, equal to $1/f_{pr}$. Due to the periodicity of the tan function (6.1), phase angles must lie in the range $-\pi < \phi < \pi$, otherwise signal aliasing can occur. To prevent aliasing, acceptable velocity ranges are input into the ADV software by the user. This is achieved by setting the desired flume speed, and adjusting the velocity range bounds accordingly, ensuring no aliasing is present. Phase data from (6.1) is then converted to velocities via

$$U = \frac{c}{4\pi f_a}\frac{\mathrm{d}\phi}{\mathrm{d}t} \quad , \tag{6.2}$$

where c is the speed of sound in the fluid ($\approx 1466\,\mathrm{m/s}$), and $f_a = 10\,\mathrm{MHz}$ is the acoustic frequency.

6.2.2 Noise removal

Noise variance in ADV measurements is a combination of noise due to the electronic circuitry (Doppler noise, signal aliasing), and flow-related noise (high turbulence intensity, air entrainment, micro-bubbles in the carrier fluid). Coherent Doppler acoustic systems are sensitive to Doppler phase noise, which causes a broadening of the Doppler spectral peak. Velocity signals corrupt with Doppler noise return an overestimation of turbulent kinetic energies. It is also noted that horizontal velocity components are far noisier than the vertical component (Lohrmann et al., 1994).

There are a number of methods to detect and remove spurious data. If velocity is recorded at high temporal resolution, it is possible to calculate acceleration and identify spikes through large values which are deemed non-physical. The threshold which separates real data from spikes is determined empirically, for example in the fitted model of Goring and Nikora (2002). Following the correlation filter of Cea et al. (2007), an ellipsoid is fitted to the fluctuating velocity phase spaces of $\{u_1\text{-}u_2,\ u_1\text{-}u_3,\ u_2\text{-}u_3\}$, based on computed statistics of the data. Idealised data

forms a cluster of points, and spikes lay outside of this cluster. Fitting an ellipse to the data requires information on the location, size, and shape. By assuming that the mean of fluctuating velocities is zero, the centre of the ellipse in the phase space is the origin $(0, 0)$. Scaling the ellipse is achieved by introducing parameter λ which depends on the expected maximum of data. From theoretical considerations, Donoho and Johnstone (1994) derived a formula for the expected maximum value of N observations with standard deviation σ to be $\lambda\sigma$, where $\lambda = \sqrt{2\ln(N)}$. The rotation axis of the ellipse is given by (Cea et al., 2007)

$$\theta = \arctan\left(\frac{\langle uv\rangle}{\langle u^2\rangle}\right) \quad . \tag{6.3}$$

The major and minor axis are

$$x_0^2 = \frac{(\lambda\sigma_U\cos\theta)^2 - (\lambda\sigma_V\sin\theta)^2}{\cos^2\theta - \sin^2\theta} \quad , \tag{6.4}$$

$$y_0^2 = \frac{(\lambda\sigma_V\cos\theta)^2 - (\lambda\sigma_U\sin\theta)^2}{\cos^2\theta - \sin^2\theta} \quad , \tag{6.5}$$

where σ_U and σ_V are the standard deviation of velocities U and V. Two advantages of the correlation filter are: (i) implementation is independent of time resolution, (ii) no tuning parameters are required. After each iteration of the correlation filter, global flow statistics change, the correlation filter can be applied once more. For the AVD data in the current study, it is generally found that no points were removed after two iterations.

Figures 6.6a, 6.6b present an example of the correlation filter on a single data set, recorded at a flume pump frequency of 8 Hz. In Figure 6.6a, a first-pass of the ellipse fitting method is applied to the data set. Points located outside of the ellipse are replaced, and the correlation method is applied repeatedly, until no points are flagged as spurious. Figure 6.6b displays a time trace of streamwise velocity .

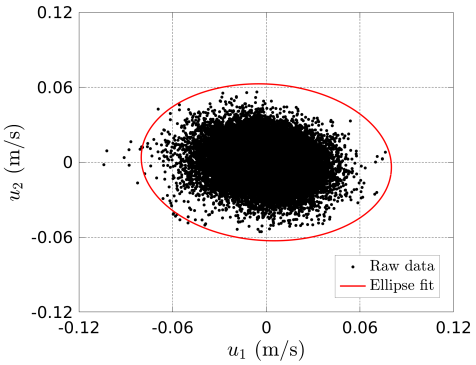

(a) First pass of the ellipse fitting on the raw data.

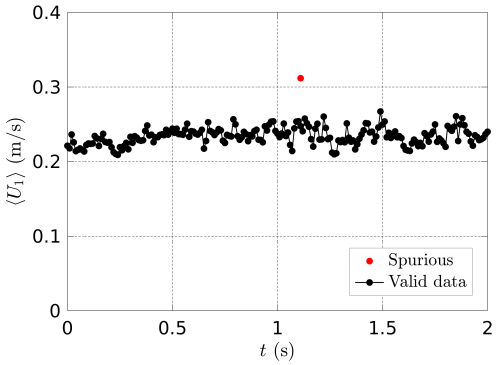

(b) Streamwise velocity time series. A spike is flagged as spurious.

Figure 6.6: Example of the ellipse fitting method of Cea et al. (2007). Data presented is collected from a 8 Hz pump frequency run, which corresponds to $U_\infty = 0.2146$.

6.3 Free-stream flow conditions

A sampling duration for the ADV data acquisition was chosen by calculating a cumulative average of velocity magnitude and turbulence intensity. For N discrete samples of an arbitrary variable $f_i = (f_1, f_2, \ldots, f_N)$, the cumulative average is defined as

$$\langle f_i \rangle_N = \frac{1}{N} \sum_{i=1}^{N} f_i \ . \tag{6.6}$$

Turbulence intensity is given by

$$I_1 = \frac{u_{\text{rms}}}{U_\infty} \ , \qquad I_2 = \frac{v_{\text{rms}}}{U_\infty} \ , \qquad I_3 = \frac{w_{\text{rms}}}{U_\infty} \ , \tag{6.7}$$

where $u_{\text{rms}} = \sqrt{\langle u^2 \rangle}$, $v_{\text{rms}} = \sqrt{\langle v^2 \rangle}$, $w_{\text{rms}} = \sqrt{\langle w^2 \rangle}$ are, respectively, the root-mean-square (r.m.s.) velocity fluctuations in the x, y, and z directions.

In Figures 6.7a and 6.7b, cumulative averages of the velocity magnitude and turbulence intensity become almost constant when averaged over $t \gtrsim 200$ s. Therefore, a minimum of 200 seconds is used when time-averaging any ADV data.

In Figure 6.8 time-averaged streamwise velocity is plotted as a function of distance from the flume bottom. This run is carried out in the streamwise posi-

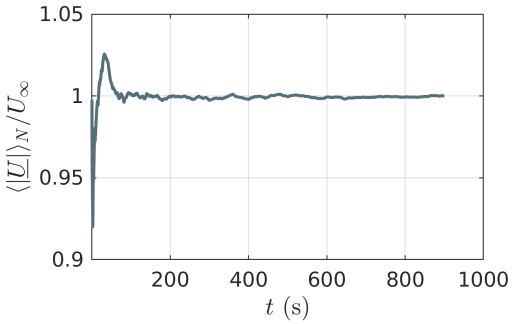

(a) Cumulative average of velocity magnitude.

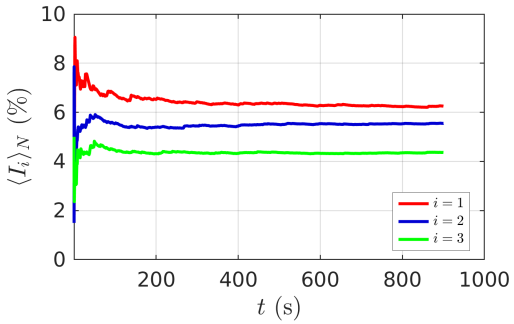

(b) Cumulative average of turbulence intensity.

Figure 6.7: Sensitivity of velocity magnitude and turbulence intensity with respect to run duration.

tion where the cylinder will be placed, i.e. 2 m downstream from the turbulence generating grid. A linear fit has been added, showing probes positioned at heights greater than 0.1 m are out of the logarithmic profile. This flow corresponds to a circular cylinder Reynolds number of $Re_D = 4200$.

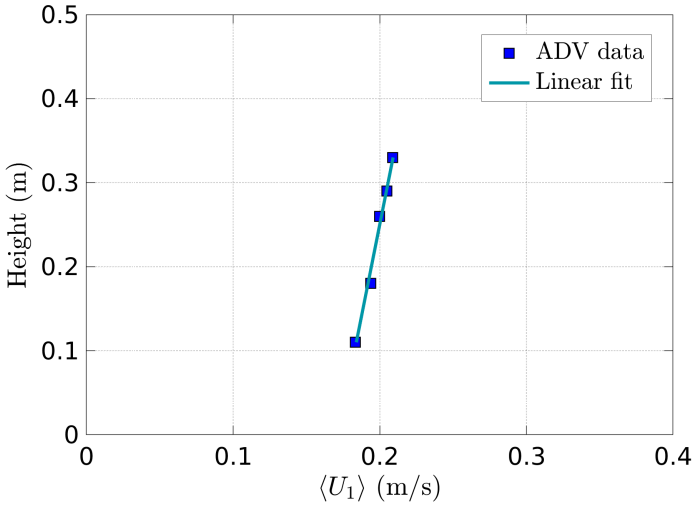

Figure 6.8: Time-averaged streamwise velocity recorded at the centre of the working section, as a function of distance from the flume bottom. Measurements taken 2 m downstream from the turbulence-generating grid without a cylinder.

6.4 End-plate effects

Similar to the investigation of Stäger and Eckelmann (1991), probes were positioned in multiple locations along the cylinder axis at downstream position $x/D = 5$, and heights $y/D = 0, 2$. In the lower Reynolds number range ($Re_D = 1600$), Stäger and Eckelmann (1991) reported a shedding frequency $f_2 < f_1$ near the end plates, where f_1 is the Strouhal shedding frequency defined by $St = f \cdot D/U_\infty$. A lower frequency f_2 is due to the horseshoe vortex at the leading edge of the end plate. End effects were found to fade away with increasing Reynolds number. For large Reynolds numbers $Re_D = 4800$, no secondary frequency f_2 is detected, even as close as one diameter away from the end plate The wake is divided into two regions: (i) affected by the end plates, (ii) sufficiently far enough away from the end plates where the flow is unaffected. The boundary between the affected and unaffected region is referred to as the node, and defined by the point at which the energy present in f_1 and f_2 is equal.

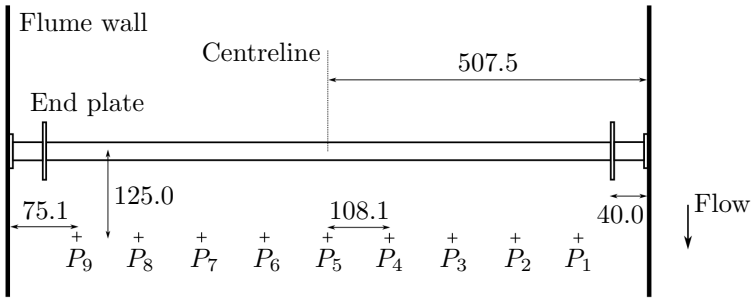

Figure 6.9: Probe positioning along cylinder axis, denoted by crosses. Units are in millimetres.

Figure 6.10 presents the results for a cylinder Reynolds number of $Re_D = 4200$, at position $x/D = 5$, $y/D = 0$. In total, 9 axial positions were used. Noise is present in all axial positions, but close to the cylinder midpoint, a pronounced shedding frequency of $f_1 \approx 1.65$ is recorded. As the ADV probe moves closer to the cylinder end plates, f_1 decreases towards $f_1 \approx 1.35$, the amplitude of f_1 decreases, and more noise is present. From these ADV results, it is concluded that the mid-point of the cylinder is unaffected by end plate shedding.

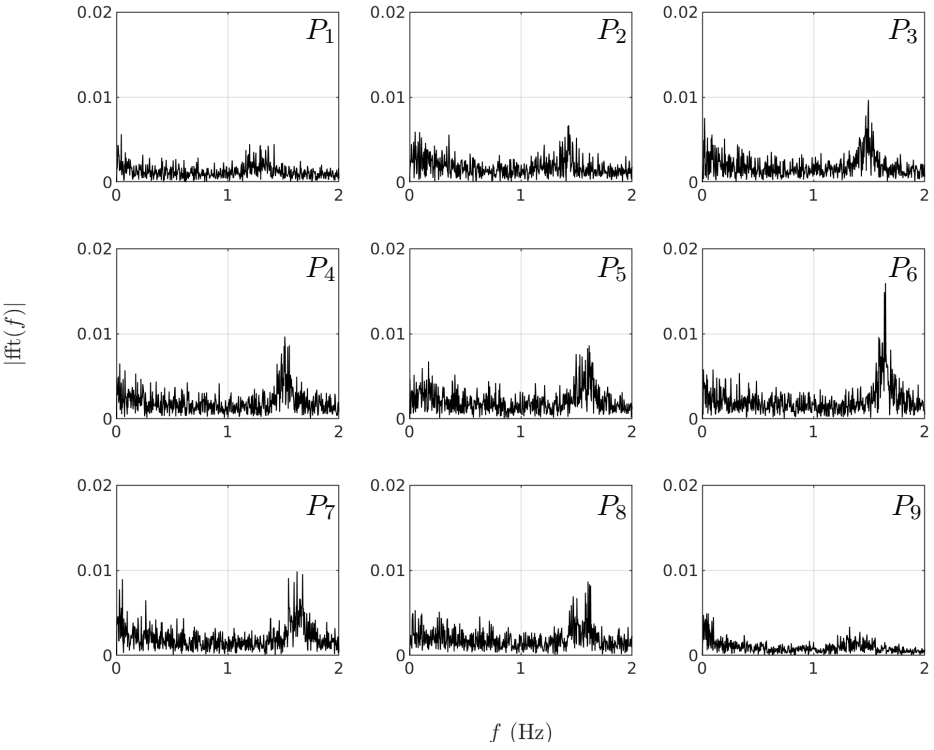

Figure 6.10: Velocity time series in the frequency domain. Single-sided amplitude spectrum of $U_x(t)$ at 9 different axial locations ($x/D = 5$, $y/D = 0$). Positions given in Figure 6.9.

6.5 Cylinder shedding visualisation

Dye visualisation experiments are ran to gain a better qualitative description of the wake. Dye is released from the back of the cylinder by 5 holes with diameter 1 mm. Spacing between the holes is 25 mm, ensuring axial correlation length of πD is sufficiently covered, ensuring at least 3 holes cover the axial correlation length. A fluorescent dye solution is made by combining 7 litres of tap water with 2 Cole-Parmer yellow/green dye tablets. For each run, a Watson Marlow 520S peristaltic pump is turned on for 20 seconds. This is found to correspond to approximately 65 ml of dye solution. Sampling 20 seconds of data is sufficient for analysis, and that it allowed for a number of runs before the water became too strongly coloured. Images were captured with a Vision Research Phantom Miro M120 high-speed camera at a resolution of 1920×1080 pixels and 24 frames per second (fps).

Figure 6.11 presents a snapshot of the circular cylinder wake at a Reynolds number of $Re_D = 2100$. The vortex street is clearly visible from the periodic shedding. Each run displays short periods of time where the periodic shedding is disrupted, and the wake becomes symmetrical. Despite this, counting the amount of sheds for the full 60 s returns a frequency close to the expected Strouhal number for flows of similar Reynolds number.

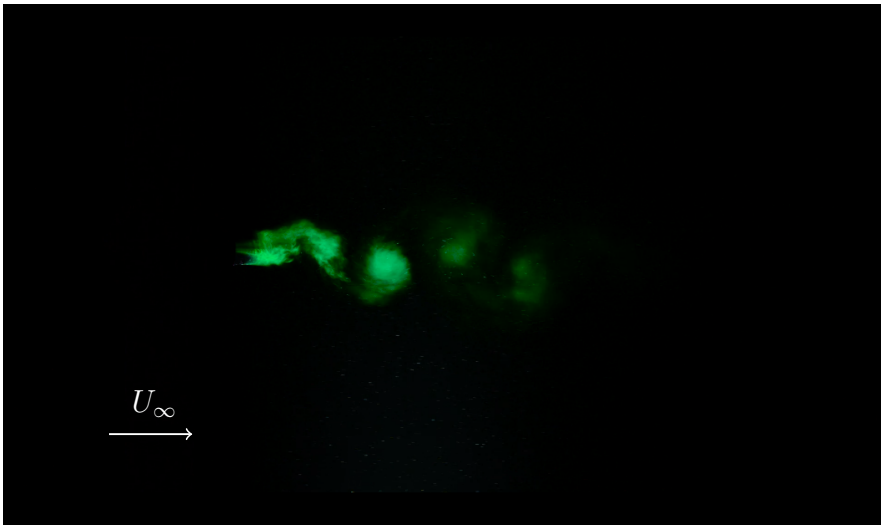

Figure 6.11: Dye flow visualisation of the circular cylinder wake at $Re_D = 2100$.

6.6 Particle image velocimetry description

6.6.1 Data acquisition

PIV is a non-intrusive optical technique used to obtain instantaneous flow velocity. PIV utilises one or more cameras to record successive images of illuminated seeding particles suspended in a fluid. Figure 6.12 presents an overview of the steps taken from image acquisition of the flow field, to generation of velocity vectors. A detailed description of the PIV technique can be found in Adrian and Westerweel (2011).

Images are captured by the camera sensor and converted from light energy to electrical energy. The most common sensors used in PIV applications are charge coupled devices (CCD), and complementary metal oxide semiconductors (CMOS). A comparative study between CCD and CMOS sensors is provided in Hain et al. (2007). A major advantage of CMOS sensors is their fast readout- a requirement for time-resolved PIV. Also, unlike with CCD sensors, a CMOS sensor houses individual circuitry for each pixel. This allows for electronic processing directly on the chip, including pre-amplification, non-linear signal transformations, and AD-conversion (Raffel et al., 2018). However, CMOS sensors are typically less sensitive than CCD sensors and therefore require a larger sensor surface. A larger pixel surface produces a higher signal-to-noise ratio (SNR) (Hain et al., 2007), but also increases the probability of pixel locking.

Image pairs A and B are taken at a fixed time displacement δt, which is set according to the flow dynamics. Each image is split into a number of sub-images, called interrogation areas. Images A and B are correlated to find the most probable particle displacement from image A to B in each interrogation area (Raffel et al., 2018). For a sufficiently small increment δt, which is constrained by the typical time scale of the flow, this provides particle displacement which is used to calculate velocity. The cross-correlation function is given by (Huang et al., 1997)

$$C(m,n) = \sum_{i} \sum_{j} A(i,j)B(i-m, j-n) \ . \tag{6.8}$$

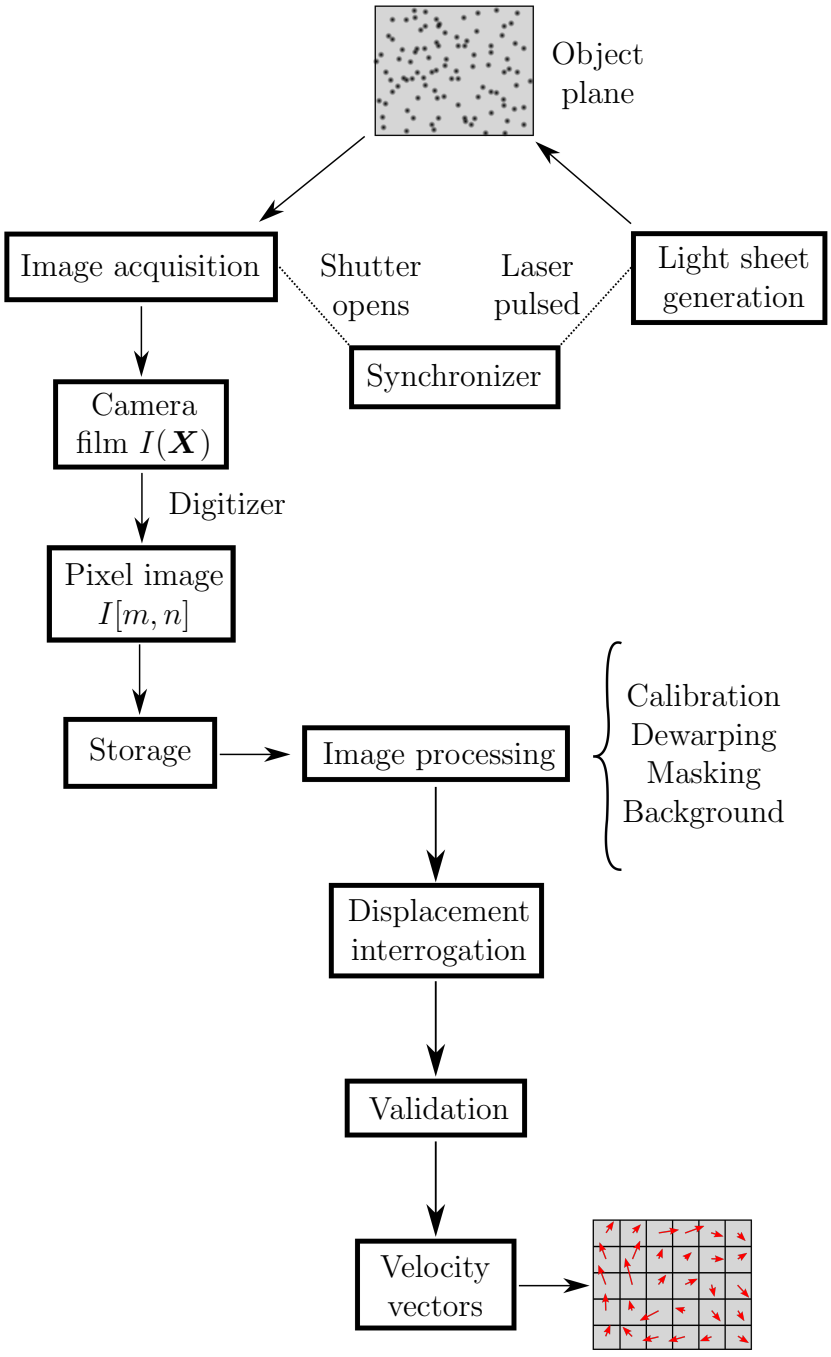

Figure 6.12: Overview of the processes required for PIV, adapted from Adrian and Westerweel (2011).

The largest peak in $C(m,n)$ corresponds to the most probable particle displacement, and is referred to as the displacement-correlation peak. The displacement-correlation peak should be considerably larger in amplitude than the surrounding noise. By taking the ratio of amplitudes between the displacement-correlation peak and the tallest noise signal, a cut-off can be imposed on the peak height ratio. It is possible to solve (6.8) in the spatial domain by direct cross-correlation, or in the frequency domain by a fast-Fourier transform (Willert and Gharib, 1991).

There are a number of considerations for flow seeding of a PIV experiment. Ideally, particles are non-intrusive, follow the fluid motion accurately, are distributed throughout the fluid medium, and scatter enough light back to the camera sensor. In an accelerating fluid, the slip velocity $\boldsymbol{U}_s$ is defined as the difference between the particle velocity and the fluid velocity, and can be estimated by Stokes drag law (Raffel et al., 2018)

$$\boldsymbol{U}_s = \boldsymbol{U}_p - \boldsymbol{U} = D_p^2 \frac{\rho_p - \rho}{18\nu\rho} \boldsymbol{a} \quad , \tag{6.9}$$

where $\boldsymbol{U}_p$ is the particle velocity, D_p is the particle diameter, ρ_p is the particle density, and $\boldsymbol{a}$ is the fluid acceleration. Without changing the experimental conditions, one method to minimise $\boldsymbol{U}_s$ is to match the fluid and particle density, i.e. neutrally buoyant seeding. Tracer particles made from polyamide and hollow glass spheres are approximately neutrally buoyant in water (Raffel et al., 2018). The second method of minimising $\boldsymbol{U}_s$ is to reduce the particle diameter. However, particles must also scatter sufficient light with a low SNR from the laser sheet, which favours larger diameters (Melling, 1997).

For a particle to accurately trace a fluid flow, it must respond to the smallest turbulent motions to resolve those structures. To check this, the particle relaxation time and the characteristic flow response time are compared. The particle relaxation time is a measure of how quickly particles attain velocity equilibrium with the fluid (Raffel et al., 2018), and is given by

$$\tau_P = \gamma \frac{D_P^2}{18\nu} \quad , \tag{6.10}$$

where $\gamma = \rho_p/\rho$ is the ratio of particle to fluid density (or specific gravity), D_P

is the particle diameter, and ν is the kinematic viscosity of the fluid phase. The characteristic flow response time is taken to be the time scale of the smallest eddies, i.e. the Kolmogorov scales of turbulence. The Kolmogorov time scale is given by

$$\tau_F = \sqrt{\frac{\nu}{\varepsilon}} \ . \tag{6.11}$$

The Stokes number is defined from (6.10) and (6.11) as a nondimensional measure of the seeding particles response to accelerations of the surrounding flow

$$S_k = \frac{\tau_P}{\tau_F} \ , \tag{6.12}$$

where $S_k < 0.1$ is found to be sufficient for tracer particles (Samimy and Lele, 1991).

To seed the fluid flow, 10 g of Dantec silver coated hollow glass spheres (S-HGS) are suspended in a mixing tank holding 40 litres of water. The seeding has an average diameter of $D_P = 10\,\mu$m, with relative density $\gamma = 1.1$. Each seeding particle has a thin silver coating to increase reflectivity. To suppress flocculation, 0.1 ml of Ilford RA50 rinse aid is added to act as a surfactant. As an indication of how well the seeding follows the flow, the Stokes number (6.12) is calculated. The estimated response time of the particles from (6.10) is $\tau_P \approx 5\,\mu$s. The characteristic flow response time (6.11), given by the time scale of the smallest eddies, is $\tau_F = \sqrt{\nu/\varepsilon}$. Since ε is unknown at this stage, an estimation is taken from the numerical modelling, i.e. Figure 5.20. This yields a peak dissipation of $\varepsilon = 0.02(U_\infty^3/D)$, which gives a flow response time of $\tau_F = 12$ ms. From these approximations, $S_k \approx 4.2 \times 10^{-4}$ ($\ll 1$), and it is concluded that the seeding is a reasonable flow tracer.

The light sheet is generated by a Litron Bernoulli double cavity PIV laser, with a 50 mJ energy pulse per cavity. A top hat optic generates the laser sheet and an adjustment module controls the sheet thickness. The light sheet illuminates the flow on a vertical plane, orientated parallel to the flow direction, and perpendicular to the axis of the cylinder. A Dantec SpeedSense 9040 complementary metal oxide semiconductor (CMOS) camera with 24 GB of on-board memory is placed perpendicularly to the laser light sheet, and angled towards the cylinder

wake. A total of 6400 image pairs are acquired at a sampling frequency of 99 Hz in double-frame mode from two synchronization pulses at an interframe time of 1500 ns. The synchroniser ensures the light sheet and camera trigger simultaneously. Light spots are recorded on the image plane from the illuminated seeding particles, converted to electrical charge, and held on the CMOS. The CMOS has 1600×1200 pixels, with spacing $10\,\mu$m, and dynamics of 8 bits. A Nikon PC macro lens is fitted to the camera. The lens has a focal length of 85 mm and a max aperture of f/2.8. An aperture of f/4 was found to provide an optimal balance between depth of field and image quality.

Data for each run is acquired until the on board camera memory is full, which under the current set-up yields 60 s of data. Parnaudeau et al. (2008) investigated the number of shedding cycles required for statistical convergence, finding 52 shedding periods to be satisfactory. For the flow past a cylinder at $Re = 3900$, reported values across literature for the Strouhal number take a mean value of $St \approx 0.21$. This corresponds to a shedding frequency of $f = 1.7$ Hz. If the cylinder wake is sampled for 60 s, approximately 100 shedding cycles will be captured, and therefore 60 seconds of recorded data in the current study is sufficient. A summary of the experimental parameters used in this study is provided in Table 6.2.

Seeding	Type	S-HGS
	Specific gravity	1.1
	Diameter	$10\,\mu$m
Light sheet	Laser type	Nd:YAG
	Maximum energy	50 mJ
	Wave length	532 nm
Camera	Type	CMOS
	Resolution	1600×1200 px
	Pixel size	$11.5\,\mu$m
	Lens focal length	85 mm
	f#	4
Imaging	Magnification	0.45
	Viewing area	$30\,\text{mm} \times 30\,\text{mm}$
PIV analysis	Interrogation area	24×24 px
	Overlap	50%
	Approx. resolution	$2.2\,\text{mm} \times 2.2\,\text{mm}$

Table 6.2: PIV experimental parameters.

6.6.2 Pre-processing: outlier detection and replacement

Once the images have been collected and transferred from the camera, image pre-processing is required before PIV analysis. A calibration target of size 200 mm × 200 mm with 37 × 37 markers is placed in the flume directly behind the cylinder, parallel to the bulk flow. Image calibration is carried out in the commercial PIV software DynamicStudio to map points from the calibration target to the image plane. A direct linear transfer image model is selected to account for the effects of imaging through the glass viewing window, and water medium. From the calibration, de-warping is carried out. To remove constant artefacts, such as cylinder surface glare, a mean of the full data set is taken, and subtracted from each individual image. The cylinder and supports were then masked from each image. Interrogation areas (IA) are set to a minimum and maximum size of 24 × 24. A grid step size of 12 × 12 corresponds to an overlap of 50%. A low-pass Gaussian filter with $k = 3$ is applied to attenuate the random vector measurement error, and produce data which is more suitable for subsequent differentiation (Adrian and Westerweel, 2011).

Figure 6.13 presents a graphical description of the steps taken in the pre-processing of raw images. It can be seen how surface glare on the cylinder is removed once the background mean image is subtracted. However, an artefact is still present on top of the cylinder, corresponding to laser reflection from the water surface. This artefact oscillates in the axial direction, therefore cannot be captured in an image mean. A mask is applied for the cylinder and support. Masked regions are ignored by the PIV analysis.

There are two considerations with data outliers- (i) method to identify spurious vectors, (ii) method of replacement. The universal outlier detection (UOD) of Westerweel and Scarano (2005) detects outliers based on local flow statistics. However, if a cluster of outlier vectors exist, local statistics are effected. Higham et al. (2016) proposed a method of outlier detection and removal based on the POD technique. In their study, artificial noise introduced into a velocity time series was detected in the time-dependent expansion coefficients $\alpha_j(t)$ as a high-frequency oscillation. By applying a moving average to coefficients $\alpha_j(t)$, a filtered decomposition of the flow is obtained. A difference matrix between the raw and

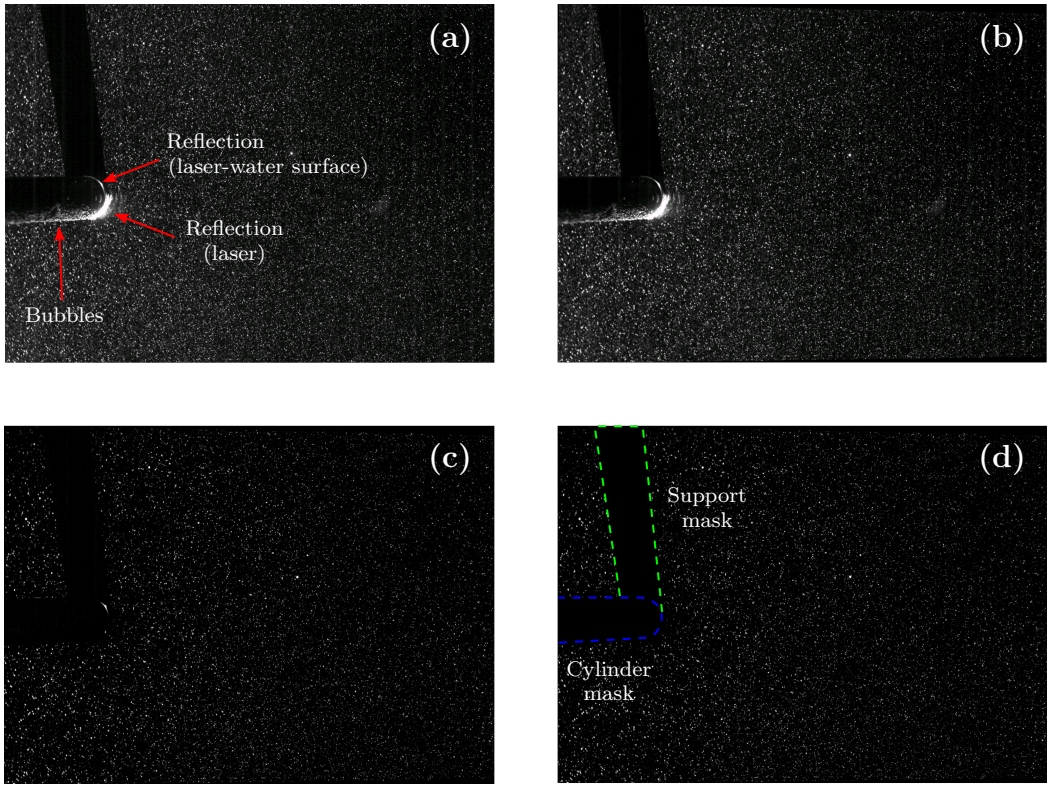

Figure 6.13: Example of the steps taken to process images before cross-correlation: (a) raw image, (b) de-warp applied using calibration image, (c) mean subtracted, (d) final masked image.

filtered velocity field is constructed, and ordered by magnitude. The largest $p\%$ of entries in the difference matrix correspond to spikes, and are replaced in the raw field by the filtered field. Further details of the method can be found in Higham et al. (2016).

Figure 6.14 displays velocity vectors in the cylinder wake, before and after application of the outlier detection and replacement method of Higham et al. (2016) for some arbitrary snapshot in time. The $p\% = 5\%$ largest entries from the difference matrix have been replaced. A vortex street is clearly visible in each data set and the data looks reasonably clean. Clusters of outliers has been identified visually and circled in each plot.

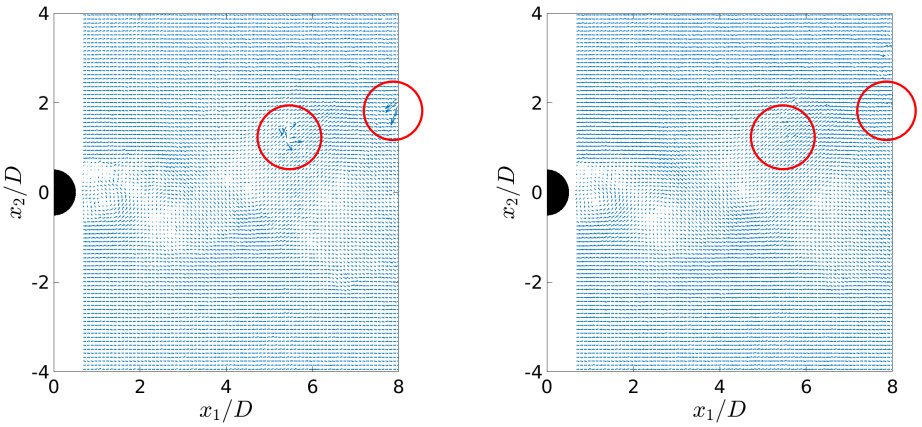

Figure 6.14: Velocity vectors generated in the wake of the cylinder at $Re_D = 4200$. Left: raw vectors, right: after application of the outlier detection and replacement method of Higham et al. (2016). A cluster of outliers has been identified and circled on both plots.

Chapter 7

Dissipation in the circular cylinder wake

This chapter presents an experimental investigation into the wake of a circular cylinder placed in a free-stream turbulent flow. Experiments are carried out in the recirculating water flume documented in Chapter 6. Free-stream turbulence is controlled by passing the inflow through a turbulence-generating grid. This leads to a non-negligible free-stream turbulence intensity, in contrast to previous experimental and numerical investigations of laminar inflow past cylinders. Effects of inflow turbulence on the wake are highlighted by considering time-averaged velocity profiles and wake width development. Non-negligible turbulence in the free-stream is found to deform the wake, such that it is squeezed towards the cylinder base. Measurements are collected in the x-y plane using particle image velocimetry, therefore only two components of velocity are recorded. Dissipation is calculated from the surrogate ε_{xy} derived in Chapter 5. This is achieved by applying the method of proper orthogonal decomposition (POD) to detect and extract coherent motions in the wake, from which the dissipation term can be decomposed into coherent $\widetilde{\varepsilon}_{xy}$ and stochastic ε''_{xy} contributions. A locking between coherent and stochastic motions is suggested from the constant ratio $\varepsilon''_{xy}/\widetilde{\varepsilon}_{xy}$. This behaviour has been previously linked to non-equilibrium turbulence, and has been detected here.

7.1 Introduction

Flow past a circular cylinder has received significant attention in fluid dynamics due to its widespread application across engineering and environmental flows. Experiments and simulations are often used in tandem to gain a better understanding of the complex wake, for example see Dong et al. (2006) and Parnaudeau et al. (2008). However, discrepancies exist between experiments and simulations, which is discussed in Chapter 2. Despite advances in turbulence modelling and computing, there will always be a requirement to investigate this flow experimentally. One challenge in experiments, which is not an issue in simulations, is lack of access to the flow field. Dye visualisation provides a full picture of the wake and can be used to identify structures, but no quantitative data is generated. Velocities can be recorded using hot-wire anemometry (HWA), but this technique is intrusive and can only be deployed at one fixed position. With the development of PIV, the velocity field can be measured instantaneously at multiple points in space (Adrian, 1991). PIV is therefore well suited to study the spatio-temporal organisation of the vortex street in the circular cylinder wake.

The von Kármán street vortices are the most recognisable signature of the circular cylinder wake, and can be identified from measurements on the x-y plane, where x is the streamwise direction running parallel to the bulk flow, y is the normal direction, and z is the axial direction. Streamwise ribs, which connect von Kármán rollers, are most commonly identified through streamwise vorticity ω_x in the y-z plane. However, ribs are inclined and also cut through the x-z plane, which leaves a signature in ω_y (Hayakawa and Hussain, 1989). Planar PIV, which records two components of velocity on a two-dimensional slice, can therefore be used to construct a three-dimensional picture of coherent wake structures. Wu et al. (1994) used planar PIV to determine the pattern and circulation of ω_y in the circular cylinder wake for a Reynolds number of $Re_D = 525$. Lin et al. (1995b) visualised the organisation of streamwise ribs from ω_x using PIV at a Reynolds number of $Re_D = 1 \times 10^4$, and found the average circulation of streamwise ribs is approximately one-tenth of the von Kármán rollers. Huang et al. (2006) used planar PIV with a pre-displaced second light sheet in order to investigate the

size, strength, and evolution of streamwise vortices for the circular cylinder wake in the Reynolds number range $Re_D = 2 \times 10^3$ to 1×10^4.

Coherent structures in the wake can also be investigated through the use of a phase averaging procedure. Each snapshot of the wake velocity field is attributed to a phase angle of shedding. Lourenco et al. (1997) reconstructed phase averaged velocity and vorticity fields in the circular cylinder wake for a Reynolds number of $Re_D = 3000$. Perrin et al. (2007) investigated coherent structures and turbulent kinetic energy in the wake of a circular cylinder at a Reynolds number of 1.4×10^5 by three-component stereoscopic and planar two-component PIV measurements. Turbulent kinetic energy was found to be concentrated in two different regions: within the primary rollers of the vortex street, and in the vicinity of streamwise ribs which connect primary rollers. In the current thesis, phase averaging was utilised in the numerical modelling of Chapter 5 to decompose the dissipation term into coherent and stochastic components. This led to the development of a surrogate for the dissipation term which can be evaluated using only two components of velocity.

Dissipation is a key process in the wake of a bluff body as it acts to dampen turbulent kinetic energy. A recent investigation into the wake of a square cylinder (Alves Portela et al., 2018), confirmed existence of non-classical dissipation scaling behaviour, such that the Kolmogorov equilibrium constant C_ε varies like the reciprocal of a local Reynolds number. This is in disagreement with the widely accepted assumption that C_ε is a constant, whose value is fixed by global turbulence properties of a given flow (Taylor, 1935). Although this non-classical behaviour has been confirmed for flows which are approximately homogeneous and isotropic, e.g. grid turbulence (Vassilicos, 2015), velocities in the wake of a cylinder have a strong periodic component. Following the decomposition method of Hussain and Reynolds (1970), Alves Portela et al. (2018) isolated large-scale coherent motions in the wake of the square cylinder to extract stochastic turbulent motions. Non-equilibrium dissipation scaling was observed in a region where the ratio of stochastic to coherent dissipation was constant, therefore suggesting that non-equilibrium scaling was linked to a locking between the dissipation terms.

In addition to investigating dissipation along the wake centreline, the current chapter will also investigate the influence of free-stream turbulence on the wake. To the author's best knowledge, very few PIV studies exist concerning the circular cylinder wake for a turbulent inflow. A contribution of this chapter is to add towards the experimental data of turbulent flow past a circular cylinder. This will be compared to the numerical results of Chapter 5. Introduction of turbulence into the free-stream lowers the critical Reynolds number at which the shear layers become unstable (Prasad and Williamson, 1997a), and shortens the recirculation region. Lourenco and Shih (1993) found a reduced recirculation length in their PIV experiments of flow past a circular cylinder at $Re_D = 3900$. Kravchenko and Moin (2000) noted that "inflow disturbances" in the experiment of Lourenco and Shih (1993) caused a reduction in the recirculation length, however, no further information on the turbulence characteristics were provided. In the current experiment, flume speeds are adjusted to achieve cylinder Reynolds numbers in the range 2100-6500. A wealth of studies have been undertaken in this range for the laminar inflow case, which allows for a direct comparison. This range also lies within the "disturbance-sensitive Reynolds number range", where the wake dynamics are sensitive to inflow conditions (Gerrard, 1965).

The first objective of this chapter is to highlight the influence of free-stream turbulence on the flow past a circular cylinder. Planar PIV measurements in the wake region at high turbulence levels are directly compared to literature results from numerical simulations and experiments of low free-stream turbulence levels. One such comparison is with the PIV study of Parnaudeau et al. (2008), where a circular cylinder was placed in low-level free-stream turbulence ($I < 0.1\%$) with a cylinder Reynolds number of 3900. The second objective of this study is to estimate the dissipation term from only two resolved components of velocity. From two-dimensional slices of data, the POD method is applied to decompose the velocity field into coherent and stochastic components. Dissipation scaling along the wake centreline is then investigated for each Reynolds number.

7.2 Coherent motion detection

7.2.1 Triple decomposition method

An introduction to the triple decomposition method of Hussain and Reynolds (1970) was covered in Chapter 5, where the lift coefficient on the cylinder surface was processed to extract periodicity from turbulent signals in the wake. The phase averaging procedure is outlined once again here.

Velocities downstream of a wake generator, such as a circular cylinder, can be decomposed into time-averaged $\langle \boldsymbol{U} \rangle$, phase averaged $\widetilde{\boldsymbol{u}}$, and stochastic $\boldsymbol{u}''$ components. Periodic shedding contributes to the phase averaged component of velocity. If the phase averaging procedure is correctly implemented, the stochastic component is uncorrelated to organised motion. The decomposition follows Hussain and Reynolds (1970)

$$U_i = \langle U_i \rangle + \widetilde{u}_i + u_i'' \ , \tag{7.1}$$

where the subscript notation ($i = 1, 2, 3$) is used to denote the 3 directional components of velocity. In this study, the Cartesian coordinate system x_i is used interchangeably with x, y, z. Turbulent fluctuating velocity is recovered from the phase averaged and stochastic components by: $u_i = \widetilde{u}_i + u_i''$. Phase averaged velocity is defined by (Hussain and Reynolds, 1970)

$$\widetilde{u}_i = \lim_{N \to \infty} \frac{1}{N} \sum_{n=0}^{N} U_i(t + n\tau) - \langle U_i \rangle \ , \tag{7.2}$$

where τ is the wave period, corresponding to the periodic vortex shedding of the circular cylinder.

A trigger signal can be extracted from force measurements on the cylinder surface (Braza et al., 2006), or by velocity signals in the wake (Sung and Yoo, 2001; Lourenco et al., 1997; Kim et al., 2002). However, surface measurements are not directly recorded in PIV. A more robust method of coherent motion detection, which does not rely on conditional averaging, is modal decomposition (Lumley, 1981). In the current study, two-components of velocity in the cylinder wake are recorded on a plane, therefore modal decomposition is well suited to the current study. Wlezien and Way (1979) present a review on analysing phase information

from the circular cylinder wake. Perrin et al. (2006) used a modal decomposition to extract energetic modes of the cylinder wake. A trigger signal was then defined from the coefficients of the two most energetic modes, which are associated with the convection of von Kármán street vortices. From the coefficients of the first two modes, the phase angle of shedding was deduced.

7.2.2 Proper orthogonal decomposition

Modal decomposition provides a statistical method for decomposing data into a minimal number of energetic modes. It has been used extensively in a variety of applications, such as: detection, estimation, pattern recognition, and image processing (Taira et al., 2017). The proper orthogonal decomposition is a form of modal decomposition. Although the POD technique can be utilised in a variety of applications where it is known by other names, such as Karhunen–Loève decomposition, it was first introduced in the context of turbulence as a means of identifying coherent structures in turbulent flow fields (Lumley, 1967). Energetic modes can be determined from the flow field data, or theoretically from the governing equations. Proper orthogonal decomposition is introduced in this study for two primary reasons: (i) detection and replacement of spurious PIV vectors, (ii) to provide a trigger signal for the phase averaging procedure.

The process of conducting POD analysis is described by first considering the collection and storage of velocity data. At each time step in the PIV data collection, velocity is recorded at a number of positions spanning a two-dimensional plane. Data are stacked into a single column vector, from which a data matrix $\boldsymbol{X}$ is formed, where each column corresponds to a stacked vector representing the dynamical system at a single time step (see Figure 7.1). The covariance matrix is constructed from the data matrix by $\boldsymbol{R} = \boldsymbol{X}\boldsymbol{X}^T$, where $(\cdot)^T$ is the conjugate transpose operator. If the total number of points in space is n, then $\boldsymbol{R} \in \mathbb{R}^{n \times n}$, and this matrix is potentially very large. To combat this, the snapshot POD method developed by Sirovich (1987) reformulates the covariance matrix $\boldsymbol{R}$. Instead of processing all time steps, a collection of s snapshots are extracted, and the temporal correlation matrix is calculated by $\boldsymbol{R} = \boldsymbol{X}^T\boldsymbol{X} \in \mathbb{R}^{s \times s}$. Crucially, $\boldsymbol{X}^T\boldsymbol{X}$ and $\boldsymbol{X}\boldsymbol{X}^T$ share the same non-zero eigenvalues (Taira et al., 2017), and

yield the same dominant modes. The snapshot method produces a considerably smaller correlation matrix, but the total number of time steps taken must be sufficient to capture the flow physics (Sirovich, 1987).

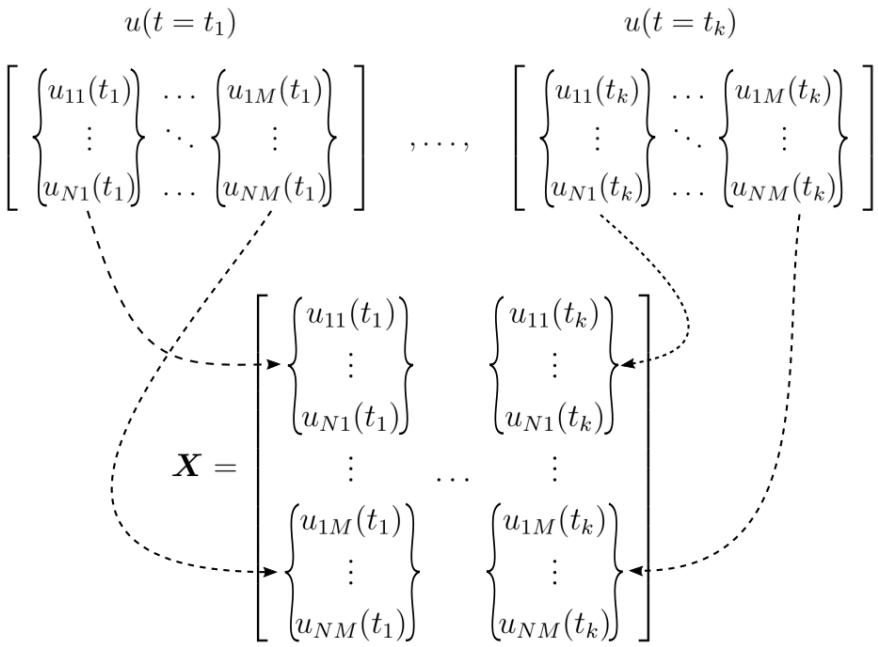

Figure 7.1: Construction of data matrix $\boldsymbol{X}$ in preparation for POD analysis.

The POD technique extracts energetic modes by optimizing the mean square of a given variable, which in the case of a fluid flow is the fluctuating velocity. A fluctuating fluid flow is decomposed into a sum of weighted basis functions by the generalised Fourier series

$$\boldsymbol{u}(\boldsymbol{x}, t) = \sum_{j=1} \alpha_j(t)\boldsymbol{\phi}_j(\boldsymbol{x}) \ , \tag{7.3}$$

where $\alpha_j(t)$ are time-dependent expansion coefficients, and $\boldsymbol{\phi}_j(\boldsymbol{x})$ are incompressible vector fields which can be thought of as characteristic eddies (Moin and Moser, 1989). The method of snapshot POD seeks to represent $\boldsymbol{u}$ by an optimal set of modes $\boldsymbol{\phi}$. This is achieved by recasting (7.3) into an eigenvalue problem, such that

$$\boldsymbol{X}^T\boldsymbol{X}\boldsymbol{\psi}_j = \lambda_j\boldsymbol{\psi}_j \ , \tag{7.4}$$

where $\boldsymbol{\psi}_j$ are the eigenvectors, and λ_j are eigenvalues corresponding to energy levels. Setting up the eigenvalue problem in (7.4) is described in Eckart and Young (1936), and Section 3.1 of Holmes et al. (2012). POD modes are recovered from (Taira et al., 2017)

$$\boldsymbol{\phi}_j = \boldsymbol{X}\boldsymbol{\psi}_j \frac{1}{\sqrt{\lambda_j}} \ . \tag{7.5}$$

A Hilbert transform of the expansion coefficients $\alpha_j(t)$ is taken to yield a reference phase, associated with the cylinder vortex shedding. The reference phase is then discretised into 32 bins. For each time-step, the velocity fields are placed into the bin corresponding to their phase. Within each bin, an average is taken over all velocity fields to obtain phase averaged velocities. From time traces of $\alpha_j(t)$, it is also possible to identify intermittent features in the wake. Intervals of weak shedding can be identified by periods where the amplitude of $\alpha_j(t)$ momentarily decreases. Roshko (1952) observed such a phenomenon of intermittent low-frequency irregularities in the wake-transition regime, due to the growth of large vortical structures in the wake (Williamson, 1996). A consequence of this is that turbulent structures are less organised for $Re_D > 5000$ (Prasad and Williamson, 1997b).

7.3 Circular cylinder wake structure

7.3.1 Vortex shedding characteristics

Formation of a vortex street in the wake is a consequence of periodic shedding from the cylinder surface. A nondimensional measure of the eddy shedding is given by the Strouhal number $St = f_s D/U_\infty$, where f_s is the shedding frequency. Periodic shedding from the cylinder induces a force transverse to the flow direction, which can lead to vortex-induced vibration, and even structural failures. Shedding frequencies can be extracted from velocity time signals in the wake by various methods. Matsumura and Antonia (1993) estimated the shedding frequency from the primary spike found in the spectra of normal velocity fluctuation u_2. Instead of using velocity data, Ma et al. (2000) used the lift coefficient to obtain a time-averaged Strouhal frequency. Parnaudeau et al. (2008) computed the Strouhal number from examination of the peaks and troughs of the fluctuating normal velocity time signal $u_2(t)$. This was achieved by identifying a peak at the start and end of the full data, and counting the number of sheds in the interval.

POD analysis was carried out in Section 6.6.2 to detect and remove spurious vectors, from which the expansion coefficients $\alpha_j(t)$ are generated and can be analysed to deduce shedding characteristics. Figure 7.2 displays the results of POD analysis on the case of $Re_D = 4200$. In Figure 7.2a, the percentage of energy in each mode for the fluctuating velocity signal is plotted. Included are the data of Perrin et al. (2006) from a considerably higher Reynolds number of $Re_D = 140000$. The POD method sorts and arranges modes by energy in descending order. This is confirmed in Figure 7.2a, where it can be seen that after approximately 10 modes, energy decays exponentially. The first two modes carry approximately the same amount of energy- 13.6% and 12.8%, respectively. This is in agreement with previous studies where the first two modes were attributed to the primary vortex shedding, from $Re_D = 100$ (Deane et al., 1991), to $Re_D = 140000$ (Perrin et al., 2006). The third mode contributes 3.1%, after which, all modes have energy $< 1\%$. A low-dimensional model of a fluid flow can be constructed from a small number (< 10) of modes. Phase information of the primary vortex shedding is contained within the expansion coefficients of the first two modes. A time-series

of the first expansion coefficient α_1, normalised by $\max\{|\alpha_1|\}$, is presented in Figure 7.2b for 20 seconds of data. It was noted that $\alpha_1(t)$ and $\alpha_2(t)$ differ only by a translation in t, as confirmed in Perrin et al. (2006), therefore phase averaging of the periodic shedding process can be deduced from only α_1.

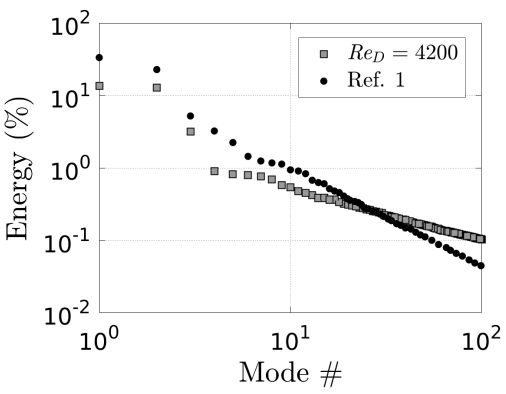

(a) Energy in each POD mode.

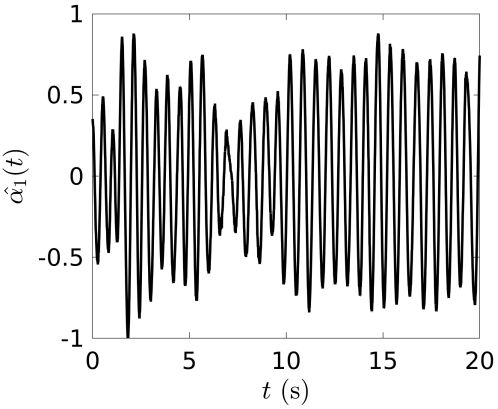

(b) Normalised coefficient $\hat{\alpha}_1(t)$.

Figure 7.2: Energy contained in each POD mode, and time trace of the first POD coefficient $\hat{\alpha}_1 = \alpha_1 / \max\{|\alpha_1|\}$. Ref. 1: PIV of Perrin et al. (2006).

The Strouhal shedding frequency St is calculated from the time-series of α_1 by taking a Fourier transform and extracting the dominant frequency. This method is checked by taking a Fourier transform of the normal fluctuating velocity at various downstream positions along the wake centreline, and confirming both methods return the same shedding frequency.

Table 7.1 presents details of current flow conditions, and time-averaged statistics in the wake. Turbulence intensity is calculated in the free-stream. Included are computational results from the LES study of Chapter 5, first presented in Table 5.3. Reported values from the literature for the Strouhal number, as discussed in Section 2.2, are varied. However, the current PIV data at $Re_D = 4200$ agrees closely with the PIV experiment of Parnaudeau et al. (2008). This is despite the differences in free-stream turbulence. There is no clear trend between Re_D and St for results in the current PIV data. Results from the current PIV data show that as the Reynolds number increases, the recirculation length reduces.

Between the simulations of Chapter 5 and the current PIV, it is expected that the results of RGI and Case II would be comparable, because the freestream

flow conditions are similar. The RGI simulation returns a Strouhal number of $St = 0.207$, in close agreement to Case II, where $St = 0.203$. This is not the case in the FGI simulation, where $St = 0.224$. However, a recirculation length of $L_r/D = 1.30$ is reported in Case II, compared to $L_r/D = 0.88$ and 0.96 for the RGI and FGI simulations, respectively. This may suggest that the recirculation length is more sensitive to inflow turbulence than the shedding frequency.

Reference	Type	Re_D	St	L_r/D	I (%)	L_{11}/D
Literature						
Norberg (1987)	HWA	3900	0.215	1.33	...	...
Lourenco and Shih (1993)	PIV	3900	...	1.18	...	...
Ong and Wallace (1996)	PIV	3900	0.215	...	...	...
Ma et al. (2000), case II	DNS	3900	0.219	1.59	...	...
Parnaudeau et al. (2008)	PIV	3900	0.208	1.51	< 0.2	...
Simulations (Chapter 5)					I_1, I_2 (%)	
LI	LES	3900	0.218	1.49	0.0, 0.0	0.00
RGI	LES	3850	0.207	0.88	7.1, 7.1	0.67
FGI	LES	4050	0.224	0.96	3.9, 6.7	0.56
Current PIV					I_1, I_2 (%)	
Case I	PIV	2100	0.180	1.92	6.5, 6.5	0.58
Case II	PIV	4200	0.203	1.30	6.8, 5.3	0.94
Case III	PIV	6500	0.189	1.03	6.3, 6.1	1.63

Table 7.1: Characteristic flow conditions from experimental and numerical studies on the flow past a circular cylinder. Turbulent intensity: $I_1 = u_{\text{rms}}/U_\infty$, $I_2 = v_{\text{rms}}/U_\infty$.

7.3.2 Mean velocity wake profiles

Isocontours of first and second order statistics are presented in Figure 7.3. High gradients of streamwise velocity $\langle U_1 \rangle$ are present in the shear layers. In contours of streamwise velocity variance $\langle u_1^2 \rangle$, a maximum is present either side of the

cylinder, which takes the shape of an ellipse in the contour plot. Although the current PIV data and results of Parnaudeau et al. (2008) agree in their shape, it can be seen that streamwise distances of maxima and minima are slightly different. For example, in the map of $\langle u_1 u_2 \rangle / U_\infty^2$, the butterfly pattern identified in Parnaudeau et al. (2008) has also been seen in the current PIV data. However, the location of maxima and minima is shifted towards the cylinder in the current PIV data. The most likely cause of this is the free-stream turbulence which causes earlier transition in the shear layers. A similar effect was seen in Lourenco and Shih (1993), where free-stream disturbances also caused earlier transition.

Figure 7.4 presents time-averaged velocity profiles across $-2 < x_2/D < 2$ at fixed downstream position in the near wake for $x_1/D = 1.54$. This corresponds to the approximate downstream position on the wake centreline at which streamwise velocity experiences a minimum, and where the streamwise variance reaches a maximum. Results from the current experiment at Reynolds number 4200 have been compared to the PIV studies of Lourenco and Shih (1993) and Parnaudeau et al. (2008), which were both ran at a Reynolds number of 3900. Additionally, simulation results from Chapter 5 have been included for comparison.

Profiles of $\langle U_1 \rangle$ for the current PIV data is in close agreement to the data of Lourenco and Shih (1993), but deviate from the PIV data of Parnaudeau et al. (2008), and the LES results of LI. Both turbulent inflow simulations RGI and FGI show a rapid recovery of the mean streamwise velocity in the wake, which is particularly pronounced on the centreline ($x_2/D = 0$), and at the wake edge ($x_2/D \approx \pm 0.8$). Streamwise velocity on the centreline appears to increase as the freestream turbulence increases. This suggests that inflow disturbances, i.e. free-stream turbulence, cause an earlier transition in the shear layers, leading to a shorter recirculation length. However, freestream flow conditions for the runs of Case II, RGI, and FGI are similar in level of turbulence, as reported in Table 7.1.

The amplitude and location of peaks for $\langle U_2 \rangle$ match closely to Parnaudeau et al. (2008) and the current LES results LI. Lourenco and Shih (1993) report smaller amplitudes. However, in the middle portion ($-1 < x_2/D < 1$), a clearly defined inflection point observed in the LES results of LI and the PIV of Parnaudeau et al. (2008) is not found in the current PIV or turbulent inflow data of

RGI or FGI. Nor is it observed in the results of Lourenco and Shih (1993). This is once again believed to be an effect of early transition in the shear layers.

In profiles of $\langle u_1^2 \rangle / U_\infty^2$, the experimental results of Parnaudeau et al. (2008) display two peaks either side of the centreline. Two inner peaks at $x_2/D \approx \pm 0.25$ form as a result of primary vortex shedding. Two outer peaks $x_2/D \approx \pm 0.5$ originate from the transitional behaviour of the shear layers (Parnaudeau et al., 2008). Profiles of $\langle u_1^2 \rangle / U_\infty^2$ and $\langle u_2^2 \rangle / U_\infty^2$ differ between the current results and those from literature. There is considerable scatter between data sets. This is especially true for the LES FGI case, where particularly large values of $\langle u_2^2 \rangle / U_\infty^2$ are reported along the centreline. A possible explanation is that freestream turbulence has become entrained into the wake centreline. Profiles of $\langle u_1 u_2 \rangle / U_\infty^2$ for Parnaudeau et al. (2008) and the LES of LI are closely matched. The shape of $\langle u_1 u_2 \rangle / U_\infty^2$ is similar to $\langle U_2 \rangle / U_\infty^2$, i.e. it displays asymmetry.

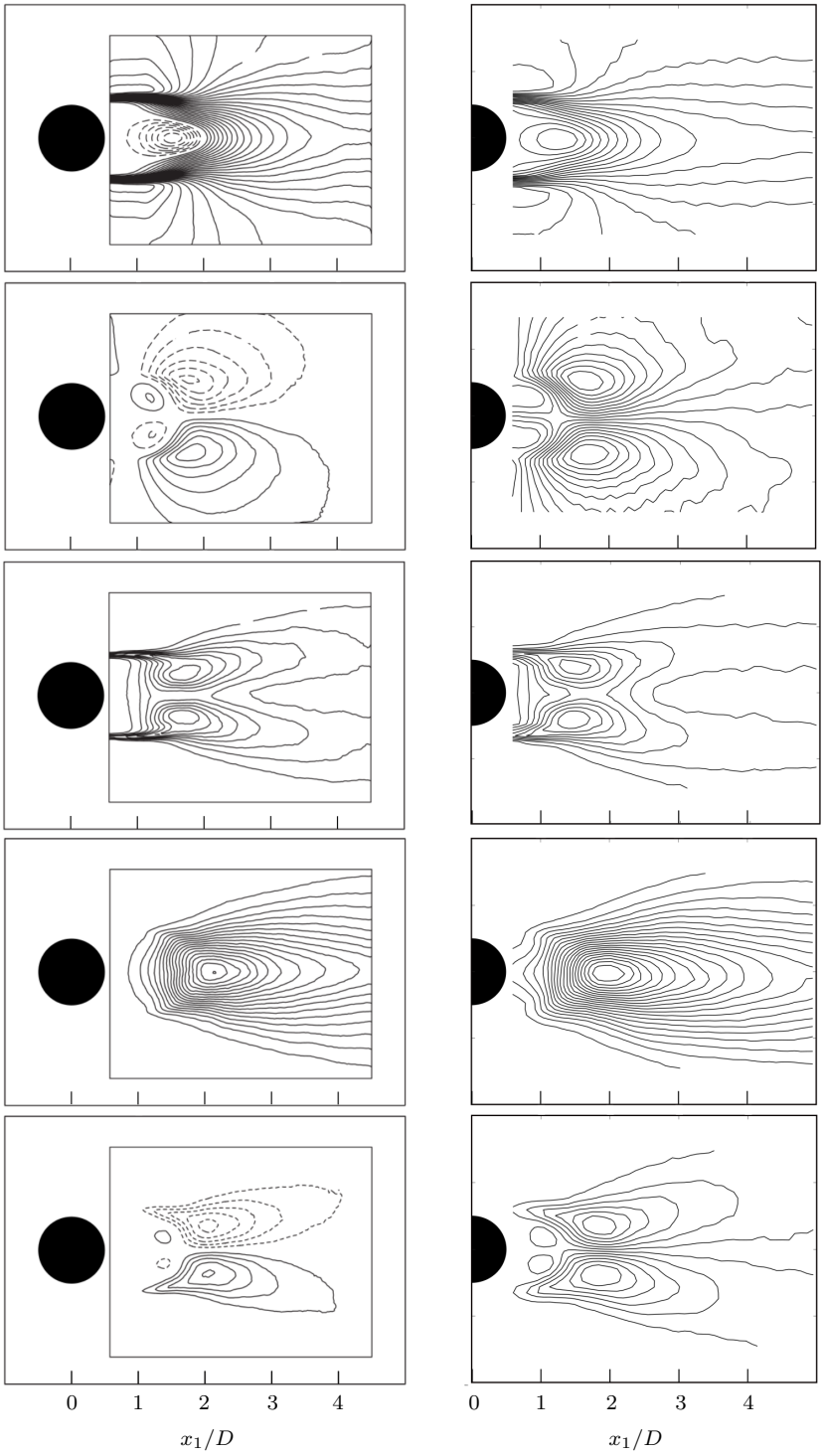

Figure 7.3: Isocontours of first and second order velocity statistics in the cylinder wake. From top to bottom: $\langle U_1 \rangle / U_\infty$, $\langle U_2 \rangle / U_\infty$, $\langle u_1^2 \rangle / U_\infty^2$, $\langle u_2^2 \rangle / U_\infty^2$, $\langle u_1 u_2 \rangle / U_\infty^2$. Left: Parnaudeau et al. (2008), right: current PIV data.

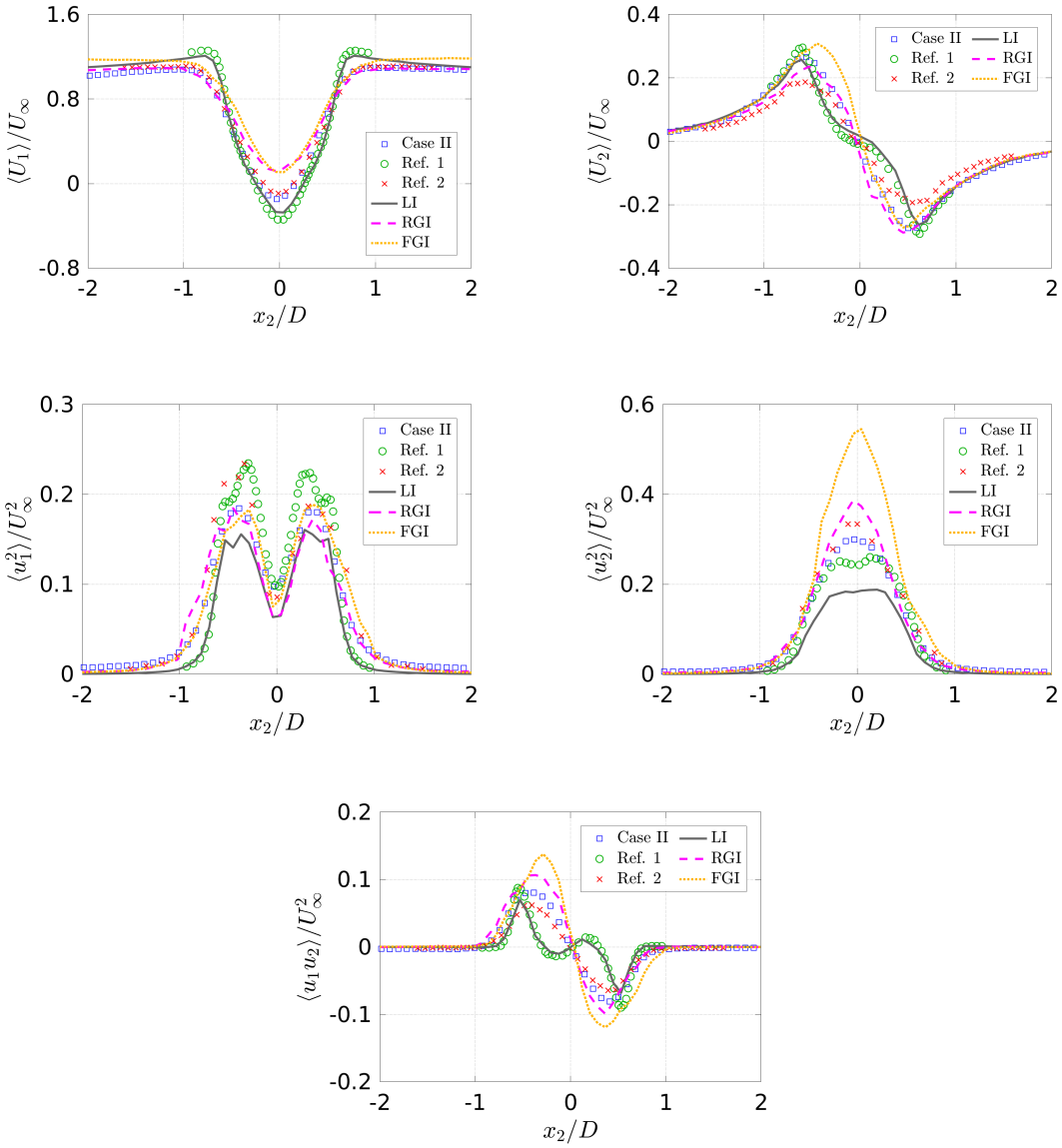

Figure 7.4: Velocity profiles in the cylinder wake at downstream position $x_1/D = 1.54$, as a function of crossflow position x_2/D. Case II of the current PIV at $Re = 4200$. Ref. 1: Parnaudeau et al. (2008), Ref. 2: Lourenco and Shih (1993). Simulations LI, RGI, FGI of Chapter 5.

7.3.3 Shedding structures

To visualise vortex shedding in the cylinder wake, vorticity is computed

$$\omega_z = \frac{\partial U_y}{\partial x} - \frac{\partial U_x}{\partial y} \ , \tag{7.6}$$

which, for a discrete set of locations (Figure 7.5), can be estimated by a second-order central differencing scheme

$$\omega_z(i,j) \approx \frac{U_y(i+1,j) - U_y(i-1,j)}{2\Delta x} - \frac{U_x(i,j+1) - U_x(i,j-1)}{2\Delta y} \ . \tag{7.7}$$

Adrian (1991) note that (7.7) amplifies noise in the measured velocity data. A remedy is to first apply a low-pass filter to the velocity data to replace high-frequency noise. Landreth and Adrian (1988) propose calculating vorticity via circulation, such that

$$\omega_z = \lim_{\mathcal{A}\to 0} \frac{1}{\mathcal{A}} \oint_{\mathcal{C}} \boldsymbol{U} \cdot \mathrm{d}l \ , \tag{7.8}$$

where $\mathcal{C}$ is the contour that encloses area $\mathcal{A}$. The discrete form of (7.8) is a filtered second-order difference (Westerweel, 1993; Landreth and Adrian, 1988)

$$\omega_z = \frac{1}{4\delta x \delta y} \begin{bmatrix} \delta y \cdot U_y(i+1,j) + \frac{1}{2}\delta y \cdot \{U_y(i+1,j-1) + U_y(i+1,j+1)\} \\ -\delta x \cdot U_x(i,j+1) - \frac{1}{2}\delta x \cdot \{U_x(i-1,j+1) + U_x(i+1,j+1)\} \\ -\delta x \cdot U_y(i-1,j) - \frac{1}{2}\delta y \cdot \{U_y(i-1,j-1) + U_y(i-1,j+1)\} \\ \delta y \cdot U_x(i,j-1) + \frac{1}{2}\delta x \cdot \{U_x(i-1,j-1) + U_x(i+1,j-1)\} \end{bmatrix} \ .$$

Contour plots of z-vorticity are presented in Figure 7.6 for $Re_D = 4200$. Time-averaged z-vorticity contour plots are symmetrical about the wake centreline. Maximum vorticity is found in the shear layers either side of the cylinder. In the recirculation region directly behind the cylinder, low levels of vorticity are found, as reported in Lin et al. (1995a). A comparison is made between the current results at $Re_D = 4200$, and the combined DNS/PIV of Dong et al. (2006) for $Re_D = 3900$, $Re_D = 10000$. Surprisingly, the current PIV results for effective shear layer length L_s are in closer agreement to the higher Reynolds number of Dong et al. (2006). This is more supporting evidence to suggest free-stream turbulence has caused early transition in the shear layer instability. Instantaneous z-vorticity contours

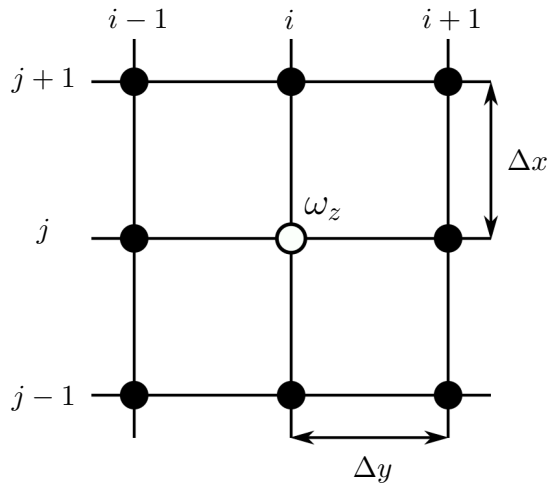

Figure 7.5: Grid point definitions in the current 2D PIV coordinate system. Out of plane vorticity at the central node (i, j) requires velocity data from neighbouring grid points.

shown in Figure 7.6 illustrate the process of periodic shedding. A vortex can be seen to break off from the bottom surface of the cylinder.

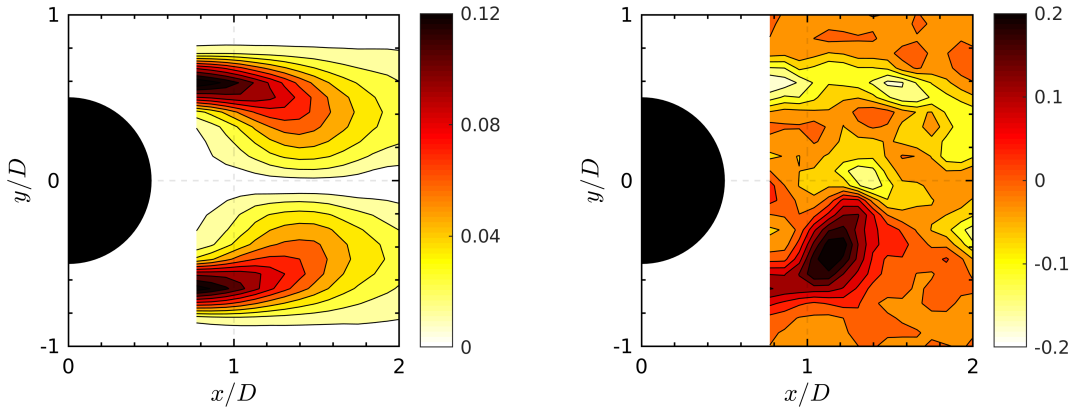

Figure 7.6: Contours of normalised z-vorticity $\omega_z(D/U_\infty)$ in the near wake at $Re_D = 4200$. Left: time-averaged profiles displaying symmetry. Right: instantaneous profile showing the shedding of a vortex from the bottom surface of the circular cylinder.

Figure 7.7 presents a typical velocity decomposition. The mean profile repre-

sents a symmetrical wake with a small recirculation region. In the phase averaged component, a von Kármán vortex street is clearly identified by alternating vortices, created at the top and bottom cylinder surface and advected downstream. No such coherent structures are identified in the stochastic signal, confirming phase averaging has successfully removed the periodic component of velocity.

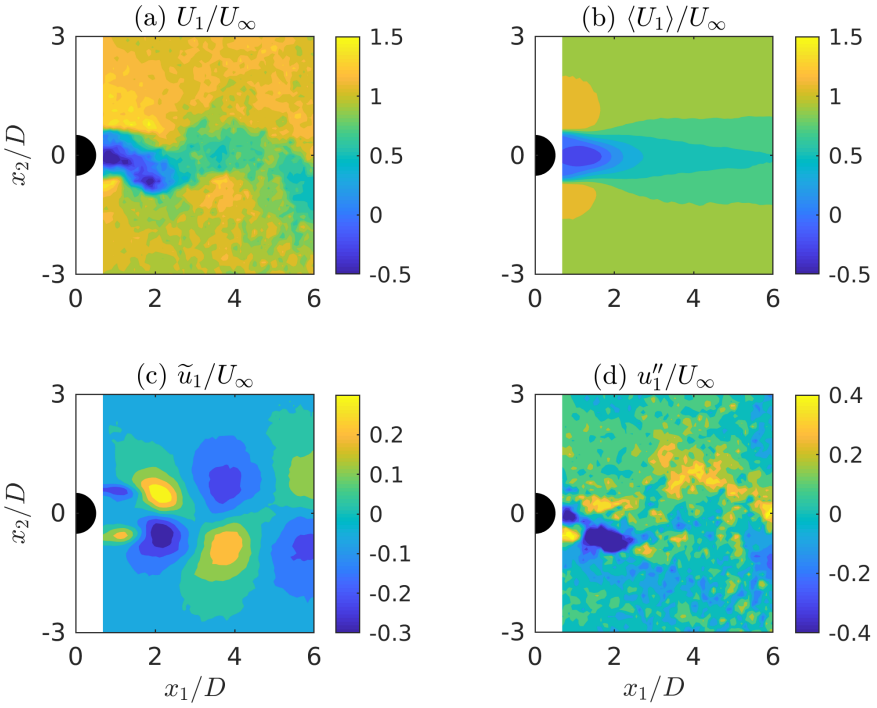

Figure 7.7: Instantaneous velocity contours in the cylinder wake. The raw velocity signal is decomposed into mean, phase, and stochastic components. A von Kármán vortex street is clearly visible in the phase averaged component.

To illustrate the operation of decomposing the velocity field into mean, phase, and stochastic components, two time-series of streamwise velocity are presented in Figure 7.8. These time series were chosen along the centreline at downstream position $x_1/D = 6$ to produce a strong influence from the cylinder shedding for at least three wave periods. Phase component $\widetilde{u}_1$ follows a sinusoidal profile which is driven by periodic shedding from the cylinder.

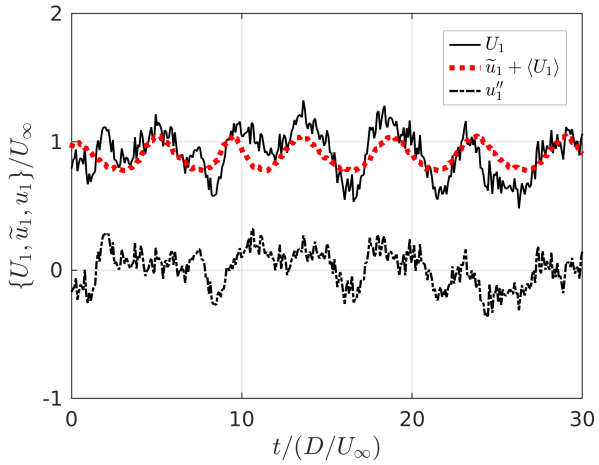

Figure 7.8: Time-series of phase and stochastic components of U_1 at a point in the wake $x/D = 6$, $y/D = 0$.

7.3.4 Wake width development

In applications where an object is placed in the vicinity of a circular cylinder, it is important to predict time-averaged properties of the cylinder wake. A simple example is the tandem cylinder configuration, where a downstream cylinder sits in the wake of a primary cylinder. Periodic shedding from the primary cylinder can cause wake-induced transverse forcing on the downstream cylinder (Bearman, 2011), but this is dependent on the wake development from the primary cylinder. If the downstream cylinder is to be placed at a certain position of the primary cylinder wake, one important consideration is the streamwise development of the wake width. For purposes of energy harvesting, devices such as piezoelectric beams are positioned in the wake where primary vortex shedding is strong (Akaydın et al., 2010). Behind a bluff body, a region of displaced fluid is generated which leads to a velocity deficit. The velocity deficit is defined by $U_w = U_\infty - \langle U_1 \rangle$, and has centreline value U_m. The wake width y_w is defined to be the distance from the centreline where the velocity deficit has decayed to $e^{-1/2}$ its maximum value.

Wake width development is dependent on characteristics of free-stream turbulence, such as turbulence intensity and integral length scale. In their wind tunnel experiment, Symes and Fink (1978) found free-stream turbulence levels of 5% had a significant influence on the cylinder wake, increasing the rate of turbu-

lent diffusion. Eames et al. (2011) developed a theoretical model to predict wake spreading in the presence of intense free-stream turbulence. Initially, a region of ballistic spreading is found, where the velocity deficit U_m/U_∞ decays like $1/x_1$. This is followed by diffusive spreading, where U_m/U_∞ decays like $1/\sqrt{x_1}$.

Figure 7.9 presents the nondimensionalized inverse of the velocity deficit along the wake centreline, for cylinder Reynolds numbers $Re_D = 2100, 4200, 6500$. A minimum is reached close to the cylinder base in the recirculation region, followed by a region of linear growth where $U_m \propto 1/x_1$. Lines of $Ax_1 + B$, where A and B are constants, have been superimposed on top of the data to highlight regions of ballistic spreading, as described in the theoretical model of Eames et al. (2011).

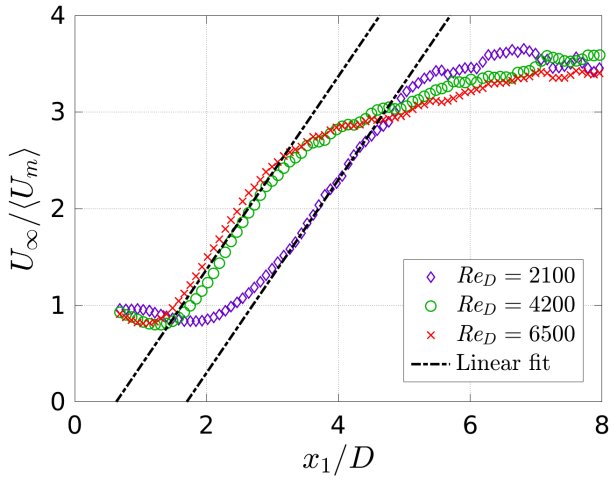

Figure 7.9: Inverse of the velocity deficit, as a function of downstream position from the cylinder. Dashed lines follow linear growth, typical of ballistic spreading.

7.3.5 Centreline development

Figure 7.10a displays time-averaged streamwise velocities along the wake centreline. In the near wake ($x_1/D < 2$) there is a velocity deficit, where the flow is highly separated and recirculating. Profiles at the cylinder base ($x_1/D = 0.5$) approach zero velocity due to the no-slip condition. It reaches a minimum of $U_{\min}$ in the recirculation region. The length of the recirculation region L_r is defined as the distance from the cylinder base to the streamwise location at which $\langle U_1 \rangle$

crosses zero. The current PIV results are in closest agreement with the PIV data of Lourenco and Shih (1993) for size of recirculation region, and magnitude. Inflow turbulence in the current PIV has created a smaller region of recirculation, with a smaller magnitude of recirculation. A short recirculation region found in Lourenco and Shih (1993) was explained by Kravchenko and Moin (2000) to be due to early transition to turbulence in the shear layers.

Figure 7.10b displays profiles of $\langle u_1^2 \rangle / U_\infty^2$ along the wake centreline. Directly behind the cylinder ($x_1/D < 3$) turbulence intensity is dominated by background noise and cylinder aspect ratio (Ma et al., 2000). In the far wake, turbulence intensity is dominated by primary von Kármán shedding. Profiles of u_1^2/U_∞^2 are characterised by a sharp increase in the near wake region, followed by a peak and eventual decay to an apparent asymptotic value. Increasing the Reynolds number shifts the peak towards the cylinder, and profiles approach their asymptote closer to the cylinder. Two peaks are visible in the results of Parnaudeau et al. (2008), which are not visible in the current PIV data. There is reasonable agreement between the current PIV data at $Re = 4200$, and the results of Parnaudeau et al. (2008) at $Re = 3900$, with regards to location and amplitude of peak $\langle u_1^2 \rangle$.

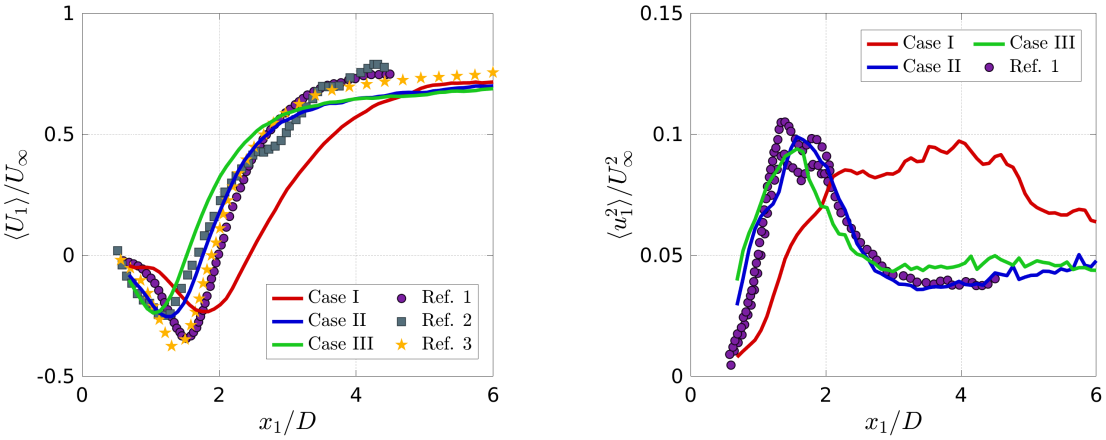

(a) Mean streamwise velocity.

(b) Variance of streamwise velocity.

Figure 7.10: Time-averaged streamwise velocity along the wake centreline. Ref. 1: PIV Parnaudeau et al. (2008), Ref. 2: PIV of Lourenco and Shih (1993), Ref. 3: DNS (case II) of Ma et al. (2000).

7.4 Dissipation in the wake

Taylor (1935) investigated the decay of grid-generated turbulence and reasoned, on ad hoc grounding, that dissipation is balanced by energy loss from the large scale motions. If the largest turbulent eddies have length and velocity scales $\mathcal{L}$ and $\mathcal{U}$ respectively, the assumed form of dissipation is given by

$$\varepsilon = C_\varepsilon \frac{\mathcal{U}^3}{\mathcal{L}} \ , \tag{7.9}$$

where C_ε is the dimensionless dissipation constant. Although C_ε does not have a universal value, it is considered to be constant for "geometrically similar boundaries", and far enough away from the grid where the shadow disappears and the mean velocity becomes uniform. The assumption that C_ε is constant has been referred to as "one of the cornerstone assumptions in turbulence theory" by Tennekes and Lumley (1972). With the advent of fractal-type grids in wind tunnel experiments, a non-classical dissipation behaviour has been confirmed in the decay region. This non-classical dissipation scaling is given by (Vassilicos, 2015)

$$C_\varepsilon \propto \frac{\sqrt{Re_I}}{Re_\lambda} \ , \tag{7.10}$$

where Re_I is an inlet/global Reynolds number, and Re_λ is the local Reynolds number based on the Taylor microscale λ, such that

$$Re_\lambda = \frac{\mathcal{U}\lambda}{\nu} \ . \tag{7.11}$$

7.4.1 Characteristic scales of turbulence

In order to investigate the behaviour of $C_\varepsilon Re_\lambda$ as an indicator of non-equilibrium turbulence, typical scales of length and velocity must be chosen. Any velocity scale $\mathcal{U}$ which does not incorporate the effects of the vortex shedding was found suitable in the study of Alves Portela et al. (2018). A strong periodic signal in $\mathcal{U} = k^{1/2}$ was detected because of the normal component $\widetilde{u}_2$. Here the choice of $\mathcal{U}$ is given by

$$\mathcal{U} = \sqrt{\frac{1}{2}\langle (u_1'')^2 \rangle} \ . \tag{7.12}$$

Alves Portela et al. (2018) investigated the behaviour of (7.10) with different choice of length scale λ. The isotropic value is given by

$$\lambda = \sqrt{15\nu\frac{\mathcal{U}^2}{\varepsilon}} \ , \tag{7.13}$$

however, a different choice of length scale can be taken, for example

$$\lambda_{ij} = \sqrt{\frac{2\langle u_i^2\rangle}{\langle(\partial_j u_i)^2\rangle}} \ , \tag{7.14}$$

where $\partial_i \equiv \partial/\partial x_i$, and there is no summation over repeated indices. Alves Portela et al. (2018) found the ratio λ_{ij}/λ to be approximately constant in the downstream region $4 \lesssim x_1/D < 10$, therefore without the third component of velocity in the PIV measurements, it is possible instead to take (7.14) for $i = j = 1$. Following Alves Portela et al. (2018), the characteristic length scale is taken to be $\mathcal{L} = U_1\Theta_{u_1''}$, where $\Theta_{u_1''}$ is the integral time scale given by

$$\Theta_{u_1''} = \frac{1}{\langle u_1''(\boldsymbol{x},t)^2\rangle}\int_0^{r_0}\langle u_1''(\boldsymbol{x},t)u_1''(\boldsymbol{x},t+\tau)\rangle\,\mathrm{d}\tau \ , \tag{7.15}$$

where r_0 is the first zero-crossing of the integrand, and τ is a separation in time. It is noted that (7.12) and (7.15) do not contain any phase component of velocity, and therefore large-scale coherent motions have been removed from characteristic scales $\mathcal{U}$, $\mathcal{L}$.

7.4.2 Dissipation term decomposition

A surrogate of the dissipation term was introduced in Chapter 5.5.2. The main points are revisited here before the method is used to evaluate dissipation along the circular cylinder wake centreline. The pseudo dissipation term ε_{xy} only requires measurements of velocity and velocity derivatives from a two-dimensional slice on the x-y plane, which is available here in the planar PIV measurements. For the circular cylinder wake, ε_{xy} was found to be close approximation to ε. Dissipation is split into coherent and stochastic components from the phase averaging

procedure such that $\varepsilon_{xy} = \widetilde{\varepsilon}_{xy} + \varepsilon''_{xy}$, where

$$\widetilde{\varepsilon}_{xy} = 2\nu \left[\langle (\widetilde{S}_{11})^2 \rangle + \langle (\widetilde{S}_{22})^2 \rangle + 2\langle (\widetilde{S}_{12})^2 \rangle \right] \quad , \tag{7.16}$$

$$\varepsilon''_{xy} = 3\nu \left[\langle (S''_{11})^2 \rangle + \langle (S''_{22})^2 \rangle + 4\langle (S''_{12})^2 \rangle \right] \quad , \tag{7.17}$$

where $\widetilde{S}_{ij}$ and S''_{ij} are the strain rate of phase averaged and stochastic velocity components, respectively.

Dissipation along the wake centreline for Reynolds numbers $Re_D = 2100, 6500$ is displayed in Figure 7.11. The combined dissipation due to phase and stochastic motions displays a peak in the near wake and then decays in the streamwise direction. Profiles of stochastic dissipation ε''_{xy} follow the same trend as ε_{xy} and have therefore been omitted. It can also be seen that coherent motions make little contribution towards dissipation, in agreement with the findings of Hussain (1983) and Alves Portela et al. (2018). Interestingly, at the lowest Reynolds number, $\widetilde{\varepsilon}_{xy}$ displays two pronounced peaks at $x_1/D \approx 2, 3$. The first peak at $x_1/D \approx 2$ corresponds to the point at which the variance of the streamwise velocity u_c^2 begins to plateau towards its maximum value (Figure 7.10b), and where $U_c = U_{\min}$ (Figure 7.10a). The second peak at $x_1/D \approx 3$ corresponds to the point at which the ballistic spreading regime begins.

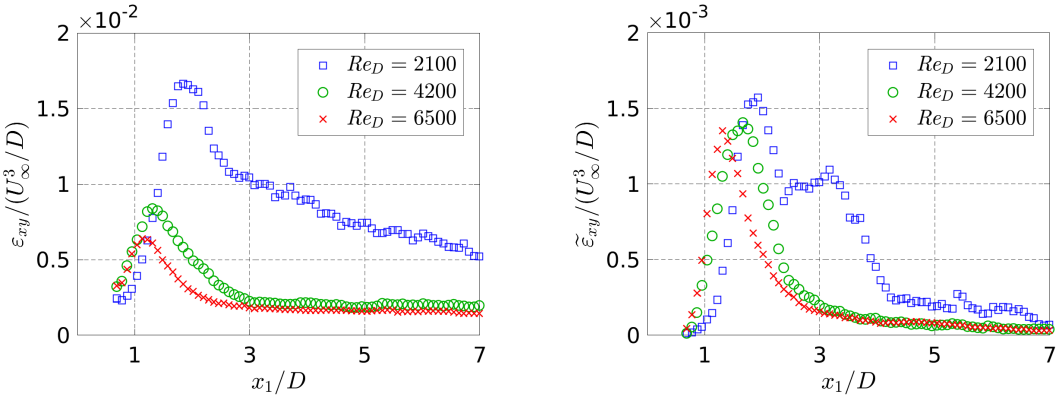

Figure 7.11: Centreline development of turbulent dissipation, and dissipation due to coherent motions, both nondimensionalized by U_∞^3/D.

Non-equilibrium turbulence is believed to result from a locking of dissipation between stochastic and coherent motions, which leads a constant ratio of $\varepsilon''/\widetilde{\varepsilon}$

(Goto and Vassilicos, 2015). Figure 7.12 plots the ratio $\varepsilon''/\widetilde{\varepsilon}$ along the wake centreline. Strictly speaking, it is the ratio $\varepsilon''_{xy}/\widetilde{\varepsilon}_{xy}$ which is calculated for the current PIV. Results from the current PIV at Reynolds numbers 2100 and 4200 are compared to the LES regular grid inlet (RGI) case ran in Chapter 5. Also included are the DNS data in the square cylinder wake of Alves Portela et al. (2017), which was later re-analysed by Alves Portela et al. (2018). The ratio $\varepsilon''/\widetilde{\varepsilon}$ is approximately constant with a value of 10 in the current PIV data at $Re_D = 2100$ for the region $2 < x_1/D < 4$. This is followed by a sharp increase and a second plateau at $4 < x_1/D < 6$. However, results from the Reynolds number of 4200 display a steady increase through $x_1/D > 2$, with no observable plateau. A close agreement is found between the PIV data and the LES data in the region $2 < x_1/D < 4$. In the region $4 < x_1/D < 6$, the current PIV data begins to deviate from the LES, and looks to be approaching the DNS of Alves Portela et al. (2018). An increase in $\varepsilon''/\widetilde{\varepsilon}$ may occur when a flow transitions out of equilibrium. However, this isn't suggested by the simulations, because $\varepsilon''/\widetilde{\varepsilon}$ remains constant for a least 10 diameters downstream of the cylinder. It is possible that noise in the PIV data begins to contaminate the stochastic component of dissipation far enough away from the cylinder.

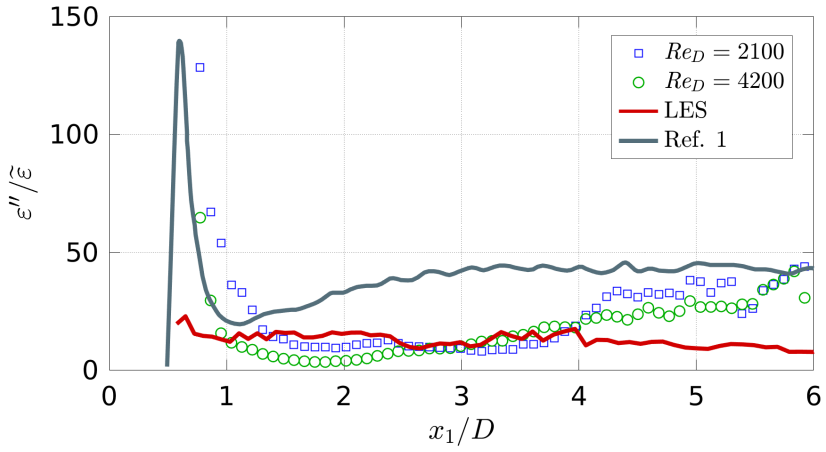

Figure 7.12: Centreline development of turbulent dissipation. LES: results of Chapter 5 for the RGI turbulent inflow case at $Re_D = 3900$. Ref. 1: Alves Portela et al. (2018) DNS of square prism wake at a Reynolds number of 3900.

7.4.3 Dissipation scaling

Profiles of $C_\varepsilon Re_\lambda/\sqrt{Re_D}$ (Figure 7.13), display similar behaviour for Reynolds numbers $Re_D = 2100, 6500$. Profiles collapse when normalised by $\sqrt{Re_D}$, further strengthening the claim of $C_\varepsilon \propto \sqrt{Re_I}/Re_\lambda$ (Vassilicos, 2015), where the global Reynolds number here is the cylinder Reynolds number. However, this behaviour can be split into two categories: (i) C_ε, Re_λ are both constant; (ii) one increases as the other decreases, in proportion to one another. It can be seen from Figure 7.14 that C_ε increases at the same rate that Re_λ decreases for $Re_D = 2100$. At the highest Reynolds number $Re_D = 6500$, it can be deduced that constant $C_\varepsilon Re_\lambda$ is due to both terms becoming constant.

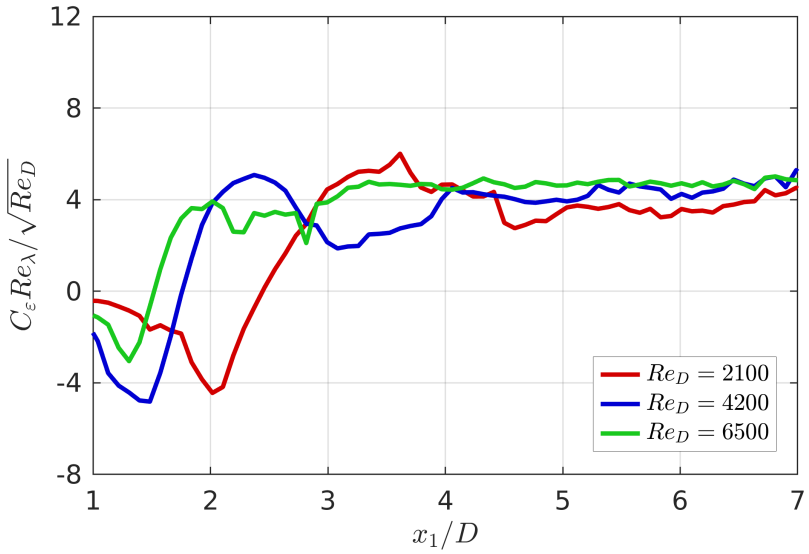

Figure 7.13: Relationship between dissipation constant C_ε, and local Reynolds number Re_λ.

The non-equilibrium dissipation scaling is written out in full by expanding each term (7.9), (7.11)

$$C_\varepsilon Re_\lambda = \frac{\varepsilon}{\nu}\frac{\lambda \mathcal{L}}{\mathcal{U}^2} \quad , \tag{7.18}$$

$$= \frac{\varepsilon}{\nu}\frac{\mathcal{L}}{\lambda}\left(\frac{\lambda}{\mathcal{U}}\right)^2 \quad . \tag{7.19}$$

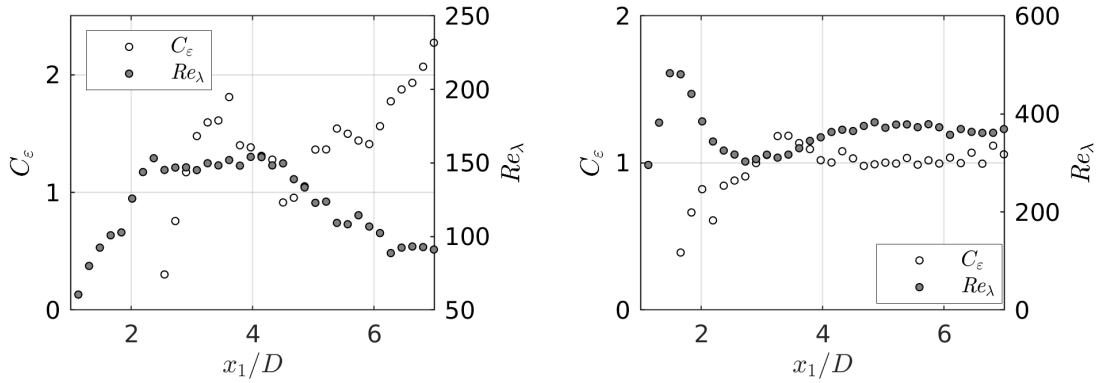

(a) $Re_D = 2100$. (b) $Re_D = 6500$.

Figure 7.14: Development of dissipation constant C_ε, and local Reynolds number Re_λ along the centreline.

If $\mathcal{L}/\lambda$ is constant (Vassilicos, 2015), (7.19) simplifies to

$$C_\varepsilon Re_\lambda \propto \frac{\varepsilon \mathcal{T}^2}{\nu} \quad , \tag{7.20}$$

where $\mathcal{T} = \lambda/\mathcal{U}$ is some local turbulent time scale. The development of $\varepsilon\mathcal{T}^2$ along the wake centreline is shown in Figure 7.15. It is evident that $\varepsilon\mathcal{T}^2$ asymptotes to a constant value for approximately $x_1/D > 3$.

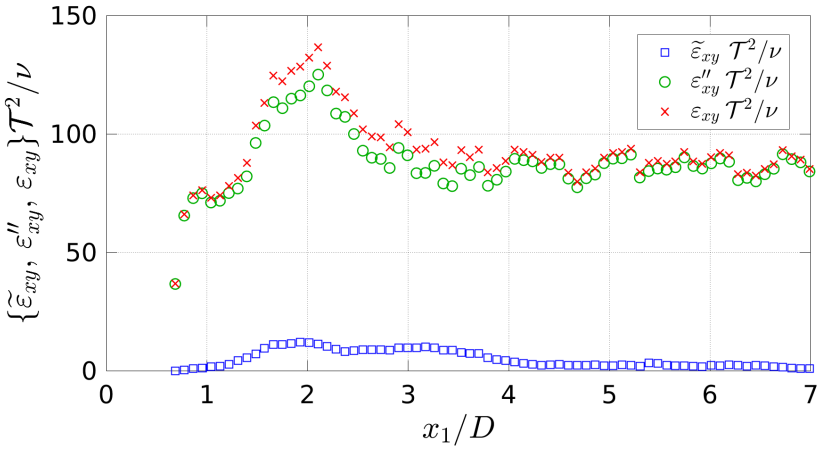

Figure 7.15: Development of $\varepsilon_{xy}\mathcal{T}^2$ along the wake centreline for $Re_D = 2100$.

7.5 Chapter conclusions

Turbulent flow past a circular cylinder in a recirculating water flume has been investigated using two-dimensional particle image velocimetry in the subcritical range of Reynolds numbers. Turbulence upstream from the cylinder has been generated by passing the flow through a biplane grid, yielding non-negligible turbulence intensities of 5-10%. Free-stream turbulence has been found to squeeze the wake closer to the cylinder base. Results agree with previous experiments, where flow disturbances have been inadvertently added to the free-stream.

Proper orthogonal decomposition has been used in this study to identify coherent motions in the circular cylinder wake, and provide a trigger signal for phase averaging. The two-dimensional velocity field has been decomposed into mean, phase averaged, and stochastic components. It is demonstrated that phase averaging successfully extracts coherent motions, which correspond to the von Kármán street vortices. Calculating turbulence dissipation requires a total of 9 terms from the velocity gradient tensor, only 4 of which are resolved in planar PIV. By decomposing turbulence dissipation into coherent and stochastic components, the surrogate ε_{xy} can be used as an approximation. This was developed in Chapter 5 and validated on LES data.

The non-equilibrium dissipation scaling $C_\varepsilon \propto 1/Re_\lambda$ has been observed in the near wake in the current study. However, there is different behaviour between the low and high Reynolds number cases. As the cylinder Reynolds number is increased, C_ε and Re_λ quickly asymptote to a constant value, at least for the range of wake extent monitored. For the lowest Reynolds number tested in the current experiment, C_ε increases as Re_λ decreases at the same rate, giving $C_\varepsilon \propto 1/Re_\lambda$.

For the wake of a square prism at Reynolds number 3900, Alves Portela et al. (2018) propose the scaling $C_\varepsilon \propto 1/Re_\lambda$ is a consequence of locking between stochastic and phase averaged dissipation components, such that the ratio $\varepsilon''_{xy}/\widetilde{\varepsilon}_{xy}$ is constant along the centreline in the wake. Although the study of Alves Portela et al. (2018) concerned a square prism, and a circular cylinder has been used in the current investigation, reasonable agreement is found between the two cases. In the current study, the ratio $\varepsilon''_{xy}/\widetilde{\varepsilon}_{xy}$ becomes constant in the downstream region at the lowest Reynolds number $Re_D = 2100$, but is steadily increasing in

the same region for the higher Reynolds numbers tested. Yiu et al. (2004) studied the circular cylinder wake in the Reynolds number range $Re_D = 2500$ to 10000 and found two-dimensionality of the wake broke down as the Reynolds number was increased. Here it has been observed that centreline dissipation due to stochastic turbulent motions dominates dissipation due to coherent shedding as the Reynolds number is increased, even in the small Reynolds number range tested here for $Re_D = 2100$ to 6500. This is in disagreement to the LES results of Chapter 5, where the ratio $\varepsilon''/\widetilde{\varepsilon}$ is constant for at least 10 diameters along the centreline.

To further investigate the non-equilibrium dissipation scaling, individual terms of $C_\varepsilon Re_\lambda$ are expanded. It is shown that non-equilibrium dissipation behaviour coincides with regions of constant $(\widetilde{\varepsilon}_{xy} + \varepsilon''_{xy})\mathcal{T}^2$, where $\mathcal{T}$ is a turbulent time scale based on the Taylor microscale. Further work is required to understand the mechanism responsible for the sensitivity of C_ε to inflow conditions in the wake of bluff bodies.

Chapter 8

Conclusions and outlook

8.1 Thesis conclusions

Simulations of grid turbulence have been carried out to investigate the generation and decay of freestream turbulence. A comprehensive study was undertaken using LES to compare turbulence characteristics behind 4 grid designs. A new fractal grid design has been compared to 3 standard grids: regular, multiscale, and square-fractal. Fractal shapes are ubiquitous in nature, and this type of flow can be exploited in the engineering industry, e.g. for applications of vortex shedding and mixing. To the author's knowledge, this is the first time multiscale and fractal shapes have been considered in such a study.

Clustering in the vorticity field has been reported in wind tunnel experiments for the turbulence generated by fractal grids. The reason for this has been confirmed in the current simulations- if solidarity is not sufficiently spread across the inlet patch, this can lead to prominent jets and wakes which are not broken up as they travel downstream. Evidence for this has been provided by taking slices through the domain to visualise high velocity streaks. Vorticity clumping has also been observed in the fractal designs, especially along the perimeter of the square-fractal grid.

Turbulence decay in the wake of the regular and multiscale grids differs to the fractal-type grids. Along the centreline, the decay exponent measured behind the fractal-type grids builds rapidly. This is in agreement with previous experiments, where a higher exponent is measured behind fractal grids compared to regular or multiscale grids. A region of non-equilibrium turbulence has been detected in the wake of all 4 grid designs, although to a varying degree. This is attributed to forcing of turbulence at multiple length scales, which disrupts the flow of energy down the cascade.

Building directly on the grid turbulence simulations, Chapter 5 investigated turbulent flow past a circular cylinder using LES. Two types of turbulent flow were generated upstream by using a regular and fractal grid design, projected onto the inlet patch. A laminar inflow was also simulated as the base case. An increase in drag is experienced between the laminar inflow (LI), and the two fractal grid cases. This is to be expected. However, taking inflow turbulence conditions into consideration, i.e. integral length scale, turbulence intensity, and Reynolds

number, the RGI and FGI cases should predict a similar drag coefficient. This has not been the case. Despite the FGI case producing turbulence with a lower intensity and smaller integral length scale, a higher drag coefficient is returned. A 15% increase in drag was observed for the regular grid inlet when compared to the laminar inflow case. This increases further to 33% when comparing the fractal grid inlet to the laminar inflow case. This suggests that characterising inflow turbulence on intensity and integral length scale alone is insufficient.

Structures in the wake were then identified for each inflow case, and it was possible to detect rollers and streamwise ribs in each simulation. In the Reynolds number range studied in this thesis, the circular cylinder wake consists of rollers, streamwise ribs, saddle points, high mixing regions, and engulfed free-stream. This is reasonably well understood, and models have been developed to describe these processes. However, there is less understanding on how dissipation is concentrated in relation to coherent structures, with the current theory being that it resides in the primary rollers. When the dissipation field is visualised and superimposed on top of the coherent motions, it is seen that high levels of dissipation are concentrated in between the streamwise ribs. This is a significant result which has not been reported before in the literature. An updated model of the circular cylinder wake is introduced with this new information on the dissipation field.

Along the wake centreline, dissipation is split into coherent and stochastic contributions by implementing a phase averaging technique. The ratio of stochastic to coherent dissipation is approximately constant in the near wake of the circular cylinder, up to at least 10 diameters. Locking between coherent and stochastic dissipation has been detected in the wake of a square-cylinder, but this is believed to be the first time this has been observed in the circular cylinder wake. This locking phenomenon is important to study, because it is suspected to be linked to non-equilibrium dissipation. A surrogate of the dissipation term, denoted by ε_{xy}, has been developed which has been successfully verified on the circular cylinder wake. Not only does ε_{xy} perform equally well compared to other commonly used surrogates of ε from the literature, but it also only requires those components of velocity measured with planar PIV.

The cylinder wake was then investigated experimentally using particle image velocimetry. A turbulence inflow was generated using a regular grid. Freestream

flow conditions were comparable to the RGI case of Chapter 5. A total of 3 runs were analysed at Reynolds numbers $Re_D = 2100, 4200, 6500$. It was found that a turbulent inflow causes an early transition in the wake, leading to a smaller recirculation region. This was also observed in the simulations of Chapter 5. A phase averaging procedure was applied to extract coherent motions from the wake. A trigger signal to characterise the phase angle of periodic shedding was deduced from analysis of the proper orthogonal decomposition (POD) modes. This is in contrast to the LES study of Chapter 5, where a trigger signal was available from a time series of the lift coefficient. POD has also been used in the pre-processing of data to remove spurious vectors. Dissipation along the centreline has been calculated from the two-dimensional data using the surrogate method developed in Chapter 5, and split into coherent and stochastic contributions. The ratio between dissipation due to stochastic motions and dissipation due to coherent motions is found to be constant in the wake, and is in close agreement to the current LES. Non-equilibrium turbulence has been detected at each Reynolds number, but it is especially pronounced in the lowest Reynolds number case.

To summarise the overriding conclusions from this thesis- a method to generate bespoke turbulence in simulations has been explored, which has been considered in isolation, and as a method to create free-stream turbulence upstream of a circular cylinder. An alternative method of calculating dissipation in the wake of a periodic shedding bluff body has been developed, which is validated using CFD of flow past a circular cylinder, and used to calculate dissipation in the cylinder wake from planar PIV data. A new model of the circular cylinder wake has been proposed, which describes the configuration of dissipation and coherent structures. Results and methods presented in this thesis are relevant not only to the study of turbulent flow past a circular cylinder, but also to the subjects of grid-generated turbulence, and bluff body flow.

8.2 Research aims revisited

Research objectives were set out in Chapter 1 to "...improve understanding of the circular cylinder wake for a turbulent inflow. In particular, the relationship

between coherent turbulent structures and dissipation will be investigated". Each objective is revisited here:

I. *Develop a method to generate free-stream turbulence in simulations which can replicate bespoke grid turbulence from experiments.*

   (a) *Review the experimental literature of grid turbulence.*
   Chapter 2 presented a review of classical grid turbulence, alongside more recent developments in multiscale/fractal grid turbulence experiments. Despite the wide applications of fractal grid turbulence in the engineering industry, there are a lack of studies reported in the literature which consider the case of multiscale turbulent flow past bluff bodies. There is also no consensus on the best way to generate multiscale free-stream turbulence in simulations.

   (b) *Simulate grid turbulence using different designs to compare turbulence produced by classical and novel grids.*
   Large-eddy simulations of free-stream turbulence have been carried out by projecting grid designs onto the inlet patch in Chapter 4. This has been shown to be a suitable method for generating realistic grid turbulence in simulations, even reproducing universal laws from wind tunnel experiments.

   (c) *Identify important parameters in grid construction which influence turbulence level, homogeneity, and length scales.*
   A crucial finding from Chapter 4 is that common fractal designs used in wind tunnel experiments can display poor homogeneity across the grid element. This has been observed in wind tunnel experiments and has been explained here by considering one fractal grid element in isolation. The central cross of each grid element plays a vital role in flow homogeneity and also on the turbulent length scales produced. A similar level of turbulence is produced from each grid because the inflow speed has been fixed, rather than fixing the grid inlet Reynolds number Re_0.

II. *Explore the relationship between coherent structures and dissipation for simulations of laminar and turbulent flow past a circular cylinder.*

   (a) *Investigate the influence of free-stream turbulence on lift and drag of the circular cylinder.*
   An increase in drag has been observed when turbulence is introduced in the free-stream. This has been reported in the numerical simulations of Chapter 5. For the laminar inflow, the drag coefficient of $C_d = 1.03$ matches well to literature. This increases to 1.18 for the regular grid inlet, and 1.37 for the fractal grid inlet.

   (b) *Evaluate alternative methods of estimating the dissipation term which require fewer terms of the velocity gradient tensor.*
   An alternative method of calculating dissipation from only two components of velocity has been developed by decomposing the velocity field into coherent and stochastic contributions, which is denoted by ε_{xy}. It has been shown that ε_{xy} is a good approximation to ε for the circular cylinder wake, and can also be evaluated using only two components of the velocity field. A locking between the dissipation due to coherent motions and the dissipation due to stochastic motions was observed.

   (c) *Construct a three-dimensional picture of the wake, including: rollers, ribs, and the dissipation field.*
   A model to describe the interaction between concentrated regions of dissipation and coherent motions in the wake was proposed in Chapter 5. It has been previously reported in the literature that dissipation is concentrated within the primary vortex rollers. However, it is shown in Chapter 5 that dissipation resides between the streamwise rib structures.

III. *Investigate the circular cylinder wake experimentally using planar particle image velocimetry (PIV) for a turbulent free-stream, validating findings from the numerical modelling.*

   (a) *Estimate dissipation along the centreline from a two-dimensional plane in the circular cylinder wake.*

The surrogate of dissipation ε_{xy} developed in Chapter 5 has been measured experimentally in Chapter 7 from two-dimensional PIV velocity data.

(b) *Decompose the circular cylinder wake structures into coherent and stochastic motions, verifying the relationship between coherent and stochastic dissipation.*
The method of proper orthogonal decomposition has been implemented on the velocity field to extract dissipation due to coherent motions $\widetilde{\varepsilon}_{xy}$ and stochastic motions ε''_{xy}. Stochastic motions are a greater contributor to the centreline dissipation, which validates the results from the numerical simulations of Chapter 5.

8.3 Suggestions for future work

This thesis has investigated the circular cylinder wake for a turbulent inflow. A suitable method of producing grid turbulence in simulations has been explored for a number of different grid designs, and universal laws of turbulence production and decay have been successfully validated against experiments. There are two main motivations for producing grid turbulence in simulations: (i) study the fundamental nature of grid turbulence and assess grid designs; (ii) produce realistic free-stream turbulence upstream of a bluff body. Both points have been explored in this thesis, but further avenues for research follow naturally from this:

I. *Simulating grid turbulence in isolation.*
A total of 4 grid designs were considered in this thesis, and the new combined-fractal grid showed promise as an alternative to the regular and fractal grids. However, there is scope to further investigate novel grid designs in simulations. Additionally, the introduction of a solid wall running along the streamwise direction would provide researchers with a test case for investigating the interaction between grid turbulence and a boundary layer flow. For applications of wind engineering where there are bursts and gusts of turbulent flow, it is possible to set a time varying inflow speed, i.e. representing pulsing grid turbulence.

II. *Simulating grid turbulence upstream of a bluff body.*
This thesis has provided a method to simulate the flow of grid turbulence past a circular cylinder, but this can be applied to various geometries of aerodynamic and engineering interest. Beyond the scope of this thesis, there is potential to apply the methods of simulating free-stream turbulence to the study of fluid-structure interaction (FSI) of a flexible body placed in a turbulent flow.

Another focus of this thesis has been dissipation. Dissipation plays a key role in the dynamics of turbulence decay, and has a close relationship with coherent structures in the circular cylinder wake. Further work is required in the following areas:

I. *Dissipation modelling.*
In Chapter 3, dissipation modelling in LES was discussed in the context of free-stream turbulence. There is potential to develop subgrid-scale models which take into account the non-equilibrium dissipation behaviour which has been observed in wind tunnel experiments. An alternative to the model equation for dissipation was proposed, where the constant $C_{\varepsilon 2}$ is allowed to vary depending on the local turbulence level.

II. *Coherent structures and dissipation.*
A new model of the circular cylinder wake was proposed in Chapter 5, where it was concluded that dissipation is concentrated in between the streamwise ribs. This contradicts the experiments of Chen et al. (2018). To the author's knowledge, no volumetric experimental data set for the dissipation field exists in the wake of the circular cylinder. A next step towards understanding dissipation in the wake is to collect DNS or volumetric PIV velocity data.

Appendix A

Default OpenFOAM settings

Default numerical schemes chosen throughout the current study are presented in Table A.1, unless stated otherwise. An adjustable time-step is enforced, guaranteeing a Courant-Friedrichs-Lewy (CFL) condition of less than 0.75. Crank Nicolson is employed for time discretisation, with blending coefficient 0.8 for improved stability. Upwind discretisation schemes implemented in LES are overly dissipative (Beaudan and Moin, 1994), therefore they have been avoided in this study. Instead, central based schemes, which control aliasing by an energy conservation principle, and do not introduce spurious damping in the small scales (Mittal, 1995), have been favoured. Laplacian terms are discretised using Gaussian integration with linear interpolation for diffusivity, and surface normal gradients are calculated using the corrected scheme to maintain second-order accuracy.

In a segregated pressure-based solver, the momentum equation is solved separately from the pressure equation (Patankar and Spalding, 1983). The pressure equation, which enforces mass conservation, is estimated to account for between 50-80% of total simulation time (Jasak et al., 2007). Therefore, linear solver efficiency has a great bearing on the overall computational time required. In the current study, the generalised geometric-algebraic multi-grid (GAMG) solver is favoured over the Preconditioned Conjugate-Gradient (PCG) solver. The GAMG solver is generally considered to be faster than the PCG solver, and this was found to be true for jobs of $\lesssim 120$ cores (D'Allessandro et al., 2016). Further details on OpenFOAM solvers, smoothers, and preconditioners can be found in Behrens (2009). Initially GAMG is used in the current study with the `GaussSeidel`

Operator	Current selection	Description
Time derivative	`CrankNicolson 0.8`	2nd-order implicit, bounded.
Gradient	`Gauss linear`	2nd-order, linear face-interpolation.
Divergence	`Gauss linear`	2nd-order, unbounded.
Laplacian	`Gauss linear`	2nd-order, unbounded, conservative.
SN grad.	`corrected`	Explicit non-orthogonal correction.

Table A.1: Numerical schemes sub-dictionaries in OpenFOAM.

smoother to reduce the residuals down to a tolerance of 10^{-3}, or relative tolerance of 10^{-2}. Finally, the combined DIC/GaussSeidel smoother `DICGaussSeidel` is chosen with a tolerance of 10^{-7}.

The computational domain is split into sub-domains through the utility `decomposePar`, before running simulations in parallel. The `scotch` decomposition method has been selected to minimise the number of shared cells between processors. OpenFOAM is highly parallelizable- Robertson et al. (2015) found OpenFOAM to scale well up to 192 processors on a mesh of 11 million cells.

Computational work in this thesis was undertaken on ARC3 and ARC4, part of the High Performance Computing (HPC) facilities at the University of Leeds, UK. OpenFOAM v4.1 is compiled on the ARC systems with the gnu/6.3.0 compiler and runs in parallel using the message passing interface OpenMPI.

Appendix B

Mesh independence study for Chapter 4

Simulations are ran on the combined-fractal grid with various mesh densities. The combined-fractal grid has been chosen because it has the greatest range of bar lengths and widths, therefore is expected to require the most refinement. Hexahedral control volumes are chosen to mesh the geometry to achieve an orthogonal structured mesh with zero skew. Meshes are generated in the `blockMesh` application of OpenFOAM. There are a total number of $N = n_x \times n_y \times n_z$ cells. All control volumes are cubes, therefore no grading is applied in any direction. For each grid, it is only necessary to choose n_y, from which it is then possible to set $n_z = n_y$. Since the channel has a length of $4W$, where W is the width, it therefore follows that $n_x = 4 \times n_y$. Refinement of a grid is obtained from multiplying n_y by some expansion factor α. Here the expansion factor between each grid is kept at an approximately constant $\alpha = 1.135$. Table B.1 presents the mesh densities used in the mesh independence study.

Time-averaged streamwise velocity profiles along the centreline are displayed in Figure B.1. An area of recirculation is present near grid, corresponding to the centreline probes sitting directly behind a large middle bar. Along the centreline, streamwise velocity converges towards approximately half the inlet velocity for all grids. As the mesh resolution is increased, the recirculation region shortens considerably. Here it can be seen that the mesh of CF1 is too coarse to resolve

Mesh	n_x	n_y, n_z	N $(\times 10^6)$
CF1	520	130	8.8
CF2	580	145	12.2
CF3	660	165	18.0
CF4	760	190	27.4

Table B.1: Cell density for mesh independence studies on the combined-fractal grid.

the flow directly behind the grid. Profiles of CF3 and CF4 collapse on top of one another, however CF2 begins to deviate at $x_1/W \approx 0.2$.

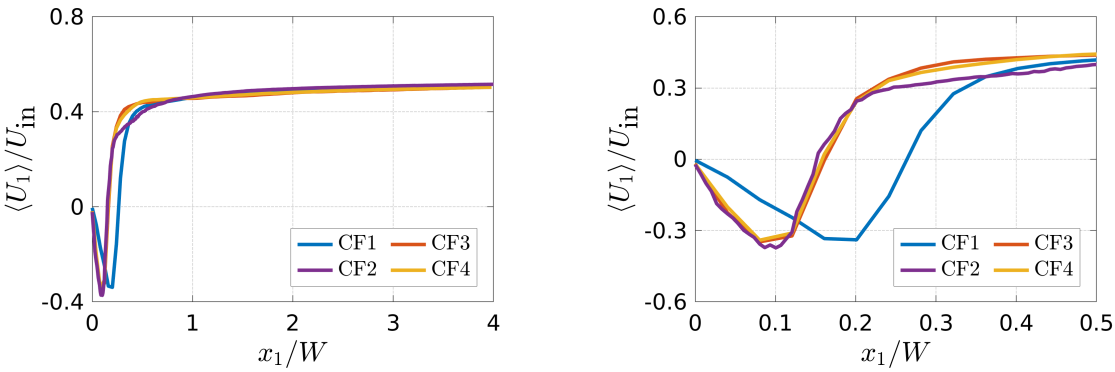

Figure B.1: Time-averaged streamwise velocity along the domain centreline.

Figures B.2 and B.3 display profiles of time-averaged streamwise and normal velocity cross-channel at downstream positions $x_1/W = 1, 2, 3, 4$. Peaks and troughs across the channel correspond to the grid shadow, which is more pronounced at $x_1/W = 1$. Profiles of $\langle U_1 \rangle$ and $\langle U_2 \rangle$ begin to flatten at increasing distances from the grid. It is generally observed that the solution generated from CF1 deviates significantly from the other mesh densities. This is particularly true for profiles of $\langle U_2 \rangle$, which corresponds to shedding in the grid wake. Apart from the coarsest mesh CF1, profiles of $\langle U_2 \rangle$ are reasonably well collapsed. A similar outcome is observed in profiles of $\langle U_1 \rangle$. However, near grid for $x_1/W = 1$, velocity profiles produced by CF2 are in similar agreement to CF1. This leads to the conclusion that if CF1 is too coarse, so is CF2.

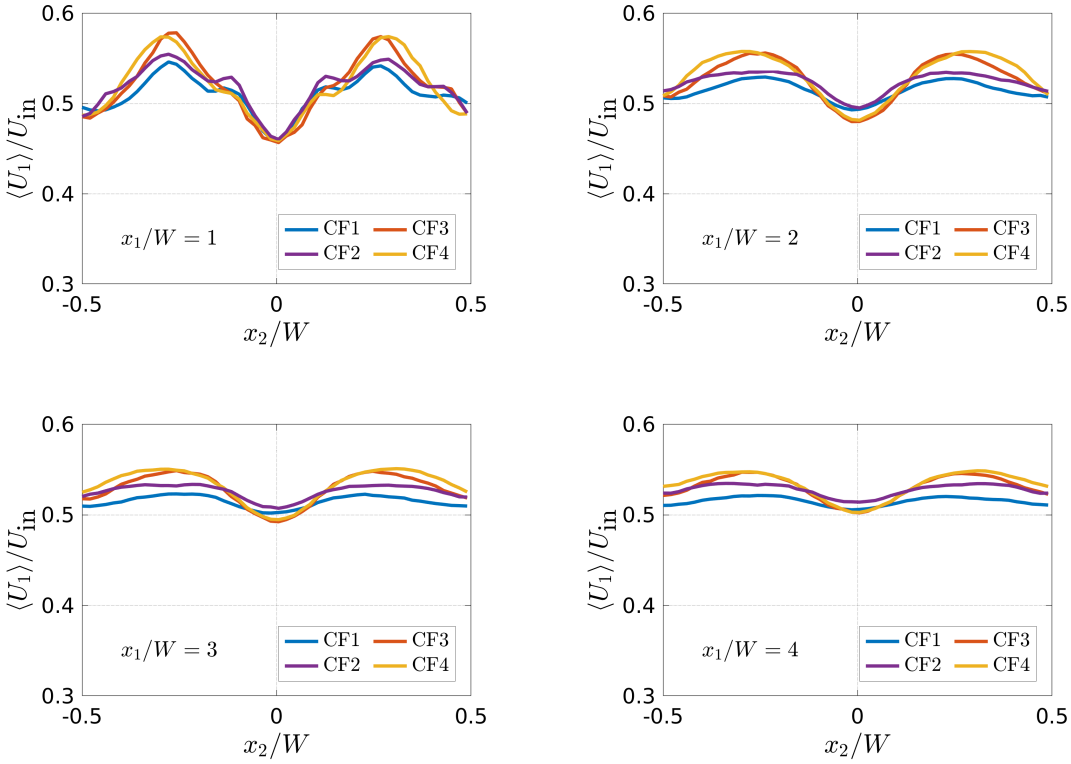

Figure B.2: Time-averaged streamwise velocity across the channel.

Figure B.4 presents the downstream development of $\langle q^2 \rangle / 3 \langle u_1^2 \rangle$, where $\langle q^2 \rangle = \langle u_1^2 + u_2^2 + u_3^2 \rangle$. This serves as a measure of isotropy. The flow is highly anisotropic near grid in the production region, but settles towards isotropy in the far field. Profiles of CF3 and CF4 are roughly constant, even close to the grid. However, the coarser meshes CF1 and CF2 take longer to reach a constant value.

It is concluded from this mesh resolution study that a minimum requirement is $n_y = 165$ elements. This results in a total number of 18.0 million cells.

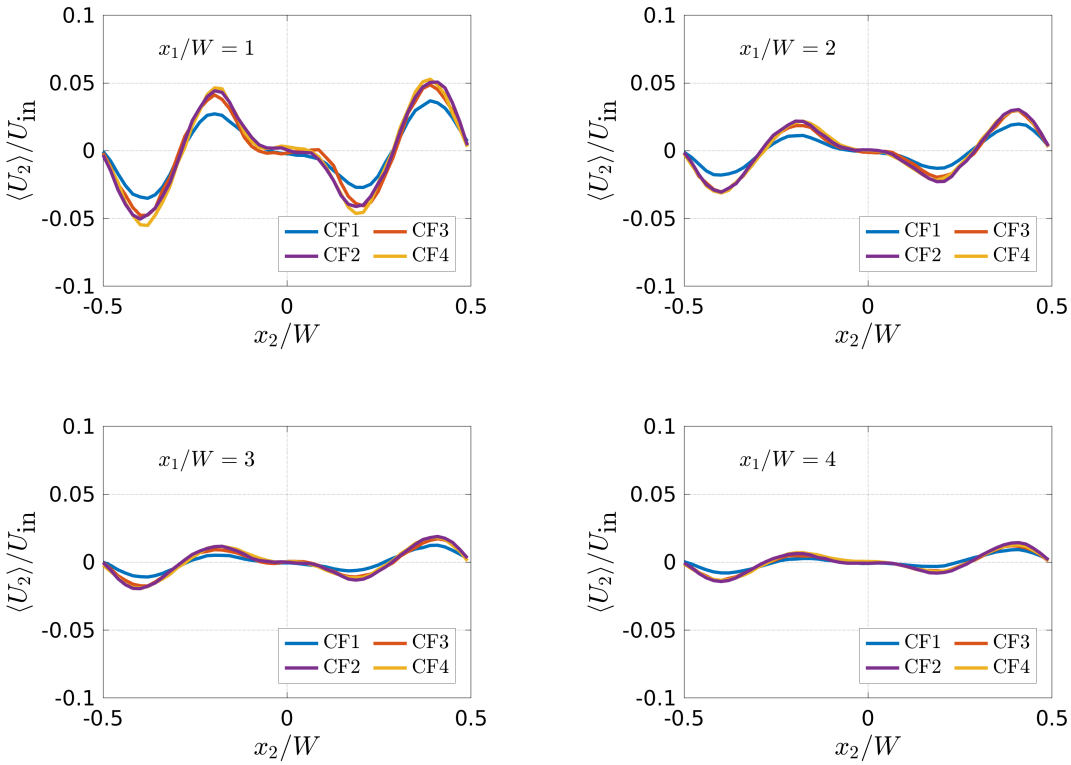

Figure B.3: Time-averaged normal velocity across the channel.

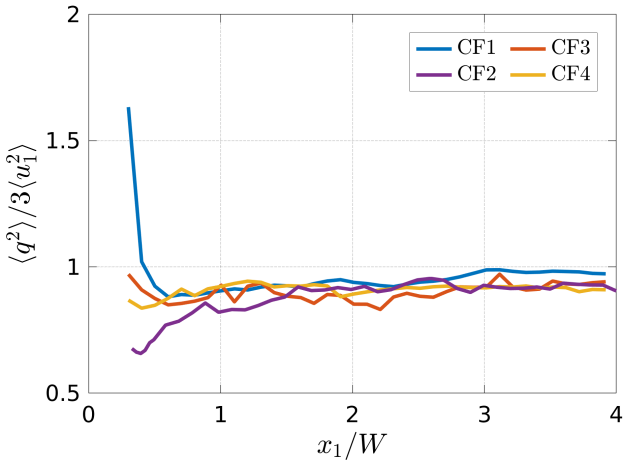

Figure B.4: Streamwise development of isotropy along the centreline.

References

J. R. Aarnes, H. I. Andersson, and N. E. L. Haugen. Numerical investigation of free-stream turbulence effects on the transition-in-wake state of flow past a circular cylinder. *Journal of Turbulence*, 19(3):252–273, 2018. 3, 34, 116

R. J. Adrian. Particle-imaging techniques for experimental fluid mechanics. *Annual Review of Fluid Mechanics*, 23(1):261–304, 1991. 182, 196

R. J. Adrian and J. Westerweel. *Particle image velocimetry*. Number 30. Cambridge University Press, 2011. XIX, 172, 173, 178

J. Aider, A. Danet, and M. Lesieur. Large-eddy simulation applied to study the influence of upstream conditions on the time-dependant and averaged characteristics of a backward-facing step flow. *Journal of Turbulence*, (8):N51, 2007. 67

H. D. Akaydın, N. Elvin, and Y. Andreopoulos. Wake of a cylinder: a paradigm for energy harvesting with piezoelectric materials. *Experiments in Fluids*, 49 (1):291–304, 2010. 30, 199

N. Alkishriwi, M. Meinke, and W. Schröder. A large-eddy simulation method for low mach number flows using preconditioning and multigrid. *Computers & Fluids*, 35(10):1126–1136, 2006. 31

F. Alves Portela, G. Papadakis, and J. C. Vassilicos. The turbulence cascade in the near wake of a square prism. *Journal of Fluid Mechanics*, 825:315–352, 2017. 205

F. Alves Portela, G. Papadakis, and J. C. Vassilicos. Turbulence dissipation and the role of coherent structures in the near wake of a square prism. *Physical Review Fluids*, 3(12):124609, 2018. XXI, 3, 18, 147, 148, 151, 183, 202, 203, 204, 205, 208

R. A. Antonia and B. R. Pearson. Effect of initial conditions on the mean energy dissipation rate and the scaling exponent. *Physical Review E*, 62(6):8086, 2000. 15

G. Aubard, P. S. Volpiani, X. Gloerfelt, and J. C. Robinet. Comparison of subgrid-scale viscosity models and selective filtering strategy for large-eddy simulations. *Flow, Turbulence and Combustion*, 91(3):497–518, 2013. 53

D. Barkley and R. D. Henderson. Three-dimensional Floquet stability analysis of the wake of a circular cylinder. *Journal of Fluid Mechanics*, 322:215–241, 1996. 25

G. K. Batchelor. *The theory of homogeneous turbulence*. Cambridge University Press, 1953. 2, 11, 12, 14, 15, 73

G. K. Batchelor and A. A. Townsend. Decay of isotropic turbulence in the initial period. *Proceedings of the Royal Society of London. Series A, Mathematical and Physical Sciences*, 193(1035):539–558, 1948. 14, 72

J. P. Batham. Pressure distributions on circular cylinders at critical Reynolds numbers. *Journal of Fluid Mechanics*, 57(2):209–228, 1973. 33

P. Batten, U. Goldberg, and S. Chakravarthy. Interfacing statistical turbulence closures with large-eddy simulation. *AIAA journal*, 42(3):485–492, 2004. 68

B. Bays-Muchmore and A. Ahmed. On streamwise vortices in turbulent wakes of cylinders. *Physics of Fluids A: Fluid Dynamics*, 5(2):387–392, 1993. 23

P. W. Bearman. Circular cylinder wakes and vortex-induced vibrations. *Journal of Fluids and Structures*, 27(5-6):648–658, 2011. 199

P. W. Bearman and T. Morel. Effect of free stream turbulence on the flow around bluff bodies. *Progress in Aerospace Sciences*, 20(2-3):97–123, 1983. 3, 32

P. Beaudan and P. Moin. Numerical experiments on the flow past a circular cylinder at sub-critical Reynolds number. Technical report, DTIC Document, 1994. 20, 24, 25, 116, 220

T. Behrens. OpenFOAM's basic solvers for linear systems of equations. *Chalmers, Department of Applied Mechanics*, 18(02), 2009. 220

W. H. Bell. The influence of turbulence on drag. *Ocean Engineering*, 6(3):329–340, 1979. 2, 33

W. H. Bell. Turbulence vs drag- some further considerations. *Ocean Engineering*, 10(1):47–63, 1983. 32

H. Bénard. A cinematographic study of eddies and ripples produced by towed obstacle (in French). *Comptes Rendus Academic des Sciences*, 147:970–972, 1908a. 21

H. Bénard. Formation of centers of circulation behind a moving obstacle (in French). *Comptes Rendus Academie des Science*, 147:970–972, 1908b. 21

L. C. Berselli. On the large-eddy simulation of the Taylor-Green vortex. *Journal of Mathematical Fluid Mechanics*, 7(2):S164–S191, 2005. 55

H. M. Blackburn and W. H. Melbourne. The effect of free-stream turbulence on sectional lift forces on a circular cylinder. *Journal of Fluid Mechanics*, 306: 267–292, 1996. 34, 134

T. Blackmore, W. M. J. Batten, and A. S. Bahaj. Inlet grid-generated turbulence for large-eddy simulations. *International Journal of Computational Fluid Dynamics*, 27(6-7):307–315, 2013. XV, 70, 80, 93, 94, 112

M. S. Bloor. The transition to turbulence in the wake of a circular cylinder. *Journal of Fluid Mechanics*, 19(2):290–304, 1964. 3, 32

M. Braza, P. H. H. M. Chassaing, and H. H. Minh. Numerical study and physical analysis of the pressure and velocity fields in the near wake of a circular cylinder. *Journal of Fluid Mechanics*, 165:79–130, 1986. 24

M. Braza, R. Perrin, and Y. Hoarau. Turbulence properties in the cylinder wake at high Reynolds numbers. *Journal of Fluids and Structures*, 22(6-7):757–771, 2006. 133, 185

M. Breda and O. R. H. Buxton. Influence of coherent structures on the evolution of an axisymmetric turbulent jet. *Physics of Fluids*, 30(3):035109, 2018. 18

M. Breuer. Large-eddy simulation of the subcritical flow past a circular cylinder: numerical and modeling aspects. *International Journal for Numerical Methods in Fluids*, 28(9):1281–1302, 1998a. 34

M. Breuer. Numerical and modeling influences on large-eddy simulations for the flow past a circular cylinder. *International Journal of Heat and Fluid Flow*, 19 (5):512–521, 1998b. 116

R. E. Britter, J. C. R. Hunt, and J. C. Mumford. The distortion of turbulence by a circular cylinder. *Journal of Fluid Mechanics*, 92(2):269–301, 1979. 2

L. W. B. Browne, R. A. Antonia, and D. A. Shah. Turbulent energy dissipation in a wake. *Journal of Fluid Mechanics*, 179:307–326, 1987. 117, 118

H. H. Bruun and P. O. A. L. Davies. An experimental investigation of the unsteady pressure forces on a circular cylinder in a turbulent cross flow. *Journal of Sound and Vibration*, 40(4):535–559, 1975. 33, 128

J. R. Bull and A. Jameson. Simulation of the compressible Taylor-Green vortex using high-order flux reconstruction schemes. In *7th AIAA Theoretical Fluid Mechanics Conference*, page 3210, 2014. XIII, 53, 54, 56, 59, 60

B. Cahalan. NASA Earth Observatory image from Landsat 7 satellite. `https://earthobservatory.nasa.gov/images/625`, 1999. XII, 21

G. S. Cardell. Flow past a circular cylinder with a permeable splitter plate. *California Institute of Technology*, 1993. 24, 31

H. G. Castro, R. R. Paz, J. L. Mroginski, and M. A. Storti. Evaluation of the proper coherence representation in random flow generation based methods.

Journal of Wind Engineering and Industrial Aerodynamics, 168:211–227, 2017. 45

L. Cea, J. Puertas, and L. Pena. Velocity measurements on highly turbulent free surface flow using ADV. *Experiments in Fluids*, 42(3):333–348, 2007. XIX, 163, 164, 165, 166

H. E. Cekli and W. van de Water. Tailoring turbulence with an active grid. *Experiments in Fluids*, 49(2):409–416, 2010. 13

H. Chanson. Acoustic doppler velocimetry (ADV) in the field and in laboratory: practical experiences. 2008. 163

G. Chen, Q. Xiong, P. J. Morris, E. G. Paterson, A. Sergeev, and Y. Wang. OpenFOAM for computational fluid dynamics. *Not. AMS*, 61(4):354–363, 2014. 41

J. G. Chen, Y. Zhou, R. A. Antonia, and T. M. Zhou. Characteristics of the turbulent energy dissipation rate in a cylinder wake. *Journal of Fluid Mechanics*, 835:271, 2018. XIII, XIX, 3, 26, 27, 117, 118, 146, 148, 149, 150, 155, 156, 158, 217

C. K. Cheung and W. H. Melbourne. Wind tunnel blockage effects on a circular cylinder in turbulent flows. In *7th Australasian Conference on Hydraulics and Fluid Mechanics 1980: Preprints of Papers*, page 127. Institution of Engineers, Australia, 1980. 33

H. Choi, W.P. Jeon, and J. Kim. Control of flow over a bluff body. *Annual Review of Fluid Mechanics*, 40:113–139, 2008. 29

C. K. Chyu and D. Rockwell. Near-wake structure of an oscillating cylinder: effect of controlled shear-layer vortices. *Journal of Fluid Mechanics*, 322:21–49, 1996. 32

G. Comte-Bellot and S. Corrsin. The use of a contraction to improve the isotropy of grid-generated turbulence. *Journal of Fluid Mechanics*, 25(4):657–682, 1966. 72

T. Dairay, M. Obligado, and J. C. Vassilicos. Non-equilibrium scaling laws in axisymmetric turbulent wakes. *Journal of Fluid Mechanics*, 781:166–195, 2015. 18

V. D'Allessandro, S. Montelpare, and R. Ricci. Detached-eddy simulations of the flow over a cylinder at $Re = 3900$ using OpenFOAM. *Computers & Fluids*, 136 (1):152–169, 2016. 120, 220

C. Dalton, Y. Xu, and J. C. Owen. The suppression of lift on a circular cylinder due to vortex shedding at moderate Reynolds numbers. *Journal of Fluids and Structures*, 15(3):617–628, 2001. 1

B. Dargahi. Controlling mechanism of local scouring. *Journal of Hydraulic Engineering*, 116(10):1197–1214, 1990. 1

L. Davidson and M. Billson. Hybrid LES-RANS using synthesized turbulent fluctuations for forcing in the interface region. *International Journal of Heat and Fluid Flow*, 27(6):1028–1042, 2006. 68

P. Davidson. *Turbulence: an introduction for scientists and engineers*. Oxford University Press, 2015. 9, 10, 40, 136, 137

E. De Villiers. The potential of large-eddy simulation for the modeling of wall bounded flows. *Imperial College of Science, Technology and Medicine, London (UK)*, 2006. 42

A. E. Deane, I. G. Kevrekidis, G. E. Karniadakis, and S. A. Orszag. Low-dimensional models for complex geometry flows: application to grooved channels and circular cylinders. *Physics of Fluids A: Fluid Dynamics*, 3(10):2337–2354, 1991. 189

J. W. Deardorff. A numerical study of three-dimensional turbulent channel flow at large Reynolds numbers. *Journal of Fluid Mechanics*, 41(2):453–480, 1970. 40, 43

J. DeBonis. Solutions of the Taylor-Green vortex problem using high-resolution explicit finite difference methods. In *51st AIAA Aerospace Sciences Meeting including the New Horizons Forum and Aerospace Exposition*, page 382, 2013. XIII, XIV, 53, 54, 56, 57, 58, 61, 62

C. Demartino and F. Ricciardelli. Aerodynamics of nominally circular cylinders: A review of experimental results for Civil Engineering applications. *Engineering Structures*, 137:76–114, 2017. 28, 32

N. S. Dhamankar, G. A. Blaisdell, and A. S. Lyrintzis. Overview of turbulent inflow boundary conditions for large-eddy simulations. *AIAA journal*, pages 1–18, 2017. 68

S. Discetti, I. B. Ziskin, T. Astarita, R. J. Adrian, and K. P. Prestridge. PIV measurements of anisotropy and inhomogeneity in decaying fractal generated turbulence. *Fluid Dynamics Research*, 45(6):061401, 2013. 18

S. Dong, G. E. Karniadakis, A. Ekmekci, and D. Rockwell. A combined direct numerical simulation-particle image velocimetry study of the turbulent near wake. *Journal of Fluid Mechanics*, 569:185–207, 2006. 30, 31, 116, 182, 196

D. L. Donoho and J. M. Johnstone. Ideal spatial adaptation by wavelet shrinkage. *Biometrika*, 81(3):425–455, 1994. 165

I. Eames, C. Jonsson, and P. B. Johnson. The growth of a cylinder wake in turbulent flow. *Journal of Turbulence*, (12):N39, 2011. 3, 34, 200

C. Eckart and G. Young. The approximation of one matrix by another of lower rank. *Psychometrika*, 1(3):211–218, 1936. 188

A. Fage and J. H. Warsap. The effects of turbulence and surface roughness on the drag of a circular cylinder. *British Aeronautical Research Council. Rep, Memo.*, 1, 1929. 3, 32, 128

J. Franke and W. Frank. Large-eddy simulation of the flow past a circular cylinder at Reynolds number 3900. *Journal of Wind Engineering and Industrial Aerodynamics*, 90(10):1191–1206, 2002. 1, 31, 116, 120

U. Frisch, P-L. Sulem, and M. Nelkin. A simple dynamical model of intermittent fully developed turbulence. *Journal of Fluid Mechanics*, 87(4):719–736, 1978. XII, 8

W. K. George. The decay of homogeneous isotropic turbulence. *Physics of Fluids A: Fluid Dynamics*, 4(7):1492–1509, 1992. 18

W. K. George and H. J. Hussein. Locally axisymmetric turbulence. *Journal of Fluid Mechanics*, 233:1–23, 1991. 11

W. K. George and H. Wang. The exponential decay of homogeneous turbulence. *Physics of Fluids*, 21(2):025108, 2009. 18

J. H. Gerrard. A disturbance-sensitive Reynolds number range of the flow past a circular cylinder. *Journal of Fluid Mechanics*, 22(1):187–196, 1965. 3, 32, 33, 184

J. H. Gerrard. The wakes of cylindrical bluff bodies at low Reynolds number. *Philosophical Transactions of the Royal Society of London A: Mathematical, Physical and Engineering Sciences*, 288(1354):351–382, 1978. 25

S. Goldstein. *Modern Developments in Fluid Dynamics*, volume 2. Dover, 1965. 32

R. Gomes-Fernandes, B. Ganapathisubramani, and J. C. Vassilicos. Particle image velocimetry study of fractal-generated turbulence. *Journal of Fluid Mechanics*, 711:306–336, 2012. 18, 77, 92

D. G. Goring and V. I. Nikora. Despiking acoustic doppler velocimeter data. *Journal of Hydraulic Engineering*, 128(1):117–126, 2002. 164

S. Goto and J. C. Vassilicos. Energy dissipation and flux laws for unsteady turbulence. *Physics Letters A*, 379(16-17):1144–1148, 2015. 3, 13, 18, 151, 205

S. Goto, Y. Saito, and G. Kawahara. Hierarchy of antiparallel vortex tubes in spatially periodic turbulence at high Reynolds numbers. *Physical Review Fluids*, 2(6):064603, 2017. 19

R. Hain, C. J. Kähler, and C. Tropea. Comparison of CCD, CMOS and intensified cameras. *Experiments in Fluids*, 42(3):403–411, 2007. 172

F. Hampp and R. P. Lindstedt. Fractal grid generated turbulence- a bridge to practical combustion applications. In *Fractal Flow Design: How to Design Bespoke Turbulence and Why*, pages 75–102. Springer, 2016. 17

Z. Hao, T. Zhou, L. P. Chua, and S. C. M. Yu. Approximations to energy and temperature dissipation rates in the far field of a cylinder wake. *Experimental Thermal and Fluid Science*, 32(3):791–799, 2008. 117

M. Hayakawa and F. Hussain. Three-dimensionality of organized structures in a plane turbulent wake. *Journal of Fluid Mechanics*, 206:375–404, 1989. 182

R. J. Hearst and P. Lavoie. Decay of turbulence generated by a square-fractal-element grid. *Journal of Fluid Mechanics*, 741:567–584, 2014. 17, 18, 78, 80, 89, 91, 112

M. Hideharu. Realization of a large-scale turbulence field in a small wind tunnel. *Fluid Dynamics Research*, 8(1-4):53, 1991. 13

J. E. Higham, W. Brevis, and C. J. Keylock. A rapid non-iterative proper orthogonal decomposition based outlier detection and correction for PIV data. *Measurement Science and Technology*, 27(12):125303, 2016. XX, 178, 179, 180

J. O. Hinze. *Turbulence: an introduction to its mechanism and theory*. New York: McGraw-Hill, 1975. 10, 105, 145

P. Holmes, J. L. Lumley, G. Berkooz, and C. W. Rowley. *Turbulence, coherent structures, dynamical systems and symmetry*. Cambridge University Press, 2012. 188

H. Huang, D. Dabiri, and M. Gharib. On errors of digital particle image velocimetry. *Measurement Science and Technology*, 8(12):1427, 1997. 172

J. F. Huang, Y. Zhou, and T. Zhou. Three-dimensional wake structure measurement using a modified PIV technique. *Experiments in Fluids*, 40(6):884–896, 2006. 182

L. Hufnagel, J. Canton, R. Örlü, O. Marin, E. Merzari, and P. Schlatter. The three-dimensional structure of swirl-switching in bent pipe flow. *Journal of Fluid Mechanics*, 835:86–101, 2018. 69

J. C. R. Hunt, A. A. Wray, and P. Moin. Eddies, streams, and convergence zones in turbulent flows. 1988. 59, 136, 137

D. Hurst and J. C. Vassilicos. Scalings and decay of fractal-generated turbulence. *Physics of Fluids*, 19(3):035103, 2007. 3, 17, 18, 65, 67, 72, 76, 78, 89, 92, 112

A. K. M. F. Hussain. Coherent structures- reality and myth. *The Physics of Fluids*, 26(10):2816–2850, 1983. 204

A. K. M. F. Hussain. Coherent structures and turbulence. *Journal of Fluid Mechanics*, 173:303–356, 1986. 22, 26, 117

A. K. M. F. Hussain and M. Hayakawa. Eduction of large-scale organized structures in a turbulent plane wake. *Journal of Fluid Mechanics*, 180:193–229, 1987. XIII, 3, 24, 26, 27, 117, 155

A. K. M. F. Hussain and W. C. Reynolds. The mechanics of an organized wave in turbulent shear flow. *Journal of Fluid Mechanics*, 41(2):241–258, 1970. 133, 147, 183, 185

J. C. Isaza, R. Salazar, and Z. Warhaft. On grid-generated turbulence in the near-and far field regions. *Journal of Fluid Mechanics*, 753:402–426, 2014. 18

N. Jarrin, S. Benhamadouche, D. Laurence, and R. Prosser. A synthetic-eddy method for generating inflow conditions for large-eddy simulations. *International Journal of Heat and Fluid Flow*, 27(4):585–593, 2006. 68

N. Jarrin, R. Prosser, J. C. Uribe, S. Benhamadouche, and D. Laurence. Reconstruction of turbulent fluctuations for hybrid RANS/LES simulations using a synthetic-eddy method. *International Journal of Heat and Fluid Flow*, 30(3): 435–442, 2009. 68

H. Jasak. *Error analysis and estimation for finite volume method with applications to fluid flow*. PhD thesis, University of London, 1996. 41

H. Jasak, A. Jemcov, and J. P. Maruszewski. Preconditioned linear solvers for large-eddy simulation. In *CFD 2007 Conference, CFD Society of Canada*, 2007. 220

J. Jeong and A. K. M. F. Hussain. On the identification of a vortex. *Journal of Fluid Mechanics*, 285:69–94, 1995. 137

H. Jiang. Separation angle for flow past a circular cylinder in the subcritical regime. *Physics of Fluids*, 32(1):014106, 2020. 22

W. P. Jones and B. E. Launder. The prediction of laminarization with a two-equation model of turbulence. *International Journal of Heat and Mass Transfer*, 15(2):301–314, 1972. 9, 39

C. J. Keylock. The Schur decomposition of the velocity gradient tensor for turbulent flows. *Journal of Fluid Mechanics*, 848:876–905, 2018. XVIII, 142, 143, 144

K. C. Kim, M. B. Lee, S. Y. Yoon, J. S. Boo, and H. H. Chun. Phase averaged velocity field in the near wake of a square cylinder obtained by a PIV method. *Journal of Visualization*, 5(1):29–36, 2002. 133, 185

M. Kiya, Y. Suzuki, M. Arie, and M. Hagino. A contribution to the free-stream turbulence effect on the flow past a circular cylinder. *Journal of Fluid Mechanics*, 115:151–164, 1982. 33, 128, 129

A. N. Kolmogorov. Dissipation of energy in locally isotropic turbulence. In *Dokl. Akad. Nauk SSSR*, volume 32, pages 16–18, 1941. 8

A. G. Kravchenko and P. Moin. Numerical studies of flow over a circular cylinder at Reynolds number 3900. *Physics of Fluids*, 12(2):403–417, 2000. 25, 30, 31, 116, 119, 184, 201

P-Å. Krogstad and P. A. Davidson. Is grid turbulence Saffman turbulence? *Journal of Fluid Mechanics*, 642:373–394, 2010. 71, 72

P-Å. Krogstad and P. A. Davidson. Freely decaying, homogeneous turbulence generated by multi-scale grids. *Journal of Fluid Mechanics*, 680:417–434, 2011. 17, 71, 74, 94

P-Å. Krogstad and P. A. Davidson. Near-field investigation of turbulence produced by multi-scale grids. *Physics of Fluids*, 24(3):035103, 2012. 72, 80, 89, 112

S. Laizet and J. C. Vassilicos. Multiscale generation of turbulence. *Journal of Multiscale Modelling*, 1(01):177–196, 2009. 17, 69

S. Laizet and J. C. Vassilicos. DNS of fractal-generated turbulence. *Flow, Turbulence and Combustion*, 87(4):673–705, 2011. 101, 102

S. Laizet, J. C. Vassilicos, and C. Cambon. Interscale energy transfer in decaying turbulence and vorticity-strain-rate dynamics in grid-generated turbulence. *Fluid Dynamics Research*, 45(6):061408, 2013. 18, 75

C. C. Landreth and R. J. Adrian. Measurement and refinement of velocity data using high image density analysis in particle image velocimetry. In *4th International Symposium on Applications of Laser Anemometry to Fluid Mechanics*, pages 6–14, 1988. 196

B. E. Launder and B. I. Sharma. Application of the energy-dissipation model of turbulence to the calculation of flow near a spinning disc. *Letters in Heat and Mass Transfer*, 1(2):131–137, 1974. 39, 49, 50

N. Lefeuvre, F. Thiesset, L. Djenidi, and R. A. Antonia. Statistics of the turbulent kinetic energy dissipation rate and its surrogates in a square cylinder wake flow. *Physics of Fluids*, 26(9):095104, 2014. 12, 27, 146

A. Leonard. Energy cascade in large-eddy simulations of turbulent fluid flows. *Advances in Geophysics*, 18:237–248, 1975. 42

M. Lesieur, O. Métais, and P. Comte. *Large-eddy simulations of turbulence*. Cambridge University Press, 2005. 46, 137

Y. Li, E. Perlman, M. Wan, Y. Yang, C. Meneveau, R. Burns, S. Chen, A. Szalay, and G. Eyink. A public turbulence database cluster and applications to study Lagrangian evolution of velocity increments in turbulence. *Journal of Turbulence*, (9):N31, 2008. XVII, 138, 139, 143

J. C. Lin, J. Towfighi, and D. Rockwell. Instantaneous structure of the near-wake of a circular cylinder: on the effect of Reynolds number. *Journal of Fluids and Structures*, 9(4):409–418, 1995a. 196

J. C. Lin, P. Vorobieff, and D. Rockwell. Three-dimensional patterns of streamwise vorticity in the turbulent near-wake of a cylinder. *Journal of Fluids and Structures*, 9(2):231–234, 1995b. 182

A. Lohrmann, R. Cabrera, and N. C. Kraus. Acoustic-doppler velocimeter (ADV) for laboratory use. In *Fundamentals and Advancements in Hydraulic Measurements and Experimentation*, pages 351–365. ASCE, 1994. 164

L. M. Lourenco and W. C. L. Shih. Characteristics of the plane turbulent near wake of a circular cylinder, a particle image velocimetry study. *Private communication published in Ong and Wallace (1996)*, 1993. XVII, XX, XXI, 30, 31, 116, 124, 130, 132, 157, 184, 191, 192, 193, 195, 201

L. M. Lourenco, S. Subramanian, and Z. Ding. Time series velocity field reconstruction from PIV data. *Measurement Science and Technology*, 8(12):1533, 1997. 133, 183, 185

J. L. Lumley. The structure of inhomogeneous turbulence. *In: A. M. Yaglom and V. I. Tatarski, Eds., Atmospheric Turbulence and Wave Propagation, Nauka, Moscow, 1967, pp. 166-178.*, 1967. 186

J. L. Lumley. Coherent structures in turbulence. In *Transition and Turbulence*, pages 215–242. Elsevier, 1981. 185

D. A. Lysenko, I. S. Ertesvåg, and K. E. Rian. Large-eddy simulation of the flow over a circular cylinder at Reynolds number 3900 using the OpenFOAM toolbox. *Flow, Turbulence and Combustion*, 89(4):491–518, 2012. 31, 34, 116

X. Ma, G. S. Karamanos, and G. E. Karniadakis. Dynamics and low-dimensionality of a turbulent near wake. *Journal of Fluid Mechanics*, 410: 29–65, 2000. XXI, 23, 28, 30, 31, 119, 122, 189, 191, 201

M. Matsumura and R. A. Antonia. Momentum and heat transport in the turbulent intermediate wake of a circular cylinder. *Journal of Fluid Mechanics*, 250: 651–668, 1993. 189

N. Mazellier and J. C. Vassilicos. Turbulence without Richardson-Kolmogorov cascade. *Physics of Fluids*, 22(7):075101, 2010. XIV, 18, 72, 77, 78, 92

A. Melling. Tracer particles and seeding for particle image velocimetry. *Measurement Science and Technology*, 8(12):1406, 1997. 174

F. R. Menter. Zonal two equation k-turbulence models for aerodynamic flows. *AIAA paper*, 23:2906, 1993. 40

F. R. Menter. Review of the shear-stress transport turbulence model experience from an industrial perspective. *International Journal of Computational Fluid Dynamics*, 23(4):305–316, 2009. 40

M. Meyer, S. Hickel, and N. A. Adams. Assessment of implicit large-eddy simulation with a conservative immersed interface method for turbulent cylinder flow. *International Journal of Heat and Fluid Flow*, 31(3):368–377, 2010. 31, 116

R. Mittal. Large-eddy simulation of flow past a circular cylinder. 1995. 220

R. Mittal and P. Moin. Suitability of upwind-biased finite difference schemes for large-eddy simulation of turbulent flows. *AIAA journal*, 35(8):1415–1417, 1997. 31, 116

M. S. Mohamed and J. C. Larue. The decay power law in grid-generated turbulence. *Journal of Fluid Mechanics*, 219:195–214, 1990. 14, 71, 72

P. Moin and R. D. Moser. Characteristic-eddy decomposition of turbulence in a channel. *Journal of Fluid Mechanics*, 200:471–509, 1989. 187

L. Mydlarski and Z. Warhaft. Passive scalar statistics in high-Péclet-number grid turbulence. *Journal of Fluid Mechanics*, 358:135–175, 1998. 13

K. Nagata, H. Suzuki, Y. Sakai, T. Hayase, and T. Kubo. Direct numerical simulation of turbulence characteristics generated by fractal grids. *International Review Physics*, 2(6):400–409, 2008. 70, 77

K. Nagata, Y. Sakai, T. Inaba, H. Suzuki, O. Terashima, and H. Suzuki. Turbulence structure and turbulence kinetic energy transport in multiscale/fractal-generated turbulence. *Physics of Fluids*, 25(6):065102, 2013. 18, 72, 92

K. Nagata, T. Saiki, Y. Sakai, Y. Ito, and K. Iwano. Effects of grid geometry on non-equilibrium dissipation in grid turbulence. *Physics of Fluids*, 29(1):015102, 2017. XV, 18, 67, 73, 88, 89, 91, 93, 94, 109

J. Nedić, S. Tavoularis, and I. Marusic. Dissipation scaling in constant-pressure turbulent boundary layers. *Physical Review Fluids*, 2(3):032601, 2017. 18

F. C. G. A Nicolleau. Fractal orifices in pipe. In *Fractal Flow Design: How to Design Bespoke Turbulence and Why*, pages 103–156. Springer, 2016. 17

H-J. Niemann and N. Hölscher. A review of recent experiments on the flow past circular cylinders. *Journal of Wind Engineering and Industrial Aerodynamics*, 33(1-2):197–209, 1990. 20

C. Norberg. Effects of Reynolds number and a low-intensity freestream turbulence on the flow around a circular cylinder. *Chalmers University, Goteborg, Sweden, Technological Publications*, 87(2), 1987. 20, 25, 191

C. Norberg. An experimental investigation of the flow around a circular cylinder: influence of aspect ratio. *Journal of Fluid Mechanics*, 258:287–316, 1994. 32

C. Norberg. LDV-measurements in the near wake of a circular cylinder. *ASME Paper No. FEDSM98-521*, 1998. 130

C. Norberg. Fluctuating lift on a circular cylinder: review and new measurements. *Journal of Fluids and Structures*, 17(1):57–96, 2003. 24, 25

L. Ong and J. Wallace. The velocity field of the turbulent very near wake of a circular cylinder. *Experiments in Fluids*, 20(6):441–453, 1996. 191, 238

S. A. Orszag, I. Staroselsky, W. S. Flannery, and Y. Zhang. Introduction to renormalization group modeling of turbulence. *Simulation and Modeling of Turbulent Flows*, pages 155–184, 1996. 50

S. Ossia and M. Lesieur. Energy backscatter in large-eddy simulations of three-dimensional incompressible isotropic turbulence. *Journal of Turbulence*, 1(1): 010–010, 2000. 72

H. Ouvrard, B. Koobus, A. Dervieux, and M. V. Salvetti. Classical and variational multiscale LES of the flow around a circular cylinder on unstructured grids. *Computers & Fluids*, 39(7):1083–1094, 2010. 31

N. Park, S. Lee, J. Lee, and H. Choi. A dynamic subgrid-scale eddy viscosity model with a global model coefficient. *Physics of Fluids*, 18(12):125109, 2006. 31

P. Parnaudeau, J. Carlier, D. Heitz, and E. Lamballais. Experimental and numerical studies of the flow over a circular cylinder at Reynolds number 3900. *Physics of Fluids*, 20(8):085101, 2008. XVII, XX, XXI, XXII, 30, 31, 119, 120, 121, 122, 123, 124, 130, 131, 132, 157, 176, 182, 184, 189, 190, 191, 192, 193, 194, 195, 201

S. V. Patankar and D. B. Spalding. A calculation procedure for heat, mass and momentum transfer in three-dimensional parabolic flows. In *Numerical Prediction of Flow, Heat Transfer, Turbulence and Combustion*, pages 54–73. Elsevier, 1983. 220

I. Paul, G. Papadakis, and J. C. Vassilicos. Direct numerical simulation of heat transfer from a cylinder immersed in the production and decay regions of grid-element turbulence. 2018. 3

J. B. Perot and J. Gadebusch. A self-adapting turbulence model for flow simulation at any mesh resolution. *Physics of Fluids*, 19(11):115105, 2007. XIII, 49, 50, 51

R. Perrin, M. Braza, E. Cid, S. Cazin, A. Barthet, A. Sevrain, C. Mockett, and F. Thiele. Phase averaged turbulence properties in the near wake of a circular cylinder at high Reynolds number using POD. In *Proc. 13th Int. Symp. Applications of Laser Techniques to Fluid Mechanics, Lisbon, Portugal*, 2006. XX, 186, 189, 190

R. Perrin, E. Cid, S. Cazin, A. Sevrain, M. Braza, F. Moradei, and G. Harran. Phase-averaged measurements of the turbulence properties in the near wake of a circular cylinder at high Reynolds number by 2C-PIV and 3C-PIV. *Experiments in Fluids*, 42(1):93–109, 2007. 183

A. E. Perry and M. S. Chong. A description of eddying motions and flow patterns using critical-point concepts. *Annual Review of Fluid Mechanics*, 19(1):125–155, 1987. XXII, 138

R. Poletto, T. Craft, and A. Revell. A new divergence free synthetic-eddy method for the reproduction of inlet flow conditions for LES. *Flow, Turbulence and Combustion*, 91(3):519–539, 2013. XIV, 68, 69

S. B. Pope. *Turbulent Flows*. IOP Publishing, 2001. 8, 10, 29, 39, 42, 49, 50, 72, 73, 91

A. Prasad and C. H. K. Williamson. The instability of the shear layer separating from a bluff body. *Journal of Fluid Mechanics*, 333:375–402, 1997a. 25, 32, 34, 184

A. Prasad and C. H. K. Williamson. Three-dimensional effects in turbulent bluff-body wakes. *Journal of Fluid Mechanics*, 343:235–265, 1997b. 25, 188

M. A. Prsic, M. C. Ong, B. Pettersen, and D. Myrhaug. Large-eddy simulations of flow around a smooth circular cylinder in a uniform current in the subcritical flow regime. *Ocean Engineering*, 77:61–73, 2014. 31, 116

M. Raffel, C. E. Willert, F. Scarano, C. J. Kähler, S. T. Wereley, and J. Kompenhans. *Particle image velocimetry: a practical guide*. Springer, 2018. 172, 174

M. Ricci, L. Patruno, S. de Miranda, and F. Ubertini. Flow field around a 5:1 rectangular cylinder using LES: Influence of inflow turbulence conditions, spanwise domain size and their interaction. *Computers & Fluids*, 149:181–193, 2017. 2, 67

L. F. Richardson. *Weather prediction by numerical process*. Cambridge University Press, 1922. 8

E. Robertson, V. Choudhury, S. Bhushan, and D. K. Walters. Validation of OpenFOAM numerical methods and turbulence models for incompressible bluff body flows. *Computers & Fluids*, 123:122–145, 2015. 41, 221

A. Roshko. *On the development of turbulent wakes from vortex streets*. PhD thesis, California Institute of Technology, 1952. 21, 25, 188

P. G. Saffman. Note on decay of homogeneous turbulence. *The Physics of Fluids*, 10(6):1349–1349, 1967. 14, 71, 72

P. Sagaut. *Large-eddy simulation for incompressible flows: an introduction*. Springer Science & Business Media, 2006. 40, 42, 43

Y. Sakai and J. C. Vassilicos. *Fractal flow design: how to design bespoke turbulence and why*, volume 568. Springer, 2016. 3, 17, 116

M. Samimy and S. K. Lele. Motion of particles with inertia in a compressible free shear layer. *Physics of Fluids A: Fluid Dynamics*, 3(8):1915–1923, 1991. 175

R. E. Seoud and J. C. Vassilicos. Dissipation and decay of fractal-generated turbulence. *Physics of Fluids*, 19(10):105108, 2007. 3, 18, 65, 72, 73, 89

E. Sergent. *Vers une methodologie de couplage entre la Simulation des Grandes Echelles et LES modeles statistiques*. PhD thesis, Ecully, Ecole centrale de Lyon, 2002. 68

W. C. L. Shih, C. Wang, D. Coles, and A. Roshko. Experiments on flow past rough circular cylinders at large Reynolds numbers. *Journal of Wind Engineering and Industrial Aerodynamics*, 49(1-3):351–368, 1993. 32

L. F. G. Simmons and C. Salter. Experimental investigation and analysis of the velocity variations in turbulent flow. *Proceedings of the Royal Society of London. Series A, Containing Papers of a Mathematical and Physical Character*, 145(854):212–234, 1934. 14

S. P. Singh and S. Mittal. Flow past a cylinder: shear layer instability and drag crisis. *International Journal for Numerical Methods in Fluids*, 47(1):75–98, 2005. 23

L. Sirovich. Turbulence and the dynamics of coherent structures. i. coherent structures. *Quarterly of Applied Mathematics*, 45(3):561–571, 1987. 186, 187

A. Skillen, A. Revell, and T. Craft. Accuracy and efficiency improvements in synthetic-eddy methods. *International Journal of Heat and Fluid Flow*, 62: 386–394, 2016. 69

L. Skrbek and S. R. Stalp. On the decay of homogeneous isotropic turbulence. *Physics of Fluids*, 12(8):1997–2019, 2000. 14

J. Smagorinsky. General circulation experiments with the primitive equations: I. the basic experiment. *Monthly weather review*, 91(3):99–164, 1963. 40, 57, 65

P. Spalart and S. Allmaras. A one-equation turbulence model for aerodynamic flows. In *30th Aerospace Sciences Meeting and Exhibit*, page 439, 1992. 39

C. G. Speziale, S. Sarkar, and T. B. Gatski. Modelling the pressure-strain correlation of turbulence: an invariant dynamical systems approach. *Journal of Fluid Mechanics*, 227:245–272, 1991. 48

K. R. Sreenivasan. On the scaling of the turbulence energy dissipation rate. *The Physics of Fluids*, 27(5):1048–1051, 1984. XII, 15, 16

K. R. Sreenivasan and R. A. Antonia. The phenomenology of small-scale turbulence. *Annual Review of Fluid Mechanics*, 29(1):435–472, 1997. 9, 145

R. Stäger and H. Eckelmann. The effect of endplates on the shedding frequency of circular cylinders in the irregular range. *Physics of Fluids A: Fluid Dynamics*, 3(9):2116–2121, 1991. 168

J. Sung and J. Y. Yoo. Three-dimensional phase averaging of time-resolved PIV measurement data. *Measurement Science and Technology*, 12(6):655, 2001. 133, 185

D. Surry. Some effects of intense turbulence on the aerodynamics of a circular cylinder at subcritical Reynolds number. *Journal of Fluid Mechanics*, 52(3): 543–563, 1972. 33, 128, 129

H. Suzuki, K. Nagata, Y. Sakai, and T. Hayase. Direct numerical simulation of turbulent mixing in regular and fractal grid turbulence. *Physica Scripta*, 2010 (T142):014065, 2010. 70

H. Suzuki, K. Nagata, Y. Sakai, T. Hayase, Y. Hasegawa, and T. Ushijima. Direct numerical simulation of fractal-generated turbulence. *Fluid Dynamics Research*, 45(6):061409, 2013. 70

C. R. Symes and L. E. Fink. Effects of external turbulence upon the flow past cylinders. In *Structure and Mechanisms of Turbulence I*, pages 86–102. Springer, 1978. 33, 199

G. R. Tabor and M. H. Baba-Ahmadi. Inlet conditions for large-eddy simulation: a review. *Computers & Fluids*, 39(4):553–567, 2010. 67

K. Taira, S. L. Brunton, S. T. M. Dawson, C. W. Rowley, T. Colonius, B. J. McKeon, O. T. Schmidt, S. Gordeyev, V. Theofilis, and L. S. Ukeiley. Modal analysis of fluid flows: An overview. *AIAA journal*, pages 4013–4041, 2017. 186, 188

T. Tanaka and J. K. Eaton. A correction method for measuring turbulence kinetic energy dissipation rate by PIV. *Experiments in Fluids*, 42(6):893–902, 2007. 148

S. Taneda. Experimental investigation of the wakes behind cylinders and plates at low Reynolds numbers. *Journal of the Physical Society of Japan*, 11(3): 302–307, 1956. 23

G. I. Taylor. Diffusion by continuous movements. *Proceedings of the London Mathematical Society*, 2(1):196–212, 1922. 14

G. I. Taylor. Statistical theory of turbulence. *Proceedings of the Royal Society of London. Series A, Mathematical and Physical Sciences*, 151(873):421–444, 1935. 11, 14, 15, 183, 202

G. I. Taylor and A. E. Green. Mechanism of the production of small eddies from large ones. *Proc. R. Soc. Lond. A*, 158(895):499–521, 1937. 53

H. Tennekes and J. L. Lumley. *A first course in turbulence*. MIT press, 1972. 16, 202

F. Thiesset, L. Danaila, and R. A. Antonia. Dynamical effect of the total strain induced by the coherent motion on local isotropy in a wake. *Journal of Fluid Mechanics*, 720:393–423, 2013. 148

R. E. Thomas, L. Schindfessel, S. J. McLelland, S. Creëlle, and T. De Mulder. Bias in mean velocities and noise in variances and covariances measured using a multistatic acoustic profiler: The Nortek Vectrino Profiler. *Measurement Science and Technology*, 28(7):075302, 2017. 163

M. Thompson, K. Hourigan, and J. Sheridan. Three-dimensional instabilities in the cylinder wake. In *International Colloquium on Jets, Wakes and Shear Layers, CSIRO, DBCE, Highett. Melbourne, Australia, April*, pages 18–20, 1994. 23

F. Tremblay. *Direct and large-eddy simulation of flow around a circular cylinder at subcritical Reynolds numbers*. PhD thesis, Technische Universität München, 2002. 31

R. Tunstall, D. Laurence, R. Prosser, and A. Skillen. Large-eddy simulation of a T-Junction with upstream elbow: The role of Dean vortices in thermal fatigue. *Applied Thermal Engineering*, 107:672–680, 2016. 69

P. C. Valente and J. C. Vassilicos. The decay of turbulence generated by a class of multiscale grids. *Journal of Fluid Mechanics*, 687:300–340, 2011. XVI, 18, 49, 72, 77, 91, 109, 111

P. C. Valente and J. C. Vassilicos. Universal dissipation scaling for non-equilibrium turbulence. *Physical Review Letters*, 108(21):214503, 2012. 18, 19, 105

P. C. Valente and J. C. Vassilicos. The non-equilibrium region of grid-generated decaying turbulence. *Journal of Fluid Mechanics*, 744:5–37, 2014. 19

M. Van Dyke. *An Album of Fluid Motion*, volume 176. Parabolic Press Stanford, 1982. XII, 14, 22

J. C. Vassilicos. Dissipation in turbulent flows. *Annual Review of Fluid Mechanics*, 47:95–114, 2015. 9, 15, 16, 49, 65, 67, 92, 101, 109, 145, 183, 202, 206, 207

P. Vieillefosse. Internal motion of a small element of fluid in an inviscid flow. *Physica A: Statistical Mechanics and its Applications*, 125(1):150–162, 1984. 138

T. Von Karman and L. Howarth. On the statistical theory of isotropic turbulence. *Proceedings of the London Mathematical Society*, 164(917):192–215, 1938. 11, 70

G. Voulgaris and J. H. Trowbridge. Evaluation of the acoustic Doppler velocimeter (ADV) for turbulence measurements. *Journal of Atmospheric and Oceanic Technology*, 15(1):272–289, 1998. 162

J. M. Wallace. Twenty years of experimental and direct numerical simulation access to the velocity gradient tensor: What have we learned about turbulence? *Physics of Fluids*, 21(2):021301, 2009. 3, 10, 117, 145

M. Wan, S. Chen, G. Eyink, C. Meneveau, E. Perlman, R. Burns, Y. Li, A. Szalay, and S. Hamilton. Johns Hopkins Turbulence Database (JHTDB). `http://turbulence.pha.jhu.edu/datasets.aspx.`, 2016. 138

Z. J. Wang, K. Fidkowski, R. Abgrall, F. Bassi, D. Caraeni, A. Cary, H. Deconinck, R. Hartmann, K. Hillewaert, H. T. Huynh, et al. High-order CFD methods: current status and perspective. *International Journal for Numerical Methods in Fluids*, 72(8):811–845, 2013. 53, 54, 57

H. G. Weller, G. Tabor, H. Jasak, and C. Fureby. A tensorial approach to computational continuum mechanics using object-oriented techniques. *Computers in Physics*, 12(6):620–631, 1998. 41

J. Westerweel. *Digital particle image velocimetry: Theory and application*. PhD thesis, TU Delft, Delft University of Technology, 1993. 196

J. Westerweel and F. Scarano. Universal outlier detection for PIV data. *Experiments in Fluids*, 39(6):1096–1100, 2005. 178

C. E. Willert and M. Gharib. Digital particle image velocimetry. *Experiments in Fluids*, 10(4):181–193, 1991. 174

C. H. K. Williamson. The existence of two stages in the transition to three-dimensionality of a cylinder wake. Technical report, DTIC Document, 1988. XII, 23, 24, 25

C. H. K. Williamson. Vortex dynamics in the cylinder wake. *Annual Review of Fluid Mechanics*, 28(1):477–539, 1996. 2, 20, 23, 32, 142, 188

C. H. K. Williamson and R. Govardhan. Vortex-induced vibrations. *Annual Review of Fluid Mechanics*, 36:413–455, 2004. 29

C. H. K. Williamson and R. Govardhan. A brief review of recent results in vortex-induced vibrations. *Journal of Wind Engineering and Industrial Aerodynamics*, 96(6-7):713–735, 2008. 29

C. H. K. Williamson and A. Roshko. Vortex formation in the wake of an oscillating cylinder. *Journal of Fluids and Structures*, 2(4):355–381, 1988. 25

J. G. Wissink and W. Rodi. Numerical study of the near wake of a circular cylinder. *International Journal of Heat and Fluid Flow*, 29(4):1060–1070, 2008. 31

R. W. Wlezien and J. L. Way. Techniques for the experimental investigation of the near wake of a circular cylinder. *AIAA journal*, 17(6):563–570, 1979. 185

J. Wu, J. Sheridan, M. C. Welsh, K. Hourigan, and M. Thompson. Longitudinal vortex structures in a cylinder wake. *Physics of Fluids*, 6(9):2883–2885, 1994. 182

X. Wu. Inflow turbulence generation methods. *Annual Review of Fluid Mechanics*, 49:23–49, 2017. 67

X. Wu, J. Schlüter, P. Moin, H. Pitsch, G. Iaccarino, and F. Ham. Computational study on the internal layer in a diffuser. *Journal of Fluid Mechanics*, 550:391–412, 2006. 67

M. W. Yiu, Y. Zhou, T. Zhou, and L. Cheng. Reynolds number effects on three-dimensional vorticity in a turbulent wake. *AIAA journal*, 42(5):1009–1016, 2004. 209

A. Yoshizawa. Statistical theory for compressible turbulent shear flows, with the application to subgrid modeling. *The Physics of Fluids*, 29(7):2152–2164, 1986. 47, 57, 65, 75, 121

M. M. Zdravkovich. Conceptual overview of laminar and turbulent flows past smooth and rough circular cylinders. *Journal of Wind Engineering and Industrial Aerodynamics*, 33(1-2):53–62, 1990. 23, 32

M. M. Zdravkovich. *Flow around Circular Cylinders: Volume 1: Fundamentals*, volume 1. Oxford University Press, 1997. 20, 23, 25, 28

Y. Zhou, K. Nagata, Y. Sakai, H. Suzuki, Y. Ito, O. Terashima, and T. Hayase. Relevance of turbulence behind the single square grid to turbulence generated by regular-and multiscale-grids. *Physics of Fluids*, 26(7):075105, 2014. 70

Y. Zhou, Y. Huang, and Z. Mu. Large-eddy simulation of the influence of synthetic inlet turbulence on a practical aeroengine combustor with counter-rotating swirler. *Proceedings of the Institution of Mechanical Engineers, Part G: Journal of Aerospace Engineering*, page 0954410017745900, 2017. 67